

https://dspace.org/

Development of PGMs-modified TiAl-based alloys and their properties: Development of PGMs-modified TiAl-based alloy coatings via mechanical alloying and thermal spray

Mwamba, Ilunga Alain

2017

https://hdl.handle.net/10539/25176

Mwamba, Ilunga Alain (2017) Development of PGMs-modified TiAl-based alloys and their properties, University of the Witwatersrand, <https://hdl.handle.net/10539/25176>

Downloaded from a DSpace repository. https://dspace.org/



DEVELOPMENT OF PGMS-MODIFIED TiAl-BASED ALLOYS AND THEIR PROPERTIES

by

ILUNGA ALAIN MWAMBA, MSc

A thesis submitted to the Faculty of Engineering and the Built Environment, University of the Witwatersrand, in fulfillment of the requirements for the degree of **DOCTOR OF PHILOSOPHY.**

Johannesburg, August 2017

DECLARATION

I declare that this thesis is my own original and unaided work. It is being submitted for the degree of Doctor of Philosophy in the University of the Witwatersrand and has not been submitted before, in whole or in part, for any degree or examination at any other university or institution.

Ilunga Alain Mwamba

Johannesburg, August 10, 2017

DEDICATION

To my lovely wife Honorine and my children Ariel, Nathan, Aisha and Jordan for your support, encouragement, love and friendship during challenging times.

To my late parents for showing the path of success.

ABSTRACT

Titanium aluminides Ti_3Al (α_2), γ-TiAl and $TiAl_3$ have received much attention for potential applications where light weight for energy saving, room temperature corrosion resistance in aqueous solutions, high-temperature oxidation resistance, or where combinations of the above are needed.

Gamma-TiAl of composition Ti-47.5 at.% Al with additions of platinum group metals (PGMs: Pt, Pd, Ru and Ir) was investigated for microstructure, hardness, room temperature aqueous corrosion, high-temperature oxidation resistance, mechanical alloying and consolidation by spark plasma sintering, and coating on titanium Grade 2 and Ti-6Al-4V substrates. Gamma-TiAl of Ti-47.5 at.% Al produced by melting and casting gave a microstructure consisting of γ grains and lamellar grains with alternating of α_2 and γ phase lamellae. Additions of 0.2, 1.0, 1.5, and 2.0 at.% PGMs introduced new phases of high PGM contents. The γ and lamellar phases were still present.

The additions of PGMs significantly improved the aqueous corrosion properties at room temperature, by improving the pitting corrosion resistance of the γ-TiAl alloy by modifying its hydrogen evolution of the cathodic reaction. The presence of PGMs also influenced the oxidation behaviour of γ-TiAl at 950°by forming the Z-phase which stabilized a continuous protective Al_2O_3 phase. However, Ti-47.5 at.% Al, being a two-phase alloy ($\alpha_2+\gamma$), PGMs could not sustain a stable Z-phase, as it transformed into an oxygen supersaturated Ti_3Al, which subsequently led to the formation of $TiO_2+Al_2O_3$, a non-protective oxide mixture. The optimal PGM addition to γ-TiAl was 0.5 at.%, with iridium giving the best room temperature corrosion and high-temperature oxidation resistance.

Mechanical alloying of Ti and Al pure powders with PGM additions gave powders where α_2 and γ were only identified after heat treatment. Consolidation of the mechanically alloyed powders by spark plasma sintering gave different microstructures from the cast alloys, with continuous α_2 and γ phases and evenly distributed nanometer-sized alumina, and much higher hardnesses.

Cold spraying the mechanically alloyed powders on to titanium Grade 2 and Ti-6Al-4V substrates gave coatings of irregular thickness, dense near the substrates with porosity at the top, giving poor oxidation protection.

ACKNOWLEDGEMENTS

First of all, I thank the Almighty God for establishing me in health to complete this thesis.

I wish to express my sincere thanks to my supervisor, Prof. Lesley A. Cornish, for her guidance, encouragement and support throughout this work, and Mintek, for providing the financial and logistical support.

I would also like to extend my gratitude to the following people:

- My wife, Honorine, for her love, patience and encouragement,
- Dr Jones M. Papo for his continuous support throughout this work,
- Prof. Elma van der Lingen, for a guidance and support to run the corrosion tests,
- Dr Sabine Verryn for help with the collection of XRD data,
- Mr Edson Muhuma for helping with casting and metallography sample preparation.

I take this opportunity to record my sincere thanks to all AMD staff at Mintek for their encouragement and support.

Finally, I place on record my gratitude to all who, directly or indirectly, have lent their helping hand in this journey.

LIST OF SYMBOLS AND ACRONYMS

(αTi): Titanium solid in α phase

(βTi): Titanium solid in β phase

α_2: Titanium aluminide Ti_3Al

γ: Titanium aluminide TiAl

γ-TiAl: titanium aluminide alloy consisting of α_2 and γ phases

δ, ε, ζ, η,…: Intermediate phases

θ: Bragg angle

fcc: Face centred cubic (crystal structure)

bcc: Body centred cubic (crystal structure)

cph: Compact packed hexagonal (crystal structure)

σ: Stress in the Von Mises formula

a, b, c: Lattices parameters

Al_2O_3: Aluminium oxide (Alumina)

TiO_2: titanium dioxide (Titania)

Ti_2O_3: Titanium (III) oxide

G: Phase in the Ti-Al-Ru system

τ_1, τ_2, τ_3: Phases in the Ti-Al-Pt and Ti-Al-Pd ternary systems

B2: Ordered bcc phase

$Ti_5Al_3O_2$: Z-phase developing during oxidation of γ-TiAl alloys

PGM(s): Platinum Group Metal(s)

E_{pass}: Passivation potential

E_{corr}: Corrosion potential

E_{trans}: Transpassive potential

i_{crit}: Critical current density

i_o: Exchange current density

ASTM: American Society for Standard Materials

MPIF: Metal Powder Industries Federation

PCA: Process control agent

BPR: Ball-to-powder ratio

DSC: Differential scanning calorimetry

TGA: Thermogravimetric analysis

SEM: Scanning electron microscopy

EDX: Energy-dispersive X-ray spectroscopy

XRD: X-ray diffractometry

SST: Supersonic Spray Technologies

TABLE OF CONTENTS

DECLARATION ..... **II**

DEDICATION ..... **III**

ABSTRACT ..... **IV**

ACKNOWLEDGEMENTS ..... **V**

LIST OF SYMBOLS AND ACRONYMS ..... **VI**

TABLE OF CONTENTS ..... **VIII**

LIST OF FIGURES ..... **XV**

LIST OF TABLES ..... **XXIII**

CHAPTER 1 INTRODUCTION **1**

1.1 Titanium aluminides for high-temperature structural applications 1

1.2 Limitations and challenges in the applications of titanium aluminide alloys 1

1.3 The need to address the manufacturing challenges and improve the properties of titanium aluminide alloys 3

1.4 Hypothesis 5

1.5 Aim and objective of the study 5

CHAPTER 2 LITERATURE SURVEY **7**

2.1 Introduction to intermetallic compounds 7

2.1.1 Definition of intermetallic compounds 7

2.1.2 Ordering and superlattice 8

2.1.3 Long-range and short-range ordering 8

2.1.4 Common types of superlattice 8

2.1.5 Toughness and ductility in intermetallic compounds 10
2.2 γ-TiAl-based alloys 11
2.2.1 Microstructure formation in plain and alloyed γ-TiAl 11
2.2.2 Mechanical properties of γ-TiAl alloys 16
2.2.3 Physical properties of plain and alloyed γ-TiAl 17
2.2.4 Oxidation resistance 18
2.2.5 Effect of alloying elements on the properties of γ-TiAl 19
2.2.6 Processing of γ-TiAl alloys 20
2.2.7 Gamma TiAl and PGMs 21
2.2.8 Gamma-TiAl as coating materials 26
2.3 Corrosion and oxidation of TiAl-based alloys 27
2.3.1 Corrosion of TiAl-based alloys 27
2.3.2 Principles of cathodic modification 29
2.3.3 Alloys cathodically modified with noble metals 32
2.3.4 Cathodic modification 33
2.4 Reduction of titanium corrosion rate with addition of noble metals 33
2.5 Aqueous corrosion of intermetallic compounds 34
2.6 Powder characterisation 40
2.6.1 Apparent density, tap density and flow rate 40
2.6.2 Particle size and particle size distribution 40
2.6.3 Particle morphology 41
2.6.4 Surface area and internal structure of particles 42

2.7 Sintered compact characterisation 42

2.8 Consolidation technique-property relationship 42

2.9 High-velocity oxyfuel (HVOF) spraying and cold spray spraying as coating techniques44

2.9.1 Thermal Spray 44

2.9.2 High-velocity oxyfuel (HVOF) 44

2.9.3 Cold Spraying 44

2.9.4 Characterisation of coatings and interfaces 48

2.10 Ti-6Al-4V / Titanium Grade 2 versus plain and alloyed γ-TiAl 48

2.10.1 Ti-6Al-4V 49

2.10.2 Titanium Grade 2 52

CHAPTER 3 EXPERIMENTAL PROCEDURE 53

3.1 Preparation of γ-TiAl cast alloys 53

3.2 Sample preparation and hardness evaluation 54

3.3 Heat treatment, oxidation test and thermogravimetric analysis (TGA) 54

3.4 Electrochemical tests 55

3.5 Characterisation of the bulk and mechanically alloyed samples 56

3.5.1 Phase identification 56

3.5.2 Volume fraction of the constitutive phases 56

3.5.3 EDX mapping and line scan analysis 56

3.6 Preparation of mechanically alloyed γ-TiAl 57

3.6.1 Powder preparation 57

3.6.2 Powder characterisation 58

3.7 Powder sintering 59

3.8 Cold spray coating 59

3.8.1 Operation 63

3.8.2 Process optimisation 65

3.8.3 Heat treatment of coated samples 65

CHAPTER 4 PROPERTY EVOLUTION WITH ADDITIONS OF PLATINUM GROUP METALS 66

4.1 Introduction 66

4.2 Microstructure characterisation of cast alloys 66

4.2.1 Plain γ-TiAl alloy 66

4.2.2 PGM-alloyed γ-TiAl 68

4.3 X-ray Mapping 73

4.4 XRD analyses 73

4.5 Thermogravimetric analysis (TGA) 83

4.6 Hardness 84

4.7 Discussion 86

CHAPTER 5 CORROSION BEHAVIOUR IN AQUEOUS SOLUTIONS 88

5.1 Electrochemical behaviour 88

5.2 Effect of alloying additions on corrosion potential 91

5.2.1 Corrosion of plain TiAl 91

5.2.2 γ-TiAl alloyed with PGMs 92

5.2.3 Attempted prediction of the effect of continuous PGM increases on the corrosion potential 101
5.2.4 Corrosion rate and potential increase 105
5.2.5 Cathodic modification 105
5.2.6 Analysis of different parameters affecting the corrosion behaviour 113
5.3 Discussion 124
5.4 Conclusions 127
CHAPTER 6 HIGH-TEMPERATURE OXIDATION BEHAVIOUR 129
6.1 Oxidation behaviour tests 129
6.1.1 Thermogravimetric analysis (TGA) 129
6.1.2 Microstructural characterisation of oxidised alloys 129
6.2 Discussion 138
6.3 Summary 146
CHAPTER 7 MECHANICAL ALLOYING AND CONSOLIDATION BY SPARK PLASMA SINTERING 148
7.1 Introduction 148
7.2 Powder characterisation of mechanically alloyed powders 148
7.2.1 Apparent density, particle size distribution and particle morphology 148
7.2.2 Phase identification 152
7.3 Transformations upon heating and high-temperature oxidation behaviour 158
7.4 Consolidation by spark plasma sintering (SPS) 160
7.4.1 Microstructure 161

7.4.2 Hardness 162
7.5 Discussion 164
CHAPTER 8 COLD SPRAY COATING 168
8.1 Process optimisation 168
8.2 Surface preparation 169
8.3 Characterisation of the substrates and coatings 169
8.3.1 Chemical composition and hardness of the substrates 169
8.3.2 Microstructure of the substrate 170
8.3.3 Coating microstructure 172
8.3.4 Interface analysis 176
8.4 Effect of heat treatment on the Ti-6Al-4V and titanium Grade 2 substrates 178
8.5 Discussion 181
8.6 Summary 183
CHAPTER 9 GENERAL DISCUSSION 184
9.1 Introduction 184
9.2 Microstructure of the γ-TiAl alloy 185
9.3 Effect of PGM additions on corrosion behaviour of γ-TiAl in aqueous solutions 186
9.4 Effect of PGM additions on high-temperature oxidation behaviour of γ-TiAl 189
9.5 Mechanical alloying and consolidation by spark plasma sintering 190
9.6 Coating of MA γ-TiAl powder onto titanium Grade 2 and Ti-6Al-4V 193
CHAPTER 10 CONCLUSIONS AND RECOMMENDATIONS 196
REFERENCES 198

APPENDIX: LIST OF JOURNAL AND CONFERENCE PAPERS PUBLISHED IN THE COURSE OF THE PHD WORK..... 224

LIST OF FIGURES

*Figure 2.1. Crystal structure and unit cell of (a) γ-TiAl and (b) α_2-Ti_3Al (*Ramanujan, 2000*).*..... 12

Figure 2.2. Partial Ti-Al phase diagram near the stoichiometric TiAl composition shown in Figure 2.3b (Huang and Chesnutt, 1994)...... 13

Figure 2.3. Ti-Al diagram of (a) congruent-type (Grytsiv et al., 2003; Raghavan, 2005), and (b) peritectic type (Schuster and Palm, 2006)...... 15

Figure 2.4. Three typical microstructures of TiAl: (a) fully lamellar, (b) duplex, and (c) near fully lamellar (Wu, 2006)...... 16

Figure 2.5. Schematic representation of the oxide scale structure on Ti-50Al after oxidation in air at 900ºC before oxide scale breakaway (Schmitz-Niederau and Schutze, 1999)...... 19

Figure 2.6. Isothermal section at 770°C of the Ti-Al-Ru system (at.%) (Khataee et al., 1989b and 1989c). 23

Figure 2.7. Partial Al-Pd-Ti isothermal section at 930°C in the Pd-lean region (Zaikana et al, 2000). 24

Figure 2.8. Partial Al-Pt-Ti isothermal section at 950°C for Pt-poor side (Ding et al., 2000). 25

Figure 2.9. Ir-rich Al-Ir-Ti partial isothermal section at 1650°C (Raghavan, 2008). 25

Figure 2.10. Principles of cathodic modification: a) active, b) passive-active, c) passive, and d) transpassive, after Potgieter et al. (1990)...... 31

Figure 2.11. Effect of platinum and palladium on the corrosion rate of titanium in a) boiling chloridric acid solution, and b) sulphuric acid solutions (Stern and Wissenberg, 1959b)...... 34

Figure 2.12. Influence of alloying elements on the dissolution potential of aluminium alloys (Burleigh et al., 1993). 36

Figure 2.13. Typical polarization curves for Al, Ni and Ni_3Al in a 0.5M NaCl solution (Ricker et al., 1990). 38

Figure 2.14. Typical polarization curves for Al, Ni and Ni_3Al in a 0.5M H_2SO_4 solution (Ricker et al., 1990). 38

Figure 2.15. Typical polarization curves for Al, Ni and Ni_3Al in a 0.5M NaOH solution (Ricker et al., 1990). 39

Figure 2.16. Schematic diagram of the operating principle of the low-pressure cold spray system (Supersonicspray, 2014). 47

Figure 2.17. Schematic diagram of the operating principle of the low-pressure cold spray system (Singh et al., 2012). 47

Figure 2.18. Comparison of burning velocity of γ-TiAl and various Ti alloys at 427 °C (Lasalmonie, 2006). 50

Figure 2.19. Specific strength of TiAl alloys compared to Ti- and Ni-based alloys (Lasalmonie, 2006). 51

Figure 2.20. Specific elastic moduli of γ-TiAl, Ni- and Ti-based alloys (Lasalmonie, 2006). 52

Figure 3.1. FCT HP-D5 spark plasma sintering furnace. 60

Figure 3.2. SST low-pressure cold spray system. 61

Figure 3.3. Compressor. 61

Figure 3.4. Powder feeder, hopper console and spray booth. 62

Figure 3.5. Spray booth and exhaust system (air cleaning system). 62

Figure 3.6. Process set-up PLC screen mounted on the set-up box. 64

Figure 3.7. Cold spray gun, a) during sample preparation, and b) in operation. 64

Figure 4.1. SEM-BSE micrographs of plain γ-TiAl, showing Ti_3Al (light) and γ-TiAl (dark), as well as grain orientations. 67

Figure 4.2. SEM-BSE micrograph of γ-TiAl-0.2 at.% Ru alloy showing γ-TiAl, α_2+γ-TiAl and G phase. ... 68

Figure 4.3. SEM-BSE micrograph of γ-TiAl-1.0 at.% Ru showing: (1) γ, (2) α_2 + γ, (3) two-phase mixture of G+γ and (4) last solidified liquid. 69

Figure 4.4. SEM-BSE micrograph of γ-TiAl -2.0 at.% Ru showing the eutectic-like structure, where the numbers into bracket represent the different areas. 71

Figure 4.5. SEM-BSE micrographs of γ-TiAl alloys with 0.2 at.% PGM, showing α_2, γ-TiAl, and a ternary compounds of different PGM contents. 75

Figure 4.6. SEM-BSE micrographs of γ-TiAl alloys with 2.0 at.% PGM showing α_2, γ-TiAl, and a ternary compounds (light phase with the highest PGM content). 77

Figure 4.7. Elemental mapping for γ-TiAl-0.2 at.% Pt, showing: a) Al, Ti and Pt, b) Al (blue), c) Ti (pink) and d) Pt (yellow). 78

Figure 4.8. Elemental mapping for γ-TiAl-1.0 at.% Pt, showing: a) Al, Ti and Pt, b) Al (blue), c) Ti (pink) and d) Pt (yellow). 79

Figure 4.9. Elemental mapping for γ-TiAl-1.5 at.% Pt, showing: a) Al, Ti and Pt, b) Al (blue), c) Ti (pink) and d) Pt (yellow). 80

Figure 4.10. Elemental mapping for γ-TiAl-2.0 at.% Pt, showing: a) Al, Ti and Pt, b) Al (blue), c) Ti (pink) and d) Pt (yellow). 81

Figure 4.11. XRD patterns of γ-TiAl alloys with different Ru additions. 82

Figure 4.12. XRD patterns of γ-TiAl alloys with different Pt additions. 82

Figure 4.13. XRD patterns of γ-TiAl alloys with different Ir additions. 82

Figure 4.14. XRD patterns of γ-TiAl alloy with different Pd additions. 83

Figure 4.15. Effect of PGM content on mass gain for different γ-TiAl alloys at 1185 °C. 85

Figure 4.16. Effect of PGM content on the Vickers hardness for as-cast γ-TiAl alloys. 85

Figure 5.1. Potentiodynamic scans for plain γ-TiAl in HCl solution of different concentrations. 92

Figure 5.2. Potentiodynamic scans for γ-TiAl-1.0 at.% Pd in HCl solutions of different concentrations...... 93

Figure 5.3. Potentiodynamic scans for γ-TiAl with (a)1.0 at.% Ir, (b)1.0 at.%Pt and 1.0 at.% Ru in HCl solutions of different concentrations. 94

Figure 5.4. Potentiodynamic scans for γ-TiAl with (a) 0.2 at.% Pd, (b) 0.2 at.%Pt, (c) 0.2 at.% Ru and 95

Figure 5.5. Potentiodynamic scans for γ-TiAl with (a) 1.5 at.% Pd, (b) 1.5 at.%Pt, (c) 1.5 at.% Ru and 96

Figure 5.6. Potentiodynamic scans for γ-TiAl with (a) 2.0 at.% Pd, (b) 2.0 at.%Pt, (c) 2.0 at.% Ru and 97

Figure 5.7. Variation of corrosion potentials with HCl solution concentration in γ-TiAl with 1.0 at.% PGMs.. 99

Figure 5.8. Variation of corrosion potentials with HCl solution concentration in γ-TiAl with 0.2 at.% PGMs.. 99

*Figure 5.9. Variation of corrosion potentials with HCl solution concentration in γ-TiAl with 1.5 at.% PGMs.*100

Figure 5.10. Variation of corrosion potentials with HCl solution concentration in γ-TiAl with 2.0 at.% PGMs. 100

Figure 5.11. TiAl corrosion potential evolution with different ruthenium additions. 103

Figure 5.12. TiAl corrosion potential evolution with different platinum additions. 103

Figure 5.13. TiAl corrosion potential evolution with different iridium additions. 104

Figure 5.14. TiAl corrosion potential evolution with different palladium additions. 104

Figure 5.15. Corrosion rates of TiAl alloys with PGM additions in 5, 15 and 25 wt% HCl solutions. 105

Figure 5.16. Effect of PGM additions on the polarisation scans of TiAl-1.0 at.% PGM in 5 wt% HCl solution. 107

Figure 5.17. Effect of PGM additions on the polarisation scans of TiAl-1.0 at.% PGM in 15 wt% HCl solution. 108

Figure 5.18. Effect of PGM metal additions on the polarisation scans of TiAl-1.0 at.% PGM in 25 wt% HCl solution. 108

Figure 5.19. Effect of PGM additions on the polarisation scans in 5 wt% HCl solution. 109

Figure 5.20. Effect of PGM additions on the polarisation scans in 15 wt% HCl solution. 110

Figure 5.21. Effect of PGM additions on the polarisation scans in 25 wt% HCl solution. 111

Figure 5.22. Corrosion rates of TiAl alloys with 1.0 at.% PGM additions in 5, 15 and 25 wt% HCl solutions (Apparent missing data were negligible corrosion rates). 113

*Figure 5.23. Potential-pH diagrams for PGM-water system at 25°C (*Pourbaix *et al.*, 1963). 116

Figure 5.24. SEM-BSE images of the corroded surface of TiAl-1.0 at.% PGM after potentiodynamic scanning in 25 wt% HCl solution showing PGM-containing phases on the surface. 118

Figure 5.25. Open circuit potential curves for Ti-47.5 at.% Al alloyed with various PGMs tested in 5 wt% HCl. 120

Figure 5.26. Open circuit potential curves for Ti-47.5 at.% Al alloyed with various PGM additions tested in 5 wt% HCl. 121

Figure 5.27. Variation of corrosion potentials with Pd additions in 5, 15 and 25 wt% HCl solutions, where the γ-TiAl with 2.0 at.%Pd in 25 wt% HCl was totally destroyed. 122

Figure 5.28. Variation of corrosion potentials with Pt additions in 5, 15 and 25 wt% HCl solutions. 122

Figure 5.29. Variation of corrosion potentials with Ru additions in 5, 15 and 25 wt% HCl solutions. 123

Figure 5.30. Variation of corrosion potentials with Ir additions in 5, 15 and 25 wt% HCl solutions. 123

Figure 6.1. Effect of PGM content on mass gain for TiAl alloys at 1185 °C. 130

Figure 6.2. SEM-BSE image of oxides in γ-TiAl with 1 at.% Ru, showing (1) TiO_2, (2-3) TiO_2+Al_2O_3, .. 131

Figure 6.3. SEM-BSE image of oxides in TiAl with 1 at.% Pt, showing (1) Al_2O_3, (2) TiO_2, ... 133

Figure 6.4. SEM-BSE image of oxides in TiAl with 1 at.% Ir, showing (1) TiO_2 (2-3) $TiO_2+Al_2O_3$,..... 135

Figure 6.5. SEM-BSE image of oxides on TiAl with 1 at.% Pd, showing (1) TiO_2, (2) Al_2O_3 136

Figure 6.6. XRD patterns of the oxide scales on TiAl with 1.0, 1.5 and 2.0 at.% Pd, showing TiO_2, Al_2O_3, Pd_2Al_3 and Pd peaks. 136

Figure 6.7. XRD patterns of the oxide scales on TiAl with 1.0, 1.5 and 2.0 at.% Ir, showing TiO_2, Al_2O_3, AlIr and Ir peaks. 137

Figure 6.8. SEM-BSE images of internal oxidation in TiAl with 2 at.% Ru addition after 120 hours at 950°C. 137

Figure 6.9. Vertical section of the pressure-composition Ti-Al-O phase diagram at 900°C (Rahmel and Spencer, 1991). 139

Figure 6.10. Partial Ti-O binary phase diagram (Murray and Wreidt, 1986). 140

Figure 6.11. Calculated isothermal section of the Ti-Al-O ternary system at 900°C including the ternary Z-phase (Dettenwanger, 1996). 142

Figure 7.1. Bimodal particle size distribution of MA powder γ-TiAl-0.5 at.% Ru. 149

Figure 7.2. Bimodal particle size distribution of MA powder γ-TiAl-0.5 at.% Pt. 150

Figure 7.3. Trimodal particle size distribution of MA powder TiAl-0.5 at.% Pd. 150

Figure 7.4. Slightly bimodal particle size distribution of MA powder TiAl-0.5 at.% Ir. 151

Figure 7.5. Typical SEM-BSE micrographs of MA powder TiAl-0.5at.% Ru. 152

Figure 7.6. XRD pattern of mechanically alloyed TiAl-0.5 at.% Ru powder showing (Ru), (Al) and TiH_2 peaks. 154

Figure 7.7. XRD pattern of TiAl-0.5 at.% Ru powder after heat treatment at 600°C for 2 hours showing TiAl, $TiAl_3$, and (Ti) peaks. 155

Figure 7.8. XRD pattern of mechanically alloyed TiAl-0.5 at.% Pt powder showing (Pt), (Al) and TiH_2 peaks. 157

Figure 7.9. XRD pattern of TiAl-0.5 at.% Pt powder after heat treatment at 600°C for 2 hours showing TiAl, Ti_3Al, Ti_3Al, and (Ti) peaks. 157

Figure 7.10. XRD pattern of mechanically alloyed TiAl-0.5 at.% Pd powder showing (Pd), (Al) and TiH_2 peaks. 157

Figure 7.11. XRD pattern of TiAl-0.5 at.% Pd powder after heat treatment at 600°C for 2 hours showing TiAl, Ti_3Al, $TiAl_3$ and (Ti) peaks. 158

Figure 7.12. XRD pattern of mechanically alloyed TiAl-0.5 at.% Ir powder showing (Al), (Ir) and TiH_2 peaks. 158

Figure 7.13. XRD pattern of TiAl-0.5 at.% Ir powder after heat treatment at 600°C for 2 hours showing TiAl, Ti_3Al, $TiAl_3$ and (Ti) peaks. 158

Figure 7.14. DSC curves for γ-TiAl-0.5 at.% PGM powders milled for 30 hours. 160

Figure 7.15. TGA curves for γ-TiAl-0.5 at.% PGM powders milled for 30 hours. 160

Figure 7.16. SEM-BSE image of spark plasma-sintered γ-TiAl-0.5 at.% Pt powders showing the three different phases. 162

Figure 7.17. SEM-SE image of the spark plasma-sintered γ-TiAl-0.5 at.% Ir powders showing the iridium solid solution. 162

Figure 7.18. Isothermal section of Ti-Al-C system at 1000°C (Bandyopadhyay et al., 2000). 166

Figure 7.19. Isothermal section of Ti-Al-C system at 1100°C (Bandyopadhyay et al., 2000). 167

Figure 7.20. Isothermal section of Ti-Al-C system at 1300°C (Bandyopadhyay et al., 2000). 167

Figure 8.1. SEM-BSE images of Ti-6Al-4V: (a) annealed at 800°C for two hours (Andrade et al., 2010) and (b) hot rolled and annealed 750°C for 2 hours (Moskalewicz et al., 2010). 171

Figure 8.2. BSE image of the Ti-6Al-4V microstructure. 172

Figure 8.3. SEM-BSE image of the titanium Grade 2 substrate and the iridium-alloyed coating. 173

Figure 8.4. SEM-BSE image of the titanium Grade 2 substrate and the iridium-alloyed coating. 173

Figure 8.5. SEM-BSE image of the iridium-alloyed coating on titanium Grade 2 showing the different phases in Table 8.10. 174

Figure 8.6.SEM-BSE image of the titanium Grade 2 microstructure showing (1) (αTi) and (2) TiH_2. 175

Figure 8.7. SEM-BSE image of the titanium Grade 2 microstructure showing (1) (αTi), (2) TiH_2 and (3) bTi 175

Figure 8.8. SEM-BSE images of γ-TiAl coating layer with 0.5 at% (a) Pt, (b) Pd and (c) Ru additions on titanium Grade 2 substrate. 177

Figure 8.9. Titanium Grade 2 substrate-coating layer interface for coating of γ-TiAl with Ir: (a) SEM-BSE image and (b) SEM-SE image. 178

Figure 8.10. SEM-BSE images of cross-sections of: (a) coated, and (b) uncoated substrates of oxidised Ti-6Al-4V substrate. 180

Figure 8.11. SEM-BSE images of cross-sections of: (a) coated, and (b) uncoated of oxidised titanium Grade 2 substrates. 181

LIST OF TABLES

Table 2.1. Mechanical and physical properties of titanium phases and nickel alloys (Huang and Chesnutt, 1994; Donachie, 1989; Pollock, 2006). 49

Table 3.1. *Elemental composition of the γ-TiAl alloys, for x=0.2, 1.0, 1.5 and 2.0 at.%.* 54

Table 3.2. *Melting points of alloy components.* 54

Table 3.3. C*ompositions of the produced TiAl powders.* 58

Table 4.1. EDX analyses of plain γ-TiAl. 68

Table 4.2. EDX analyses of TiAl-1.0 at.% Ru. 70

Table 4.3. EDX analyses of the eutectic-like and dark structures in γ-TiAl -2.0 at.% Ru. 71

Table 4.4. EDX analyses of the γ-TiAl -0.2 at.% PGMs 74

Table 4.5. EDX analyses of the γ-TiAl -2.0 at.% PGMs 76

Table 4.6. Ti_3Al peak positions or intensities on the XRD pattern of PGM-containing γ-TiAl alloys. 83

Table 4.7. Mass change as a function of precious metal content at 1185 °C. 84

Table 4.8. Vickers hardness of as-cast γ-TiAl alloyed with different PGM contents. 86

Table 4.9. Vickers micro-hardness of as-cast γ-TiAl alloyed with different PGM contents of 1.0 at.%. 86

Table 5.1. Test parameters and resulting corrosion potentials, current densities and corrosion rates for plain γ-TiAl. 89

Table 5.2. Test parameters and resulting corrosion potentials, current densities and corrosion rates for γ-TiAl-0.2 at.% PGM. 89

Table 5.3. Test parameters and resulting corrosion potentials, current densities and corrosion rates for γ-TiAl-1.0 at.% PGM. 90

Table 5.4. Test parameters and resulting corrosion potentials, current densities and corrosion rates for γ-TiAl-1.5 at.% PGM. 90

Table 5.5. Test parameters and resulting corrosion potentials, current densities and corrosion rates for γ-TiAl-2.0 at.% PGM. 91

Table 5.6. Corrosion potentials and their increases with PGM additions. 98

Table 5.7. Determination of coefficients (R^2) for the corrosion potential variation with PGM content. 102

Table 5.8. Characteristic values of potentials and current density for plain TiAl. 107

Table 5.9. EDX analyses of light particles on corroded surface of different alloys. 117

Table 5.10. EDX analyses of alloy surfaces after potentiodynamic tests in 25 wt% HCl solution. 117

Table 5.11. Start and finish open circuit potentials. 120

Table 6.1. Mass change as a function of precious metal content at 1185 °C. 129

Table 6.2. EDX analyses of TiAl alloy with 1 at.% Ru shown in Figure 6.2. 131

Table 6.3. EDX analyses of TiAl alloy with 1 at.% Pt shown in Figure 6.3. 132

Table 6.4. EDX analyses of TiAl alloy with 1 at.% Ir shown in Figure 6.4. 134

Table 6.5. EDX analyses of TiAl alloy with 1 at.% Pd shown in Figure 6.5. 135

Table 6.6. EDX analyses of internal oxidised zones in TiAl with 2 at.% Ru shown in Figure 6.8. 137

Table 7.1. Statistical parameters of the particle size distribution in different MA powders. 148

Table 7.2. EDX results of the MA and heat treated (HT) powders. 156

Table 7.3. EDX analyses of γ-TiAl-0.5 at.%Pd, γ-TiAl-0.5 at.%Ir and γ-TiAl-0.5 at.%Pt SPS compacts. 163

Table 7.4. Vickers hardness of compacts obtained by SPS. 164

Table 8.1. *Coating parameters for Titanium Grade 2 substrate with γ-TiAl with 0.5 at.% Pt powder.* 168

Table 8.2. *Coating parameters for titanium Grade 2 substrate with γ-TiAl with 0.5 at.% Ru powder.* 169

Table 8.3. *Coating parameters for titanium Grade 2 substrate with γ-TiAl with 0.5 at.% Ir powder.* 169

Table 8.4. *Coating parameters for Ti-6Al-4V substrate with γ-TiAl with 0.5 at.% Ir powder.* 169

Table 8.5. *Coating parameters for Ti-6Al-4V substrate with γ-TiAl with 0.5 at.% Ir powder.* 169

Table 8.6. Standard composition of Titanium Grade 2. 170

Table 8.7. Composition of Ti-6Al-4V. 170

Table 8.8. EDX analyses of Ti-6Al-4V substrate. 172

Table 8.9. EDX analyses of the titanium Grade 2 coating layer with Ir. 174

Table 8.10. EDX analyses of the titanium Grade 2 substrate. 175

Table 8.11. EDX analyses of the α and β phases in Ti-6Al-4V (Peterson, 2011 and Jha et al., 2015). 178

Table 8.12. EDX analyses of the different layers of the oxidation affected zone of the coated Ti-6Al-4V (Figure 8.10a). 179

Table 8.13. EDX analyses of the different layers of the oxidation affected zone of the uncoated Ti-6Al-4V (Figure 8.10b). 179

CHAPTER 1
INTRODUCTION

1.1 Titanium aluminides for high-temperature structural applications

In the aluminium-titanium system, Ti_3Al and TiAl are potential materials for structural applications in the automotive and aerospace industries due to their particular properties (Froes *et al.*, 1992; Froes, 1994). In many ways, their properties are better than those of conventional steel and nickel-based superalloys. With densities below 4.5 g/cm^3, these alloys offer an advantage of weight reduction over high-temperature special steels such as 21-2N, or nickel-based superalloys. In addition, the goal to achieve general reduction in engine weight and higher operating temperatures, which in turn leads to a more efficient fuel burn and less environmental damage, has pushed the boundaries of the superalloys to their limits (Dimiduk *et al.*, 1992). Titanium aluminides also offer the advantage of high-temperature operating capability in conjunction with high specific strength. As intermetallic compounds, they are characterised by the strong attraction between the unlike atoms of the component metals, leading to a preference in the selection of nearest neighbour atoms, which leads to an ordered structure, a high resistance to deformation and a high melting point. The result of combined resistance to deformation and high melting point is high-temperature strength, which makes them good candidates for high-temperature structural applications.

1.2 Limitations and challenges in the applications of titanium aluminide alloys

Performance and efficiency of gas turbine engines have been a long-standing consideration. Since the development of the gas turbine blade, from the simple wrought nickel-based alloys in the 1940s, progress has been continuous in the innovation and design of these alloys, resulting in the highly refined, single crystal superalloys currently in service (Reed, 2006). However, for a more efficient fuel burn and a reduced impact on the ecosystem, the weight reduction in engine and higher operating temperatures have pushed the superalloys to their limits, raising the need of lighter weight materials, especially for less critical components of the engine (Reed, 2006). In the late 1970s, intermetallic alloys began to be seriously considered as high temperature engineering alloys once their properties

became better understood and potential applications explored (Loria, 2001). In the process of development, unalloyed titanium aluminides have found applications in the automotive industry with successful use in engine valves (Tetsui, 1999) and successful demonstrations in high-pressure compressor casings, low-pressure turbine blades, high-pressure compressor blades, blade retainers, turbine dampers and others (Wang *et al.*, 1999). However, the superiority of titanium aluminides over conventional nickel-based alloys is in the very narrow temperature range of 650-800°C, and limiting the long-time applications to 650-750°C (Tetsui, 1999).

With a ductile-to-brittle transition temperature (DBTT) between 550°C and 650°C (Wang *et al.*, 1999), the titanium aluminide alloys are in the brittle zone at room temperature. In addition, the properties of titanium aluminides are very sensitive to the composition, with a lower strength at room and medium temperatures than for conventional alloys. Strengthening by deformation is impossible, due to the low ductility. Oxidation of titanium aluminide above 800°C is still an unsolved problem to date.

From a manufacturing perspective, the presence of titanium and aluminium with a melting temperature difference of more than 1000°C in titanium aluminides has always made the production of good quality ingots difficult and costly (Wu, 2006). Alloy manufacturing is more difficult than in non-compound alloys due to the material's brittleness, for the processes involving deformation and melting.

Overall, the high-temperature properties of TiAl are not as good as for ceramics or Ni-based superalloys, while toughness, cost, and manufacturing capability are substantially inferior to those of heat-resistant steels and Ni-based superalloys. Thus, lightness is the only merit of TiAl compared to ordinary metallic alloys currently in use. To date, the most suitable applications for TiAl are small components where weight reduction is accompanied by advantages such as toughness and high temperature ductility where the use of ceramics is difficult or where TiAl shows advantages over ceramics (Lasalmonie, 2006; Appel *et al.*, 2011a). In addition, the applicable temperature range is the same or lower than for Ni-based superalloys, but at temperatures below 500°C, where light-weight Ti alloys could be used, there is no merit apart from the light weight. Thus, components used at temperatures of 500°C to 900°C would be most appropriate, e.g. exhaust valves and turbocharger turbines for automotive engines (Froes *et al.*, 1992). To date, titanium aluminide alloys cannot fully

replace the Ni-based superalloys because of the poor mechanical performance and significantly higher production costs. Even so, there have been significant advances made by the NASA Glenn Research Center, Plansee (Austria) (Locci *et al.*, 2001) and GKSS Research Center (Germany) in developing manufacturing techniques to produce titanium aluminide sheets (Draper *et al.*, 2015; ARC, 1999). As a result, the cost of titanium aluminide sheets is expected to fall to acceptable levels for commercial applications (Froes *et al.*, 1992; Kim and Dimiduk, 1991). This fact indicates that, in spite of the numerous obstacles faced in the use of titanium aluminide alloys in structural and automotive applications, efforts to improve the properties of these alloys should be continued.

1.3 The need to address the manufacturing challenges and improve the properties of titanium aluminide alloys

There is a general belief that the manufacturing challenges must be addressed and the properties of titanium aluminide alloys improved before a widespread use of these alloys can be seen. Over the last four decades, significant progresses have been made in the manufacturing process and the physical metallurgy of titanium aluminide alloys (Wu , 2006). Today, there is a better understanding of the solidification and microstructure formation of stoichiometric and non-stoichiometric TiAl, as well as the effect of alloying elements and the relationship of microstructure-mechanical and physical properties (Kim and Dimiduk, 1991). Much data are available from the early fundamental concepts which identified the potential of TiAl alloys to solve the problems hindering their use in structural, automotive and aerospace applications, indicating that the level of research on TiAl-based alloys has matured and is now moving from the fundamental studies to applications.

At the industrial level, and for the TiAl-based alloy end-user, some targeted parts have been successfully tested for replacement with titanium aluminides and these include automotive engine valves, turbocharger rotors, turbine blades and engine parts such as compressors for the automotive industry (Tetsui, 2002; Tetsui and Miura, 2002; Tetsui *et al.*, 2002; Wu, 2006). However, no significant breakthrough has been accomplished to date in the aerospace applications due to issues linked to processability, room- and high-temperature performance.

The TiAl-based alloy specific 1000 hour rupture strength and specific modulus are superior to those of other Ti alloys, Ni-based alloys, alloy steels, and Ni-based superalloys (Dinesh Kumar *et al.*, 2015). However, whilst the specific strength is higher than the competing materials, the oxidation resistance

and room temperature ductility are poor (Dimiduk, 1999). Many metals have been used as alloying elements to improve the ductility and the oxidation resistance of TiAl (Kim and Dimiduk, 1991), but the existing data show that information available on the ternary systems with noble metals, especially platinum group metals (PGMs), is very limited.

Compositions have been identified for alloys capable of carrying stresses in excess of 700MPa at service temperatures above 700°C (Kim and Dimiduk, 1991; Lan, 2011). The way forward lies in innovative processing techniques that would help achieve better material performance at room and elevated temperatures. Manufacturing improvements are needed to achieve ingot quality and hot working procedures to produce homogeneous and defect-free materials with the desired microstructures. Although significant improvement has been achieved by the addition of alloying elements such as boron, molybdenum, niobium, tungsten and carbon for better workability, a defect-free microstructure in the cast ingot is needed. This indicates the need to develop both preparation and processability techniques which will lead to desired mechanical and corrosion properties of titanium aluminide alloys. This remains a challenge to address.

Powder metallurgy techniques are efficient in refining the microstructure. Among these techniques, mechanical alloying and spark plasma sintering (Shu-long *et al.*, 2009) have allowed the production of near-net shape components with well-refined microstructures compared to ingot casting (Liu and Liu, 2007; Couret *et al.*, 2008). However, issues of porosity, even with the most efficient methods for achieving full density in powder metallurgy parts such as hot isostatic compaction, explosive compaction, and hydrostatic extrusion, have precluded the production of sound components. Spark plasma sintering, by its ability to induce melting during consolidation, has produced sound components (Liu and Liu, 2007; Lagos and Agote, 2013). Likewise, most thermal spray techniques, by their ability of melting the powder particles, have the ability to produce pore-free coatings on substrates. Unfortunately, this technique could not be used for the project, so the cold spray technique, which uses high energy induced to powder particles is also able to produce pore-free coatings on substrates, was used instead.

The alloys based on γ-TiAl have better high-temperature properties than Ti-6Al-4V, unfortunately with low room-temperature ductility (Deevi and Zhang, 2003). While many barriers still need to be overcome to make routine use of TiAl-based alloys in automotive and structural applications, it

appears that coating conventional titanium-based alloys such as Ti-6Al-4V or Titanium Grade 2 with PGM-modified TiAl-based alloys can improve their properties at high temperature. The TiAl-based alloys can be used as a thermal and oxidation barrier on Ti-6Al-4V substrates and the Ti-6Al-4V or Titanium Grade 2 provide the low-temperature ductility which is lacking in the titanium aluminides. This combination of properties should be especially effective, since good coatings can be achieved by methods such as thermal spray coating or cold spraying, resulting in stresses that can be removed or reduced by heat treatment.

1.4 Hypothesis

The lack of room temperature ductility and poor high-temperature oxidation resistance, combined with the processing problems of the TiAl alloys are the major barriers to the use of these intermetallic alloys, in spite of all the potential benefits deriving from their other properties (Lasalmonie, 2006). To date, no breakthrough has been made to allow use of these alloys in critical applications in aircraft and aerospace. While research is still continuing on the titanium aluminides, coating of Ti-based alloys with TiAl and TiAl-based alloys could address the TiAl processing issue by using powder metallurgy techniques. The room temperature ductility issue could be resolved by coating with a TiAl-based alloy a more ductile material such as Ti-6Al-4V or Titanium Grade 2. The low and high temperatures corrosion and oxidation issues could be solved by modifying the TiAl-based alloy with PGMs such as Pd, Pt, Ru and Ir.

1.5 Aim and objective of the study

The aim of the study was the preparation and testing of a coating material based on TiAl with the addition of platinum group metals. The objectives of this study was to investigate the properties of γ-TiAl alloys (Ti-47.5 at.% Al) modified with additions of platinum group metals (PGMs) as coating materials on Ti-6Al-4V or Titanium Grade 2. The γ-TiAl was expected to provide Ti-6Al-4V (or Titanium Grade 2) with protection at room and elevated temperatures. The effect of PGM additions on room temperature aqueous corrosion, as well as high-temperature oxidation resistance was investigated. Powder of the same composition was produced and characterised. The powder was consolidated and the compacts characterised in terms of microstructure and the mechanical

properties were tested. The powder was used as feedstock material for cold spray coating and the properties of the coatings were investigated.

Investigations carried out included:

- Casting of plain γ-TiAl alloy,
- Casting of γ-TiAl alloy with additions of platinum group metals,
- Microstructural characterisation of the as-cast alloys,
- Investigation of the corrosion behaviour of the as-cast alloys,
- Investigation of the high-temperature oxidation behaviour of the as-cast alloys,
- Mechanical alloying for the preparation of γ-TiAl,
- Consolidation of the mechanically alloyed (MA) powder by spark plasma sintering (SPS),
- Characterisation of the SPS compacts,
- Cold spraying of Ti-6Al-4V and Titanium Grade 2 substrates using the MA powder, and
- Characterisation of the coating.

CHAPTER 2

LITERATURE SURVEY

2.1 Introduction to intermetallic compounds

2.1.1 Definition of intermetallic compounds

Intermetallic compounds are defined as a mixture of two metallic elements, in specific proportions, that form a periodic crystalline structure different from those of the original elements (Westbrook and Fletcher, 1994). They are chemical compounds with a definite atomic formula, a nearly fixed or narrow range of chemical composition (Campbell, 2008), and high bonding strength (Desch, 1914). The atoms in conventional alloys of solid solutions are linked with relatively weak metallic bonds, described simplistically as the atomic nuclei floating in a "gas" or "sea" of electrons which are able to move relatively freely. In contrast, the bonds in intermetallic compounds may be partly ionic or covalent, and therefore stronger. Alternatively, the bonding may be entirely metallic, but the atoms of the individual elements take up preferred positions within the crystal lattice. This condition, which leads to an abrupt change in the mechanical properties of the material, is referred to as ordering. Ordering imparts to intermetallic compounds their typical properties such as high melting points, high-temperature strength, and poor ductility. In these respects, they resemble the ceramics. However, unlike ceramics, they have a metallic lustre, conduct heat and electricity well, and can generally be processed by conventional metal technology. Due to their properties, intermetallic compounds occupy an intermediate position between metals and ceramics.

A compound with a fixed chemical composition is called stoichiometric intermetallic compound or line compound and is represented on a binary phase diagram by a vertical line, since the composition has a specific value. When the chemical composition varies on a finite range, the compound is a nonstoichiometric compound or intermetallic phase and is denoted on the phase diagram by Greek letters (γ, α, β, δ, ε, η, θ etc., although α and β are generally used for terminal solid solutions). Whether the intermetallic compound is stoichiometric or nonstoichiometric, it is formed by the combination of two (or more) components forming a compound having a structure and properties different from either component.

2.1.2 Ordering and superlattice

A large number of solid solutions become ordered at low temperatures. The process of ordering involves a change from statistically nearly random distribution of atoms among the atom sites into a more regular arrangement, whereby designated sites are occupied predominantly by one kind of atom (Dimitrov, 1994). For example, in disordered alloy of composition AB, any given atom site is occupied randomly by either A or B atoms, but on ordering, A and B atoms are preferentially found on more or less completely designated atomic sites, so that the resulting arrangement can be described as a lattice of A atoms interpenetrating a lattice of B atoms. The preference of atoms for particular atom sites may take place with little or no deformation of the lattice, creating an ordered solid solution, or superlattice, or superstructure, from a random solid solution.

2.1.3 Long-range and short-range ordering

The formation of a superlattice is frequently described as long-range order (Barret and Massalski, 1980; Dimitrov, 1994). It takes place at relatively low temperatures and usually at compositions expressed by simple formulae such as AB or AB_3 or at compositions near these. At all temperatures above a certain critical temperature, the usual randomness persists; when the temperature is lowered through the critical point, order occurs and increases with time and as temperature drops, approaching perfection only at low temperatures or long times.

Over certain ranges of composition and temperatures above the critical temperature, the structures may at times be neither perfectly random nor perfectly ordered (Barret and Massalski, 1980). Even in the disordered state, certain correlations may be present between nearest, second-nearest, and more distant neighbours. This is described as short-range order.

2.1.4 Common types of superlattice

The majority of typical superlattices are related to the three principal metallic structures (Barret and Massalski, 1980):

1. fcc (A1)
2. bcc (A2)
3. cph (A3)

- ***L*1$_2$-** or **Cu$_3$AuI**-type superlattice

In the disordered state which exists at high temperature, a 75:25 at.% Cu:Au alloy has a nearly random array of Au and Cu atoms on the **fcc (*A*1)** lattice (De Graef and McHenry, 2007; Barret and Massalski, 1980). If the alloy is annealed below a critical temperature (390°C), the atoms preferably move so that Au atoms are on the cube corners and Cu atoms are on the face centres, and form Cu_3AuI, where I is the Roman numeral indicating the lattice type (Barret and Massalski, 1980).

- ***B*$_2$-** or beta-brass type superlattice

The disordered crystal structure **bcc (*A*2)** has equal probabilities of having copper and zinc atoms at each lattice point. The ordered structure has copper atoms on the cube corners and a zinc atom at the centre of the cube, and vice-versa in this structure. The unit cell can be represented in terms of two interpenetrating simple cubic sublattices.

- ***L*1$_0$-** or **CuAuI**-type superlattic

The $L1_0$ or CuAuI is an **fcc** ordered superlattice (Barret and Massalski, 1980; De Graef and McHenry, 2007), where I is the Roman numeral indicating the lattice type. In the Cu-Au system, from 47 to 63 at.% Au, a superlattice forms, in which alternate (001) planes contain only copper or only gold atoms. Hence, each atom has 8 nearest neighbours of the opposite kind in the adjacent (001) planes and 4 of the same kind in its own (001) plane.

- ***L*1$_1$-** or **CuPt**-type superlattice

In the Cu-Pt system, near 50 at.%, the **fcc** disordered lattice takes up the ordered structure (Barret and Massalski, 1980). The ordered structure consists of alternating layers of Cu and Pt atoms on (111) planes. This form of ordering produces a lattice distortion from cubic to rhombohedral for which the Strukturbericht designation is ***L*1$_1$**. CuPt is the only known example of this structure.

- ***D*O$_3$** and ***L*2$_1$** type superlattice

The ***D*O$_3$** structure is found for **Fe$_3$Al (**and ***B2*** is found for **FeAl)** with Al varying from 18 to 25 at.% and 25 to 50 at.% and Al atoms segregating to designated sites (Barret and Massalski, 1980). The ternary ***L*2$_1$**-type superlattice, which is closely related to ***D*O$_3$**, is based on the composition **A$_2$BC**. The most representative structure is **Cu$_2$MnAl**. These structures possess the remarkable

property of being ferromagnetic when in the ordered condition, despite the fact that the constituent atoms are in most cases nonferromagnetic.

- ***D*O$_{19}$** or Mg_3Cd-type superlattice

***D*O$_{19}$**-type superlattice is described in terms of four interpenetrating simple sublattices, and the arrangement of atoms in the close-packed planes of both structures is identical (Haasen, 1978; Barret and Massalski, 1980). Each sublattice is **cph** with a spacing corresponding to twice the spacing of the disordered structure and the *c* spacing remains unchanged. B atoms occupy one of the 4 sublattices, resulting in the general formula **A_3B,** for example in the case of **Mg_3Cd** or **$MgCd_3$**, which are the best-known examples of ***D*O$_{19}$** superlattices.

Many alloys possess the cph structure at high temperature and undergo ordering on cooling. Depending on the composition ranges at which the phases are stable (i.e. near **A_3B**, **A_2B**, **AB**, etc.), the number of unlike nearest neighbours and their distribution on ordering will differ, with the resulting changes in the details of ordered structure.

2.1.5 Toughness and ductility in intermetallic compounds

Limited ductility and toughness at low temperatures are serious disadvantages of intermetallic compounds. Plastic deformation is more difficult in intermetallic compounds than in conventional alloys because of the stronger atomic bounding and the consequent ordered atomic distribution. The brittleness of intermetallic compounds increases with decreasing lattice symmetry and increasing unit cell size (Tetsui and Miura, 2002).

This brittleness depends on the crystal symmetry and the specific characteristics of the particular phase. Dislocations with high mobility and low energy imply the existence of slip twinning systems (Morris, 2001). The criterion of Von Mises (Von Mises, 1913), also known as the maximum distortion energy criterion, is often used to estimate the yield of ductile materials, which can be important considering that some deformation is needed. However, since there was not enough deformation, this criterion did not have to be used.

$$\frac{1}{2}\left[(\sigma_1-\sigma_2)^2+(\sigma_2-\sigma_3)^2+(\sigma_3-\sigma_1)^2\right]\leq \sigma_y{}^2 \qquad (2.1)$$

where σ_i with i=1, 2, 3 are the principal stresses in the three Cartesian axes.

Crystal anisotropy affects the toughness of the material, as do weak grain boundaries or other microstructure heterogeneities (Fensin *et al.*, 2014).

2.2 γ-TiAl-based alloys

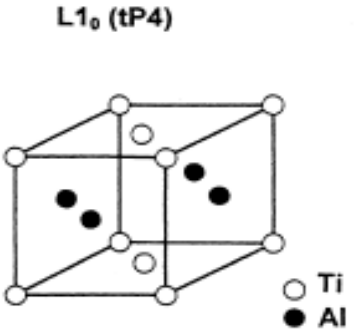
Gamma-TiAl-based alloys exhibit high ignition temperature (the lowest temperature at which a material will spontaneously ignite in a normal atmosphere without an external source of ignition, such as a flame or spark) when compared to conventional titanium alloys (Tetsui and Miura, 2002). TiAl-based alloys show superior specific strength-temperature properties when compared to conventional titanium alloys, steels and nickel-based superalloys in the temperature range from 500 to 900°C. With all these advantages over conventional high-performance alloys, TiAl alloys are promising alloys for high-temperature structural applications, the lack of room temperature ductility being the main obstacle to their use as engineering materials (Duarte *et al.*, 1999).

The γ-TiAl ($L1_0$, *tP*4) phase is an ordered, equiatomic compound of the lightweight elements Ti and Al. The high aluminium content of this compound increases the resistance to oxidation and burning, two critical concerns in the use of titanium-based materials. Gamma-TiAl remains ordered to melting at ~1440°C. The strong Ti-Al bonds cause a high activation energy for diffusion, which helps retain strength and creep resistance at high temperatures when diffusion becomes the rate-controlling process. However, the rigid bond restricts the ability to accommodate plastic deformation, and so γ-TiAl lacks the ductility and toughness which are necessary for structural applications. Figure 2.1 is a representation of two of the crystal structures occurring in TiAl-based alloys (Ramanujan, 2000): γ-TiAl and α-Ti_3Al.

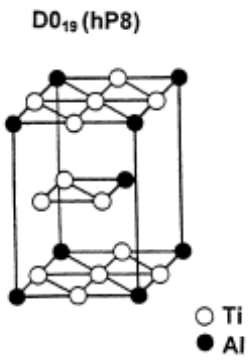
2.2.1 Microstructure formation in plain and alloyed γ-TiAl

TiAl-based alloys are fundamentally two-phase, consisting of γ, which is ordered TiAl face-centred-tetragonal with a $L1_0$ crystal structure, and a α_2 phase, which is ordered Ti_3Al close-packed-hexagonal with a DO_{19} crystal structure (Jovanović *et al.*, 2004). Gamma-TiAl-based alloys display very different microstructures depending on the composition near the 50:50 Ti:Al atomic ratio. While TiAl (γ) is found in the aluminium-rich region alloys, titanium-rich alloys exhibit a two-phase

microstructure, consisting of layers of tetragonal, $L1_0$ TiAl (γ) and hexagonal DO_{19} Ti_3Al (α_2) (Kimura and Pope, 1997).



a) γ-TiAl



b) Ti_3Al

Figure 2.1. *Crystal structure and unit cell of (a) γ-TiAl and (b) α_2-Ti_3Al (*Ramanujan, 2000*).*

Solidification and solid-state equilibria of γ-TiAl-based alloys are complex and sensitive to aluminium content and heat treatment. Three types of microstructure are usually observed in TiAl: the γ, duplex and lamellar structures (Huang and Chesnutt, 1994). Microstructural evolution involves the high-temperature liquid phase relationship and solid state transformation. Engineering TiAl-based alloys generally solidify as the β phase and go through α single-phase region and $\alpha \rightarrow \alpha + \gamma$ and $\alpha + \gamma \rightarrow \alpha_2 + \gamma$ reactions, producing a ($\alpha_2 + \gamma$) two-phase structure with decreasing temperature [(Yamaguchi *et al.*, 1999). Thus, different two-phase structures can be obtained by manipulating these phase transformation reactions.

Figure 2.2 is a portion of Ti-Al phase diagram (Huang and Chesnutt, 1994) where γ forms. There are various versions of the Ti-Al phase diagram. The transformations depicted here follow Murray's phase diagram (Murray, 1988), redrawn by Huang and Chesnut (1994). This diagram was the most used, but recently there have been significant modifications on the diagram near the γ phase field (McCullough, 1989; Ding *et al.* 1996). Later critical re-assessments of the Ti-Al phase diagram have helped clarify two major differences in the two phase diagrams (Grytsiv *et al.*, 2003; Schuster and M. Palm, 2006; Witusiewicz *et al.*, 2008), as shown in Figure 2.3.

The first difference lies in the phase relationships among (αTi), (βTi) and α_2, in the temperature range 1150°C-1400°C and in the compositional range of 20 at.%-47 at.% Al. In one phase diagram, the relationship is of congruent-type reaction, Figure 2.3a (Grytsiv *et al.*, 2003). A very narrow single-phase region exists for α_2 and both phases are in equilibrium with each other $\alpha \leftrightarrow \alpha_2$ at the congruent temperature (~1179°C) and composition between 30 at.% and 35 at.% Al. In addition, Kainuma *et al.* (1994) reported that a part of the high temperature β phase in equilibrium with α phase undergoes ordering to the β_0 phase. The other phase diagram is ''peritectoid type'' (Figure 2.3b), with the three phases (γ, (αTi) and Ti_3Al) in equilibrium with each other at 1120°C, with two peritectoid invariant temperatures 1170°C and 1200°C (Schuster and Palm, 2006).

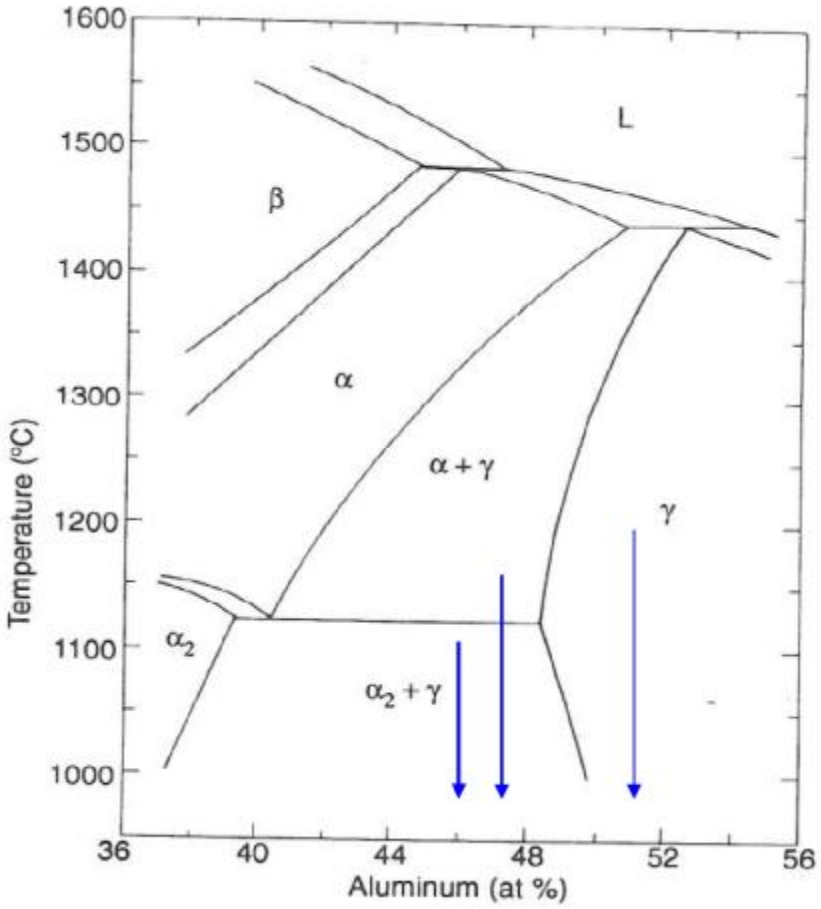


Figure 2.2. *Partial Ti-Al phase diagram near the stoichiometric TiAl composition shown in Figure 2.3b (Huang and Chesnutt, 1994).*

The second difference lies also in the high-temperature phases in the compositional range 55-75 at.% Al. First, there are differences of temperatures at which solid phases form from the

homogeneous liquid. The congruent-type phase diagram (Figure 2.3a) has a peritectic reaction at 1445°C (L + (αTi) →TiAl), a eutectoid reaction at 1170°C ($Ti_{1-x}Al_{1+x}$ → TiAl + $TiAl_2$) and a peritectoid reaction at 810°C (TiAl + $TiAl_2$ → Ti_3Al_5), resulting in the formation of Ti_3Al_5. Between 65 at.% and 75 at.%, there is a eutectoid reaction taking place at 995°C (Ti_5Al_{11} → $TiAl_2$ + $TiAl_3$). The $TiAl_3$ phase is formed as a result of a peritectoid (Ti_5Al_{11} + L → $TiAl_3$) reaction taking place at 1387°C. On the other hand, the "peritectic" phase diagram (Figure 2.3b) has a peritectic reaction (L + αTi → TiAl) taking place at 1456°C, and a congruent reaction (TiAl → $TiAl_2$) at 1215°C resulting in the formation of $TiAl_2$.

In γ-TiAl based alloys which contain hypereutectoid α, the transformed structures are lamellar with typical fine spacings of only 0.1-1 μm (Huang and Chesnutt, 1994). For alloys between 46 and 50 at.% Al, heat treatment in the α + γ phase field results in a two-phase structure upon cooling, with γ grains and grains of lamellar structure. The lamellar grains contain alternating $α_2$ and γ plates, which forms as a result of the eutectoid reaction of the primary α during cooling to room temperature. The grains are typically 10-35 μm across, and the lamellar plates are 0.1-1 μm thick. This microstructure is referred to as duplex. Finally, if alloys below 48 at.% Al are heat treated in the single-phase α field, a fully lamellar structure is formed. The grains are typically greater than 500 μm across, which reflects the rapid coarsening rate of disordered α. In a review on TiAl-based alloys, the microstructural evolution of a Ti-46 at.% Al was highlighted (Lapin, 2009). If Ti-46 at.% Al was cooled reasonably quickly from the α-phase field, a fully lamellar structure was formed as γ was precipitated on the (0001) planes of the α. If the cooling was slightly slower, a near fully lamellar structure was formed, where γ lamellae coarsened, giving rise to lamellae with contiguous γ grains in the colony (grain) boundaries. If the sample was hot worked in the two-phase region, this inherited structure from the casting was eliminated and a duplex structure consisting of γ and lamellar grains was formed on subsequent cooling. The grain size in alloys with a duplex microstructure was typically about 20 μm, which is considerably smaller than the typical grain or colony size in as-cast lamellar structures with grains of several hundred micrometers across are common, unless grain refiners are added. In this work, the "peritectic" phase diagram was used, because it is considered to be more accurate, represent the experimental data better.

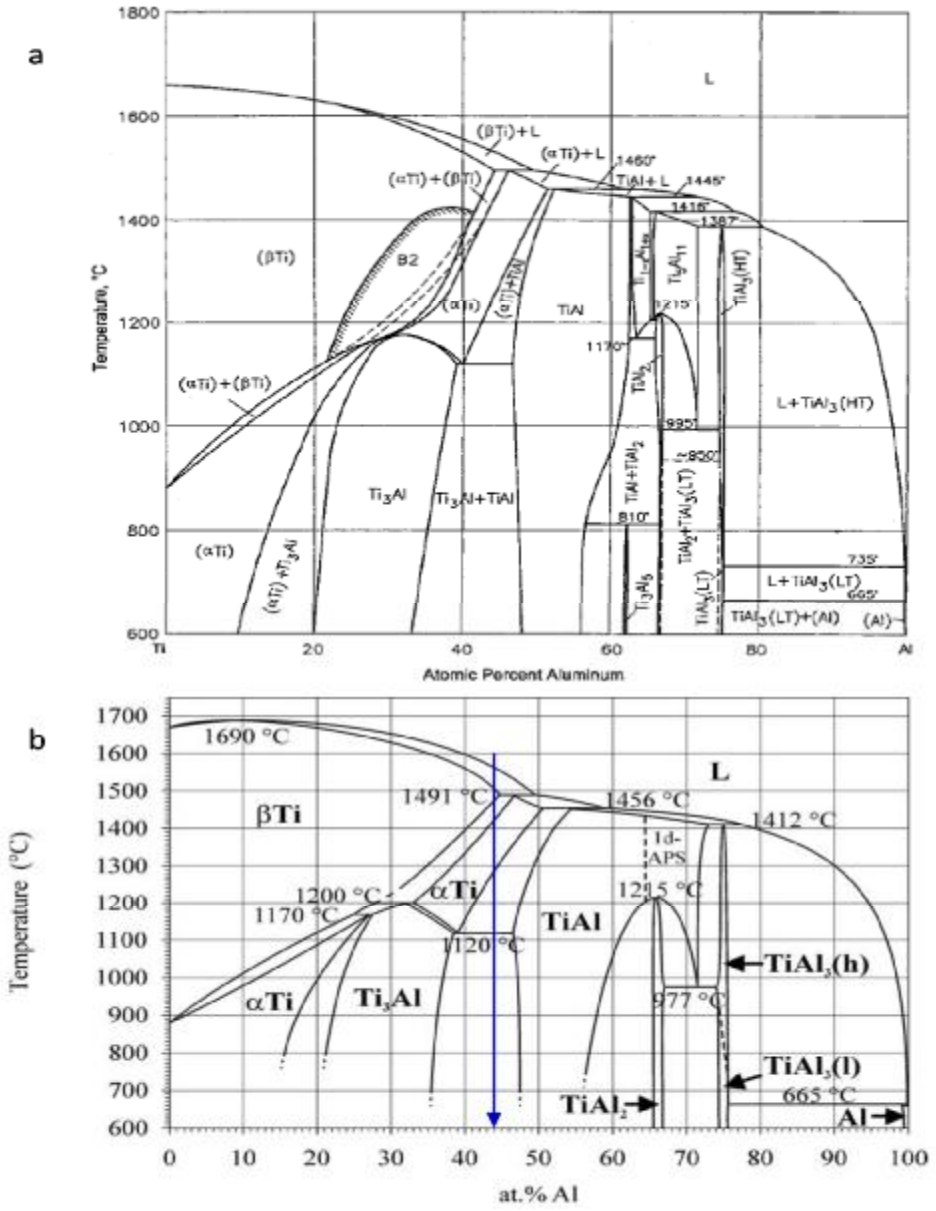


Figure 2.3. *Ti-Al diagram of (a) congruent-type (Grytsiv et al., 2003; Raghavan, 2005), and (b) peritectic type (Schuster and Palm, 2006).*

Most TiAl alloys of technical interest contain 45-50 at.% Al and they normally solidify as the bcc α primary phase, or (αTi). At 45 at.% Al (blue arrow), a single-phase structure α can be obtained by heat treatment above 1300°C. A eutectoid reaction which transforms α of 38 at.% to $\alpha_2 + \gamma$ occurs at 1120 °C (Schuster and Palm, 2006).

Alloys above 52 at.% Al generally lie in the single-phase γ-TiAl field during heat treatment, and are single-phase γ-TiAl after cooling at room temperature. The grains are equiaxed and about 50 μm across (Huang and Chesnutt, 1994). Single-phase γ-TiAl with very smooth grain boundaries was also observed in high purity TiAl containing 50 at.% Al (Murata *et al.*, 1993). Figure 2.4 shows the three common microstructures occurring in TiAl-based alloys. It shows the microstructural evolution upon cooling in the composition range of interest and in accordance with the Ti-Al phase diagram in Figure 2.2 (Huang and Chesnutt, 1994).

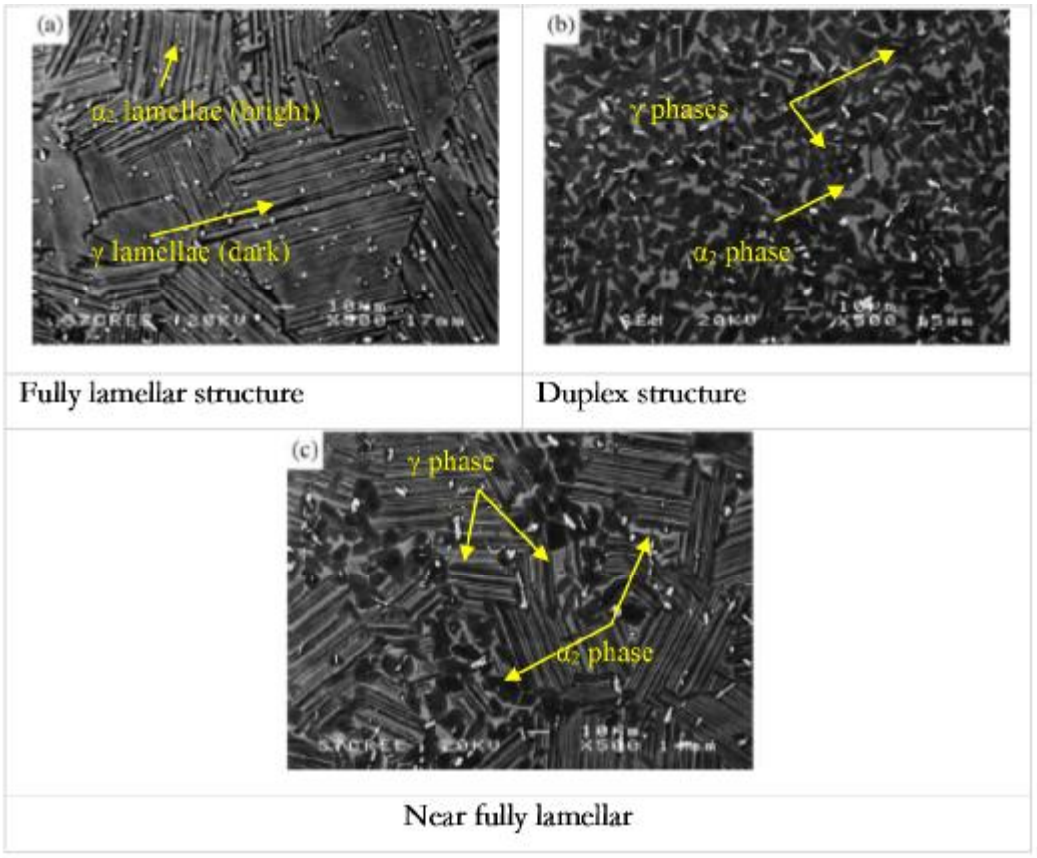


Figure 2.4. *Three typical microstructures of TiAl: (a) fully lamellar, (b) duplex, and (c) near fully lamellar (Wu, 2006).*

2.2.2 Mechanical properties of γ-TiAl alloys

The mechanical properties of TiAl alloys are microstructure-dependent. The γ-TiAl single-phase is fundamentally brittle at room temperature with a ductility of 1%, regardless of the processing route (Wu, 2006). The brittleness is the result of the limited dislocation mobility, and is inherently related

to its crystal structure, which is a faced-centred tetragonal (fct) $L1_0$ with alternating (002) planes of Ti and Al atoms (Huang and Chesnutt, 1994). The tetragonality is very small (c/a = 1.02), but the $L1_0$ ordered structure creates a non-equivalency among the <110> slip vectors. The dislocation mobility has also a significant implication for the strength and fracture behaviour of γ-TiAl (Huang and Chesnutt, 1994; Kim *et al.*, 1999).

Duplex and lamellar microstructures exhibit very different mechanical properties. The duplex structure is significantly ductile at room temperature (Huang and Chesnutt, 1994). The lamellar microstructures are poor in ductility; although they are generally superior to the duplex structures in other mechanical properties, such as fracture toughness, fatigue resistance and high-temperature creep strength (Yamaguchi *et al.*, 1999; Tetsui and Miura, 2002). The ductile duplex structure exists in a narrow range of Al concentration; only the duplex alloys containing 45-50 at.% Al show appreciable plasticity. The ductility peak occurs at 48 at.% Al, particularly when the alloy is heat treated near the centre of the α+γ phase field, i.e. where the two phases have equal volume fractions. Alloys outside this composition range tend to have either the single-phase γ or the lamellar structure, and they are relatively brittle. Since the low-temperature ductility is major concern for structural applications, the 45-50 at.% Al range is usually the basis for further alloying.

Mechanical properties of the lamellar microstructures in TiAl-based alloys depend on the lamellar orientation with respect to the loading axis and lamellar microstructural variables, such as grain size, thickness and spacing of γ and α_2 lamellae and γ domain size (Yamaguchi *et al.*, 1999). A fully lamellar structure produced for turbocharger wheels had yield strengths around 400 MPa and ultimate tensile strengths around 475 MPa (Jovanović *et al.*, 2004). The refinement of the lamellar thickness to nanoscale values resulted in exceptionally high strength of 800 MPa, together with 3-5% elongation and 30 $MPa.m^{1/2}$ fracture toughness at room temperature. These results suggested that the key to high strength in fully lamellar TiAl-based alloys lies in refining the lamellar size, rather than the grain size (Yamaguchi *et al.*, 1999).

2.2.3 Physical properties of plain and alloyed γ-TiAl

Alloyed γ-TiAl shows thermal conductivity comparable to that of currently-used superalloys in the temperature range 200-900ºC and slightly higher than Ti-50 at.% Al (Zhang *et al.*, 2001). The

thermal conductivity of Ti-6Al-4V is lower than that of alloyed γ-TiAl for a wide range of temperatures.

The coefficient of thermal expansion of alloyed γ-TiAl (TiAl-4 at.% (Nb,W,B)) is lower than that of plain Ti-50 at.%Al, and close to that of Ti-6Al-4V (Appel *et al.*, 2011a). It is also lower than that of currently-used superalloys and heat-resistant steel 21-4N. The Young's modulus of the alloyed γ-TiAl is lower than that of nickel and steel superalloys and substantially higher than Ti-6Al-4V. The specific heat of alloyed γ-TiAl is higher than that of superalloys and Ti-6Al-4V. The electrical resistivity of alloyed γ-TiAl is lower than Ti-6Al-4V and superalloys in the temperature range 0-950ºC.

2.2.4 Oxidation resistance

Gamma-TiAl has a low resistance to oxidation at temperatures above 800ºC (Rahmel *et al.*, 1995). The mechanisms of oxidation of plain and alloyed TiAl were widely investigated (Meier, 1989; Rahmel *et al.*, 1995). Different mechanisms have been proposed for the growth of oxide scale on TiAl and two phenomena are mostly accepted. The first is the formation of a TiO_2 layer on the external surface of γ-TiAl. Secondly, the oxide scale is protective only if a continuous layer of Al_2O_3 is formed during oxidation. This layer of Al_2O_3 has been observed under the TiO_2 layer (Yang and Wu, 2003) and $TiAl_3$ forms under the oxide scale as a result of Ti depletion (Chuprina and Shalya, 2007). This protective layer of alumina readily forms on γ-TiAl alloys containing more than the stoichiometric amount of Al (Reddy *et al.*, 2001). The low resistance to oxidation at elevated temperatures is due to the high kinetics of TiO_2 formation compared to the growth rate of Al_2O_3. During oxidation of TiAl, aluminium forms a very slow growing oxide α-Al_2O_3, while titanium forms several oxides (TiO, TiO_2, Ti_2O_3, etc.), which have relatively high growth rates. Figure 2.5 is a schematic representation of the scale structure on the Ti-50Al after oxidation in air at 900°C, before oxide scale breakaway (Schmitz-Niederau and Schutze, 1999), where a new cubic phase (NCP) was also identified.

To date, many attempts have been made to improve the high temperature oxidation resistance of stoichiometric TiAl, which include the sputtering of an Al film and subsequent interdiffusion treatment at 600ºC for 24 h in a high vacuum (Chu and Wu, 2003; Hui-Ren *et al.*, 2008; Xin *et al.*, 2003; Braun *et al.*, 2010), sputtering of a Ag-containing TiAl coating and insertion of silicon in the

coating material of TiAl (Goral *et al.*, 2006). The beneficial influence of the coatings on the heat resistance of the alloy is due to the aluminium-rich silicon-modified $TiAl_3$ phase (Moskal, 2007). The $TiAl_3$ phase is the most oxidation-resistant phase of the Ti-Al system. A number of refractory metals have been found to significantly improve the oxidation resistance of γ-TiAl-based materials, which include Nb, W, and Cr (Huang and Chesnutt, 1994). Silver was also added to TiAl with a significant improvement of the oxidation resistance by promoting the formation of a continuous external alumina base scale (Niewolak, 2004).

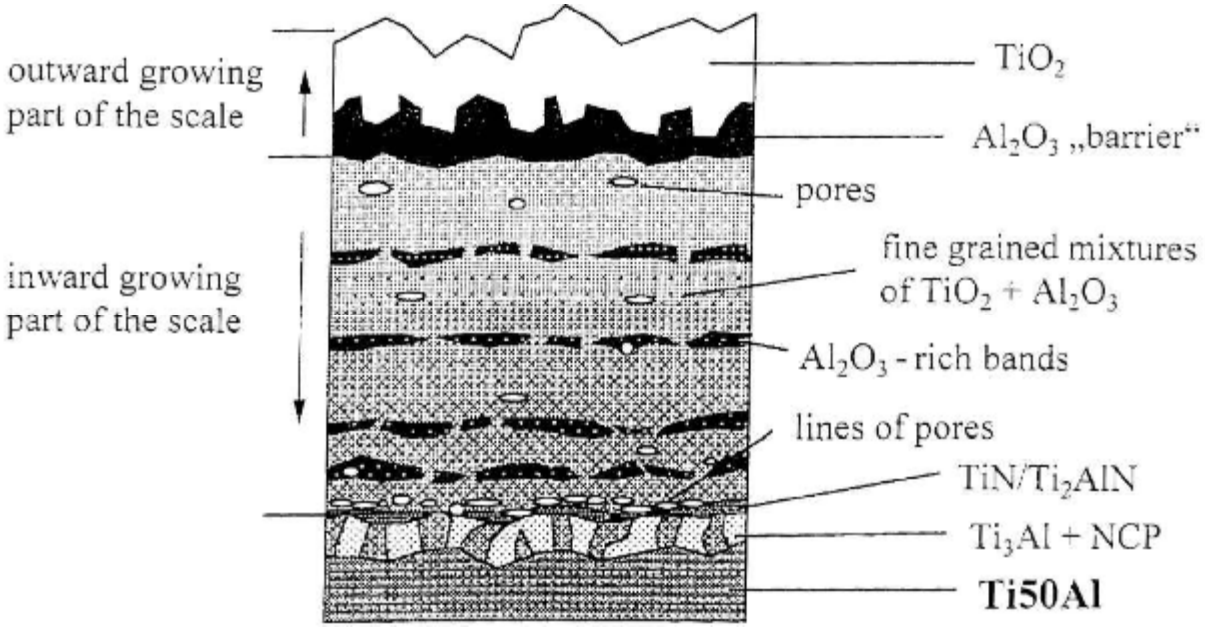


Figure 2.5. *Schematic representation of the oxide scale structure on Ti-50Al after oxidation in air at 900ºC before oxide scale breakaway (Schmitz-Niederau and Schutze, 1999).*

2.2.5 Effect of alloying elements on the properties of γ-TiAl

The microstructure can be modified by ternary or multi-element additions with an impact on the mechanical and physical properties. In most cases, the additions will lead to an improvement of some properties and simultaneous deterioration of others (Appel *et al.*, 2011c). A compromise needs to be found between the benefits obtained and advantages lost.

Vanadium, manganese and chromium have been found effective in increasing ductility at 1-3 at.% additions to alloys with 45-50 at.% Al and a duplex structure (Lapin, 2009). Boron and magnesium enhance hot workability. Tungsten and carbon increase creep resistance (Huang and Chesnutt,

1994; Tetsui and Miura, 2002). Niobium, tantalum, vanadium and phosphorus have also been reported to significantly decrease the oxidation rate (Schumacher *et al.*, 2000). Silicon was also reported to decrease the oxidation rate by forming a SiO_2 layer which is more protective than TiO_2 (Huang and Chesnutt, 1994; Goral *et al.*, 2006; Moskal, 2007).

2.2.6 Processing of γ-TiAl alloys

The difficulty in processing of γ-TiAl is one of the reasons preventing the manufacture of engineering components from γ-TiAl-based alloys (Lapin, 2009). The processing problems are worsened by the complicated heterogeneous microstructures found in the castings, which are difficult to modify by heat treatment (Huang and Chesnutt, 1994). Cast γ-TiAl-based materials, even those having the duplex structure and containing the ductilising elements Cr, Mn and V, are generally weaker and less ductile than wrought materials, because the coarse as-cast structure is usually retained after heat treatment, without recrystallisation.

Due to their brittleness, γ-TiAl-based alloys are difficult to deform. Manufacturing techniques include extrusion, forging, machining, tapping, drilling and joining (Lasalmonie, 2006). Most of these processes have proved to be feasible, but with many limitations in the design and always at high cost. Casting offers the most cost-effective route for the production of complex shapes, since investment casting is a well-established process. However, in spite of all the enormous efforts made over the last two decades, no cast components have been produced which meet aerospace requirements on reliability and cost. Thus, at this stage, casting technology is inadequate to produce aero-engine components from γ-TiAl-based alloys (Lapin, 2009). Melting-and-casting is the method most often used for combining metallic constituents into alloys or intermetallic compounds and has been used to produce γ-TiAl and γ-TiAl-based alloys. However, unlike other systems where conventional eutectic or monotectic solidification results in normal segregation, cascading peritectic reactions can occur in the production of γ-TiAl, resulting in heavy segregation and serious difficulties in obtaining chemical homogeneity in conventional ingots (Appel *et al.*, 2011d). One method to address the segregation issues is to increase the solidification rate by applying rapid solidification techniques, such as atomisation, melt spinning, splat/ribbon cooling and self-substrate quenching (Huang and Chesnutt, 1994).

Difficulties in accommodating the intrinsic properties of γ-TiAl to manufacturing limitations, and vice-versa, have led to the consideration of powder metallurgy as a potentially efficient approach to component production at lower cost, without chemical heterogeneity and imperfections in the final product. Powder metallurgy is a well-established process to successfully produce and consolidate alloyed powders in a wide variety of systems. As a powder metallurgy process involving rapid solidification, atomisation leads to chemical homogeneity of the product. Gamma-TiAl-based alloy powder has been successfully produced and HIP consolidated (Martin and Hardwick, 1994; Gerling, 2001), and γ-TiAl-based alloys can be produced by reacting elemental aluminium and titanium powders (Jacob *et al.*, 1993). Other processes involving rapid solidification use free-forming processes such as spray forming (Schimansky *et al.*, 1999).

Powder metallurgy products, even those manufactured under the best conditions, usually exhibit inferior quality compared to bulk materials, because of the density. Sintering often leads to less than theoretical density, with a negative impact on the mechanical properties (German, 2005). A 90% dense γ-TiAl alloy, showed no room temperature bend ductility, even though it had compressive ductility (Martin and Hardwick, 1994).

Milling was used on pre-alloyed TiAl powder to refine the microstructure, resulting in an ultrafine microstructure with nanoscale crystallite size, partial amorphisation and transformation of Ti_3Al into γ-TiAl (Jacob *et al.*, 1993). Mechanical alloying has been used to produce stoichiometric γ-TiAl and γ-TiAl-based alloys from elemental powders (Sun and Hashimoto, 2003), resulting in the formation of a metastable (Gauvin *et al.*, 1993) or an amorphous TiAl phase (Chen and Wang, 1993). The consolidated powders showed microstructures similar to bulk alloys and a brittle fracture mode (Sun and Hashimoto, 2003). However, even the most efficient consolidation techniques, such as explosive sintering and hydrostatic extrusion, have failed to yield full density, with negative impacts on the mechanical properties (Li *et al.*, 1993). Increasingly, research has focused on the properties of γ-TiAl powder such as creep resistance, high-temperature ductility and oxidation resistance. In this regard, TiAl-based coatings were produced by TIG surface melting (Mridha *et al.*, 2001).

2.2.7 Gamma TiAl and PGMs

TiAl alloys are known to be susceptible to cracking in low pH environments (Liu and Kim, 1992;

Brass and Chêne, 1998; Tonneau *et al.*, 1998). The response of these materials in environments containing hydrogen is of interest, partly because of the possibility of future hydrogen-fuelled aircraft, and a number of studies have been conducted on the effects of hydrogen (Eliezer *et al.*, 1991; Froes *et al.*, 1992; Govender *et al.*, 2012). In order to minimise the sensitivity of TiAl alloys to hydrogen-bearing environments, stabilising elements such as Mo, Nb, V, Zr, Mn and Cr have been explored (Kim, 1994a). However, little is known about the influence of alloying additions such as Fe, Co, Ni at elevated temperatures, and virtually no systematic information is available on TiAl alloys with additions of platinum group metals. This is particularly true for the solid solubility limits as a function of temperature, with respect to possible age hardening for improved long-term creep resistance (Ding *et al.*, 2000).

Platinum group metals (PGMs) were used since the late 1980s as alloying additions in TiAl-based alloys for the improvement of environmental and mechanical properties (Khataee *et al.*, 1989a, 1989b, 1989c). These have been used in titanium metallurgy for the improvement of corrosion resistance and as oxidation resistant coatings (Khataee, 1989a). PGMs have also been used as alloying additions in steels and nickel aluminides in order to enhance environmental and mechanical properties (Wolff *et al.*, 1998; Wu, 2007; Sherif, 2009). Among PGMs, Pd has long been used in titanium alloys at about 0.2 at.%, resulting in outstanding corrosion resistance in low pH environments (Cotton, 1967). Ruthenium is also attractive because of its relatively low cost compared to Pd (Schutz, 1996), and provides titanium alloys with improved strength and hardness. Research on crystallographic parameters and site occupancy of TiAl alloyed with Ru also suggested ductility improvement (Kimura and Pope, 1997). Ruthenium partitioned to the γ phase in TiAl-Ru alloys (Kim *et al.*, 1999).

Khataee *et al.* (1989b) studied the Ti-Al-Ru system, and concluded that the solubility of ruthenium in γ is higher than in the α_2 phase. In a Ti-17-37Al-1-5Ru (at.%) alloy, Ru was a β stabiliser and a complete retention of metastable β occurred at 5 at.% Ru addition (Khataee *et al.*, 1989c). The solubility of ruthenium in Ti_3Al (α_2) was very low (~0.5 at.%), slightly higher in TiAl ($\leq$1 at.%), but considerably high in $TiAl_3$ (~7 at.%), albeit at higher temperatures. This indicated that the ruthenium solubility in the titanium aluminides increased with the aluminium content. Grytsiv *et al.* (2003) reported that the solubility limit of Ru in titanium aluminides was lower than 1 at.%, and

attributed the 7 at.% to a ternary compound. In a study on partitioning of solutes in multiphase Ti-Al alloys, Benedek *et al.* (2005) showed that late transition metals such Mn, Fe, and Ru showed a preference for partitioning to the γ phase. Phase equilibria in the Ti-Al-Ru system were also largely influenced by a ternary intermetallic compound, the G phase, present between 1250-770°C. The compositional range for the G phase was 36-52 at.% Al and about 19-28 at.% Ru (Kathaee *et al.*, 1989b and 1989c). An isothermal section at 770°C of the Ti-Al-Ru system is shown in Figure 2.6 (Khataee *et al.*, 1989b and 1989c)

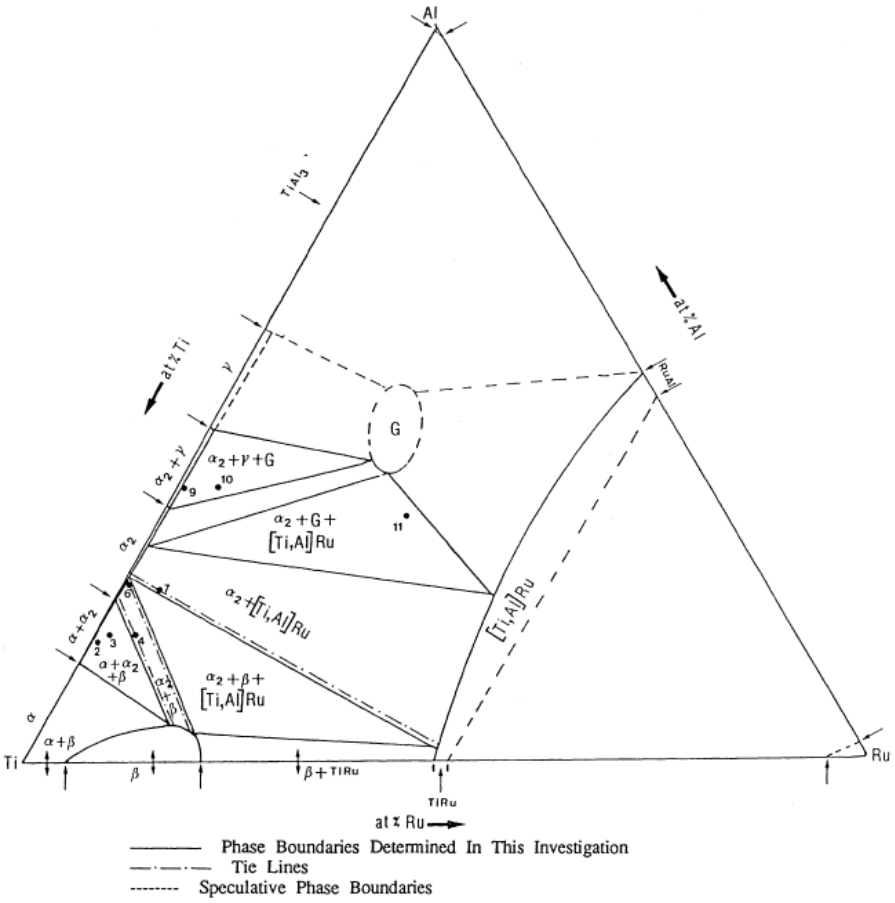
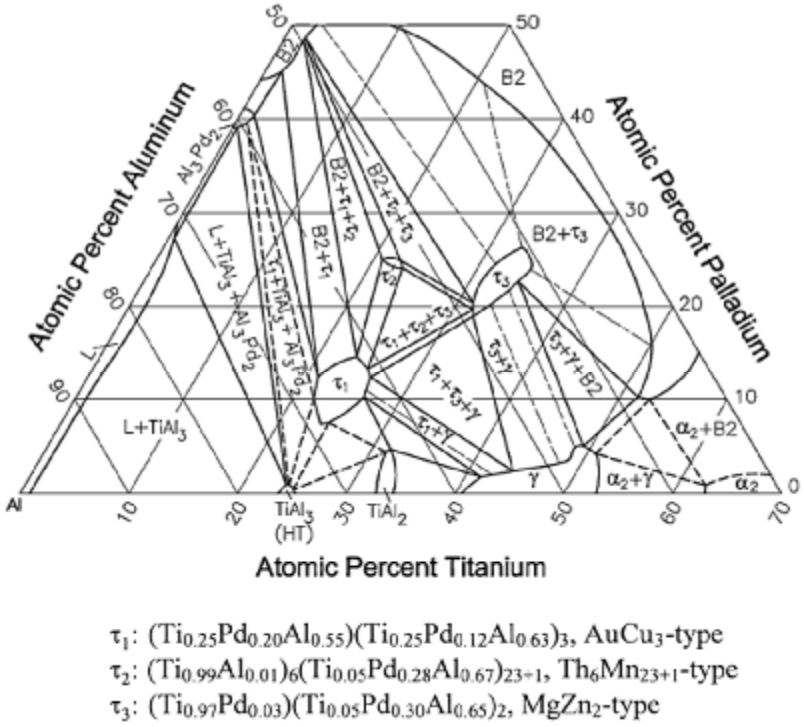


Figure 2.6. *Isothermal section at 770°C of the Ti-Al-Ru system (at.%) (Khataee et al., 1989b and 1989c).*

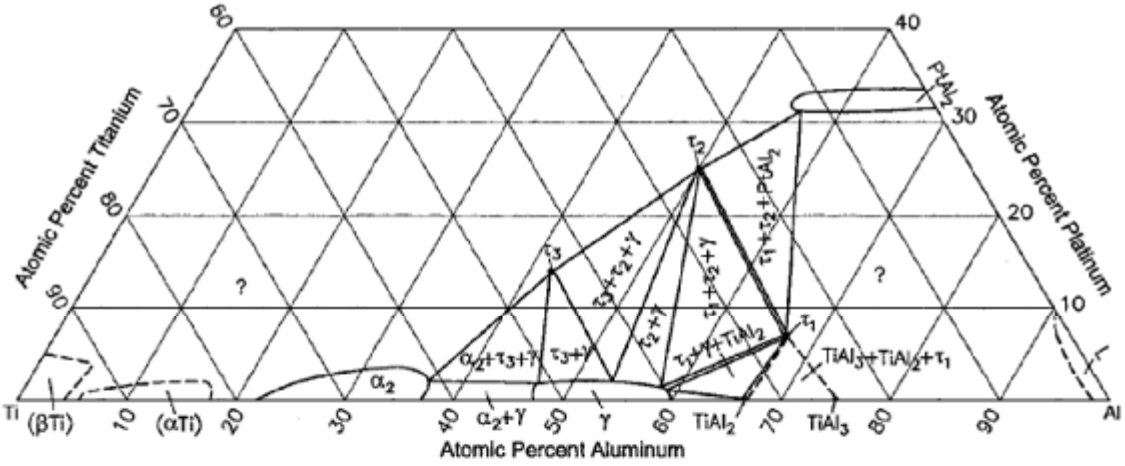
Alloying additions to improve corrosion performance in titanium alloys are also important (Ding et al., 2000). Platinum significantly improved the corrosion resistance of pure titanium in fluoride-containing environments (Nakagawa et al., 2005), and is also used as a coating in the pure state (Kim et al., 2007). The phase equilibria of the Ti-Al-Pd and Ti-Al-Pt systems were investigated in

the regions adjoining the duplex alloy α_2-Ti_3Al+γ-TiAl at 950° and 930°C, as shown in Figures 2.7 and 2.8 (Ding et al., 2000). These figures show that phases similar to the G phase in the Ti-Al-Ru system were observed in the Ti-Al-Pt and Ti-Al-Pd systems: τ_2 around $(Ti, Al)_6(Ti,Pd,Al)_{23+1}$ in the Al-Pd-Ti system and τ_2 around the composition TiPtAl in the Al-Pt-Ti system, both of the $Mn_{23}Th_6$-type, cubic structure. Information about the Ti-Al-Ir system is scarce. Figure 2.9 shows an Ir-rich Al-Ir-Ti partial isothermal section at 1650°C (Raghavan, 2008).



τ_1: $(Ti_{0.25}Pd_{0.20}Al_{0.55})(Ti_{0.25}Pd_{0.12}Al_{0.63})_3$, $AuCu_3$-type
τ_2: $(Ti_{0.99}Al_{0.01})_6(Ti_{0.05}Pd_{0.28}Al_{0.67})_{23+1}$, Th_6Mn_{23+1}-type
τ_3: $(Ti_{0.97}Pd_{0.03})(Ti_{0.05}Pd_{0.30}Al_{0.65})_2$, $MgZn_2$-type

Figure 2.7. *Partial Al-Pd-Ti isothermal section at 930°C in the Pd-lean region (Zaikana et al, 2000).*



τ_1: $Ti_{0.26}Pt_{0.07}Al_{0.67}$, Cu-type
τ_2: $(Ti_{0.82}Al_{0.18})_6(Ti_{0.09}Pt_{0.29}Al_{0.62})_{23+1}$, Th_6Mn_{23+1}-type
τ_3: $(Ti_{0.83}Al_{0.17})(Ti_{0.26}Pt_{0.20}Al_{0.54})_2$, $MgZn_2$-type

Figure 2.8. *Partial Al-Pt-Ti isothermal section at 950°C for Pt-poor side (Ding et al., 2000).*

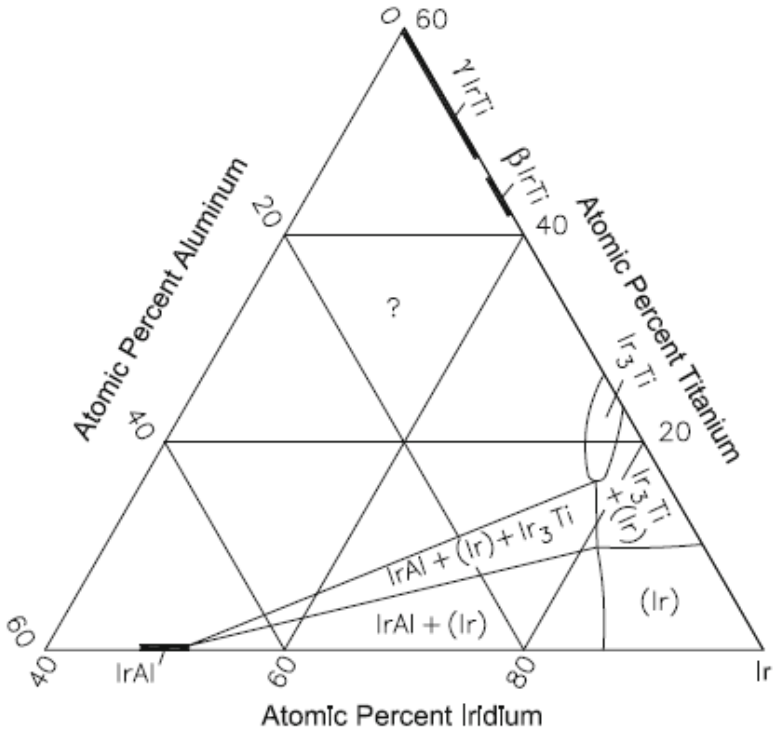


Figure 2.9. *Ir-rich Al-Ir-Ti partial isothermal section at 1650°C (Raghavan, 2008).*

2.2.8 Gamma-TiAl as coating materials

Plain γ-TiAl is characterised by the lack of oxidation resistance above 750°C (Okafor and Reddy, 1999; Ebach-stahl *et al.*, 2008 and 2009). Conventional coatings for superalloys, such as aluminide coatings (coatings with aluminium, e.g. PtAl) and "MCrAlY" coatings (where M = Co, Ni or Co / Ni (base metals) and Al = aluminium with Y = yttrium, which enhances the bonding of the stable oxide layer formed by aluminium and chromium), are not suitable for the protection of TiAl alloys, due to the poor coating-substrate compatibility resulting from the formation of brittle intermetallic compounds at the interface substrate-coating, and consequently new coating systems have to be developed (Tang *et al.*, 2002).

Coatings such as Ti-50Al-10Cr (at.%) were very effective in improving the oxidation resistance of γ-TiAl due to the formation of a protective Al_2O_3 scale and excellent coating-substrate compatibility. The combined effect of Cr and Ag on γ-TiAl oxidation was investigated, with preliminary results indicating excellent oxidation resistance of the Ti-48Al-7Cr-2Ag (at.%) alloy at 800°C and 900°C, with good mechanical properties (Tang *et al.*, 2002).

Overlay coatings, which can help combine the optimised mechanical properties of coatings and substrates, have been proved to be one of the most efficient ways to further improve the oxidation resistance of γ-TiAl-based components (Brady *et al.*, 1996; Tang *et al.*, 1997; Narita *et al.*, 2000). Gamma-TiAl-(10-15) at.% Cr and γ-TiAl-Ag are both alumina formers, and therefore are considered coating candidates (Leyens and Braun, 2004). The major disadvantage for γ-TiAl-Cr alloys is that a high Cr content can lead to coating embrittlement (Brandt, 1996; Narita *et al.*, 2000; Leyens and Braun, 2004). By contrast, Ag in γ-TiAl did not seem to deteriorate its mechanical properties so much, and may even slightly improve the surface hardness at elevated temperatures, due to the Ti(Al,Ag) precipitates (Tian and Nemoto, 1999). The oxidation behaviour of γ-TiAl-Ag alloys and their coatings at 775°C in air were studied by Niewalak *et al.* (2004). Their results showed that γ-TiAl alloys containing more than 1.0 at.% Ag were alumina formers, and could sustain long term oxidation attack. Liu and Narita (2003) also showed that coatings containing more than 1.0 at.% Ag were resistant to oxidation attack in wet air. Both Ag content in the coatings and H_2O content in the atmosphere had significant influence on the oxidation behaviour of γ-TiAl-Ag coatings. Higher H_2O contents resulted in the formation of duplex oxide scale with a thin layer of

TiO_2+Al_2O_3 on top of the continuous Al_2O_3. The coatings showed good compatibility with the substrate after the oxidation tests.

The development of coatings based on γ-TiAl alloys shows much promise for coating materials (Brady *et al.*, 1996; Oliker and Kresanov, 2000 and 2003). Studies were conducted on plating of titanium with wear-resistant coatings (Krienke, 1969; Turns *et al.*, 1975) corrosion- and oxidation-resistant coatings (Gurrapa, 2001a and 2001b). The similarity between the chemical compositions of the substrate and coatings creates good conditions for strong adhesion between them, which is one of the most important conditions for the use of the engineering component. Using the detonation-gas spraying method with mechanically alloyed Ti-50 at.% Al powder, Oliker *et al.* (2005) produced a coating based on Al_2TiO_5 by the oxidising action of the working gas on the powder, and they manufactured a coating based on titanium aluminides with TiN inclusions by nitriding action.

There is little information on γ-TiAl-coating applied by high velocity oxygen fuel (HVOF), although γ-TiAl has been investigated as potential coating for titanium-based alloys since the late 1990s (Leyens *et al.*, 1997). The TiAl coating was applied by plasma spray and isostatically pressed (Khor *et al.*, 1996). More recently, the HVOF technique was also applied to thermally spray a TiAl-Al_2O_3 composite for the improvement of the Ti-6Al-4V substrate wear resistance (Hung *et al.*, 2008; Salman *et al.*, 2009). Porosity was one of the drawbacks of thermal spray coating (Schütze *et al.*, 2006). Cold spraying, which is a new and developing technique for coating is a solid state process in which sprayed particles are deposited via supersonic velocity impacts at a temperature much below the melting point of the spray material. To date, materials for cold spraying, as presented by some private institutions (Sandvik, 2015; Supersonicspray, 2015), includes steels, MCrAlY alloys, cobalt alloys, aluminium alloys, nickel alloys, copper alloys and pure metals.

2.3 Corrosion and oxidation of TiAl-based alloys

2.3.1 Corrosion of TiAl-based alloys

Very limited information is available on room or near room temperature aqueous corrosion properties of titanium aluminides. Most investigations conducted to date on the titanium aluminide alloys were aimed at high temperature performance and therefore, high temperature properties such

as oxidation and corrosion resistances were investigated (Meier, 1989; Rahmel *et al.*, 1995; Reddy *et al.*, 2001; Chu and Wu, 2003; Yang and Wu, 2003; Chuprina and Shalya, 2007). Gamma-TiAl, originally designed for high temperature applications, appears to have excellent potential for bone repair and replacement, with the biological response expected to be similar to other titanium-based biomaterials (Rivera-Denizard *et al.*, 2008). Observations from early tests triggered recent research activities on γ-TiAl as human body implants (Long and Rack, 1998), with assessments of the properties of γ-TiAl in aqueous media simulating human body fluids (Escudero *et al.*, 2004; Jafariana *et al.*, 2009; Bello *et al.*, 2010).

In most aqueous environments, titanium and titanium alloys show good corrosion resistance, due to the stable oxide films that form spontaneously on the surface. However, in chloride and/or fluoride solutions, titanium alloys are susceptible to attack, showing pitting and crevice corrosion (Brossia and Cragnolino, 2001). Alloying elements, including nickel and molybdenum, have been added to titanium and titanium alloys to improve the corrosion resistance to pitting (Trufanov *et al.*, 1989; Schutz, 1996). Precious metals were added to titanium to increase the corrosion resistance in non-oxidising acids (Hoar, 1960; Potgieter, 2010). They were also used to increase the corrosion resistance of other alloys, such as stainless steel (Potgieter and Brookes, 1995; Olubambi *et al.*, 2009) and their use for corrosion resistance improvement originated when Monnartz (1911) reported that the rapid corrosion of iron-chromium alloys in certain acids was suppressed by winding a platinum wire around the corrosion-test specimen or by adding platinum as an alloying element to steel. Stainless steel (Streicher, 1977; McGill, 1990) and nickel-based alloys (Kim and Frankel, 2007) were alloyed with platinum group metals to improve their corrosion resistance.

Several methods for controlling or improving corrosion resistance of metals and alloys are available in the literature (Korb and Olson, 1987). Corrosion resistance can be controlled and/or improved by cathodic modification (Stern and Wissenberg, 1959a and 1959b; Potgieter, 1990; van der Lingen and Sandenbergh, 2001). For some metals and their alloys, such as aluminium, modification of anodic layers has been also used for corrosion resistance improvement (Krasicka-Cydzik *et al.*, 2007; Lee *et al.*, 2008; Černý and Filípek, 2011). Beneficial alloying elements mostly used in cathodic modification include platinum group metals, nickel and/or molybdenum (Satoh *et al.*, 1987; Schutz,

1996). When present in stainless steel, molybdenum led to better corrosion resistance by cathodic modification (McGill, 1990).

PGMs, nickel or molybdenum additions facilitate cathodic depolarization by providing sites of low hydrogen overvoltage, which shift the alloy potential in the positive direction, where oxide film passivation is possible (Tomashov, 1990, Potgieter, 1991; van der Lingen and Sandenbergh, 2001). A comprehensive description of the cathodic modification mechanism was given by Potgieter (1990 and 2010). Relatively small concentrations of certain precious metals, ~0.1 wt%, are sufficient to significantly improve the corrosion resistance of titanium in reducing acid media (Trufanov *et al.*, 1989; Schutz, 1996).

Alloys used in critical engine components, such as turbine blades and turbocharger casings, are exposed to by-products from fuel combustion, which form corrosive solutions when in contact with moisture-containing environments, leading to pitting and crevice corrosion (DMI Global, 2012; Nordtest, 2012), in addition to the hot corrosion usually observed in gas turbine components (Lozitskii *et al.*, 1974; Eliaz *et al.*, 2002). Alloying plays an important role in the corrosion resistance of materials in such environments, as the microstructural components of the alloy have different responses, if subjected individually to the same environment. It is also difficult to predict the response of the alloy to the corrosive medium, as the presence of new phases, compounds and microstructures can lead to pitting and/or galvanic corrosion.

2.3.2 Principles of cathodic modification

Potgieter *et al.* (1990), described the principles of cathodic modification which is shown schematically in Figure 2.10 and presented the four distinct states that can be displayed by a system with an active-passive transition: active, active-passive, passive and transpassive. The different states depend on the relative efficiency of the cathodic process (or processes) in each case.

Active state

When the rate of the cathodic process is relatively low (green line in Figure 2.10a), the system will be in the active state. The metal or alloy undergoes stable active dissolution at a potential of E_{corr} with a current density of i_{corr}, and the following conditions prevail:

$$E_o{}^A < E_{corr} < E_{pass} \text{ , and } i_{cath}(E_{pass}) < i_{crit}$$

Where:

E_o^A is the transition potential from cathodic to anodic process of base metal.

i_{cath} is the a exchange current density of the modified alloy, and

i_{crit} is the critical current density of the base metal or alloy.

The active state is established spontaneously. Hence, if an external perturbation causes the system to move momentarily into the passive potential range, the active state will be spontaneously re-established.

Active-passive state

For a higher, intermediate rate of the cathodic process (green line in Figure 2.10b), there are three possible conditions for the system. These conditions are given at the three points *A*, *B*, and *C*, at which the cathodic line and anodic curve intersect. At potential *C* ($< E_{pass}$), anodic dissolution of the metal or alloy occurs at a relatively high corrosion rate. At potential B ($\sim E_{pass}$), the system is in an unstable state, rarely observed in practice. At potential A ($> E_{pass}$), the system is in the passive state, and the corrosion rate is very low. If the system is perturbed, the different conditions of the active-passive state will not be spontaneously re-established.

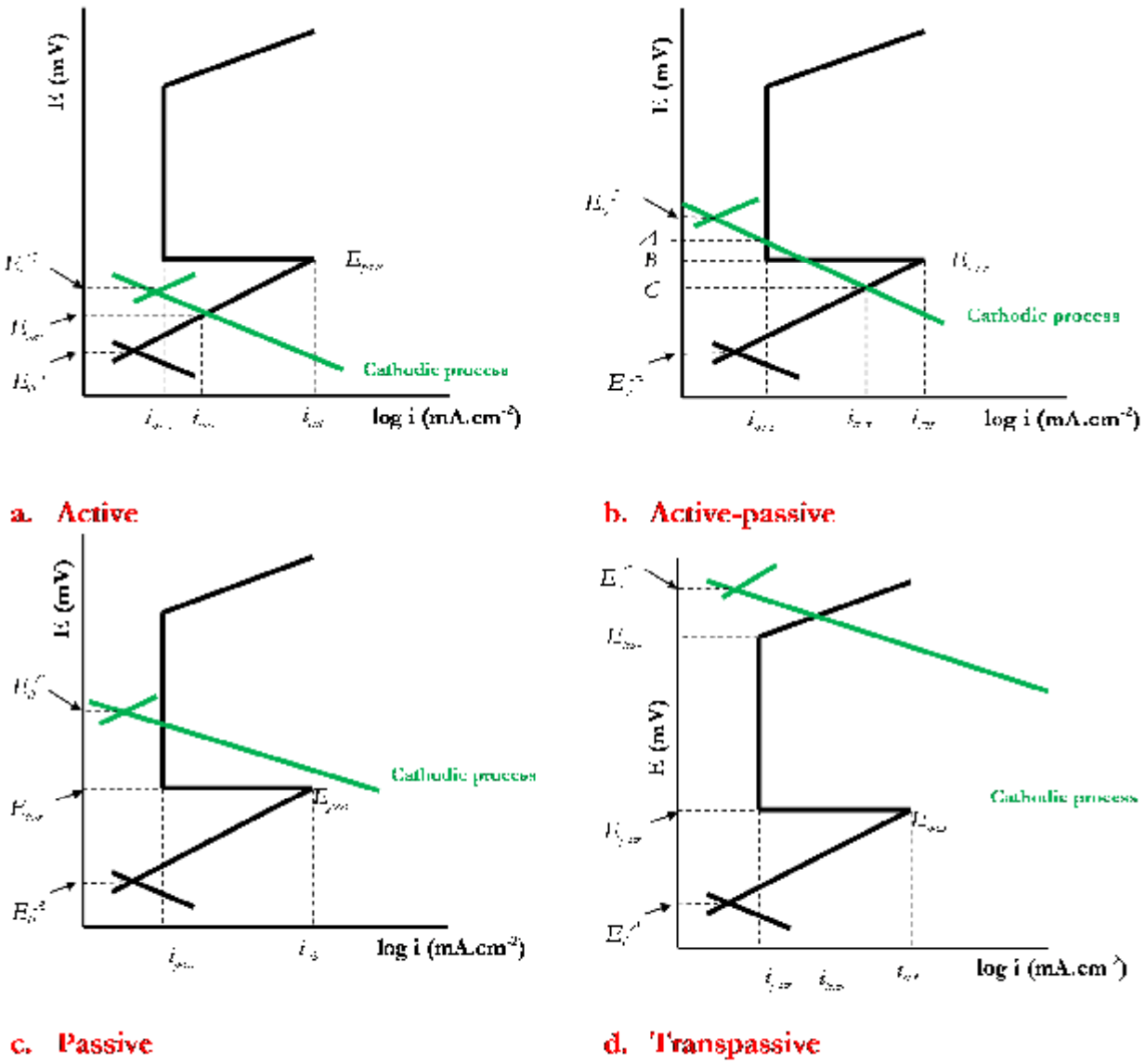


Figure 2.10. *Principles of cathodic modification: a) active, b) passive-active, c) passive, and d) transpassive, after Potgieter et al. (1990).*

Passive state

For a high rate of the cathodic process (solid line in Figure 2.10c), the anodic and cathodic curves intersect at only one point. The system is in a stable, passive state. The following conditions prevail:

$$E_o^C > E_{pass} \text{ and } i_{cath}(E_{pass}) > i_{crit}$$

where E_o^C is the transition potential from cathodic to anodic process of the base metal after alloying.

The rate of metal or alloy dissolution is very low, and is equal to the passive current density i_{pass}. The passive state is also spontaneously stable, which means that if the passivity is momentarily disturbed, the passive state will be spontaneously re-established. This kind of system is typical of cathodically modified chromium, stainless steel, and titanium alloys in non-oxidizing acid environments (McGill, 1990). The chromium, stainless steel and titanium alloys all have passivation potentials more negative than the evolution potential of hydrogen in acidic media. When a PGM is added to any of these alloys, a large increase in the rate of hydrogen evolution will occur, which is large enough to move the corrosion potential of the cathodically modified alloy in the region of stable passivity (Streicher, 1977; McGill, 1990; Kim and Frankel, 2007; Potgieter *et al*., 1990). Spontaneous passivation of the alloy will therefore result (Potgieter *et al*., 1990).

Transpassive state

For a very high rate of the cathodic process (green line in Figure 2.10d), or in highly oxidizing environments, it is possible that $E_o^C > E_{trans}$. At this high potential, the metal or alloy will have a higher rate of dissolution than at potentials in the passive range, and considerable corrosion can take place.

2.3.3 Alloys cathodically modified with noble metals

The use of the platinum group metals to modify the cathodic reaction on stainless steels, chromium-based alloys and titanium-based alloys has been under investigation over the last 50 years (Stern and Wissenberg, 1959a, 1959b; Hoar, 1960; Streicher, 1977; McGill, 1990; Potgieter *et al*., 1990). The corrosion resistance of alloys containing small amounts of noble metals relies on the principle that the high exchange-current density for the reduction of hydrogen can shift the corrosion potential of the alloy to a value in the passive region, causing it to passivate spontaneously (Potgieter, 1991). The effectiveness of the PGMs and other noble metals in promoting corrosion resistance was found to decrease in the order Ir > Rh > Ru > Pt > Pd> Os > Au > Re > Ag (Stern and Wissenberg, 1959a and 1959b).

2.3.4 Cathodic modification

Cathodic modification is the most documented method for increasing titanium corrosion resistance in non-oxidising acids (Stern and Wissenberg, 1959a, 1959b; van der Lingen and Sandenbergh, 2001; Potgieter, 2010). Four basic conditions are required for successful cathodic alloying (Potgieter *et al.*, 1990):

1. The base alloy must have a small critical current density (i_{crit}) that will be easily exceeded by the current of the hydrogen cathodic reaction on the added noble metal at the given passivation potential (E_{pass}).
2. The passivation potential (E_{pass}) of the base metal must be sufficiently negative to allow the cathodic component which has been introduced to change the corrosion potential (E_{corr}) of the alloy to a value in the passive range that is more positive than E_{pass}, but less positive than the potential associated with the onset of transpassive processes (E_{trans}).
3. The transpassive potential (E_{trans}) of the base alloy should be sufficiently electropositive to allow a wide passive range.

Furthermore, the cathodic alloying component should itself satisfy certain basic conditions. It should have a higher exchange current density i_0 (and lower overvoltage) for the cathodic process of hydrogen evolution than the base metal or the alloy, and it should be corrosion-resistant under the given conditions.

In non-oxidizing acids (such as sulphuric and hydrochloric acids), the condition requiring a sufficiently negative passivation potential is satisfied by stainless steels, chromium-based alloys and titanium-based alloys, while the PGMs have the necessary high exchange current density, i_0 (and low overvoltage), for hydrogen evolution.

2.4 Reduction of titanium corrosion rate with addition of noble metals

The reduction of the corrosion rate of alloys with additions of noble metals in boiling sulphuric and hydrochloric acids was investigated by Stern and Wissenberg (1959b). At various concentrations, it was found that the maximum benefit obtained by platinum metal additions was reached at ~0.1 wt%. This is shown in Figure 2.11 (Stern and Wissenberg, 1959b), where active conditions prevailed

at the beginning in the alloys with the lowest noble metals contents, until sufficient metal became exposed to give the required amount of cathodic stimulation to produce passivation.

Palladium-alloyed titanium performed better than unalloyed titanium in oxidising environments, and performed much better in non-oxidising and reducing acid solutions (Stern and Wissenberg, 1959b). It was also better than zirconium in non-oxidising and reducing acid solutions, and much better under oxidising conditions.

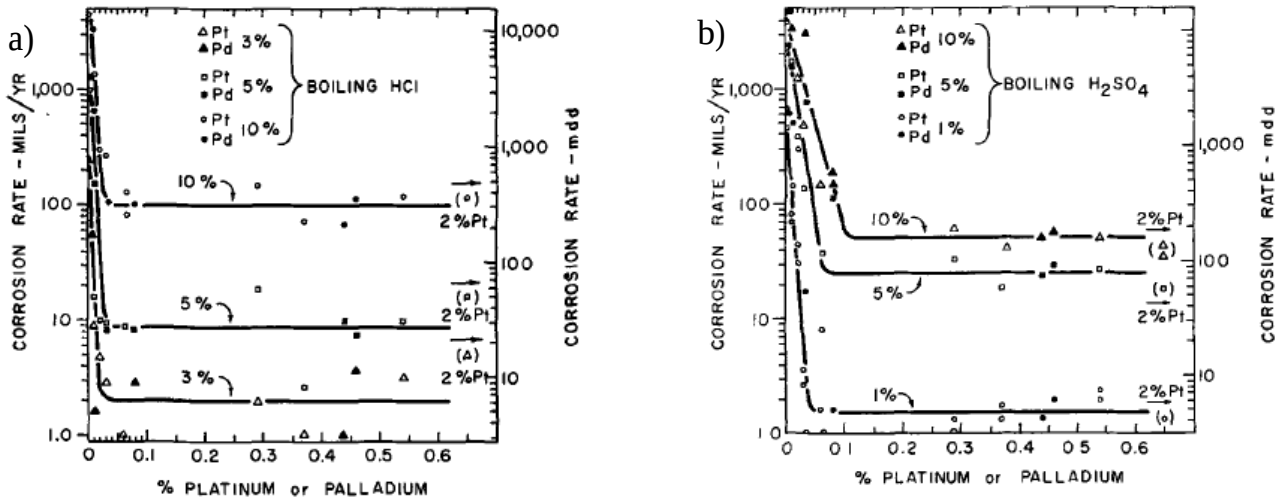


Figure 2.11. *Effect of platinum and palladium on the corrosion rate of titanium in a) boiling chloridric acid solution, and b) sulphuric acid solutions (Stern and Wissenberg, 1959b).*

2.5 Aqueous corrosion of intermetallic compounds

Intermetallic compounds have not been especially developed for resistance to low-temperature, aqueous corrosion, with only a few exceptions including Fe_3Al and some its alloys which have been developed as possible substitutes for stainless steels in intermediate-temperature applications (Duquette, 1994). In certain applications for intermetallic compounds and alloys, and other composite materials based on these compounds, exposure to moisture from the atmosphere can be expected, as well as to liquid solutions from the aerospace environment. The lack of development of intermetallic compounds for corrosion resistance means that a very limited number of aqueous corrosion studies performed on the new generation of intermetallic compounds and alloys have been done. Most of the intermetallic compounds investigated to date seem to be sensitive to

hydrogen embrittlement (Takasugi, 1988; Stoloff *et al.*, 1991; Dunfee *et al.*, 1995; Balasubramaniam, 2002; Shankar-Rao, 2004).

For single-phase alloys, the dissolution rates of the alloying elements are generally not uniform, and the rate of the overall corrosion is often controlled by the dissolution of the least active element in the alloy, assuming that there is interconnectivity of the dissolving elements (Duquette, 1994). The general result is the surface enrichment of the less active (nobler) element and a gradual reduction of the dissolution rate, provided that the atom ratio of noble/active elements is above a value specific for each system, the alloy is not covered with a film and is homogeneous (Scully, 1966). For multi-phase alloys, if the active phase is finely dispersed in the noble matrix, it will be dissolved out and further dissolution of the alloy will be determined by the noble matrix. If the active phase is continuous or present in sufficiently large proportion, the dissolution will not occur (Scully, 1966).

For aluminium alloys, alloying elements can also modify the potential of aluminium in both directions, as shown in Figure 2.12 (Burleigh *et al.*, 1993). Zinc strongly decreases the potential (Burleigh *et al.*, 1993). Therefore, Alloy 7072 with 1 at.% zinc is used as a cladding of Aluminium 3003. Copper alloys of the 2000 series have the smallest electronegative potentials. In solutions containing SCN^- anions, the alloying elements of Al-6061 and Al-Cu alloys cause enhanced uniform corrosion of copper. At the same time, the pitting corrosion is decreased by the positive increase of pitting and repassivation potentials (Amin, 2011).

In aqueous solutions, the behaviour of the intermetallic alloys depends mainly on the potential difference between the particles and matrix. The phases which are electrochemically nobler than the matrix play the role of cathodes, while the matrix undergoes anodic dissolution (Szklarska-Smialoska, 1999). If the matrix is nobler than the intermetallic phase, there will be dissolution of the precipitated phases, which will leave holes where agglomeration of aggressive species of the liquid solution can occur. These phases will therefore be the sites where pits will preferentially nucleate, giving rise to intercrystalline corrosion, or exfoliation corrosion if localised at or close to grain boundaries. Buchheit (1995) collected corrosion data in NaCl for intermetallic phases commonly found in aluminium alloys, which can help predict the galvanic cell formation in aluminium alloys.

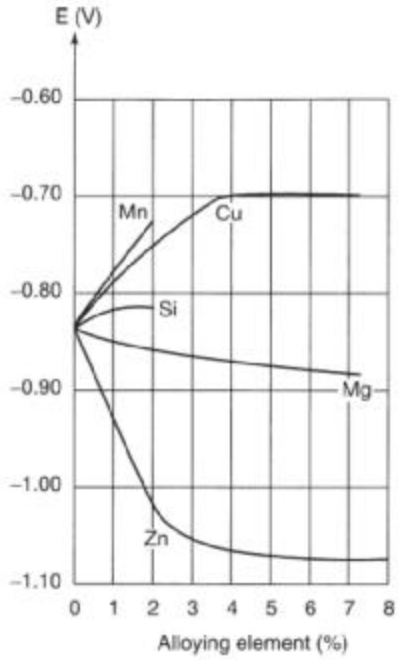


Figure 2.12. *Influence of alloying elements on the dissolution potential of aluminium alloys (Burleigh et al., 1993).*

Most intermetallic compounds of commercial interest generally contain significant amounts of aluminium or silicon in order to provide elevated-temperature oxidation resistance (Duquette, 1994). Alloys containing appreciable amounts of these elements tend to become passive in solutions with pHs in the range 4-10. The passivity is the result of the reaction with water which produces a stable aluminium oxide or hydroxide film on the surface of the alloy according to the following reactions:

$2Al + 3H_2O \rightarrow Al_2O_3 + 3H_2$

or

$2Al + 6H_2O \rightarrow 2Al(OH)_3 + 3H_2$

The oxide or hydroxide films act as an effective diffusion barrier to ionic species of the alloying elements. In solutions of either very high or very low pH, the films tend to be unstable, dissolving and forming pits, resulting in general dissolution of the alloy (Szklarska-Smialoska, 1999). However, in acid solutions, most aluminium-containing alloys can be electrochemically passivated (Duquette, 1994).

A limited number of electrochemical studies on intermetallic compounds are available, and indicate that the behaviour of aluminides is the same as other aluminium-rich alloys (Bertocci *et al.*, 1990; Buchheit *et al.*, 1995; Birbilis and Buchheit, 2005). From available data in the literature, the aqueous corrosion of Ni_3Al and Fe_3Al, aluminides with the same number of aluminium atoms in their cell structure as Ti_3Al, is discussed to obtain an understanding of what could be the possible behaviour of titanium aluminides in similar environments. The electrochemical response of Ni_3Al in neutral, acid, and basic solutions is similar to either pure nickel or pure aluminium, depending on the specific potential regime (Ricker *et al*., 1990). Figures 2.13 to 2.15 show typical polarization curves for Ni_3Al in three different pH regimes and compare the electrochemical behaviour of the intermetallic compound with those of pure nickel and pure aluminium (Ricker *et al*., 1990). Figure 2.13 shows that the pitting potential of the Ni_3Al was considerably higher than pure aluminium and was close to pure nickel. At the pitting potential, the slope of the current-potential curve suggests that the Ni_3Al resistance to pit growth was inferior to pure nickel. In the active region of the polarization curve where hydrogen is evolved, the slopes of Ni_3Al and pure nickel suggest that Ni_3Al was a more effective catalyst for hydrogen evolution than pure nickel. In strongly reducing acid (Figure 2.14), the behaviour of Ni_3Al was similar to pure nickel, except that a larger critical current density for passivation was observed and hydrogen evolution occurred more readily. In basic solution (Figure 2.15), pure nickel and Ni_3Al were virtually identical, except for a slight reversal in the tendency to evolve hydrogen.

An electrochemical study of Ni_3Al with B, Zr, Cr, or Mo showed that chromium contributed to the transpassive dissolution of the passive film at a much lower anodic potential, significantly reducing the passive region (Sulka and Jóźwik, 2011). The effect of Fe, Ga and Mo on the corrosion behaviour of NiAl in NaCl and NaOH solutions was that the best corrosion resistance in both solutions was obtained with 6 at.% Ga (Albiter *et al.*, 2004). The highest corrosion rate was obtained with NiAl+6 at.% (Mo, Fe) in NaCl solution and NiAl+6 at.% Mo in NaOH solution. NiAl alloyed with Fe was more corrosion resistant than 316L type stainless steel, with low corrosion density, higher passivation potential and high pitting potential (Colin *et al*., 2007). The corrosion density of NiAl was independent of the pH in the range 6-12 and varied significantly in acidic solution ($pH<5$) (Rybalka *et al.*, 2011).

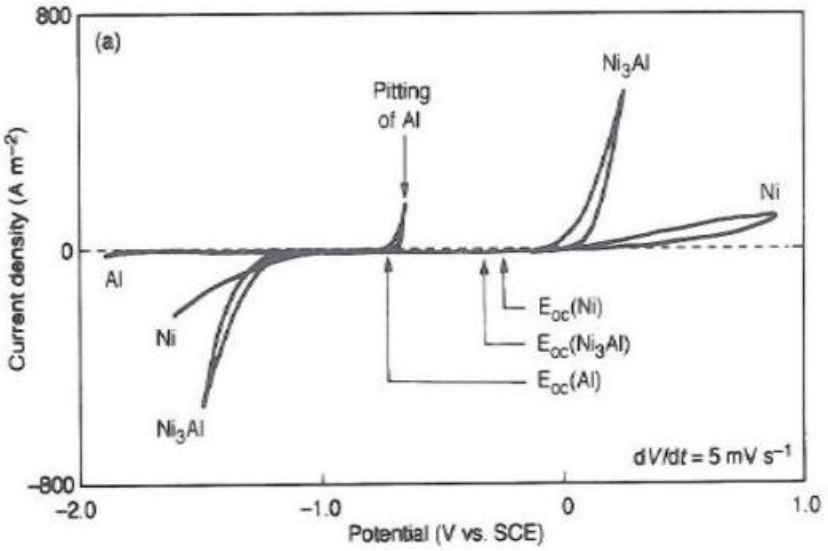


Figure 2.13. *Typical polarization curves for Al, Ni and Ni_3Al in a 0.5M NaCl solution (Ricker et al., 1990).*

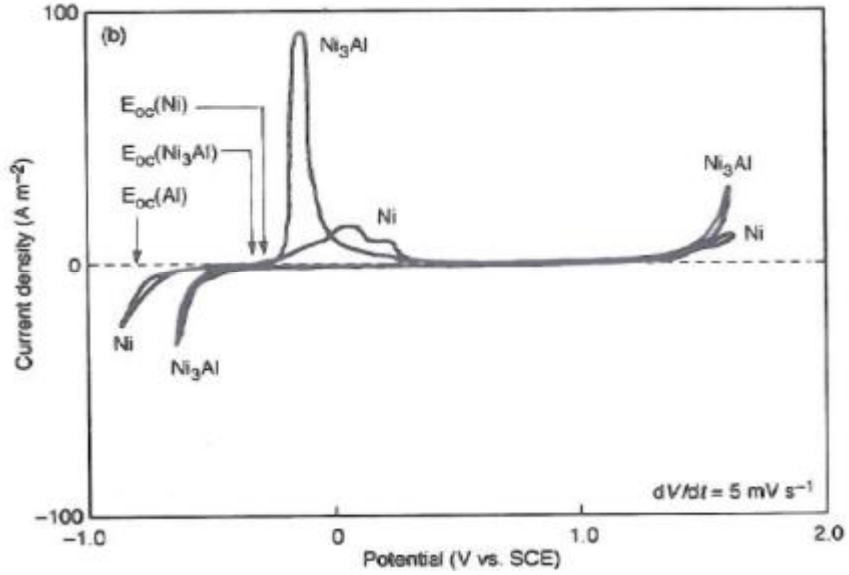


Figure 2.14. *Typical polarization curves for Al, Ni and Ni_3Al in a 0.5M H_2SO_4 solution (Ricker et al., 1990).*

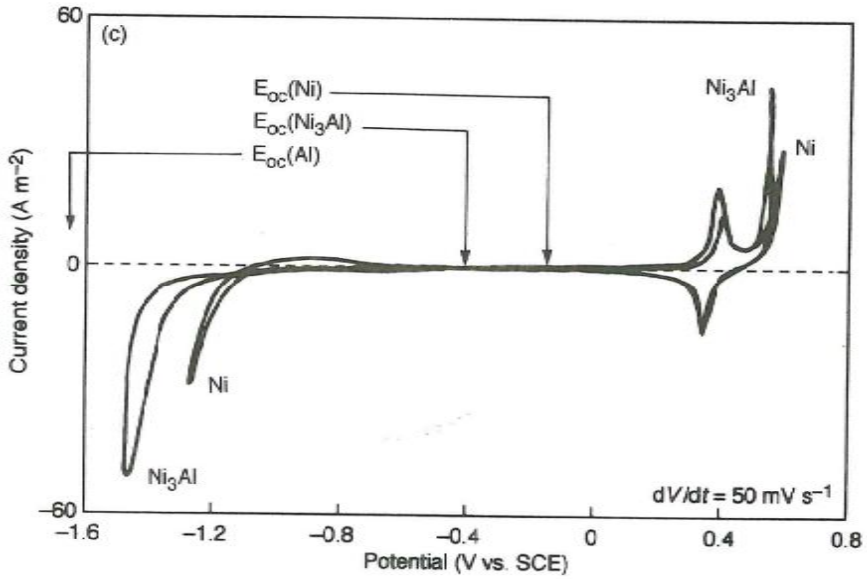


Figure 2.15. *Typical polarization curves for Al, Ni and Ni_3Al in a 0.5M NaOH solution (Ricker et al., 1990).*

Fe_3Al has been extensively researched over the last 40 years. Available data have established that additions of Cr and Mo improve resistance to localised corrosion (Buchanana and Kim, 1990; Agarwal *et al.*, 1996; Choi and Kim, 2002; Rao, 2004; Chang *et al.*, 2007, Garima *et al.*, 2007).

Most data available for γ-TiAl were for its high-temperature corrosion and oxidation resistance. However, limited data on corrosion of γ-TiAl were also available, most of which were related to hydrogen embrittlement in aqueous corrosive media (Gao *et al.*, 1996; Haruna *et al.*, 2000; Arockiasamy *et al.*, 2010). There is increasing interest in the use of γ-TiAl at room and human body temperatures and research is underway to assess the corrosion susceptibility of the γ-TiAl in simulated human body conditions (Jafariana *et al.*, 2009). Biocompatibility studies were conducted on human foetal osteoblast cells cultured on γ-TiAl (Rivera-Denizard *et al.*, 2008). Ti-47Al-2Cr (at.%) oxidized at 550°C in air for 1 hour showed good corrosion resistance in NaCl solution (Delgado and Sundaram, 2007) and in Ringer's solution, suggesting that γ-TiAl can be considered as an alternative competitive metallic biomaterial, and that thermal oxidation of γ-TiAl is a promising method to generate highly corrosion resistant and biocompatible surfaces for implant applications (Bello *et al.*, 2010). The corrosion properties of γ-TiAl as potential implants were

assessed in Ringer's solution (pH: 7.3-7.4) and 3.5 wt% NaCl solution (pH: 6.5), demonstrating that both in basic and acidic solutions, γ-TiAl oxidised by heat treatment in air exhibited high corrosion resistance.

2.6 Powder characterisation

The processing and final results achieved in sintered compacts are strongly influenced by the characteristics of the powder, which in turn depends on the production method (Cannon *et al.*, 1982; Mikli *et al.*, 2001). During the design of powder production processes, it is important to know beforehand the characteristics of the targeted powder particles, as this will dictate the choice of the powder production route (Cannon *et al.*, 1982; Datta, 2012). A powder is characterised with respect to the apparent density, tap density, flowability and packing, particle size, particle size distribution, particle shape, surface area, internal structure, composition, homogeneity and chemistry. These characteristics influence the powder response to compacting and sintering.

2.6.1 Apparent density, tap density and flow rate

The apparent density of a powder is defined as the weight per unit volume of powder after pouring through a Hall flow meter (ASTM B212 and ASTM B213) for free flowing powder or an Arnold apparent density meter (MPIF STANDARD 48) for non-free flowing meter. The tap density is the weight divided by the volume after vibrating the powder (ASTM B527 or MPIF Standard 46).

The flowability or flow rate of a metal powder is important to assess its ability to pack to high density, to fill the die cavity during compaction or injection moulding. The flow rate can be measured with a Hall flow meter (MPIF STANDARD 03).

2.6.2 Particle size and particle size distribution

The assessment of a size distribution includes the determination of the mean particle size and other parameters of the size distribution such as the d_{10}, d_{50} and d_{90}. These parameters are defined by Yule and Dunkley (1994) and German (2005) as:

d_{10}: 10 wt% of the particles are smaller than d_{10} and 90 wt% are larger than d_{10}.

d_{50}: Median diameter or medium value of particle diameter is a particle diameter or size value in case where a cumulative distribution percentage reaches 50%. 50 wt% of the particles are smaller than d_{50} and 50 wt% are larger than d_{50}.

d_{90}: 90 wt% of the particles are smaller than d_{90} and 10 wt% are larger than d_{90}.

A wide variety of methods to measure these parameters is available, the most popular being screening or sieving. In the sieving method, the powder is tapped through a set of sieves with decreasing mesh size and the amount of powder in each sieve is weighed (MPIF STANDARD 05). For very fine powder (below 100 μm), techniques based on the measurement of sedimentation, electrical conductivity, light scattering or X-rays are used. In this category, the technique based on laser diffraction is commonly used. The laser diffraction technique does not use an arithmetic mean in the characterisation of powder particle size. Instead, it makes use of the volume weighed mean D [4,3], or De Brouckere Mean Diameter and surface area mean D [3,2], or Sauter Mean Diameter (Yule and Dunkley, 1994). The De Brouckere Mean Diameter is the volume (or mass) moment mean, and the Sauter Mean Diameter (SMD, d_{32} or D [3,2]) is the diameter of a sphere that has the same volume/surface area ratio as a particle of interest.

2.6.3 Particle morphology

There is a wide variety of shapes of powder particles. Morphology influences the flowability, the apparent density and the response of the powder to compaction (Upadhyaya, 1997; German and Bose, 1997; German, 2005; Mwamba, 2007a). The particle morphology must be considered together with the size distribution, and is often determined with a scanning electron microscope. Different manufacturing techniques result in powders with different characteristics and appearance, for use in specific applications. Water atomisation usually produces irregularly-shaped particles free of internal porosity. However, depending on the operating parameters such as water pressure and melt superheat, spherical particles can be produced (Yule and Dunkley, 1994; Mwamba, 2007b, 2008). Gas atomised particles are spherical and pore-free (German, 2005). Metal powders produced by oxide reduction are irregular in shape, have a large surface area, and usually contain a substantial amount of internal porosity. Powder particles produced by milling or other mechanical methods exhibit a range of shapes, depending on the relative ductility or brittleness of the feed material (Suryanarayana, 2004). Ductile powders are generally flatter with a high aspect ratio, whereas brittle

particles can be angular and regularly-shaped. Powder particles produced chemically can have shapes ranging from spherical to angular. Electrolytic powders are highly pure with a dendritic morphology.

2.6.4 Surface area and internal structure of particles

The specific surface area (SSA) is expressed as the area per unit mass (m^2/g) and is closely related to the size and shape of particles in the powder. It defines the reactivity of the powder during sintering (Yule and Dunkley, 1994; Jillavenkatesa and Dapkunas, 2001; Horiba Scientific, 2014). The internal structure of particles, such as microsegregation, internal pores and precipitates, are characterised with optical and scanning electron microscopy together with EDX.

2.7 Sintered compact characterisation

A sintered compact is characterised with respect to the microstructure, physical, mechanical, surface-related, electrical, thermal, magnetic and optical properties (German, 2005). Microstructural characterisation involves the assessment of features such as grain size, phases, pores and defects. Pore structure in a sintered compact is particularly important, since many other mechanical properties are dependent on it, and is assessed in terms of size and shape. The physical properties are determined by the sintered density. The mechanical properties are assessed by determining the hardness, strength and dynamic properties such as impact properties. Surface-related properties include corrosion, oxidation resistance and wear resistance. The thermal properties include thermal conductivity and thermal expansion. During characterisation of a sintered compact, only properties relevant to the applications are assessed.

2.8 Consolidation technique-property relationship

The consolidation of a powder involves mixing of component powders, together with lubricant, until a homogeneous mix is obtained, subsequent loading of the mix into a die, compaction under pressure, and sintering of the compact (German, 2005; Datta, 2012). There are many ways of consolidating powder which include uniaxial compaction pressing, rolling, extrusion, injection moulding, cold and hot isostatic pressing, and spark plasma sintering (German, 2005). During uniaxial compacting, particles are interlocked and cold-welded, resulting in a relatively low strength

of the green compact that allows it to be safely handled (Upadhyaya, 1997). By heating the green compact, sintering causes particles to bond together, resulting in significant strengthening and improved properties (German, 2005). Solid state sintering occurs at temperatures below the melting point by solid-state atomic transport events, but also liquid phase sintering involves the formation of a liquid phase, which has a lower melting point than the solid phase.

Gas atomisation is the preferred technique used to produce powder for injection moulding, since the particles in gas-atomised powder best suited for injection moulding are always fine, in most cases, smaller than 20 μm in size and near-spherical in shape (Yule and Dunkley, 1994; German and Bose, 1997). German and Bose (1997) gave the properties of a powder for injection moulding, which consists of discrete dense and near-spherical particles with no satellites, free of internal voids, with clean surface, size range between 0.5 and 20 μm, d_{50} between 4 and 8 μm, packing to 60 % of theoretical density, with a wide distribution and minimal segregation. The powder particles are mixed with organic binders to form pellets that easily flow into a moulding machine. Feedstock pellets are moulded into oversized tooling that contains the desired shape. The binders are thermoplastic mixtures of waxes, polymers, oils, lubricants, and surfactants. The heated polymer allows viscous flow of the mixture to aid forming (filling of complex tool geometries). After moulding, the binder is removed (debinding) and the remaining powder structure sintered.

In cold and hot isostatic pressing (CIP and HIP), high pressure is isostatically applied to a workpiece through a fluid. In both processes, powder is sealed into a flexible tooling shaped for the application. In the CIP process, the powder-tool assembly is pressurised in a vessel filled with oil or water. The powder is thus converted from a loose aggregate into a partially dense compact which has sufficient green strength to allow careful handling and transfer to the following process operation. The tooling is rubber, latex, or polysilicone. Lubricants are rarely used. CIP is always performed at pressures below 420 MPa (Price, 1998). In the HIP process, the fluid is a gas at elevated temperature ranging from 480°C for aluminium alloy powders to 1700°C for tungsten powders. The powder is typically placed in a container or envelope made of metal or glass to a specified shape larger than the final desired size. The process plastically deforms the particles, which closes up porosity and achieves 100% theoretical density. High density argon is the most common pressure medium in HIP, but

other gases such as helium or nitrogen are used. Pressures applied in the HIP process range from 20 to 300 MPa, with 100 MPa being commonly used (Connway and Rizzo, 1998).

To obtain reproducibility in filling the mould, powder with repeatable tap density, such as spherical powder will be preferred in CIP, even though rearrangement, localised deformation, homogeneous deformation, and elastic bulk compression, take place. In the HIP process, on the other hand, the need for some plastic deformation allows the use of crushed, irregular, hydride/dehydride powders.

2.9 High-velocity oxyfuel (HVOF) spraying and cold spray spraying as coating techniques

2.9.1 Thermal Spray

Thermal spray processes use thermal energy generated by combustion or electrical methods to melt or soften, and accelerate fine dispersions of particles or droplets to speeds in the range of 50-1000 m/s (Crawmer, 2005). The high particle temperatures and speeds achieved result in significant particle deformation on impact at the substrate surface, producing thin layers or lamellae or splats adhering to the substrate surface. Solidified droplets build up rapidly, particle by particle, as a continuous stream of droplets impacts to form continuous rapidly solidified layers. These processes include flame spray, electric arc spray, and plasma arc spray, after the energy sources used to heat the coating material to a molten or semi-molten state. The coating materials include powder particles, wire or rod.

2.9.2 High-velocity oxyfuel (HVOF)

High-velocity oxyfuel (HVOF) spraying is a type of flame spray. In HVOF spraying, a fuel gas such as hydrogen, propane, or propylene is mixed with oxygen to create a combustion jet at temperatures of 2500ºC to 3000ºC. The combustion takes place internally in a high pressure chamber, exiting through a small diameter barrel to generate a supersonic gas jet with very high particle speeds (Crawmer, 2005)

2.9.3 Cold Spraying

Cold spraying is a relatively recent spray technology, known by different names such as: Cold Gas Dynamic Spraying, Kinetic Spraying, High Velocity Particle Consolidation (HVPC), High Velocity

Powder Deposition and Supersonic Particle/Powder Deposition (SPD) (Dykhuizen and Smith, 1998; Singh *et al.*, 2012). In the cold spray process, a high velocity (300 to 1200 m/s) gas jet, formed using a converging/diverging nozzle, is used to accelerate powder particles in the size range 1 to 50 μm. The powder particles are heated to required velocities and temperatures, and on impact with the substrate located 10-25 mm from the nozzle, they deform and bond to form a coating. A fine balance between particle size, density, temperature and velocity is needed to achieve the desired coating (Singh *et al*., 2012).

The kinetic energy of the particles (Padmini *et al*., 2014), rather than the high temperature as in thermal coating, helps these particles to plastically deform on impact and form splats, which bond together to produce coatings. Low temperatures in cold spray techniques avoid or minimize deleterious shortcomings of traditional thermal spray methods such as high-temperature oxidation, evaporation, melting, crystallization, residual stresses, and gas release (Ghelichi and Guagliano, 2009). In this process, powder particles are accelerated by the supersonic gas jet at temperatures generally lower than the melting point of the material, resulting in a coating formed from particles in the solid state, and hence no melting and solidification is experienced by the powders as in conventional thermal spray processes.

2.9.3.1 Basic cold spray system

The cold spray system can be designed in either portable or manual and robotic or fixed systems. The gases with aerodynamic properties generally used to propel the powder particles include He, N_2, mixture of He and N_2, dry air (79% N_2 - 21% O_2). The main components of the cold spray system are:

- High pressure powder feeder (powders used are in the range of 1 to 50 μm in diameter)
- Source of a compressed gas
- Gas heater to preheat the gas, to compensate for the cooling due to rapid expansion in nozzle
- Supersonic nozzle (Delaval nozzle)
- Spraying chamber with a motion system

- System for monitoring and controlling spray parameters (to measure and control the gas temperature and pressure).

2.9.3.2 Types of cold spray system

There are two methods of injecting the spray materials into the nozzle, corresponding to low pressure cold spray (LPCS) and high pressure (HPCS) cold spray systems. The two main distinctions of these two systems are: the pressure (5-10 bars in LPCS and 25-30 bars in HPCS), and the powder injection method (radial injection in LPCS and axial injection in HPCS). Schematic diagrams of the operating principles of LPCS (SST, 2014) and HPCS (Singh *et al*., 2012), are shown in Figures 2.16 and 2.17.

The particles remain in the solid state and are relatively cold, so the bulk reaction on impact is a solid-state one. The process imparts little to no oxidation to the spray material, so surfaces stay clean, which aids bonding. The absence of melting and the relatively low operating temperatures result in very low shrinkage on cooling. Due to the high strain induced on impact, the coatings tend to be under compressive stress and not in tension following the liquid/solid state reactions of most other thermal spray processes (Singh *et al*., 2012; Moridi *et al.,* 2014). Low temperatures also aid in retaining the original powder chemistry and phases in the coating, with only changes due to deformation and cold working.

Bonding relies on sufficient energy to cause significant plastic deformation of the particles and substrate. Under the high impact stresses and strains, interaction of the particle and substrate surfaces probably cause disruption of oxide films, promoting contact of chemically clean surfaces and high friction, generating very high localised heating promoting bonding similar to friction or explosive welding (Champagne, 2007; Hussain, 2013).

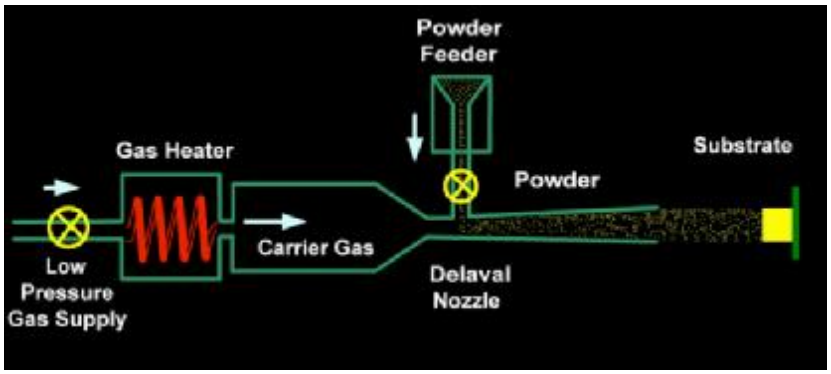


Figure 2.16. *Schematic diagram of the operating principle of the low-pressure cold spray system (Supersonicspray, 2014).*

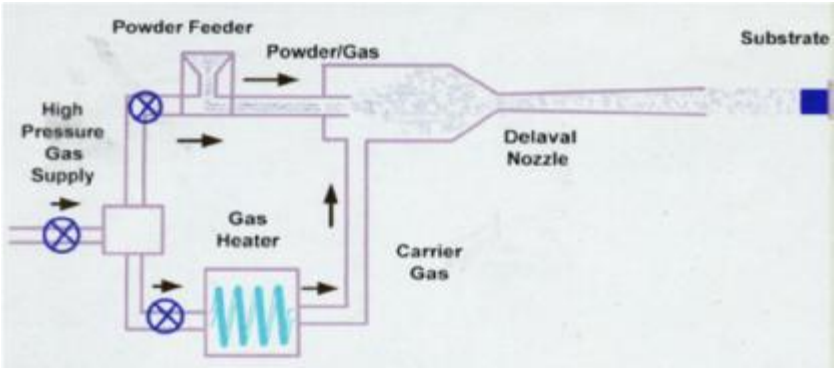


Figure 2.17. *Schematic diagram of the operating principle of the low-pressure cold spray system (Singh et al., 2012).*

2.9.3.3 Materials for cold spraying

At present, coatings are limited to ductile materials such as aluminium, stainless steel, copper, titanium and titanium alloys. They form part of the isomechanical group, that is, materials possessing similar mechanical properties (Ghelichi and Guagliano, 2009). Hard and brittle materials, such as ceramics, cannot be sprayed in the pure form, but may be applied as composites with a ductile matrix phase. Substrate materials are also limited to those that can withstand the aggressive action of the spray particles. Soft or friable substrates will erode rather than be coated. In many ways, the cold spray process is still primarily in the research and development stage, and is only now becoming commercially available.

2.9.4 Characterisation of coatings and interfaces

Analytical methods used to characterise coatings include electron spectroscopy, electron microscopy, ion spectrometry and microscopy, photospectroscopy and microscopy. Mechanical methods include the assessment of coating hardness, measurement of coating adhesion and tribological assessment of coatings. For these parameters to be fully assessed, metallography and image analysis are important (Riggs and Couch, 2008).

2.9.4.1 Electron spectroscopy

The term "electron spectroscopy" covers a wide range of techniques providing information about a surface and includes techniques such as Auger and photoelectron spectroscopy (Chalker, 1991). Auger and photoelectron spectroscopy are used to determine near-surface information of thin film, such as composition.

2.9.4.2 Scanning Electron microscopy

Scanning electron microscopy involves imaging the secondary and backscattered electrons which are stimulated by the incident (primary) electron beam. The secondary electrons are used to image the topography of the specimen or to investigate the inner microstructure of a coating using a cross-section (Minkoff, 1967; Vernon-Parry, 2000; Egerton, 2005; Bogner *et al*., 2007). Backscattered electrons are used to obtain information about the sample relative composition, phase boundaries by atomic number contrast (Lloyd, 1987).

2.9.4.3 X-ray diffraction

The X-ray diffraction technique allows phase identification and quantification, preferential orientation and texture detection, crystallite size determination, micro-strain and residual stress determinations. Powder XRD provides detailed information on the crystallographic structure and physical properties of materials and thin films.

2.10 Ti-6Al-4V / Titanium Grade 2 versus plain and alloyed γ-TiAl

A comparison of mechanical and physical properties of titanium and titanium aluminide phases usually found in the Ti-Al alloy system is give in Table 2.1 (Huang and Chesnutt, 1994; Banerjee,

1994; Pollock, 2006). The properties of nickel-based alloys are given for comparison. Thereason for this comparison is to indicate the possible improvement which coatings could bring to titanium properties.

2.10.1 Ti-6Al-4V

Alloy Ti-6Al-4V is unique in that it combines attractive properties with inherent workability (which allows it to be produced as many types of mill products, in both large and small sizes), good shop fabricability (which allows the mill products to be made into complex shapes), together with the production experience and commercial availability that lead to reliable and economic usage (Donachie, 1989). Thus, Ti-6Al-4V has become the standard alloy against which other alloys must be compared when selecting a titanium alloy (or custom-designing one) for a specific application. Ti-6Al-4V also is the standard alloy selected for castings that must exhibit superior strength. For elevated-temperature applications, the most commonly used alloy is Ti-6Al-2Sn-4Zr-2Mo + Si. Currently, Ti-6Al-4V, Ti-6Al-2Sn-4Zr-2Mo, Ti-5Al-2Sn-2Zr-4Mo-4Cr, and Ti-6Al-2Sn-4Zr-6Mo are some of the alloys used in gas turbine engine applications (Davis, 1990; Leyens and Peters, 2003).

Rotating components in gas turbine engines require titanium alloys that maximize strength and metallurgical stability at elevated temperatures. These alloys also must exhibit low creep rates along with predictable behaviour for stress rupture, and low-cycle fatigue. The most interesting attributes of γ-TiAl-based alloys are the properties at elevated temperatures, because γ-TiAl, as for all intermetallic compounds, shows very little or no ductility at room temperature (Kimura and Pope, 1997; Huang and Chesnutt, 1994). At elevated temperatures, γ-TiAl exhibits the highest burning resistance (thermal stability and resistance to burning by reaction with oxygen of any source) compared to various titanium alloys as illustrated in Figure 2.18 (Lasalmonie, 2006).

Table 2.1. *Mechanical and physical properties of titanium phases and nickel alloys (Huang and Chesnutt, 1994; Donachie, 1989; Pollock, 2006).*

Properties	**Base alloy**			
	(Ti)	**Ti_3Al**	**TiAl**	**(Ni)**
Crystallographic structure	hcp/bcc	DO_{19}	$L1_0$	fcc
Density ($g.cm^{-3}$)	4.5	4.1-4.7	3.7-3.9	8.3
Melting point (°C)	~1600	1600	1460	~1400

Young's modulus at room temperature (GPa)	96-110	120-145	160-175	206
Yield strength at room temperature (MPa)	380-1150	700-990	400-650	800-1200
Tensile strength at room temperature (MPa)	480-1200	800-1140	450-800	1250-1450
Strain to fracture (%)	10-25	2-7	1-5	3-50
Creep limit temperature (ºC)	538-600	750	900-1038	1090-1095
Oxidation resistance limit (ºC)	539-600	650	900-1038	1090-1095
Thermal conductivity ($W.m^{-1}.K^{-1}$)	20	7	22	
Phase stability limit (ºC)		1180	1440	

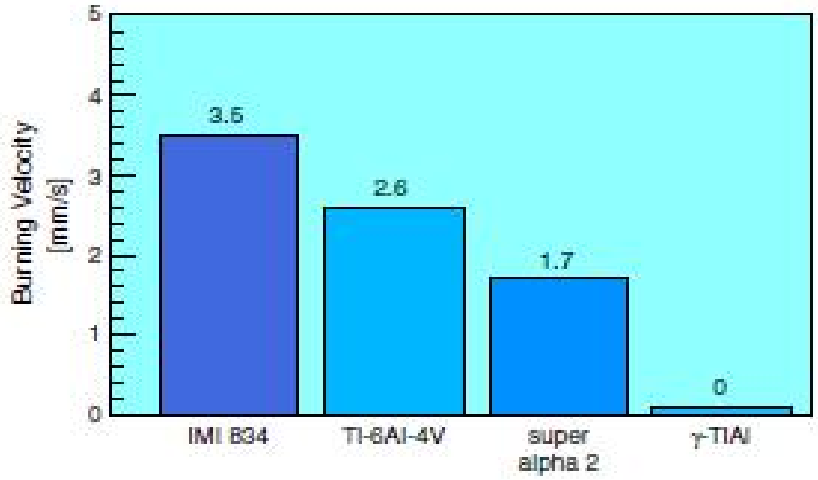


Figure 2.18. *Comparison of burning velocity of γ-TiAl and various Ti alloys at 427 °C (Lasalmonie, 2006).*

Comparison of the specific strength of γ-TiAl and conventional Ti and Ni alloys between 0 and 850ºC does not show any significant difference that can justify the replacement of the conventional Ti and Ni alloys any time soon, as shown in Figure 2.19 (Lasalmonie, 2006). However, the very high Young's modulus at low and elevated temperatures makes γ-TiAl a very promising candidate for applications where creep and oxidation resistance are of paramount importance, as illustrated in Figure 2.20 (Lasalmonie, 2006).

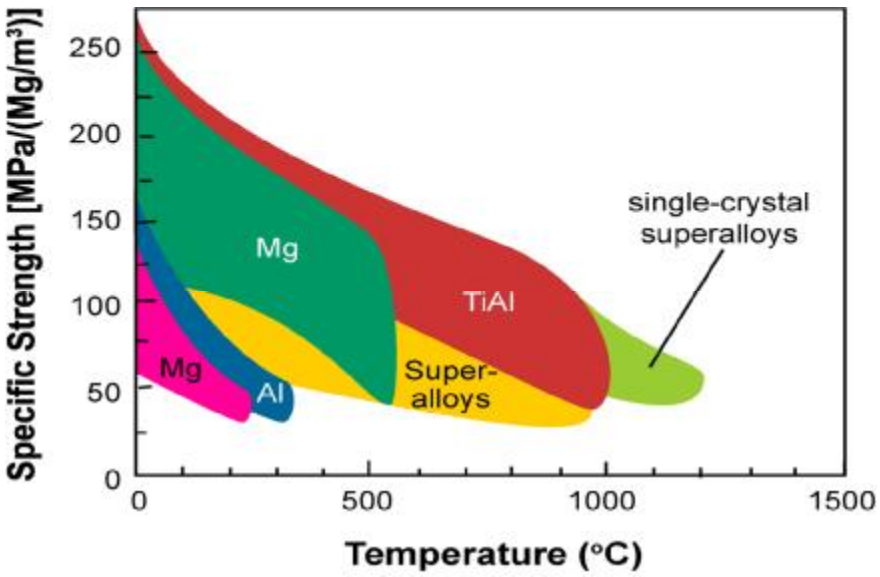


Figure 2.19. *Specific strength of TiAl alloys compared to Ti- and Ni-based alloys (Lasalmonie, 2006).*

Many protective coatings developed to date are based on aluminium, with platinum aluminides being the most investigated (Takayama, 1994; Gurrapa, 2001a; Olike *et al.*, 2005). However, there have been attempts to combine the optimised property benefits of γ-TiAl and γ-TiAl-based alloys with those from conventional Ti alloys such as Ti-6Al-4V (Leyens *et al.*, 1997, 2002). Diffusion bonding of γ-TiAl alloys to Ti-6Al-4V at different temperatures ranging from 800ºC to 900ºC under applied stresses of 100 MPa for 2 hours demonstrated that sound joints without pores or cracks could be achieved (Xiu-Feng *et al.*, 2006). The bonding of Ti-50 at.% Al to Ti-6Al-4V by infrared brazing using a Cu-Ni-containing Ti filler metals led to the formation of the brittle Ti_3Al and Ti_2Ni phases, decreasing the shear strength of the joint (Shiue *et al.*, 2008). The bonding strength of a joint can be improved by using higher brazing temperatures, longer brazing times and a low-nickel filler metal. This demonstrates that γ-TiAl and γ-TiAl-based alloys can be used as coatings on a substrate of Ti-6Al-4V for protection against oxidation in the temperature range of 650ºC to 800ºC as the diffusion bonding temperatures are above 800ºC. The similarity between the chemical compositions of substrate and coatings is expected to play an important role in the quality of the bonding.

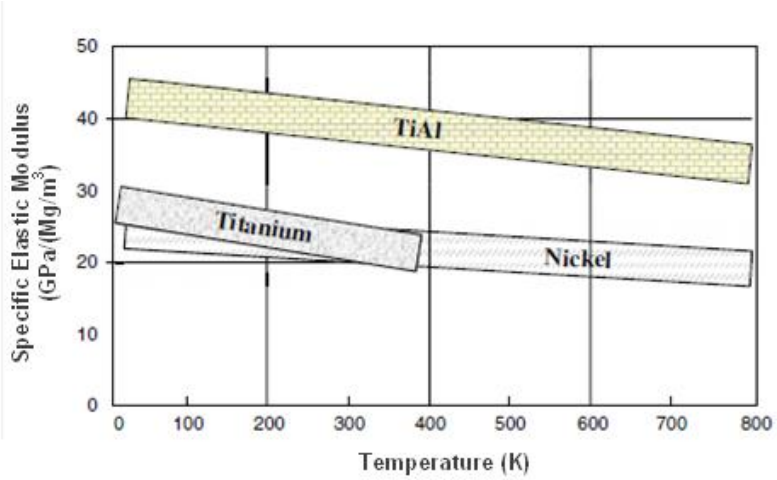


Figure 2.20. *Specific elastic moduli of γ-TiAl, Ni- and Ti-based alloys (Lasalmonie, 2006).*

2.10.2 Titanium Grade 2

Unalloyed Commercially Pure (CP) Titanium is available in four different grades, 1, 2, 3 and 4, which are used based on the corrosion resistance, ductility and strength requirements of the specific application. Titanium Grade 2 is stronger than Grade 1 and equally corrosion-resistant against most applications. Titanium Grade 2 has numerous applications in the medical industry. Biocompatibility of Titanium Grade 2 is excellent, especially when direct contact with tissue or bone is required.

Like other titanium-based materials, Titanium Grade 2 exhibits typical properties such as the high strength, low weight ratio and outstanding corrosion resistance inherent to titanium, which have led to a wide and diversified range of successful applications. Most of these applications require high levels of reliable performance in surgery, medicine, aerospace, automotive, chemical plant, power generation, oil and gas extraction, sports, and other major industries (Donachie, 1989; Davis, 1990; Lütjering and Williams, 2007). In the majority of these and other engineering applications, titanium has replaced heavier, less serviceable or less cost effective materials. Designing with titanium, and taking all factors into account, has resulted in reliable, economic and more durable systems and components, which in many situations have substantially exceeded performance and service life expectations.

CHAPTER 3

EXPERIMENTAL PROCEDURE

3.1 Preparation of γ-TiAl cast alloys

The TiAl alloy was prepared by melting titanium Grade 2 and aluminium of commercial purity in a button arc furnace under an argon atmosphere. The target composition was Ti-47.5 at.% Al. Two types of alloys were prepared: plain TiAl and TiAl containing platinum group metal (Pd, Pt, Ru and Ir). The compositions of alloys are given in Table 3.1, where the amount of precious metals was 0.2, 1.0, 1.5 and 2.0 at.% at the expense of titanium content, the aluminium content remaining 47.5 at.%. An oxygen getter (Ti button) was used to get rid of all oxygen before melting the samples. The change in mass of the buttons before and after melting was neglible, and so not recorded.

The Mintek button arc furnace operates on principles similar to an arc-welding machine, where an electrical arc is struck between two electrodes. The high-energy arc creates high temperatures ranging from 3,000 °C to 7,000 °C. The “plasma” is a highly ionized gas which is directed in a controlled manner onto the sample, to melt it. These high temperatures achieved should allow the melting of all the refractory metals of the periodic table, but if there is a wide disparity in melting point, sometime, not all of the higher melting point elements melt. To mitigate this, the samples are turned over and remelt three times.

The Mintek Button Arc furnace consists of a water-cooled stainless steel bell jar hinged from a fixed baseplate. Clamps are provided for operation at slightly positive pressure. The electrode (stinger) shaft penetrates down through the bell jar top, directed toward the hearth, which is a water-cooled copper with an interchangeable top surface. Because of its simplicity, ease of access into the furnace, and small volume, the furnace is easily purged. Provision is made for attachment to a vacuum pump for gas evacuation prior to back-filling with inert gas.

The main limitations of the button arc furnace is the inability to stir the samples during melting to ensure the homogeneity as in the induction furnace, and the lack of control on cooling, although the ware-cooled copper hearth insures a fast cooling. This can lead to inhomogeneity due to melting

point difference (Table 3.2) and non-equilibrium microstructure after solidification and cooling. As recentely proposed by Valiente Bermejo (2015), sample homogeneity is achieved by running three to four melting rounds where the sample is turned over, exposing thus a new surface to the arc. Quenching is prevented by the hot gas surrounding the molten sample.

Table 3.1. *Elemental composition of the γ-TiAl alloys, for x=0.2, 1.0, 1.5 and 2.0 at.%.*

Alloy	**Composition (at.%)**					
	Ti	Al	Ru	Pd	Pt	Ir
γ-TiAl	52.5	47.5	-	-	-	-
γ-TiAl- *x* Ru	52.5-*x*	47.5	*x*	-	-	-
γ-TiAl- *x* Pd	52.5-*x*	47.5	-	*x*	-	-
γ-TiAl- *x* Pt	52.5-*x*	47.5	-	-	*x*	-
γ-TiAl- *x* Ir	52.5-*x*	47.5	-	-	-	*x*

Table 3.2. *Melting points of alloy components.*

Metal	Ti	Al	Pd	Pt	Ru	Ir
Melting Point (°C)	1665	661	1552	1772	2272	2427

3.2 Sample preparation and hardness evaluation

Samples for hardness and oxidation tests were cut from the buttons obtained using an electric discharge machining (EDM) with hollow cylindrical copper electrodes and were in the form of disks. The as-cast and oxidation test samples were cut, prepared metallographically and observed with optical and SEM microscopes. Hardness evaluation was performed on a Duravision instrument from EMCOTEST with load of 10 kg. For each sample, ten measurements were done and averaged.

3.3 Heat treatment, oxidation test and thermogravimetric analysis (TGA)

Heat treatment was conducted in a tube furnace at 1000°C under a 65 ml/minute flow of argon. Samples were loaded at room temperature and the temperature was raised at a rate of 10°C/minute to 1000°C, held at this temperature for 1 hour and furnace-cooled to room temperature. The heat treatment temperature was set to correspond to annealing, without phase change, using the Ti-Al phase diagram (Schuster and Palm, 2006). The heat treatment was conducted at 1000ºC because

the operational temperature where the titanium aluminide alloys are expected to operate is between 900ºC and 1100ºC.

Prior to the oxidation tests, the high temperature behaviour of samples in air was determined by thermogravimetric analysis (TGA) using a NETZSCH STA 429 instrument. The weight gain was deduced. Separate samples of 10 mg cut from sample for oxidation tests were loaded in the STA and heated from room temperature to 1185°C at a heating rate of 10°C/minute under an air flow of 40ml/minute. The TGA allowed the determination of the onset of weight increase, corresponding to the onset of oxidation.

For oxidation tests, the samples were loaded in a muffle furnace, heated to 950°C at 10°C/minute and held at 950°C for 120 hours in static air. At the end of the holding time, the samples were allowed to furnace cool. For each alloy a 10 mg piece was cut for TGA and the remaining piece used for oxidation tests.

3.4 Electrochemical tests

The surfaces of the samples were ground to 1200 grit SiC paper finish, degreased with methanol, rinsed with distilled water, and dried. The surface was prepared just prior to starting the polarization experiment to limit long term oxidation.

Before conducting the scan, each sample was immersed in the solution for approximately 60 minutes to obtain a stable corrosion potential. Potentiodynamic scans and open circuit potential (OCP) measurements were conducted with an ACM AutoTafel potentiostat/galvanostat system using a conventional three-electrode system with a saturated calomel electrode (SCE). For each alloy system, tests were done in 5, 15 and 25 wt% HCl at room temperature to assess the effect of the solution concentration on the corrosion rate. Scans were conducted with the plain titanium aluminides (γ-TiAl), and aluminides with additions of precious metals. Potentiodynamic scans were conducted by scanning from -350 mV to +1000 mV versus the corrosion potential at a scanning rate of 10 mV/min. Open circuit potential (OPC) tests were run for 15 hours, during which the samples were exposed to a 5wt % HCl solution.

3.5 Characterisation of the bulk and mechanically alloyed samples

3.5.1 Phase identification

It was vital to analyse the phases accurately, to be able to identfy them correctly and obtain their true compositions, although in some cases, this was so difficult because the phases were so small. This meant that they were difficult to ressolve when they were in two-phase microstructures, and also analyses of apparent single phases were inaccurate. SEM imaging and EDX were conducted with a FEI Nova NanoSEM®, a high resolution scanning electron microscope (HR-SEM). The composition of the samples and the phases were determined using a combination of X-ray diffraction (XRD) and energy dispersive X-ray spectroscopy (EDX).

For XRD, the samples were analysed with a PANalytical X'Pert Pro powder diffractometer with an X'Celerator detector and variable divergence with fixed receiving slits and Fe filtered Co-Kα radiation. Phase identification was conducted using X'Pert Highscore plus software. Likewise, samples from mechanically alloyed powders were examined by SEM, EDX and XRD.

3.5.2 Volume fraction of the constitutive phases

The calculation of volume fractions of α_2 and γ phases was done using SEM micrographs, uploaded on the Olympus PGM optical microscope equipped with the image analysis software (Olympus Stream Motion). The images were first enhanced to obtain a full intensity spectrum and good contrast between the two phases. The total number of pixels in the image was determined. To highlight α_2, the intensity threshold method was employed and the sum of pixels constituting the selected features was performed. The average threshold of 150 was used. The ratio of the latter sum with the original number of pixels led to the determination of the volume fraction. The results obtained were the average of 8 measurements per sample.

3.5.3 EDX mapping and line scan analysis

Mapping and line scan analysis were conducted using a Zeiss EVO MAIS SEM equipped with a Bruker EDX detector run with the Bruker Esprit software. For mapping, different colours were allocated to each elements and the distribution of each element in the component phases of the microstructure observed through its colour distribution. The line scan analysis was conducted in

the backscattered mode (BSE), where a line was drawn across different phases shown in the microstructure of the alloy and the content of each element recorded step-by-step for 100 counts. In an excel spreadsheet, the content of each element at each count was reported and variation curves drawn.

3.6 Preparation of mechanically alloyed γ-TiAl

3.6.1 Powder preparation

The target alloy was γ-TiAl-0.5 at.% PGM, where PGM denotes the platinum group metals (Pt, Pd, Ru or Ir), γ-TiAl represents Ti-47.5 at.% Al. The alloy composition is shown Table 3.3, where titanium hydride powder (TiH_2) with 98.0% Ti , elemental aluminium powder of 99.7% purity and PGM sponge powder, together with 6.0 % stearic acid as the process control agent (PCA) were milled together. The material impurity was not given on the supplier certificate of analysis and the full analysis of the component metals could not be performed at Mintek and is not usually done in these types of projects.

Before milling, the powders were mixed together with steric acid for 15 minutes using the WAB Turbula mixer. The homogeneously mixed powders were transferred into a 500 ml stainless steel grinding jar containing stainless steel grinding balls (800 g of 20 mm diameter and 200 g of 10 mm diameter). The ball-to-powder ratio (BPR) was 10:1. The jar was placed and clamped into the PM100 Retsch milling machine. The ball-to-powder ration (BPR) of 10:1 was chosen as recommended in the CRC handbook on mechanical alloying and milling (Suryanarayana, 2004), denoting a 10:1 ratio for small capacity mills such as the PM100 Retsch machine used, and also to meet the double requirement of mixing by creating cascading fractioning phenomena. A milling time of 32 hours was selected based on a previous work (Mwamba and Chown, 2011) where it was found that a milling time between 30 hours and 36 hours was optimal to achieve titanium aluminide formation when titanium hydride powder was milled together with aluminium powder.

Table 3.3. *Compositions of the produced TiAl powders.*

Compounds	Alloy composition (at.%)					
	Ti	**Al**	**Pt**	**Pd**	**Ru**	**Ir**
γ-TiAl -0.5 at.% Pt	52	47.5	0.5	-	-	-
γ-TiAl -0.5 at.% Pd	52	47.5	-	0.5	-	-
γ-TiAl -0.5 at.% Ru	52	47.5	-	-	0.5	-
γ-TiAl -0.5 at.% Ir	52	47.5	-	-	-	0.5

The TiAl powder was ground to finer particles for 30 hours at a rotation speed of 400 rpm. Thereafter, the jar was removed with the clamp still tightened from the milling machine and placed inside the Labconco glove box and allowed to cool down for about 5 hours. After milling, the powder, still enclosed in the milling jar, was transferred in the glove box. An inert atmosphere was created in the glove box by pumping out to form vacuum inside the glove box and backfilling with argon at a maximum pressure of 5 mbar and on oxygen content below 1.0 vol.%. In order to prevent powder ignition or oxidation, the oxygen volumetric content inside the glove box was set to a maximum of 0.8 %. The powder was allowed to cool down under the inert atmosphere. After cooling, samples of the powder were transferred to different containers for particle size analyses, phase identification, DSC and TGA.

3.6.2 Powder characterisation

Properties characterised were apparent density, particle size, size distribution, particle morphology, chemical composition and phases formed. The apparent densities of the different mixtures were determined using an Arnold apparent density meter. The size and size distribution of powder particles were determined by laser diffraction using a Malvern Mastersizer® 2000 in the size range of 0.02–2000 μm with water as the dispersant. The particle shapes were determined by scanning electron microscopy (SEM) on a FEI Nova NanoSEM®. The XRD analyses were conducted with a PANalytical X'Pert Pro powder diffractometer with an X'Celerator detector and variable divergence- and fixed-receiving slits with Fe filtered Co-Kα radiation. The compositions of the powders and phases were determined using a combination of X-ray diffraction (XRD) and energy dispersive X-ray spectroscopy (EDX) on the SEM.

The mechanical alloying process was evaluated by a combination of XRD and differential scanning calorimetry (DSC). The high-temperature transformation and oxidation behaviour of the MA

powders was assessed by thermogravimetric analysis (TGA). The DSC and TGA were conducted in a Netzsch STA 429 instrument at 10°C/minute heating rate.

3.7 Powder sintering

The mechanically alloyed powder was sintered using a FCT HP-D5 spark plasma sintering furnace (Figure 3.1). The furnace heating rate was 240°C/min, allowing to reach the holding temperature of 1100°C in less than 5 minutes and the furnace was held at a pressure of 6.5 mbar at the holding temperature for 90 seconds.

3.8 Cold spray coating

Cold spray was the coating technique used to deposit a γ-TiAl alloy produced by mechanical alloying. The cold spray system used was a SST system from Center Line Ltd (Windsor, Canada), shown in Figure 3.2 in its basic form without the compressor. It consisted of:

1. Hopper console or control box which supplies power to the powder feeder
2. Powder feeder or Pressure Cabinet
3. Spray booth consisting of two chambers (the manual spray gun, left and the robot gun spray, right)
4. Air cleaning system
5. Compressor (Figure 3.3)

Cold spraying was conducted at 550°C, which is in the range conventionally considered as “cold” compared to temperatures reached in other coating processes. This temperature was selected as it corresponded to the point where acceptable coating occurred. Figures 3.3 to 3.5 show the different components of the SST system, as installed at the School of Mechanical, Industrial and Aeronautical Engineering, University of the Witwatersrand.



Figure 3.1. *FCT HP-D5 spark plasma sintering furnace.*



Figure 3.2. *SST low-pressure cold spray system.*



Figure 3.3. *Compressor.*



Figure 3.4. *Powder feeder, hopper console and spray booth.*



Figure 3.5. *Spray booth and exhaust system (air cleaning system).*

3.8.1 Operation

The hopper console supplied power to the powder feeder. The powder had two filling containers, one used to load Al_2O_3 for cleaning the substrate by alumina blasting, and the second used for coating. During the surface blasting, the abrasive was aluminium oxide, with a size distribution of 45-105 µm and an average penetration below 20 µm. The carrier gas was air at 4 bar pressure, a 45° spray angle and a working (standoff) distance of 30 mm. A surface decreasing treatment was done using a very dilute HCl solution (2 wt% HCl).

On the top face of the pressure cabinet was a set-up PLC screen for the process set-up (Figure 3.6). The temperature of the travelling powder particles was set up on the pressure cabinet PLC screen. The actual temperature rise took place in the hopper console through heating elements mounted around the piping system. The pressure cabinet, through the PLC screen on top, was used to regulate the powder feed rate to the substrate and the pressure of the carrier gas coming from the compressor.

The carrier gas used was air. The exhaust or air cleaning system (4 on Figure 3.2) consisted of a water blanket located under the substrate holder, which received any particles gone astray or bouncing on the substrate, and trapped them, while the carrier gas, bubbling in the water, exited on the other side and was sucked out to the atmosphere through the exhaust piping. Figure 3.7 shows photographs of the cold spray gun during sample positioning and operation. During operation, the computer, using the Sellio software, controlled the motion of gun spray robot and particle supply to the substrate from the nozzle, with the particle feed rate set up on the powder feeder PLC.



Figure 3.6. *Process set-up PLC screen mounted on the set-up box.*

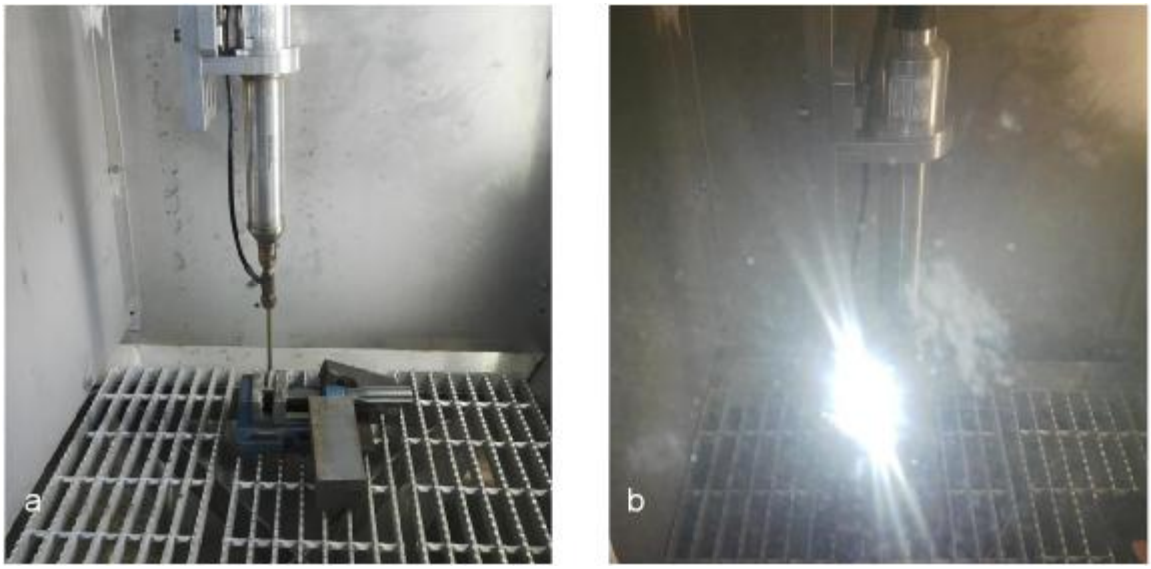


Figure 3.7. *Cold spray gun, a) during sample preparation, and b) in operation.*

The substrates used were commercially pure titanium Grade 2 plates, and Ti-6Al-4V plates. The dimensions of the plates were 50.0 x 20.0 x 4.0 mm for titanium Grade 2, and 50 x 20 x 1.5 mm for Ti-6Al-4V.

3.8.2 Process optimisation

The first step of the coating was the optimisation of the spray process, which included the temperature (T), pressure (P), powder feed rate (F) and gun nozzle-substrate inter-distance (d) set-ups. Different sets of optimisation work matrixes were followed. The substrates were titanium Grade 2 and Ti-6Al-4V of mass m_1 before coating and mass m_2 after coating.

$\Delta m = (m_2-m_1)$

$\Delta m\ \% = [(m_2-m_1)/m_1] \times 100$

The run, operating temperature (T), pressure (P), feed rate (F), gun working distance (d), m_1, m_2, Δm and $\%\ \Delta m$ were put in work matrix tables as presented in the results in Chapter 8. The coating process was stopped after three spray gun passes on the substrate. Prior to coating, the substrate surface was cleaned up by sand blasting technique, using alumina (Al_2O_3) powder.

3.8.3 Heat treatment of coated samples

Attempts to conduct oxidation tests in air on titanium Grade 2 and Ti-6Al-4V samples coated on one side at 950°C for 5 days (as carried out on γ-TiAl) resulted in the complete destruction of the titanium samples within a few minutes, due to the accelerated oxidation on the uncoated surface. A set-up which allowed a controlled oxygen infiltration in the tube furnace was used to control the oxidation of the uncoated surface. To achieve this, after being coated, the titanium Grade 2 and Ti-6Al-4V samples were inserted in the tube, heated at a rate of 10°C/minute from room temperature to 950°C, and held at this temperature for 24 hours under a flow of mixed argon and oxygen with a ratio of 5 vol.% O_2 and 95 vol.% Ar. The heat-treated samples were then assessed for their oxidation behaviour. Samples were only coated on one side to show the difference between the behaviour of the coated and uncoated surfaces during oxidation tests.

CHAPTER 4

PROPERTY EVOLUTION WITH ADDITIONS OF PLATINUM GROUP METALS

4.1 Introduction

Titanium aluminide alloys (Ti-47.5 at.% Al, also referred to as γ-TiAl in this work) were prepared by melting titanium Grade 2 and aluminium of commercial purity (CP). Platinum group metals (PGMs) were then added to the TiAl-based alloys and the alloys were characterised in terms of microstructure and oxidation behaviour.

4.2 Microstructure characterisation of cast alloys

4.2.1 Plain γ-TiAl alloy

The microstructure in the plain TiAl alloy is shown in Figure 4.1, with a duplex microstructure, consisting of lamellar grains (Areas 1) with single-phase regions between (Areas 2). Figure 4.1b shows (at higher magnification) an area where lamellar grains were adjacent. This figure also shows that different grains could be identified by the orientation of their lamellae (Areas 3 to 5). The volume fractions of α_2 and γ phases in plain γ-TiAl were 25±6 % α_2 and 75±6 % γ. The single phase regions marked 2 in Figure 4 1a comprise primary γ-TiAl formed during solidification via the peritectic reaction (Figure 2.3a. (Schuster and Palm, 2006)), while the areas marked 1 comprise a lamellar structure of γ (TiAl) and α_2 (Ti_3Al) arising from the eutectoid transformation of $\alpha_{(Ti)}$ to γ-TiAl +α_2 (Ti_3Al) around 1120ºC.

Typical EDX results of plain γ-TiAl are reported in Table 4.1. The overall composition indicates the formation of a duplex structure comprising two compounds, Ti_3Al (referred to as α_2) and γ-TiAl according to the Ti-Al phase diagram (Grytsiv *et al.*, 2003; Raghavan, 2005; Schuster and Palm, 2006; Batalu *et al.*, 2006), and that α_2 has an aluminium content between 22 and 33.5 at.% at 400ºC. From 33.5 to about 49.5 at.% Al lies the composition range of a two-phase field of Ti_3Al (α_2) and

γ. This was the case in these samples, with the lamellar region having a composition close to 47.5 at.% Al.

The EDX results, together with the Ti-Al phase diagram (Grytsiv *et al.*, 2003; Raghavan, 2005; Schuster and Palm, 2006; Batalu *et al.*, 2006), also showed that Areas 1 in Figure 4.1a comprised alternating Ti_3Al (α_2) and γ-TiAl. In the single-phase regions (Areas 2 in Figure 4.1a), the aluminium content was 50.6±1.8 at.%, and the titanium content 49.4±1.8 at.%, showing the presence of γ-TiAl. The large errors on the aluminium and titanium contents were an indication of the inaccuracy of the measurement due to the small size of these areas and the resulting interaction volume size. The microstructure was a mixture of lamellar grains (with alternating α_2 and γ parallel phases) and γ grains between the lamellar grains, typical of the duplex microstructure.

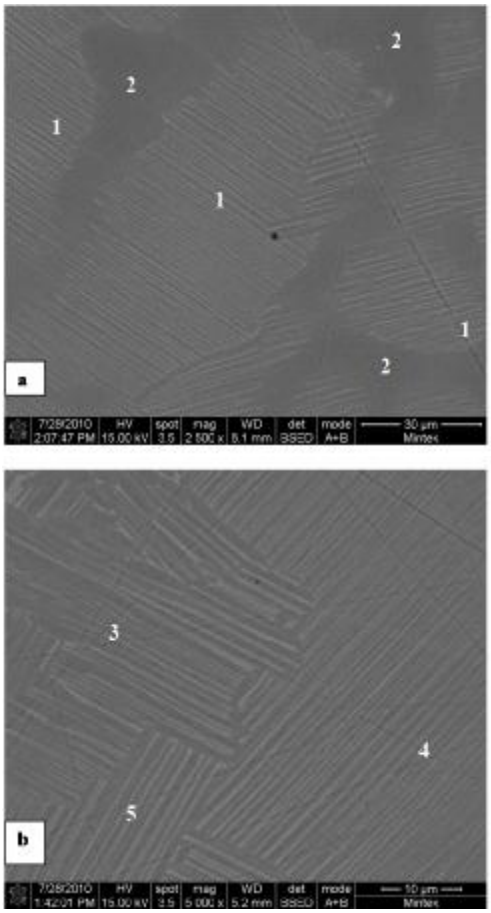


Figure 4.1. *SEM-BSE micrographs of plain γ-TiAl, showing Ti_3Al (light) and γ-TiAl (dark), as well as grain orientations.*

Table 4.1. *EDX analyses of plain γ-TiAl.*

Plain γ-TiAl	**Area**	**Composition (at.%)**		**Phase**
		Ti	Al	
	Overall	52.0±1.0	48.0±1.0	-
	Lamellae Area 1	52.7±0.7	47.3±0.7	α_2 + γ
	Single-phase Area 2	49.4±1.8	50.6±1.8	γ

4.2.2 PGM-alloyed γ-TiAl

4.2.2.1 γ-TiAl with Ru

SEM micrograph of the γ-TiAl alloy containing 0.2 at.% Ru is presented in Figure 4.2, showing that the duplex matrix was maintained, in spite of the ruthenium addition. In addition, a phase mixture γ+G was observed, mainly in the γ regions. At high magnification, the two phases γ+G were more easily resolved, similar to Fig. 4.3, which is for a different sample. Liu and Nash (2011) have analysed the effect of Ru addition on the microstructure and mechanical properties of TiAl alloys and found a microstructure developing in a similar way.

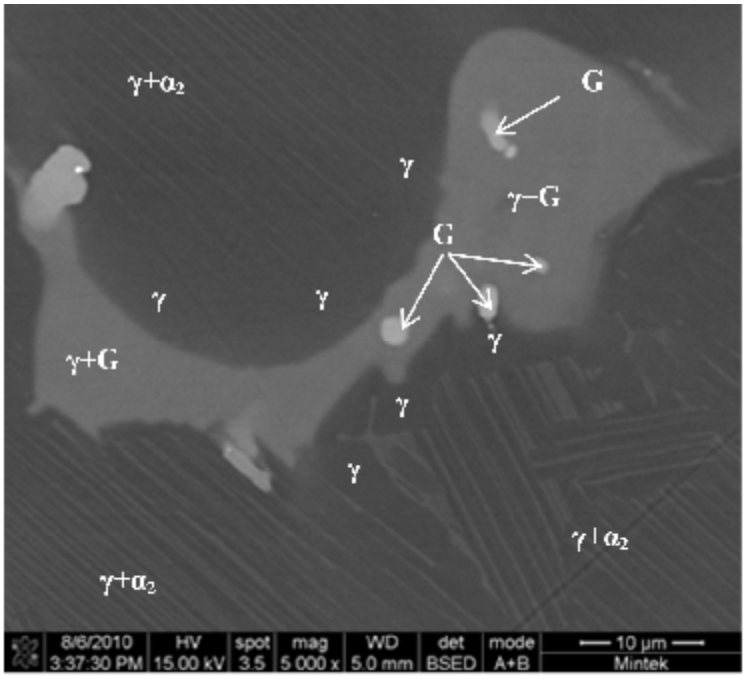


Figure 4.2. *SEM-BSE micrograph of γ-TiAl-0.2 at.% Ru alloy showing γ-TiAl, α_2+γ-TiAl and G phase.*

An SEM micrograph and EDX results of the γ-TiAl alloy containing 1.0 at.% Ru are presented in Figure 4.3 and Table 4.2. The duplex matrix was still maintained, in spite of the increased ruthenium. The microstructure in Figure 4.3 consisted of γ phase (area 1), lamellae (area 2) and fine two-phase mixture γ+G (area 3). The fine structure in Figure 4.3 suggested that it was a eutectoid structure. However, the existence of a higher temperature structure that decomposed to give rise to the eutectoid was not established. The large errors observed in the compositions of Areas 1 and 2 (Table 4.2) were attributed to the small size of the phases analysed, resulting in collection of X-rays from larger areas than the phase targeted. The precious metal content was not constant throughout the phases, resulting in large aluminium and titanium variations in the gamma and lamellar grains. The light phase had a high Ru content. The light contrast of Area 4 suggested a high Ru content. However, these areas were difficult to analyse accurately by EDX due to their small sizes.

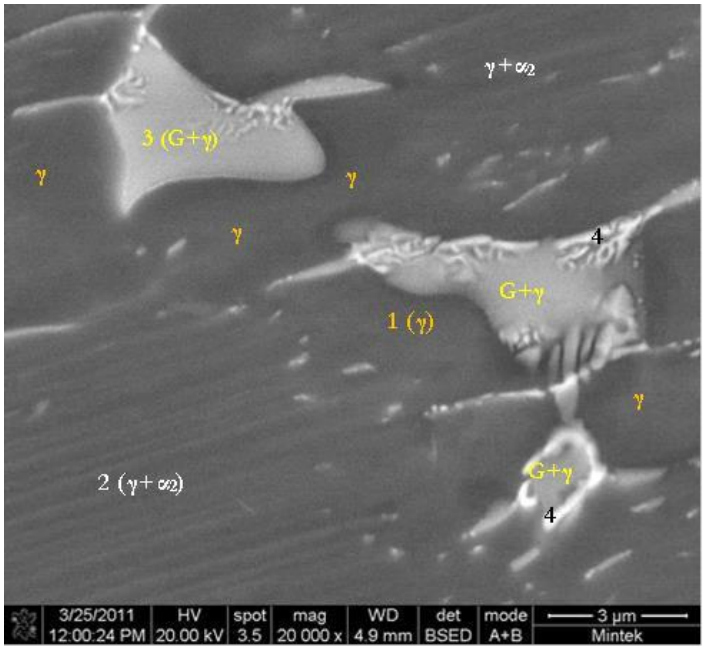


Figure 4.3. *SEM-BSE micrograph of γ-TiAl-1.0 at.% Ru showing: (1) γ, (2) α_2 + γ, (3) two-phase mixture of G+γ and (4) last solidified liquid.*

Table 4.2 allowed the G-phase to be identified. The G-phase is the $Al_{16}Ru_8Ti_6$ ternary compound with the $Mn_{23}Th_6$ structure (Khataee *et al*., 1989b and 1989c). The Ru content of the G-phase was reported in the range 23-25 at.% (Khataee *et al.*, 1989a,1989b and 1989c; Grytsiv *et al*., 2003), and varied in the range 6.0±0.3 - 10.0±0.5 at.% in this work. This lower Ru content came from the

matrix pick-up during the EDX analyses, due to the small size of the phases. Thus, the EDX results were affected by the surrounding matrix, so that the true value should be extrapolated away from the matrix. The Ru in the alloy resulted in two-phase γ+G phase regions (Figures 4.2-4.4).

Table 4.2. *EDX analyses of TiAl-1.0 at.% Ru.*

Area in Figure 4	**Composition (at.%)**			**Phase**
	Ti	Al	Ru	
Overall	51.3±0.3	47.7±0.3	1.0±0.1	γ, α_2, G
Area 1	46.9±1.5	52.4±1.7	0.7±0.1	γ
Area 2	49.5±1.0	50.1±1.2	0.4±0.1	γ +α_2 (unresolved)
Area 3	53.2±0.8	40.5±0.7	6.3±0.3	γ + G
Area 4	?	?	?	Too small for accurate analyses

As the Ru content increased, the amount of the Ru-containing γ+G mixture between the lamellar grains increased (Figures 4.3 and 4.4) and also was part of a two-phase structure with γ-TiAl. At 2 at.% Ru addition (Figure 4.4), the white phase was associated with a fine two-phase morphology, with some regions being too fine to resolve. Typical EDX analyses of the structures in Figures 4.4 are presented in Table 4.3. The large errors show that there was pick-up from the matrix surrounding the small areas, because these areas were unfortunately smaller than 2 μm, so that the beam interacted with other phases. As discussed in Section 2.2.1, the solidification and solid-state equilibria of γ-TiAl-based alloys at 47.5 at.% will solidify as the βTi phase and go through αTi single-phase region, followed by αTi → αTi + γ and α + γ → α_2 + γ transformation, producing a (α_2 + γ) two-phase structure with decreasing temperature. As suggested by Grytsiv *et al.* (2003) in the Shultz-Scheil diagram, solidification with the addition of 2.0 at.% Ru (i.e. in the Ti-Al-Ru ternary system) forms a ternary phase (G) at 1490°C in a eutectic reaction L → γ + G, which later flows down to the ternary eutectic reaction L→ γ + β + G at 1445°C. It is assumed then that, at low Ru content, β → α, a single-phase region and α → α + γ and α + γ → α_2 + γ reactions still occur, the resulting microstructure will also contain γ + G, but not γ + α_2 + G, because the liquid would have run out by then.

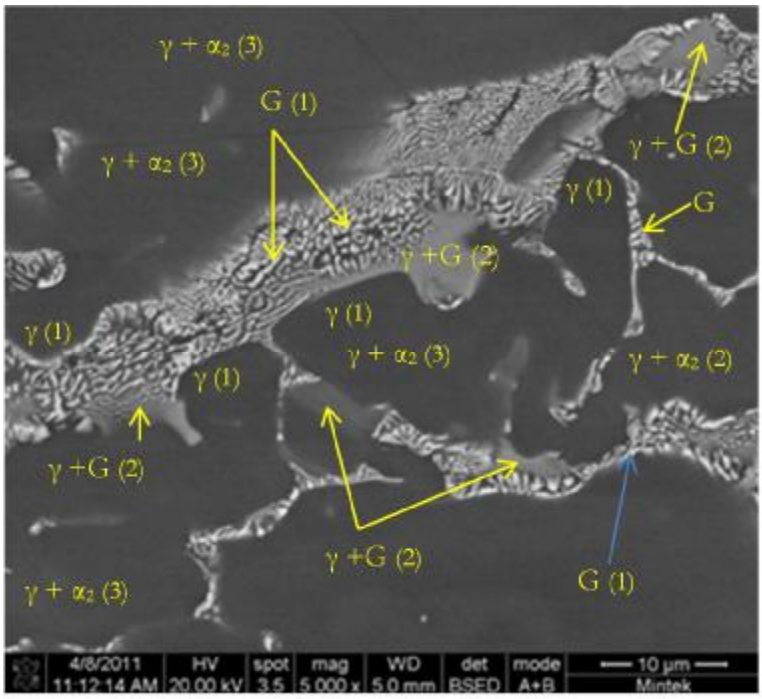


Figure 4.4. *SEM-BSE micrograph of γ-TiAl -2.0 at.% Ru showing the eutectic-like structure, where the numbers into bracket represent the different areas.*

Table 4.3. *EDX analyses of the eutectic-like and dark structures in γ-TiAl -2.0 at.% Ru.*

Area	**Ti**	**Al**	**Ru**	**Phases**
Area 1	52.4±2.1	40.5±2.2	7.1±0.3	γ +G
Area 2	56.7±0.8	36.1±0.8	7.3±0.4	γ +G
Area 3	47.2±0.6	51.0±0.6	1.8±0.4	γ +α_2
Area 4	51.4±1.8	47.4±0.6	1.2±0.4	γ

4.2.2.2 γ-TiAl alloyed with Pd, Pt and Ir

Similar microstructures were observed in samples alloyed with Pd, Pt or Ir (Figures 4.5 and 4.6). The EDX analyses and the Ti-Al-PGMs ternary phase diagrams (Figures 2.6 to 2.9) allowed the phases which formed in the γ-TiAl alloys due to the additions of the PGMs to be identified. Phase diagram studies indicated that the maximum solubility of Pd in Ti_3Al (α_2) and TiAl (γ) is 2.5 at.% (Ding *et al.*, 2000; Raghavan, 2008 and Zaikina *et al.*, 20011a), and 5.5 at.% Pt in Ti_3Al (α_2) and TiAl (γ) (Zaikina *et al.*, 20011b; Zaikina *et al.*, 2012) . In the two-phase α_2+γ composition range, what

formed with Pd additions was the three-phase mixture $\alpha_2+\gamma+B2$. Platinum additions to γ-TiAl led to the presence of $\alpha_2+\gamma$ and a three-phase mixture $\alpha_2+\gamma+\tau_3$. There were no data available for iridium solubility in the two aluminides, except the isothermal section of the ternary system Ti-Al-Ir shown in Figure 2.9 (Raghavan, 2008). At 1650°C, it shows the existence of the βIrTi intermediate phase in the Ir-Ti system and IrAl intermediate phase in the Ir-Al system. The similarity with other PGMs suggested that addition of iridium could have an effect similar to palladium. Given that βIrTi and IrAl are both B2, CsCl-type cubic, there was a possibility of solid solution extending from the Ir-Al side to the Ir-Ti side at higher temperatures, just as the B2 identified by Ding *et al.* (2000) and Zaikina *et al.* (2011a) in the Ti-Al-Pd system. Considering the atomic radii, Al and Ti are within 15% of each other (Krishna Reddy, 2008), which could allow this substitution to form an isomorphous solid solution (Hume-Rothery, 1963), although this does not apply to the ionic radii, similarly, the valences are different, which could preclude the isomorphous solid solution between βIrTi and IrAl. But the atomic radii should be more relevant.

Figures 4.2 and 4.5 show that the microstructure of γ-TiAl with 0.2 at.% PGMs consisted of grains with alternating $\alpha_2+\gamma$ lamellae, γ grains and a two- or three-phase mixture. For γ-TiAl with 0.2 at.% Ru, G developed in the γ grains to give γ+G (Figure 4.2). For γ-TiAl with 0.2 at.% Pd, Pt or Ir, the development of the new phase took place in the lamellar grains. The most visible case was γ-TiAl with 0.2 at.% Pd, where the new phase developed along the α_2 lamellae of the lamellar grains (Figure 4.5a). As the PGM addition was increased, the PGM-containing phase also increased. Microstructures similar to γ-TiAl with 2.0 at.% Ru (Figure 4.4) were obtained with additions of 2.0 at.% Pt, Pd or Ir (Figure 4.6). At 2.0 at.% PGM additions, the new phases were found both in the γ-TiAl and lamellar grains. In each micrograph of Figure 4.6, γ-TiAl, lamellar α_2 + γ, a grey phase and a bright phase were visible. The composition of the grey and bright phases could not be established accurately, as they were too small. From the isothermal sections of the different ternary systems, these regions were identified as $\alpha_2+\gamma$, $\alpha_2+\gamma+B2$ and a B2 ternary phase for γ-TiAl with Pd additions (Zaikana *et al.*, 2011), $\alpha_2+\gamma$, $\alpha_2+\gamma+\tau_3$ and a ternary compound (τ_3) for γ-TiAl with Pt additions (Ding *et al.*, 2000), and $\alpha_2+\gamma$, $\alpha_2+\gamma+\tau$ and a ternary compound τ was assumed to exist for γ-TiAl with Ir.

The following can be said on the solidification and post-solidification of γ-TiAl with 2.0 at.% Pd. Solidification and solid-state equilibria of γ-TiAl-based alloys at 47.5 at.% will solidify as the βTi phase and go through αTi single-phase region, followed by αTi → αTi + γ and α + γ → α_2 + γ transformation, producing a (α_2 + γ) two-phase structure with decreasing temperature, thus forming (α_2 + γ) dendrites. As temperature decreased, the liquid surrounding underwent the eutectic reaction L→ α_2 + γ, followed by the ternary eutectic L→ α_2 + γ + τ_1. The resulting microstructure will consist of (α_2 + γ) dendrites, and two eutectic structure α_2 + γ and a very fine eutectic α_2 + γ + τ_1.

4.3 X-ray Mapping

The distributions of the different elements in the phases were qualitatively assessed by conducting X-ray mapping. Figures 4.7 to 4.10 are typical results of X-ray mapping for γ-TiAl with Pt additions (given as an example), and show that Al and Ti were in all the phases, although negligible in the platinum-rich phases. In all cases, Pt had low distributions in some areas and was concentrated in some other areas corresponding to the ternary compounds identified by EDX (Figure 4.6).Gamma-TiAl and Ti_3Al areas were characterised by the high distribution of Ti and Al, and low distribution of Pt, in agreement with the EDX results. Similar mapping results were obtained with γ-TiAl with Pd, γ-TiAl with Ru and γ-TiAl with Ir. The original dendrites can be clearly seen and the platinum is always in the interdendritic region. This is consistent with the phase diagram of Ding *et al.* (2000) who showed less than 5 at.% Pt in all the Ti-Al phases. Although the platinum only found interdendritcally, it was well distributed throughout the sample, showing that the microstructure was unlikely to be due to unmelted platinum, rather to the distribution of the phases.

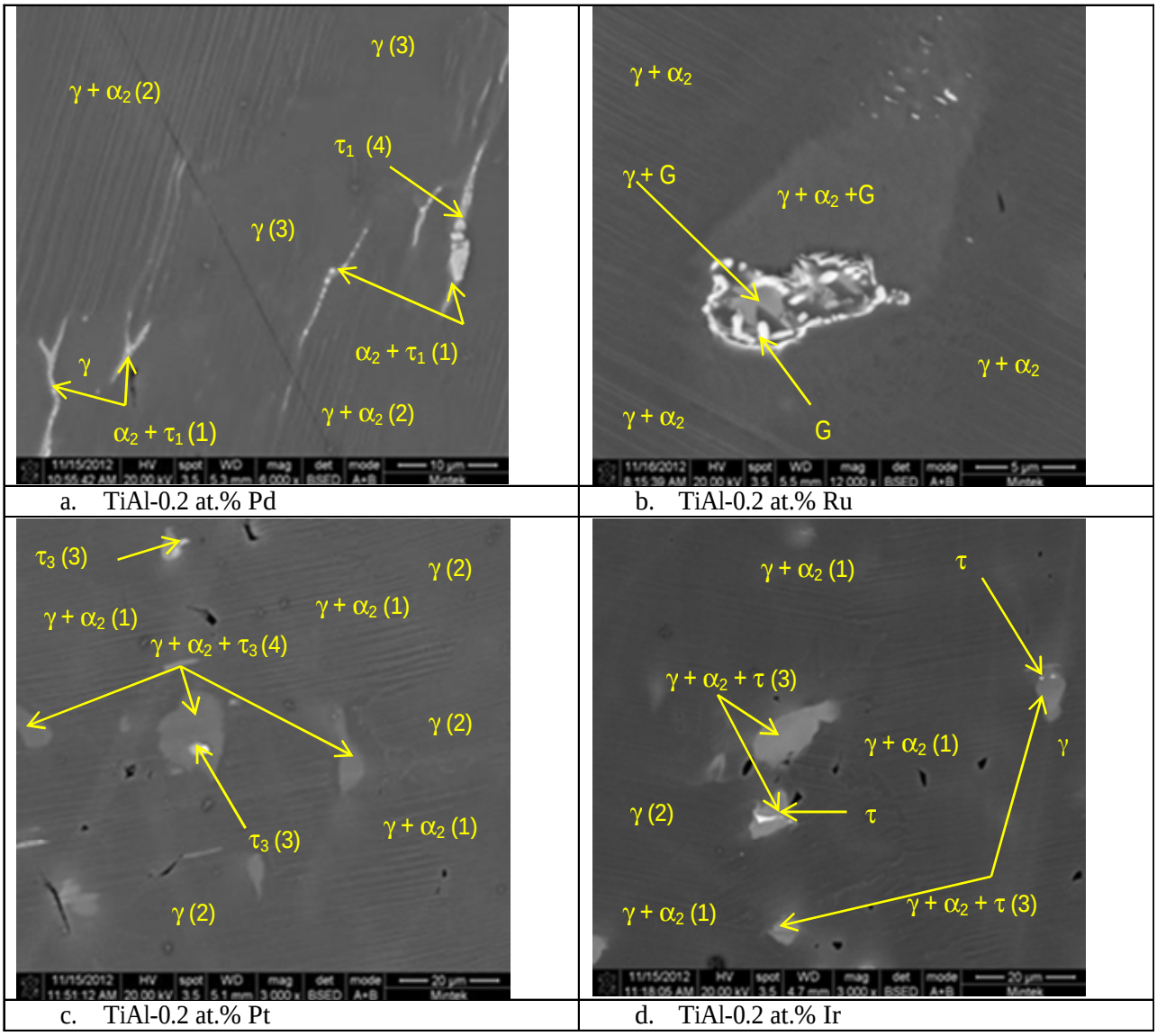
4.4 XRD analyses

The XRD patterns of γ-TiAl with different PGM additions are shown in Figures 4.11 to 4.14. It is worth noting that, even though expected peaks were present, the patterns in Figure 4.12 were poorer, lower signal and noisier. Peaks from γ-TiAl and Ti_3Al were present in all XRD patterns, irrespective of the added PGM. The PGM addition introduced some changes in the positions of certain peaks. Some of the peaks were lost in the background and were not visible in the patterns.

Table 4.6 shows the peak positions at 42°, 62.5° and 84.5° in the γ-TiAl with PGM compared to plain γ-TiAl. In general, there were shifts at larger 2θ due to the introduction of PGMs. A similar observation was made with peaks from γ-TiAl, where shifts were observed at higher 2θ. The shifts observed increased to reach maximum values, showing that the solubility limit had been reached. Only Ru additions led to a shift towards higher 2θ follow by a slight decrease (there was a maximum value for 2θ=63.5° and 2θ=86.5° for γ-TiAl with 1.0 at.% Ru), probably due to the formation of another phase.

Table 4.4. *EDX analyses of the γ-TiAl -0.2 at.% PGMs*

γ-TiAl-0.2 at.% Pd				
Area in Figure 4.5a	**Composition (at.%)**			**Phase**
	Ti	**Al**	**Pd**	
Overall	51.2±0.8	48.6±0.5	0.2±0.04	α_2, γ, , τ_1
Area 1	46.5±0.6	47.6±075	5.9±0.5	$\alpha_2 + \tau_1$
Area 2	51.3±0.5	48.1±0.5	0.6±0.07	$\gamma + \alpha_2$
Area 3	46.4±0.4	52.5±1.1	1.1±0.1	γ
Area 4	45.1±1.3	46.0±1.1	8.9±2.2	τ_1
γ-TiAl-0.2 at.% Pt				
Area in Figure 4.5c	**Composition (at.%)**			**Phase**
	Ti	**Al**	**Pt**	
Overall	51.4±0.6	48.4±0.5	0.2±0.05	
Area 1	52.5±0.8	47.3±0.8	0.20±0.05	$\gamma + \alpha_2$
Area 2	48.8±0.1	50.8±0.5	0.4±0.05	γ
Area 3	46.7±1.0	46.2±1.3	7.1±0.7	τ_3 (ternary)
Area 4	46.7±0.7	51.3±0.5	2.0±0.2	$\gamma + \alpha_2 + \tau_3$
γ-TiAl-0.2 at.% Ir				
Area in Figure 4.5d	**Composition (at.%)**			**Phase**
	Ti	**Al**	**Ir**	
Overall	51.6±0.8	48.2±0.8	0.2±0.04	γ, α_2, τ
Area 1	52.0±0.4	47.7±0.4	0.21±0.04	$\gamma + \alpha_2$
Area 2	48.7±0.4	50.9±0.5	0.4±0.1	γ
Area 3	44.7±1.5	46.7±1.2	8.6±0.6	$\gamma + \alpha_2 + \tau$
Area 4	47.0±0.3	50.6±0.5	2.3±0.3	$\gamma + \alpha_2 + \tau$



a. TiAl-0.2 at.% Pd

b. TiAl-0.2 at.% Ru

c. TiAl-0.2 at.% Pt

d. TiAl-0.2 at.% Ir

Figure 4.5. *SEM-BSE micrographs of γ-TiAl alloys with 0.2 at.% PGM, showing α_2, γ-TiAl, and a ternary compounds of different PGM contents.*

Table 4.5. *EDX analyses of the γ-TiAl -2.0 at.% PGMs*

γ-TiAl-2.0 at.% Pd				
Area in Figure	**Composition (at.%)**			**Phase**
	Ti	**Al**	**Pd**	
Overall	50.4±0.3	47.6±0.5	2.0±03	γ, α_2, τ_1
Area 1	48.4±0.4	40.3±0.7	11.3±06	Ternary Comp (τ_1)
Area 1	42.7±0.5	43.9±0.4	13.4±1.2	Ternary Comp (τ_1)
Area 2	50.6±0.5	48.0±0.6	1.4±0.3	γ+ α_2
Area 3	47.3±0.1	49.8±0.2	2.9±0.3	γ + α_2+τ_1
γ-TiAl-2.0 at.% Pt				
Area in Figure	**Composition (at.%)**			**Phase**
	Ti	**Al**	**Pt**	
Overall	51.8±0.8	48.0±0.8	0.2±0.04	γ, α_2, τ_3
Area 1	50.6	48.4±0.5	1.0±0.2	γ +α_2
Area 2	47.5±0.9	50.4±0.7	2.1±0.3	γ +α_2+τ_3
Area 3	45.1±1.3	46.0±1.1	8.9±2.2	τ_3
γ-TiAl-2.0 at.% Ir				
Area in Figure	**Composition (at.%)**			**Phase**
	Ti	**Al**	**Ir**	
Overall	50.9±1.6	47.00±1.2	2.1±0.2	γ, α_2, τ
Area 1	48.6±0.8	50.7±0.1	0.7±0.05	γ
Area 2	51.5±1.5	47.2±2.1	1.3±0.2	γ +α_2
Area 3	52.5±2.0	45.2±2.0	2.3±0.2	γ +α_2 + τ
Area 4	46.5±1.5	45.8±1.4	7.7±1.5	τ

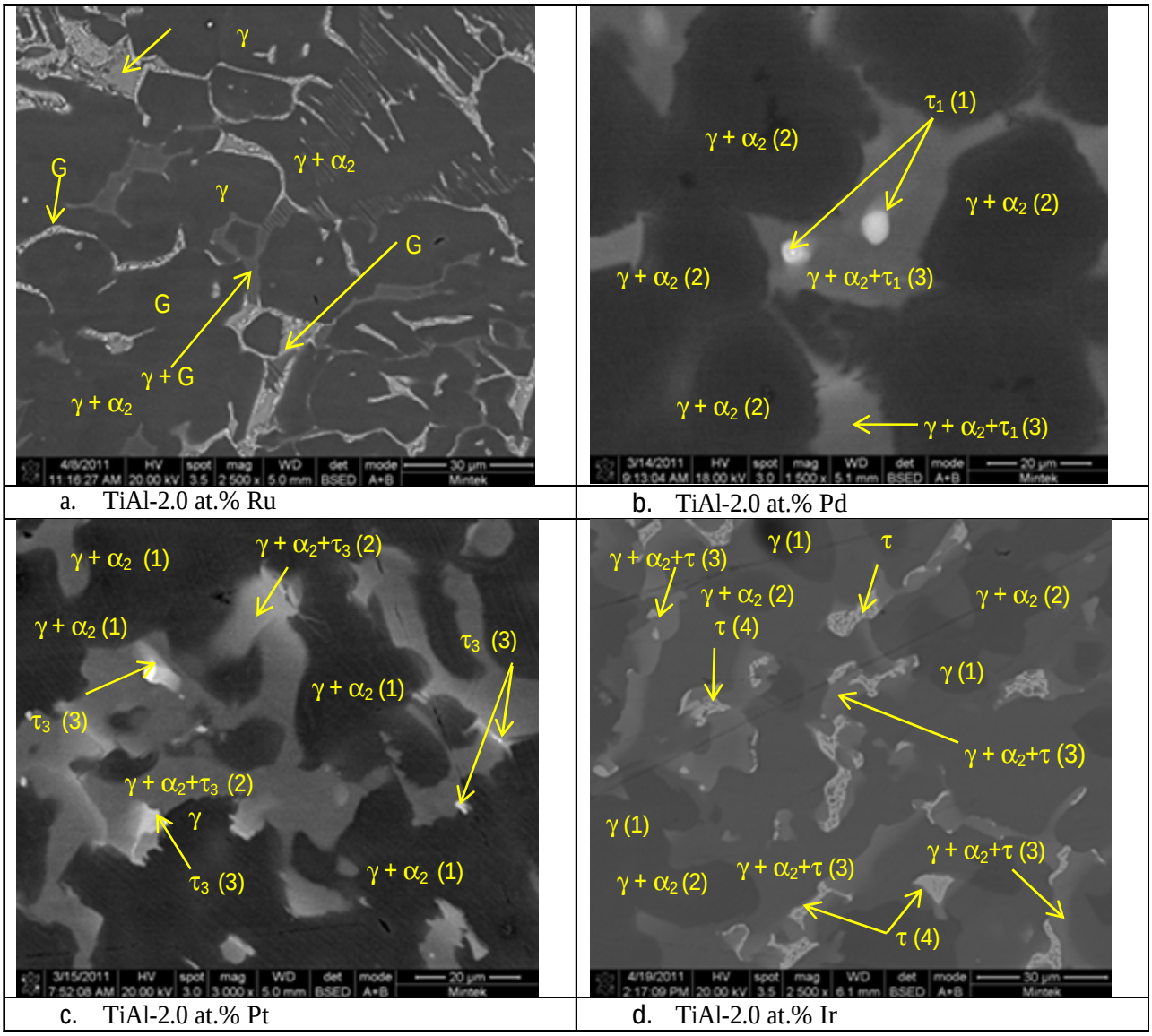


Figure 4.6. *SEM-BSE micrographs of γ-TiAl alloys with 2.0 at.% PGM showing α_2, γ-TiAl, and a ternary compounds (light phase with the highest PGM content).*

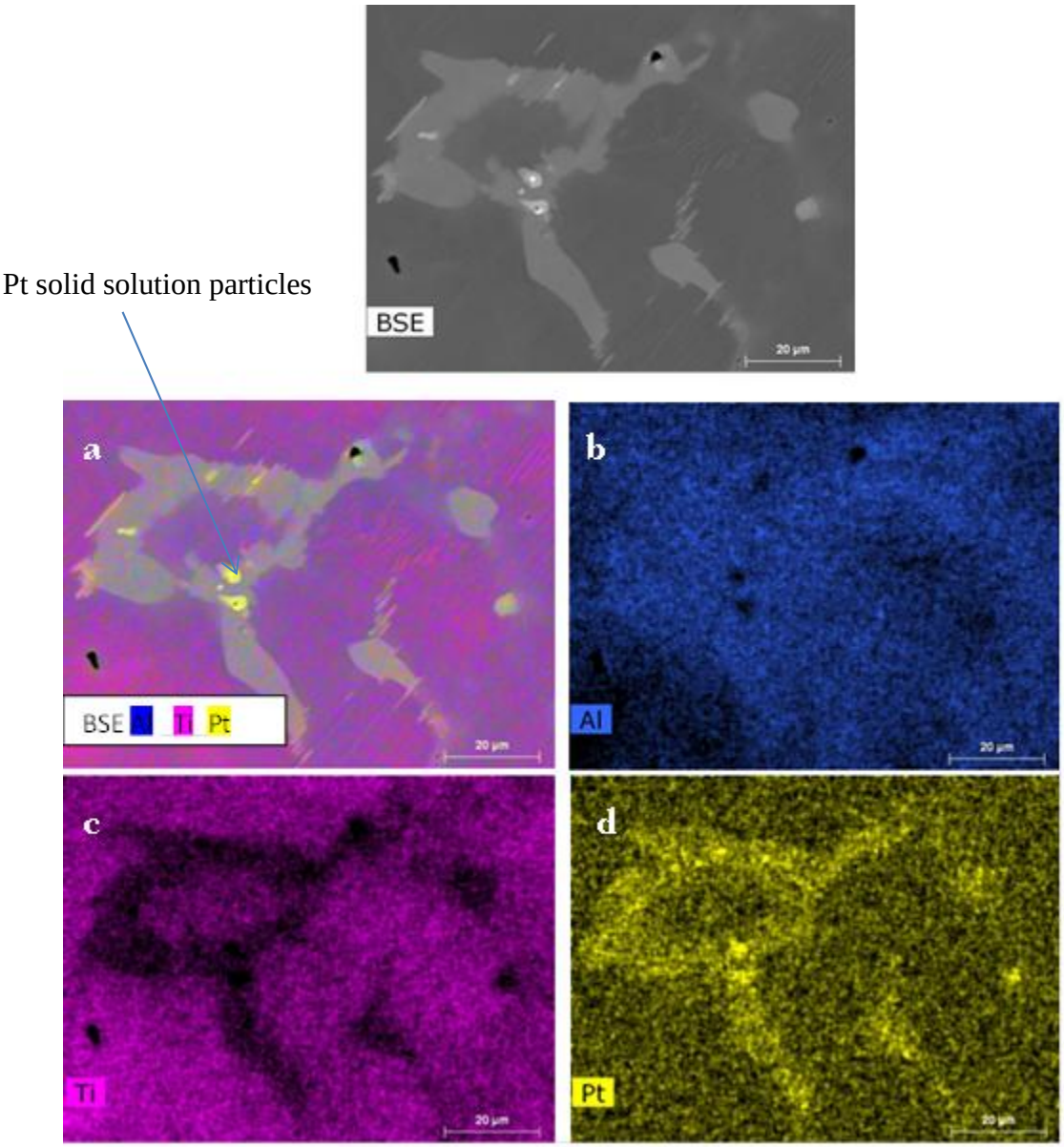


Figure 4.7. *Elemental mapping for γ-TiAl-0.2 at.% Pt, showing: a) Al, Ti and Pt, b) Al (blue), c) Ti (pink) and d) Pt (yellow).*

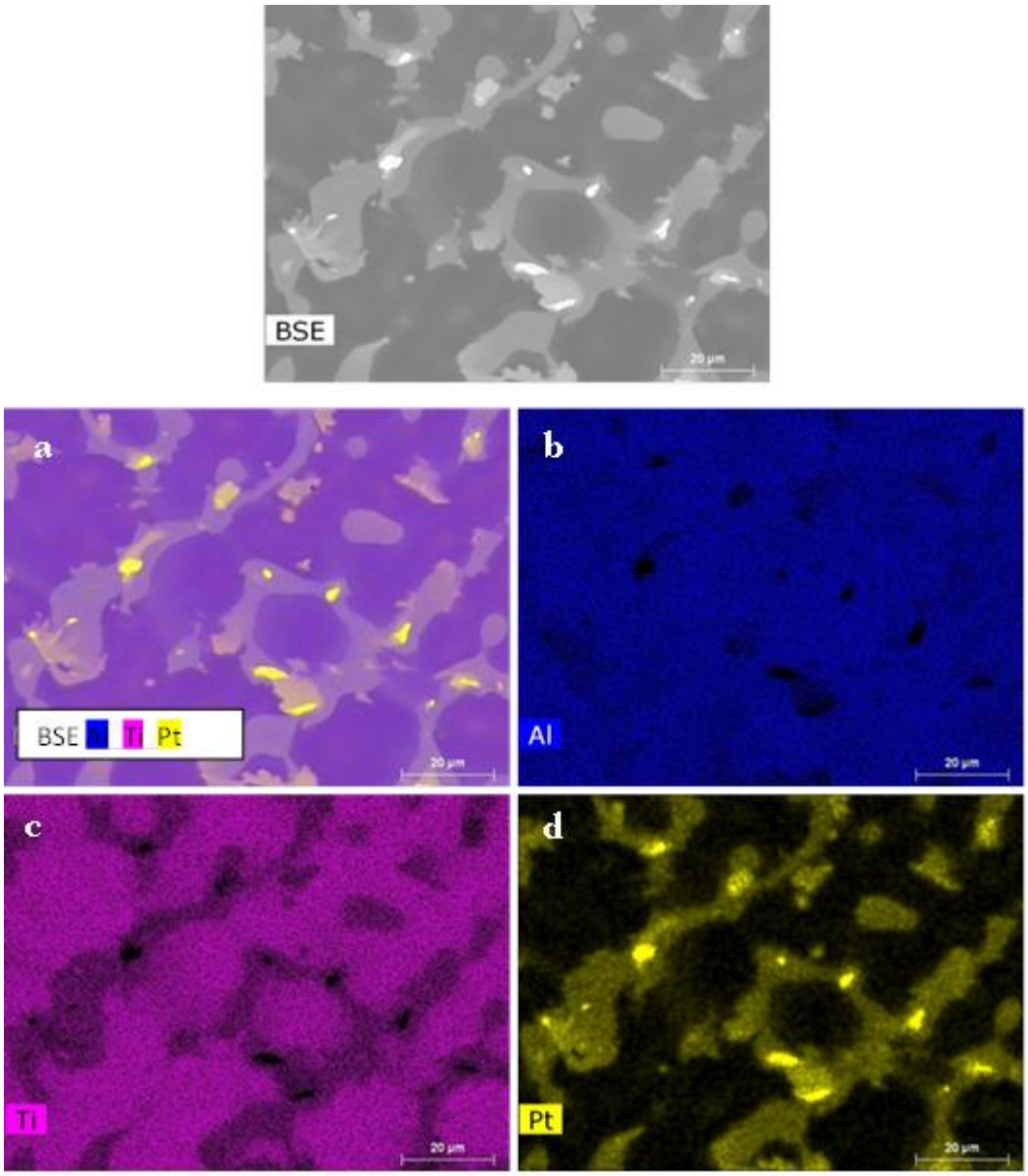


Figure 4.8. *Elemental mapping for γ-TiAl-1.0 at.% Pt, showing: a) Al, Ti and Pt, b) Al (blue), c) Ti (pink) and d) Pt (yellow).*

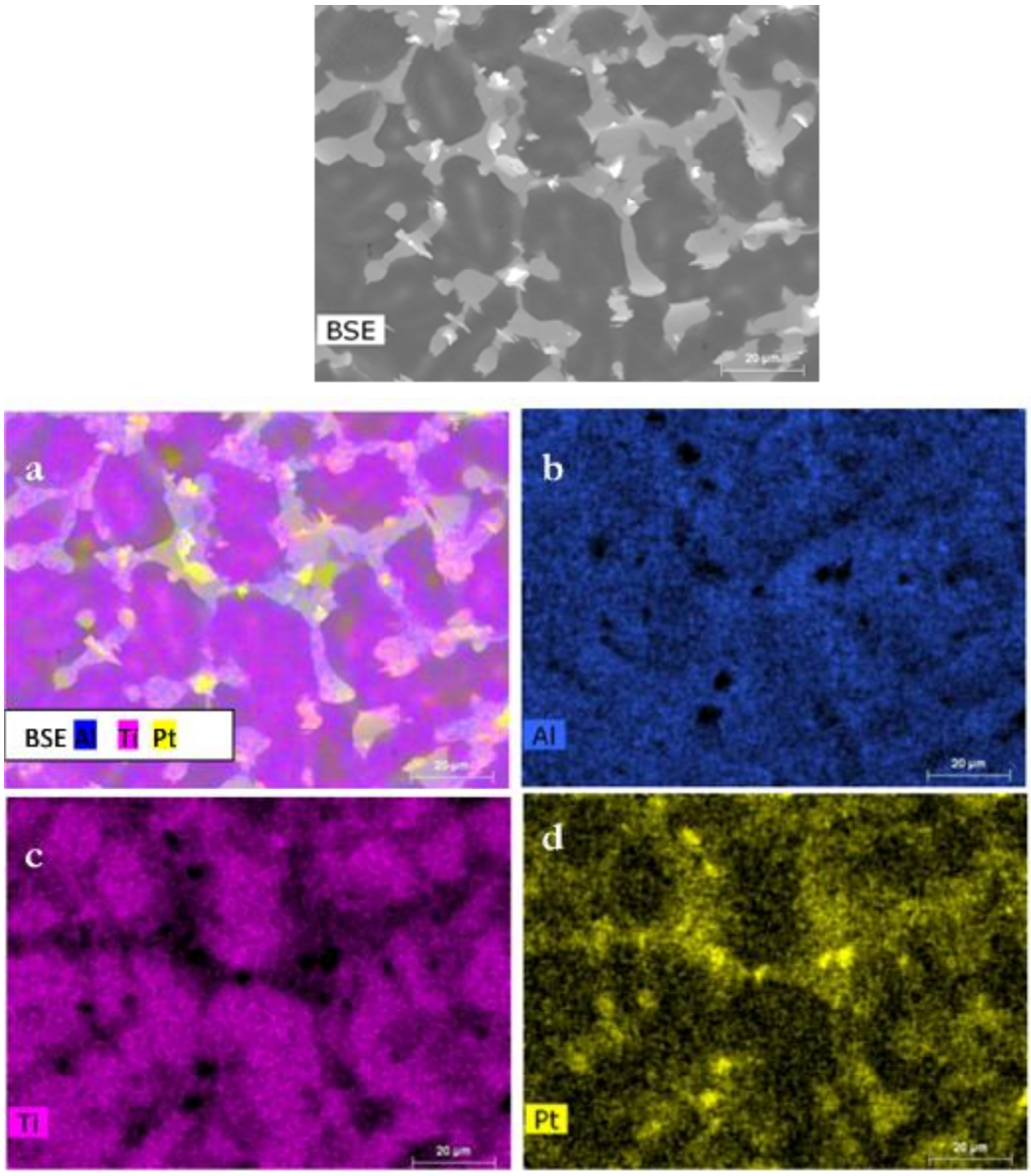


Figure 4.9. *Elemental mapping for γ-TiAl-1.5 at.% Pt, showing: a) Al, Ti and Pt, b) Al (blue), c) Ti (pink) and d) Pt (yellow).*

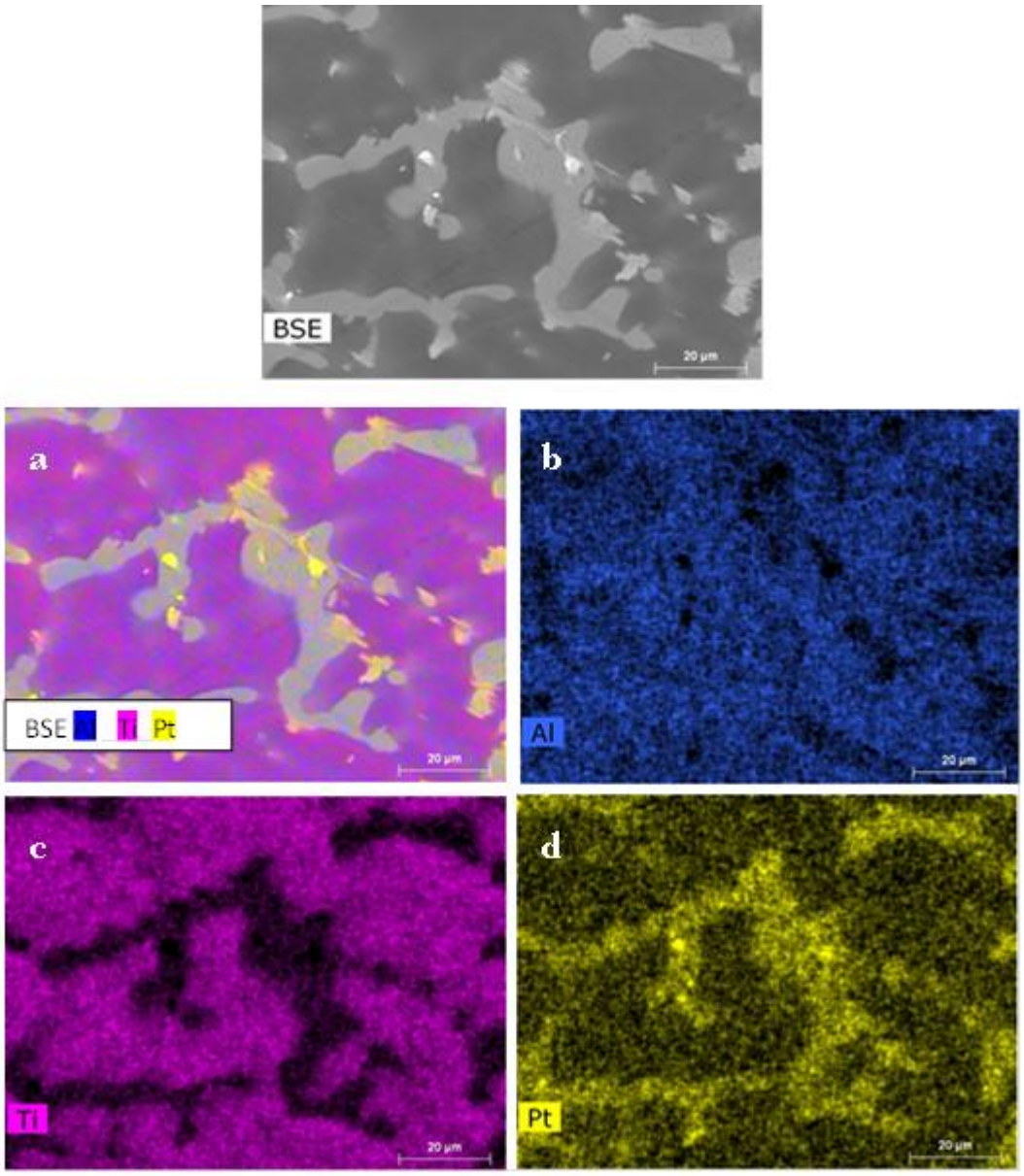


Figure 4.10. *Elemental mapping for γ-TiAl-2.0 at.% Pt, showing: a) Al, Ti and Pt, b) Al (blue), c) Ti (pink) and d) Pt (yellow).*

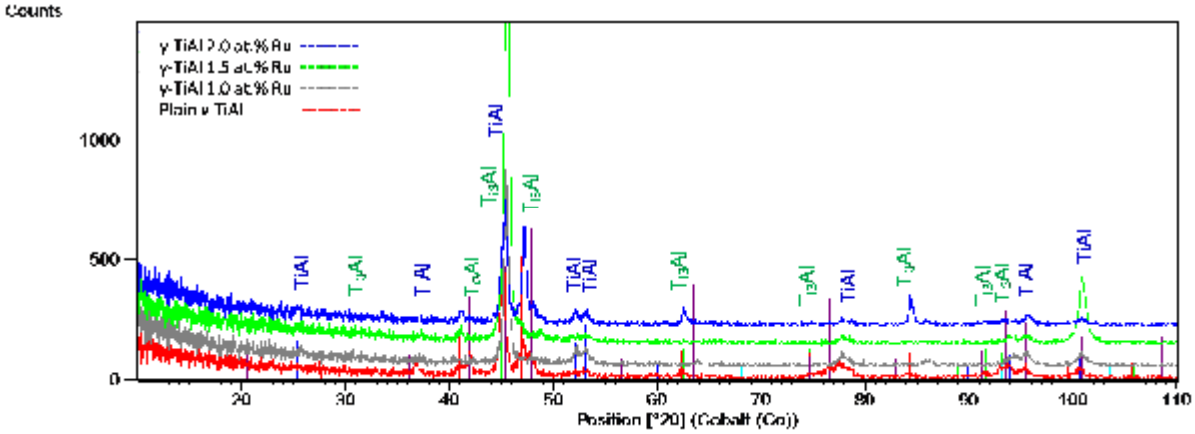


Figure 4.11. *XRD patterns of γ-TiAl alloys with different Ru additions.*

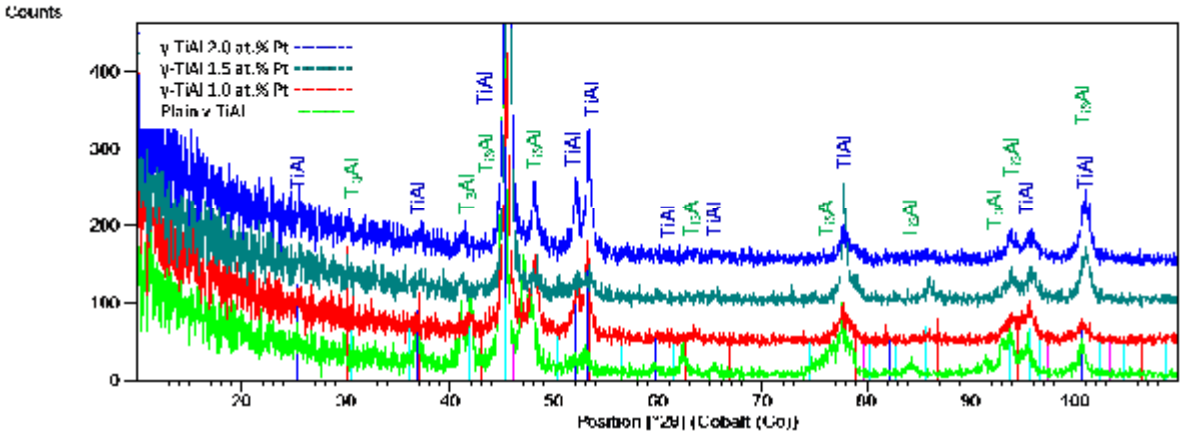


Figure 4.12. *XRD patterns of γ-TiAl alloys with different Pt additions.*

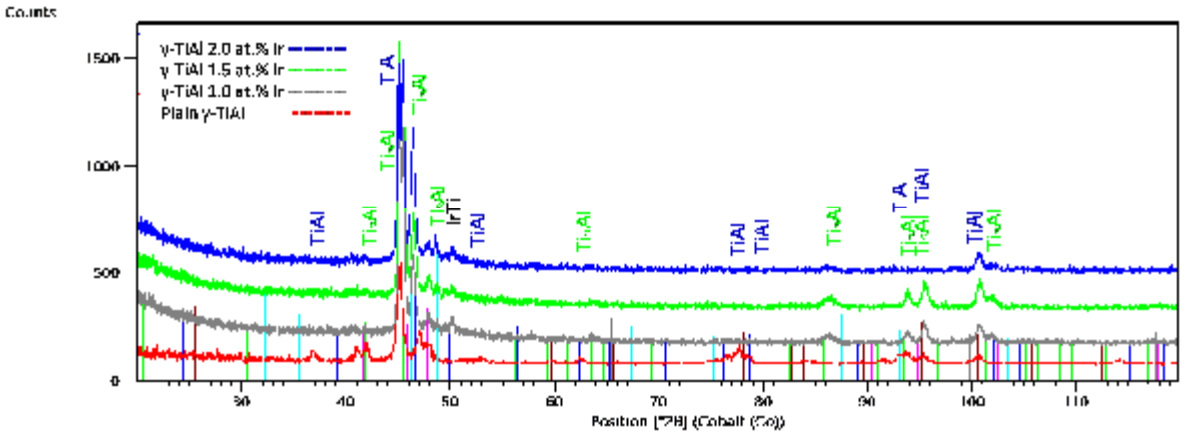


Figure 4.13. *XRD patterns of γ-TiAl alloys with different Ir additions.*

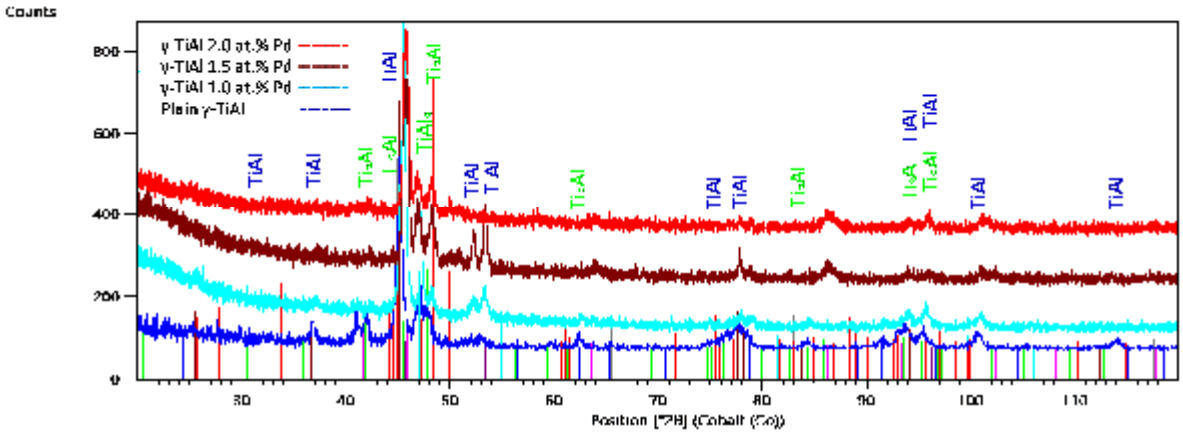


Figure 4.14. *XRD patterns of γ-TiAl alloy with different Pd additions.*

Table 4.6. *Ti_3Al peak positions or intensities on the XRD pattern of PGM-containing γ-TiAl alloys.*

Ti_3Al peak position or intensity				
Alloy	PGM	Bragg angle (2θ)		
Plain γ-TiAl	No PGM	42°	62.5°	84.5°
γ-TiAl	1.0 at.% Ru	Peak not visible	63.5°	86.5°
	1.5 at.% Ru	41°	Peak not visible	Peak not visible
	2.0 at.% Ru	41°	63°	85°
γ-TiAl	1.0 at.% Pt	Peak not visible	Peak not visible	85°
	1.5 at.% Pt	Peak not visible	Peak not visible	85°
	2.0 at.% Pt	Peak not visible	Peak not visible	85°
γ-TiAl	1.0 at.% Pd	42°	62.5°	84.5°
	1.5 at.% Pd	42°	64°	85°
	2.0 at.% Pd	42°	64°	85°
γ-TiAl	1.0 at.% Ir	Peak not visible	63.5°	86°
	1.5 at.% Ir	Peak not visible	63.5°	86°
	2.0 at.% Ir	Peak not visible	Peak not visible	86°

4.5 Thermogravimetric analysis (TGA)

The effect of precious metal content on the oxidation behaviour of the γ-TiAl alloys was assessed by TGA. Table 4.7 summarises the mass gains for the different PGM contents at 1185°C and Figure 4.15 shows the relative mass gains with increasing PGM contents. Ruthenium-alloyed TiAl had the largest mass gain was at 1.0 at.% Ru. The lowest mass gain was achieved with 1.5 at.% iridium and palladium additions.

Table 4.7. *Mass change as a function of precious metal content at 1185 °C.*

Precious metal content (at.%)	**Relative mass increase in PGM-alloyed TiAl (wt%)**			
	Ru	Pd	Pt	Ir
0.2	1.09±0.03	1.23±0.03	1.83±0.04	1.96±0.03
1.0	4.02±0.02	0.85±0.03	1.32±0.04	0.97±0.03
1.5	2.26±0.02	0.57±0.03	2.28±0.03	0.53±0.02
2.0	2.62±0.02	0.90±0.03	2.18±0.03	1.13±0.03

4.6 Hardness

The results of Vickers hardnesses of the as-cast and heat treated samples with 0.2 at.% PGM are given in Table 4.8. The Vickers hardness of the plain TiAl was around 300HV_{10}, and the introduction of PGMs resulted in a slight increase. The heat treatment at 1000 °C for 1 hour did not significantly change the hardness of the alloys, and the time might not have been long enough because the high errors show some inhomogeneity. However, there would be inhomogeneity anyway, because of the different phases in the microstructure. The samples with the highest hardness in the as-cast condition, TiAl-Pd, showed the largest decrease on heat treatment.

The effect of increased PGM content on the hardness is shown in Tables 4.8 and 4.9 and Figure 4.16. The hardness of the γ-TiAl alloys with increased PGMs remained in the same band as the addition level of 0.2 at.% Ru, Pd and Pt. However, γ-TiAl alloys with Ir showed a direct relationship, increasing to around 385±16 HV_{10} at 2.0 at.% Ir. The values of the microhardness on different phases of plain TiAl and TiAl with PGMs show that the hardness of α_2 with Ru, Pt, and Ir remained within the ranges of values of the plain TiAl, and was higher for α_2 with Pd, indicating that Pd atoms went into that phase more than other PGMs. The microhardness of γ with PGMs was generally high, except for γ with Pt, which was in the range of plain TiAl, showing that for TiAl-1.0 at.% Ru and TiAl-1.0 at.% Ir, Ir and Ru atoms went into solution with γ. Conversely, platinum and palladium atoms did not go into the γ phase substantially, making little difference there, only increasing the hardness in the interdendritic PGM-rich regions.

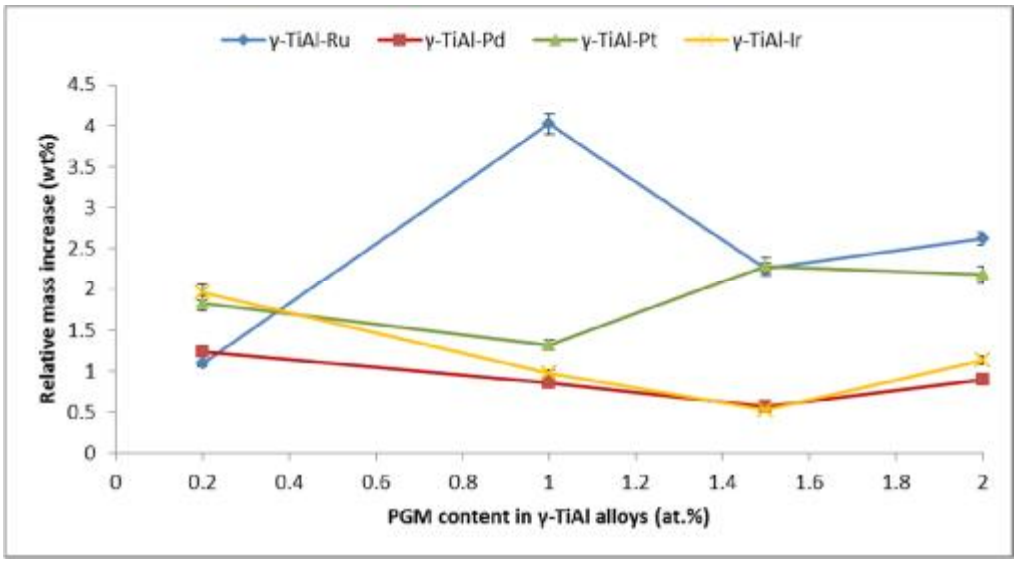


Figure 4.15. *Effect of PGM content on mass gain for different γ-TiAl alloys at 1185 °C.*

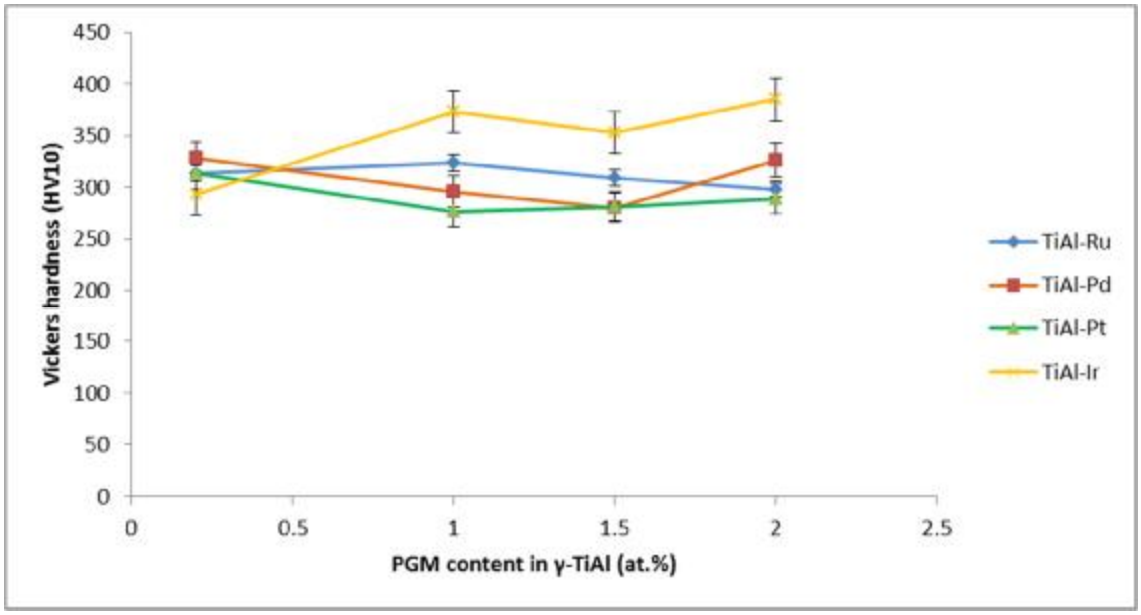


Figure 4.16. *Effect of PGM content on the Vickers hardness for as-cast γ-TiAl alloys.*

Table 4.8. *Vickers hardness of as-cast γ-TiAl alloyed with different PGM contents.*

PGM (at.%)	**γ-TiAl alloy**				
	Plain γ-TiAl	TiAl-Ru	TiAl-Pd	TiAl-Pt	TiAl-Ir
0 (As-cast)	281±23	-	-	-	-
0 (Heat treated)	269±25	-	-	-	-
0.2 (As-cast)	-	314±24	328±17	314±10	293±17
0.2 (Heat-treated)	-	303±11	311±18	298±14	300±12
1.0 (As-cast)	-	324±17	296±16	276±11	373±15
1.5 (As-cast)	-	309±33	280±21	281±15	353±11
2.0 (As-cast)	-	298±27	326±14	289±16	385±16

Table 4.9. *Vickers micro-hardness of as-cast γ-TiAl alloyed with different PGM contents of 1.0 at.%.*

PGM (at.%)	**γ-TiAl alloy**				
	Plain γ-TiAl	TiAl-Ru	TiAl-Pd	TiAl-Pt	TiAl-Ir
α_2	295±35	-	-	-	-
γ	285±23	-	-	-	-
High PGM area	-	315±15	340±15	320±5	300±14
α_2	-	300±12	315±13	305±16	302±18
γ	-	333±13	305±14	287±15	360±19

4.7 Discussion

High-temperature oxidation behaviour of γ-TiAl with PGMs

The high-temperature behaviour of γ-TiAl with PGM was assessed. As the temperature of the γ-TiAl was increased from room temperature to 1185°C under a constant flow of air, there was a mass increase, due to oxygen pick-up and the subsequent formation of oxides Al_2O_3 and TiO_2. Alumina (Al_2O_3) and rutile (TiO_2) are the oxides normally formed when aluminium and titanium are exposed to oxygen of the air (Ma *et al.*, 2004; Hanaor and Sorrell, 2011; Chen, 2014; Osorio *et al.*, 2014).

In oxidation tests, the addition of 0.2 at.% PGM resulted in a small mass increase due to oxide formation. As the PGM content was increased to 1.0, 1.5 and 2.0 at.%, there was mass reduction for TiAl with Pd and Ir up to 1.5 at.% addition. At 2 at. % additions, there was a mass increase. For TiAl with Pt additions, there was a mass decrease up to 1 at.% and a mass increase at 1.5 at.% and

2.0 at.% additions. This observations suggested that there was benefit of adding Pd and Ir up to 1.5 at% and Pt up to 1 at.%. There was no benefit of adding 2 at.% PGM. No comments can be made on Ru additions because the behaviour of TiAl with 1 at.% addition was anomalous.

The Vickers hardness of the plain γ-TiAl was around $300HV_{10}$. Heat treatment introduced a slight decrease in hardness. This was expected, as the heat treatment was to soften the TiAl-based alloys, while keeping the as-cast microstructure. Within the errors, the hardness of γ-TiAl with PGM additions were the same, except for γ-TiAl with Ir additions, which was higher. This could be attributed to solution hardening, because there were few iridium-rich precipitates, indicating more solid solution.

XRD analyses and Mapping

When comparing the XRD patterns of the plain γ-TiAl alloy to those of γ-TiAl alloys with PGMs, the patterns were marked by peak position or intensity variation at certain 2θ angles for Ti_3Al and TiAl when PGMs were added. Ti_3Al and TiAl peaks showed a shift towards larger angles at larger 2θ. Some peaks were not visible in the patterns, being lost in the background. At lower angles, there was a slight shift towards small 2θ.

A constant shift towards larger 2θ angles shows that the interplanar spacing (d parameter) decreased due to the presence of PGMs. This indicated that the presence of PGM atoms in the γ-TiAl was the cause of the peak position shift. The peak shift was not all constant, which was because the crystal structures of the two compounds were not cubic: a face centred-tetragonal for TiAl and hexagonal for Ti_3Al.

The X-ray mapping allowed the distribution of each element to be seen in the different phases. There was more titanium in α_2 phase and more Al in the γ-TiAl phase. The PGM contents were very low in the α_2 and γ phases and increased locally in the microstructure in region where new phases of relatively high PGM contents or pure PGM areas (PGM solid solution particles) were.

CHAPTER 5

CORROSION BEHAVIOUR IN AQUEOUS SOLUTIONS

5.1 Electrochemical behaviour

The results of electrochemical testing are given in Tables 5.1 - 5.5 and show the current density, corresponding corrosion rates and corrosion potentials at each concentration of the HCl solution. The potentiodynamic scans of plain γ-TiAl in solutions of different concentrations are shown in Figure 5.1. There are no data for TiAl-0.2 at.% Pd in 25 wt % HCl, because the samples completely dissolved in the solutions.

For γ-TiAl with 0.2 at.% PGMs, the corrosion rate of the TiAl-0.2 at.% Pt alloy was lower than the plain γ-TiAl alloy in 5 wt % HCl and 15 wt% HCl solutions and was higher than plain γ-TiAl alloy in the 25 wt% HCl solution. The TiAl-0.2 at.% Pd alloy corrosion rate was also lower in the 5 and 15 wt% HCl solutions, and the sample completely dissolved in 25 wt% HCl solution. Gamma-TiAl with 0.2 at% Ru and Ir additions showed corrosion rates below the plain γ-TiAl alloy in all three solutions.

For γ-TiAl with 1.0 at.% PGMs, the corrosion rates of γ-TiAl with 1.0 at.% Pd and 1.0 at.% Ir additions were lower than the plain γ-TiAl alloy in all three solutions. The corrosion rate of γ-TiAl with 1.0 at.% Pt was higher than the plain γ-TiAl alloy in 25 wt% HCl solution and γ-TiAl with 1.0 at.% Ru addition in all three solutions.

For γ-TiAl with 1.5 at.% PGMs, the corrosion rates of TiAl with Pt were higher than the plain γ-TiAl alloy in all three solutions, the corrosion rate of TiAl with Pd was lower in the 5 and 15 wt% HCl solutions and the corrosion rate of TiAl with Ru was higher than the plain γ-TiAl alloy in 5 wt% HCl solutions and lower in 15 and 25 wt% HCl solutions. The corrosion rates were lower than the plain γ-TiAl alloy in all three solutions for γ-TiAl with Ir.

For γ-TiAl with 2.0 at% PGM additions, TiAl alloys with Ru and Ir showed lower corrosion rates than the plain γ-TiAl alloy in all three solutions. Gamma-TiAl with Pd and Pt showed high corrosion

rates than the plain γ-TiAl alloy, with γ-TiAl with 2.0 at.% being completely dissolved in 25 wt% HCl solution.

Table 5.1*. Test parameters and resulting corrosion potentials, current densities and corrosion rates for plain γ-TiAl.*

Sample	**HCl (wt%)**	**I_{corr} ($mA.cm^{-2}$)**	**Corrosion rate ($mm.year^{-1}$)**	**E_{corr} [mV (SCE)]**
Plain γ-TiAl	5	0.061	0.549	-605
	15	0.130	1.161	-566
	25	0.200	1.764	-462

Table 5.2*. Test parameters and resulting corrosion potentials, current densities and corrosion rates for γ-TiAl-0.2 at.% PGM.*

Samples	**HCl (wt%)**	**I_{corr} ($mA.cm^{-2}$)**	**Corrosion rate ($mm.year^{-1}$)**	**E_{corr} [mV (SCE)]**
γ-TiAl-0.2 at.% Pt	5	0.068	0.612	-275
	15	0.110	0.990	-252
	25	0.220	1.980	-230
γ-TiAl-0.2 at.% Pd	5	0.004	0.037	-318
	15	0.039	0.351	-288
	25	-	-	-
γ-TiAl-0.2 at.% Ru	5	0.0005	0.004	-370
	15	0.016	0.144	-370
	25	0.047	0.423	-344
γ-TiAl-0.2 at.% Ir	5	0.041	0.369	-274
	15	0.092	0.828	-254
	25	0.27	2.430	-244

***Table 5.3**. Test parameters and resulting corrosion potentials, current densities and corrosion rates for γ-TiAl-1.0 at.% PGM.*

Samples	**HCl (wt%)**	**I_{corr} ($mA.cm^{-2}$)**	**Corrosion rate ($mm.year^{-1}$)**	**E_{corr} [mV (SCE)]**
γ-TiAl-1.0 at.% Pt	5	0.003	0.030	-260
	15	0.011	0.099	-234
	25	0.240	2.160	-254
γ-TiAl-1.0 at.% Pd	5	0.001	0.009	-226
	15	0.013	0.117	-268
	25	0.013	0.117	-268
γ-TiAl-1.0 at.% Ru	5	0.160	1.440	-270
	15	0.930	8.370	-238
	25	1.500	13.500	-223
γ-TiAl-1.0 at.% Ir	5	0.026	0.234	-282
	15	0.036	0.324	-275
	25	0.040	0.342	-232

***Table 5.4**. Test parameters and resulting corrosion potentials, current densities and corrosion rates for γ-TiAl-1.5 at.% PGM.*

Samples	**HCl (wt%)**	**I_{corr} ($mA.cm^{-2}$)**	**Corrosion rate ($mm.year^{-1}$)**	**E_{corr} [mV (SCE)]**
γ-TiAl-1.5 at.% Pt	5	0.5	4.500	-312
	15	1.3	11.700	-267
	25	3.8	34.200	-238
γ-TiAl-1.5 at.% Pd	5	0.039	0.351	-261
	15	0.067	0.603	-226
	25	0.39	3.510	-189
γ-TiAl-1.5 at.% Ru	5	0.12	1.080	-245
	15	0.026	0.234	-297
	25	0.059	0.531	-310
γ-TiAl-1.5 at.% Ir	5	0.01	0.090	-296
	15	0.022	0.198	-264
	25	0.024	0.216	-237

Table 5.5*. Test parameters and resulting corrosion potentials, current densities and corrosion rates for γ-TiAl-2.0 at.% PGM.*

Samples	HCl (wt%)	I_{corr} (mA.cm^{-2})	Corrosion rate (mm.year^{-1})	E_{corr} [mV (SCE)]
γ-TiAl-2.0 at.% Pt	5	0.120	1.080	-271
	15	0.170	1.530	-235
	25	0.500	4.500	-291
γ-TiAl-2.0 at.% Pd	5	4.600	41.400	-274
	15	3.400	30.600	-242
	25	-	-	-
γ-TiAl-2.0 at.% Ru	5	0.010	0.090	-270
	15	0.014	0.126	-306
	25	0.095	0.855	-325
γ-TiAl-2.0 at.% Ir	5	0.005	0.045	-281
	15	0.039	0.351	-263
	25	0.079	0.711	-244

5.2 Effect of alloying additions on corrosion potential

5.2.1 Corrosion of plain TiAl

In the 5 wt% HCl solution, plain γ-TiAl (Table 5.1 and Figure 5.1) had a corrosion potential of about -605 mV, which increased as the concentration of the HCl solution increased. Thus, the primary active-to-passive zone decreased with increasing HCl concentration. In 5 wt% HCl, the passivation potential of plain γ-TiAl was about -296 mV and the pitting potential -48 mV. In all solution concentrations, pitting corrosion occurred with increased current after passivation, e.g. transpassive region. Pitting corrosion occurred at potentials which decreased with increasing acid concentration, in agreement with Saffarian *et al.* (1996). In 25 wt% HCl solution, the passivation region almost completely vanished, suggesting an inability of the plain γ-TiAl to passivate at this high acidic concentration.

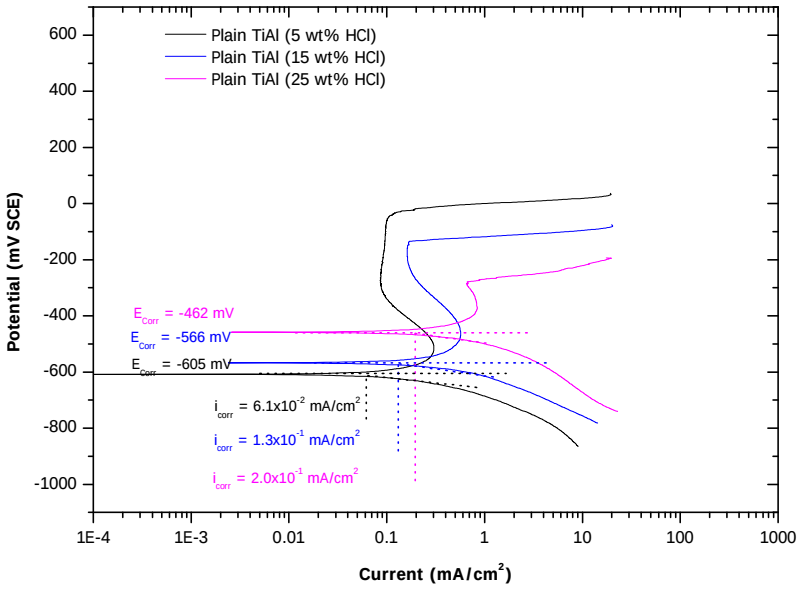


Figure 5.1. *Potentiodynamic scans for plain γ-TiAl in HCl solution of different concentrations.*

5.2.2 γ-TiAl alloyed with PGMs

The addition of PGMs to γ-TiAl increased the corrosion potential (Tables 5.2 - 5.5). Typical potentiodynamic scans are shown in Figure 5.2 for γ-TiAl alloyed with 1.0 at.% Pd. The addition of palladium shifted the corrosion potential to a more positive value. These results suggested that γ-TiAl-1 at.% Pd would passivate spontaneously in 5, 15 and 25 wt% HCl solutions. Results obtained with TiAl-1.0 at.% Pt, TiAl-1.0 at.% Ru and TiAl-1.0 at.% Ir are shown in Figure 5.3, and results for γ-TiAl with 0.2, 1.5 and 2.0 at.% PGM additions are shown in Figures 5.4 to 5.6. Table 5.6 shows the potential increase observed with increasing solution concentration (5, 15 and 25 wt% HCl) after 60 minute exposures with reference to plain γ-TiAl, obtained by the following calculations:

$\Delta E_5 = E_5 - E_{TiAl}$

$\Delta E_{15} = E_{15} - E_{TiAl}$

$\Delta E_{25} = E_{25} - E_{TiAl}$

where: ΔE = Potential increase difference

E_5 = Corrosion potential in 5 wt% HCl solution

E_{15} = Corrosion potential in 15 wt% HCl solution

E_{25} = Corrosion potential in 25 wt% HCl solution

E_{TiAl} = Corrosion potential of plain TiAl alloy.

The corrosion potential increases to nobler values are clearly illustrated in Figure 5.3. In the case of γ-TiAl with 1.0 at.% PGM additions (Table 5.6), the corrosion potentials with HCl remained between -300 and -200 mV for γ-TiAl containing platinum group metals, well above the corrosion potential for plain γ-TiAl, which was below -450 mV. Table 5.6 shows similar trends for additions of 0.2, 1.5 and 2.0 at.% PGM additions. The largest jumps (potential variation above 300 mV) were observed in 5 wt% HCl solutions, suggesting a spontaneous passivation of these alloys by cathodic modification. Figure 5.7 shows the shift of corrosion potentials to nobler values with additions of 1.0 at.% PGMs to γ-TiAl and suggests an improvement in corrosion resistance. Results for γ-TiAl with additions of 0.2, 1.5 and 2.0 at.% PGMs are shown in Figures 5.8 to 5.10, also with similar trends of the corrosion potentials. The shift of corrosion potentials towards more positive values did not necessarily lead to the corrosion resistance improvement. Some corrosion potential shifts (TiAl-0.2 at.% Pd and TiAl-2.0 at.% Pd in 25 wt% HCl) were associated with extensive sample dissolution and complete destruction, which was attributed to the corrosion potentials of the samples falling in the transpassive zone of plain TiAl after addition of the PGMs.

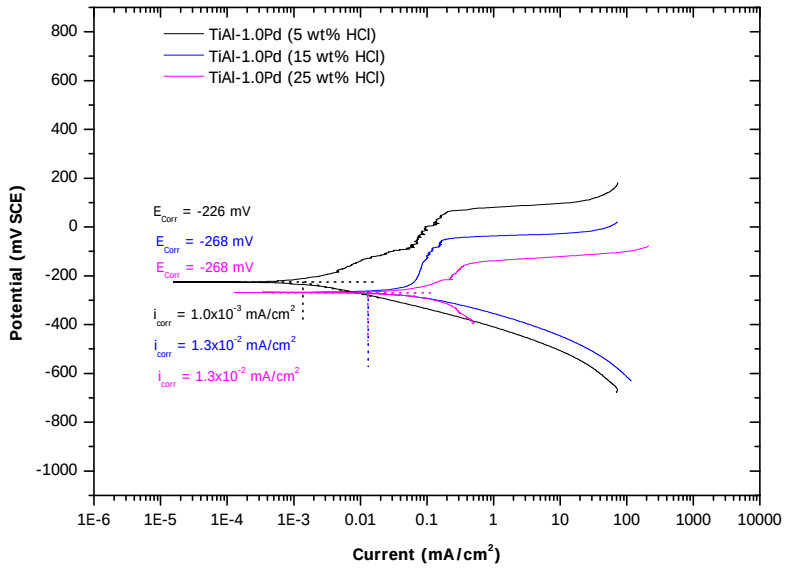


Figure 5.2. *Potentiodynamic scans for γ-TiAl-1.0 at.% Pd in HCl solutions of different concentrations.*

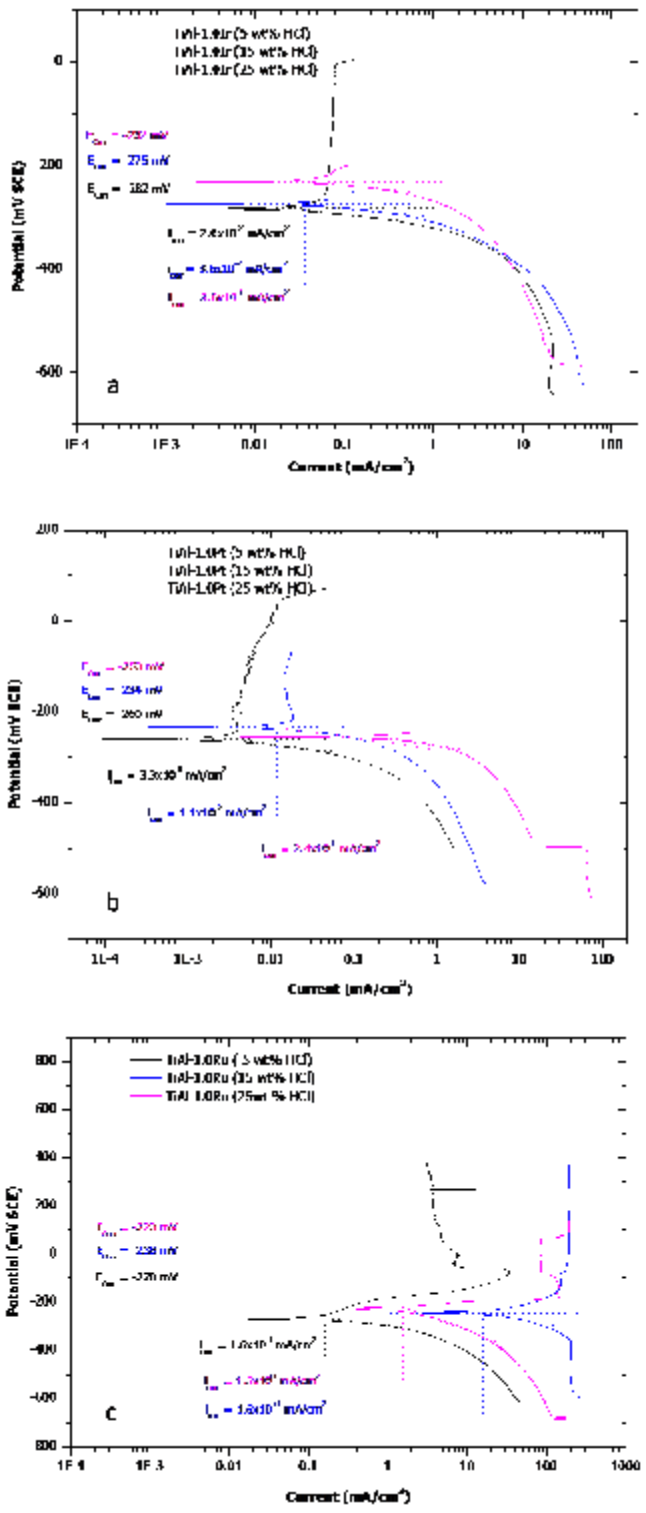


Figure 5.3. *Potentiodynamic scans for γ-TiAl with (a)1.0 at.% Ir, (b)1.0 at.%Pt and 1.0 at.% Ru in HCl solutions of different concentrations.*

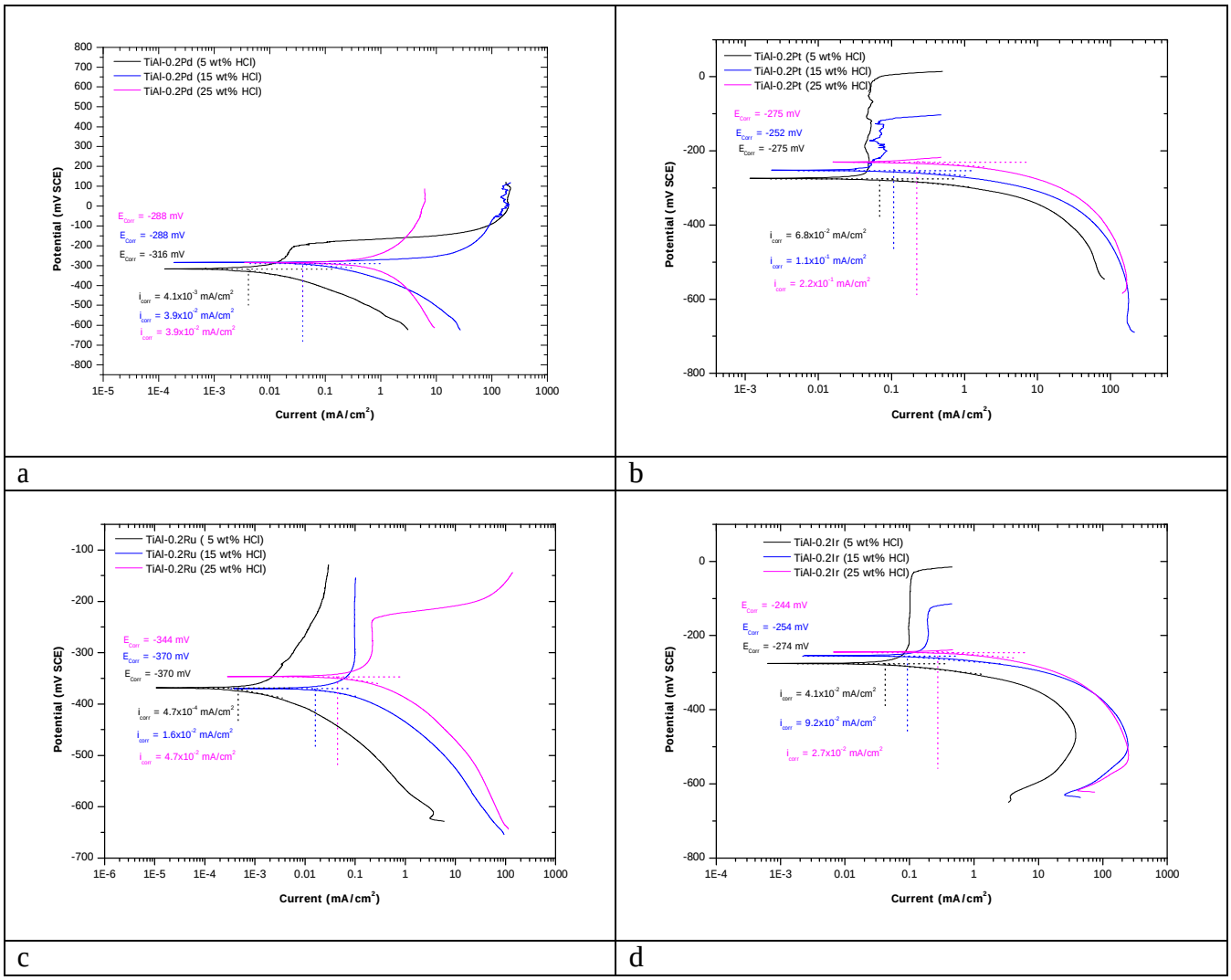


Figure 5.4. *Potentiodynamic scans for γ-TiAl with (a) 0.2 at.% Pd, (b) 0.2 at.%Pt, (c) 0.2 at.% Ru and (d) 0.2 at.% Ir in HCl solutions of different concentrations.*

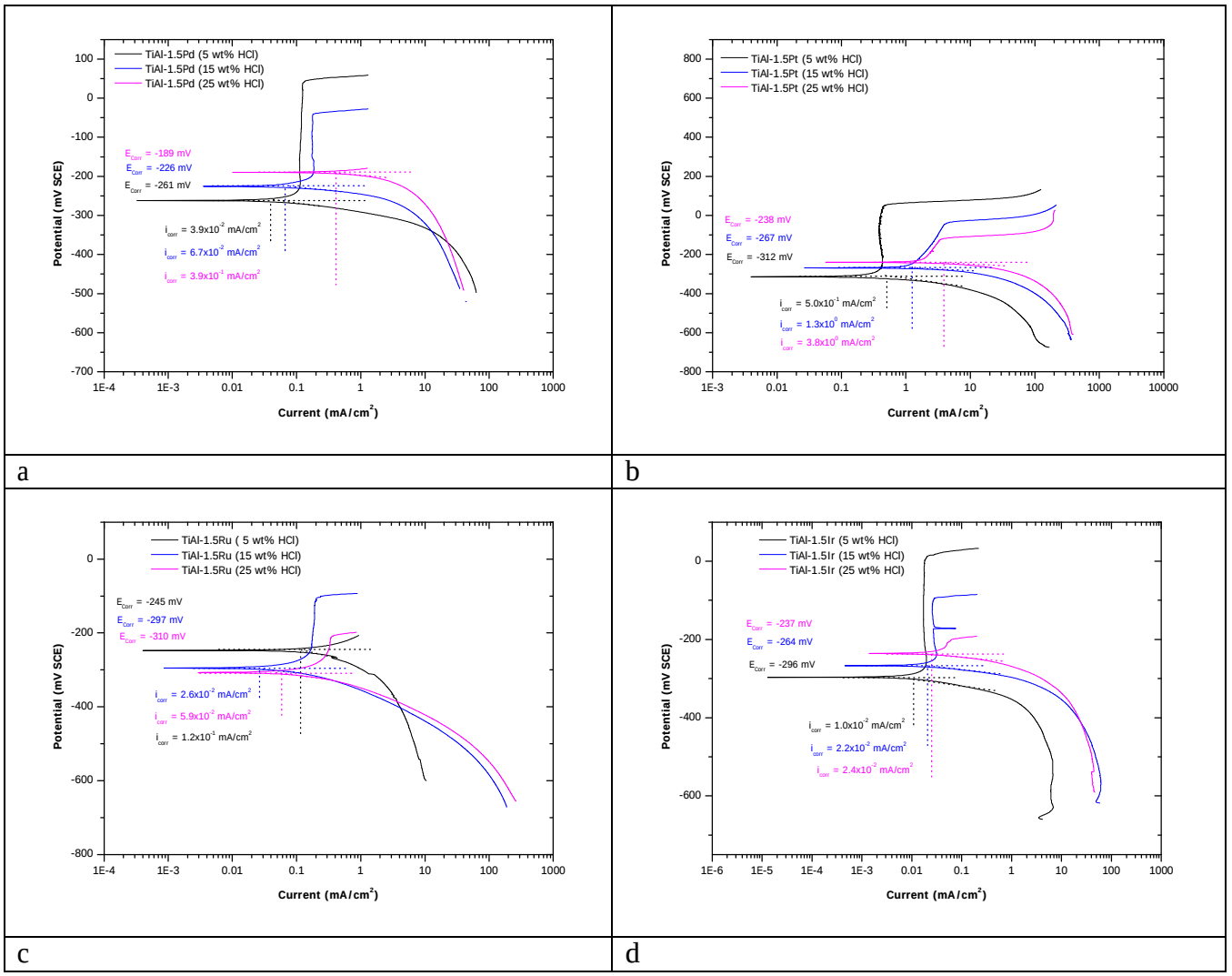


Figure 5.5. *Potentiodynamic scans for γ-TiAl with (a) 1.5 at.% Pd, (b) 1.5 at.%Pt, (c) 1.5 at.% Ru and (d) 1.5 at.% Ir in HCl solutions of different concentrations.*

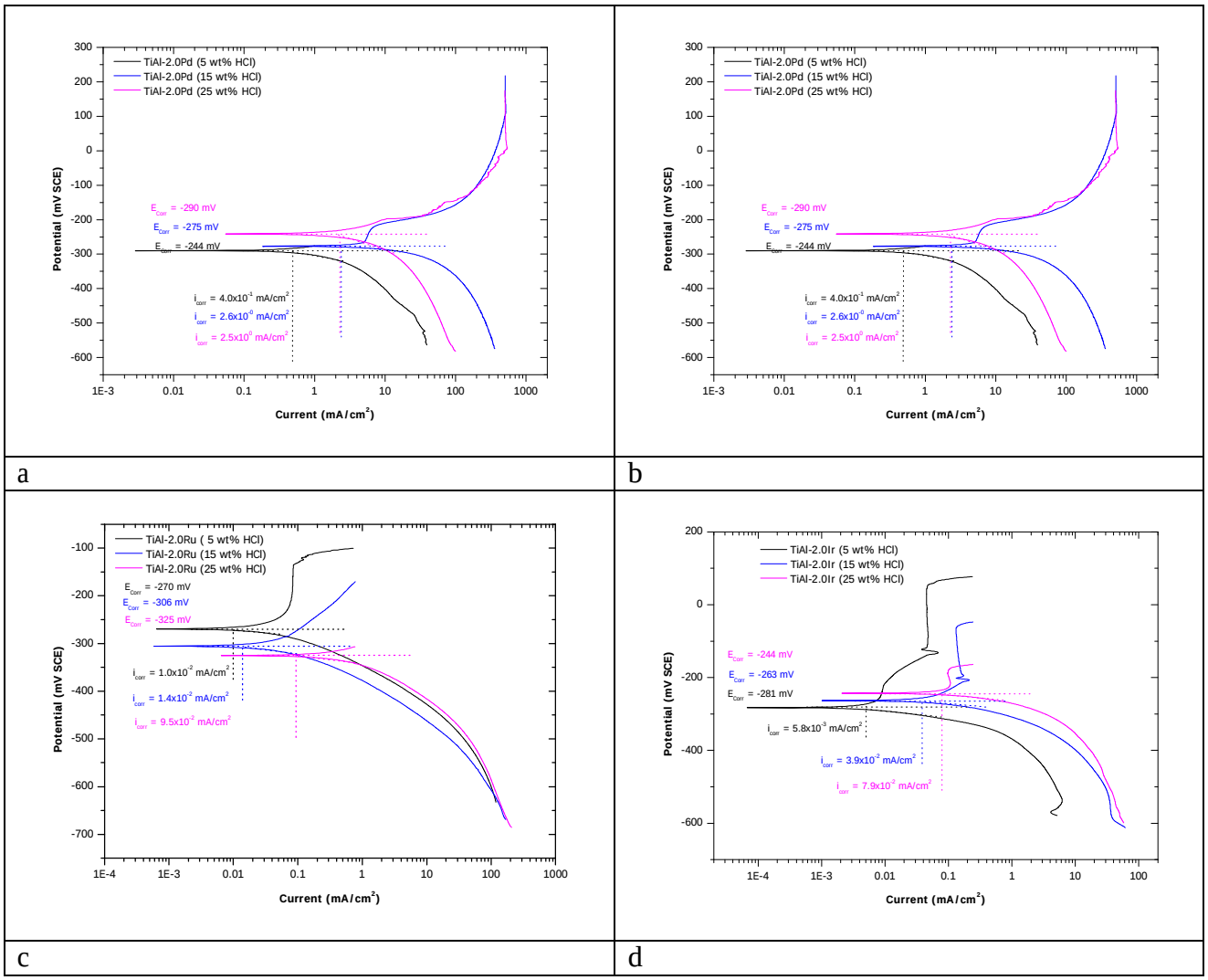


Figure 5.6. *Potentiodynamic scans for γ-TiAl with (a) 2.0 at.% Pd, (b) 2.0 at.%Pt, (c) 2.0 at.% Ru and (d) 2.0 at.% Ir in HCl solutions of different concentrations.*

Table 5.6*. Corrosion potentials and their increases with PGM additions.*

γ-TiAl-0.2 at.% PGM	**Corrosion potentials (mV)**			**Potential increase (mV)**		
	E_5	**E_{15}**	**E_{25}**	**ΔE_5**	**ΔE_{15}**	**ΔE_{25}**
Plain γ-TiAl	-605	-556	-462	0	0	0
γ-TiAl-0.2 at% Pd	-318	-288	-	287	268	
γ-TiAl-0.2 at% Ru	-370	-370	-344	235	186	118
γ-TiAl-0.2 at% Pt	-275	-252	-230	330	304	232
γ-TiAl-0.2 at% Ir	-274	-254	-244	331	302	218
γ-TiAl-1.0 at.% PGM	**Corrosion potentials (mV)**			**Potential increase (mV)**		
	E_5	**E_{15}**	**E_{25}**	**ΔE_5**	**ΔE_{15}**	**ΔE_{25}**
Plain γ-TiAl	-605	-556	-462	0	0	0
γ-TiAl-1.0 at% Pd	-226	-268	-268	379	288	194
γ-TiAl-1.0 at% Ru	-270	-238	-223	335	318	239
γ-TiAl-1.0 at% Pt	-260	-234	-254	345	322	208
γ-TiAl-1.0 at% Ir	-282	-275	-232	323	281	230
γ-TiAl-1.5 at.% PGM	**Corrosion potentials (mV)**			**Potential increase (mV)**		
	E_5	**E_{15}**	**E_{25}**	**ΔE_5**	**ΔE_{15}**	**ΔE_{25}**
Plain γ-TiAl	-605	-556	-462	0	0	0
γ-TiAl-1.5 at% Pd	-261	-226	-189	344	330	273
γ-TiAl-1.5 at% Ru	-245	-297	-310	360	259	152
γ-TiAl-1.5 at% Pt	-312	-267	-238	293	289	224
γ-TiAl-1.5 at% Ir	-296	-264	-237	309	292	225
γ-TiAl-2.0 at.% PGM	**Corrosion potentials (mV)**			**Potential increase (mV)**		
	E_5	**E_{15}**	**E_{25}**	**ΔE_5**	**ΔE_{15}**	**ΔE_{25}**
Plain γ-TiAl	-605	-556	-462	0	0	0
γ-TiAl-2.0 at% Pd	-274	-242	-	331	314	
γ-TiAl-2.0 at% Ru	-270	-306	-325	335	250	137
γ-TiAl-2.0 at% Pt	-271	-235	-291	334	321	171
γ-TiAl-2.0 at% Ir	-281	-263	-244	324	293	218

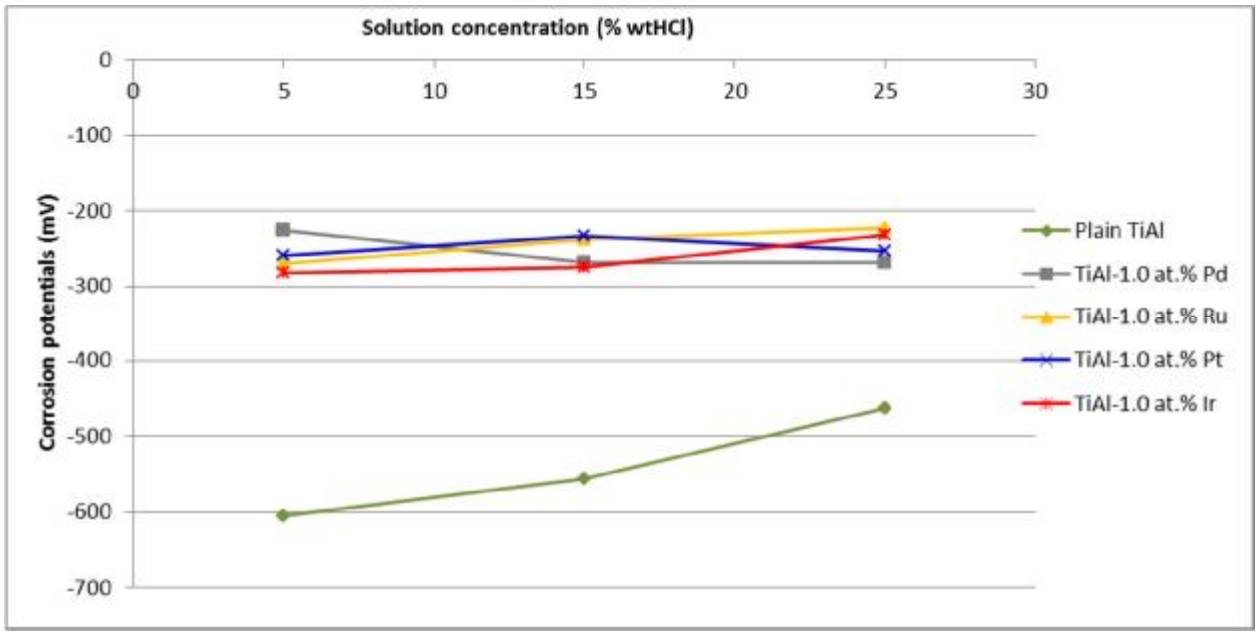


Figure 5.7. *Variation of corrosion potentials with HCl solution concentration in γ-TiAl with 1.0 at.% PGMs.*

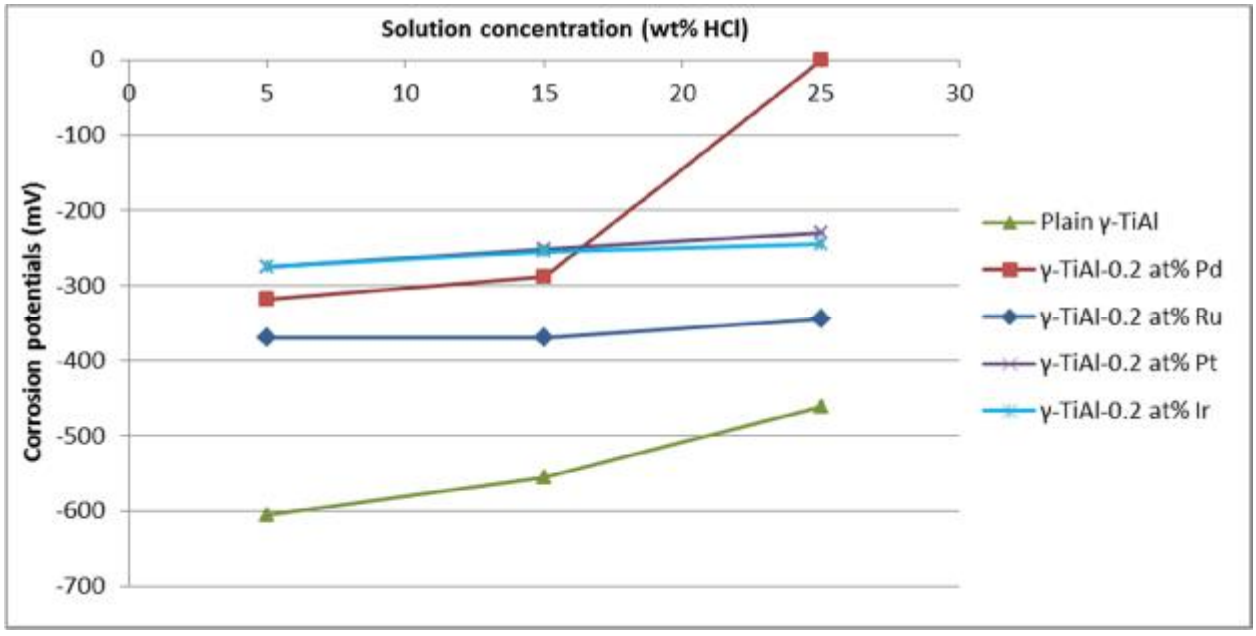


Figure 5.8. *Variation of corrosion potentials with HCl solution concentration in γ-TiAl with 0.2 at.% PGMs.*

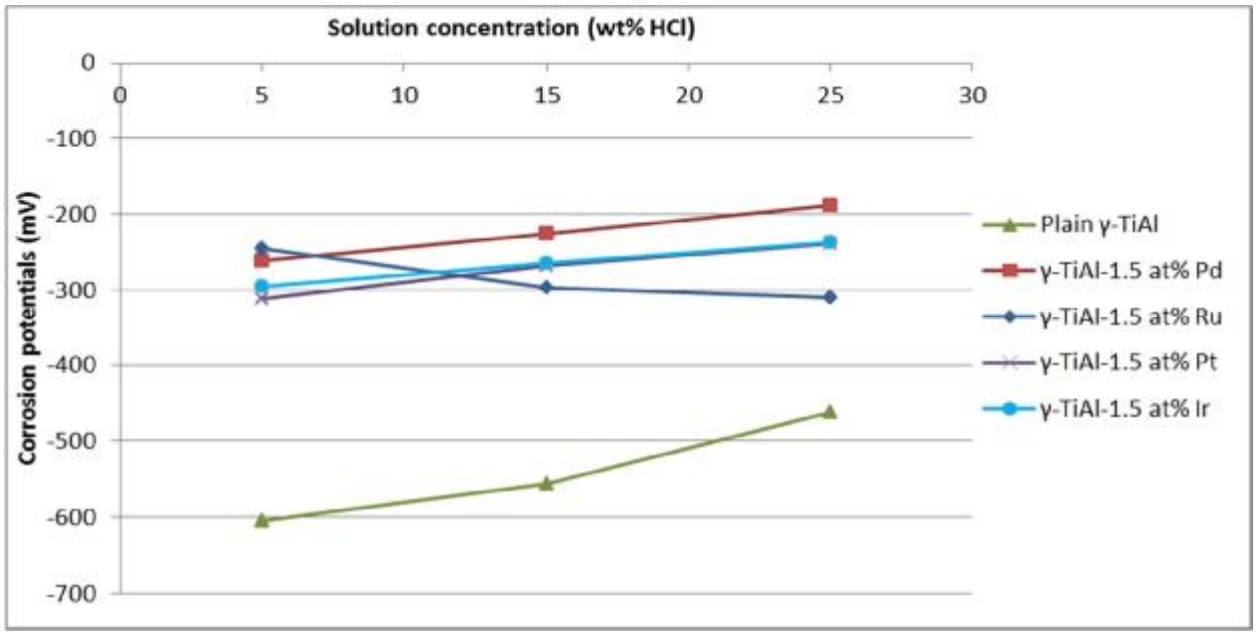


Figure 5.9. *Variation of corrosion potentials with HCl solution concentration in γ-TiAl with 1.5 at.% PGMs.*

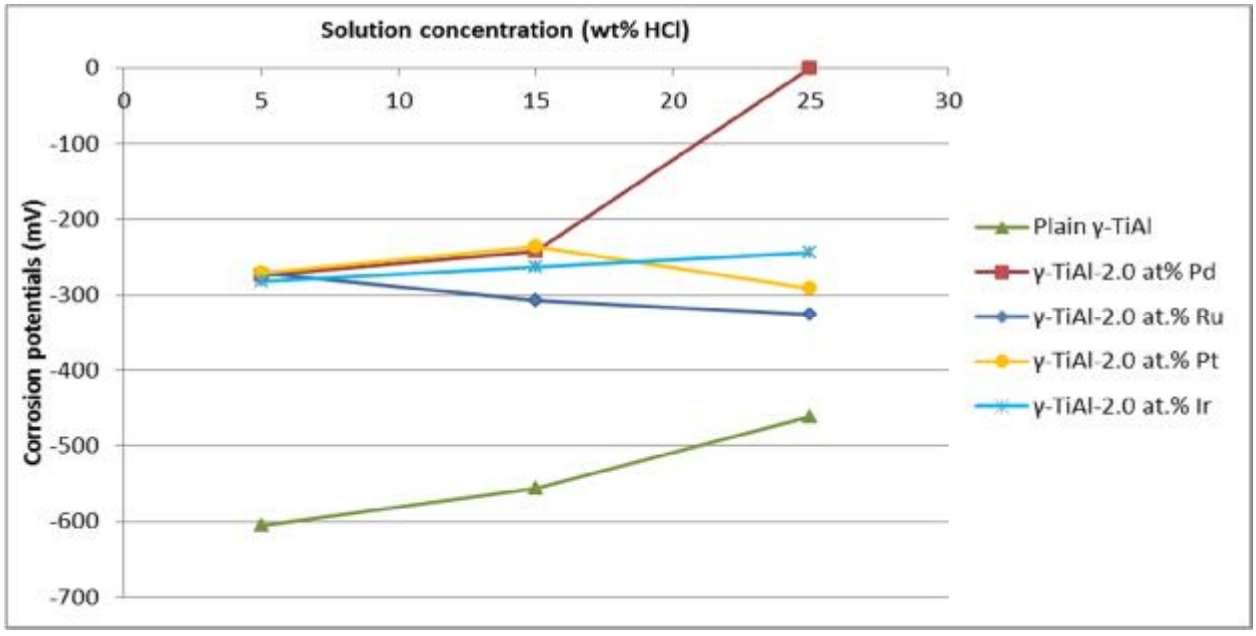


Figure 5.10. *Variation of corrosion potentials with HCl solution concentration in γ-TiAl with 2.0 at.% PGMs.*

5.2.3 Attempted prediction of the effect of continuous PGM increases on the corrosion potential

An attempt was made to predict the effect of a continuous increase of PGM on the corrosion potential of γ-TiAl and is shown in Figures 5.11 - 5.14 for γ-TiAl with 0.2-2.0 at.% PGM additions in HCl solutions of different concentrations. By joining the different points on a PGM content-corrosion potential plot with straight lines, the trend was an increase in corrosion potential between 0.2 and 1.0 at.% PGMs, followed by a decrease between 1.0 and 1.5 at.% PGMs. This decrease was then followed by either a continuous decrease or a new increase of the potential as the PGM content continued to increase. To evaluate how the corrosion potential could evolve between 0.2 and 1.0 at.% PGMs, or between 1.0 at.% PGM and 1.5 at.% PGMs, Excel linear and polynomial approximations were conducted and the regression coefficient of determination (R) was assessed. It appeared that the corrosion potential as a function of the PGMs followed a polynomial trend of an order 3 (R^2=1) or higher as shown in Table 5.7 and Figures 5.11 - 5.14. However, these curves are very speculative, because only four points were used for each relationship, so these results can only give a rough comparison Given that the corrosion potentials of all PGMs in the pure state are well above 0 in acid media (Savitsky *et al*., 1978), it could be anticipated that the curve trend in the E-PM content system could only be ascending with increasing PGM content and potential minimum values as the PGM contain increased. A perfect fit (R^2=1) is expected with four points. However, it should be noted that more data could have given results closer to the real corrosion behaviour of γ-TiAl alloys as the amount of added PGMs is progressively increased.

***Table 5.7**. Determination of coefficients (R^2) for the corrosion potential variation with PGM content.*

γ-TiAl with 0.2 - 2.0 at.% platinum additions				
Concentration (wt% HCl)	**Coefficient of determination R²**			
	Linear	Logarithmic	Polynomial order 2	Polynomial order 3
5	0.135	0.060	0.417	1
15	0.028	0.029	0.048	1
25	0.027	0.126	0.685	1
γ-TiAl with 0.2 - 2.0 at.% ruthenium additions				
Concentration (wt% HCl)	**Coefficient of determination R²**			
	Linear	Logarithmic	Polynomial order 2	Polynomial order 3
5	-13.01	0.639	0.975	1
15	0.460	0.621	0.698	1
25	0.002	0.093	0.678	1
γ-TiAl with 0.2 - 2.0 at.% iridium additions				
Concentration (wt% HCl)	**Coefficient of determination R²**			
	Linear	Logarithmic	Polynomial order 2	Polynomial order 3
5	0.300	0.316	0.381	1
15	0.053	0.216	0.668	1
25	0.000	0.085	0.960	1
γ-TiAl with 0.2 - 2.0 at.% palladium additions				
Concentration (wt% HCl)	**Coefficient of determination R²**			
	Linear	Logarithmic	Polynomial order 2	Polynomial order 3
5	0.079	0.287	0.909	1
15	0.200	0.313	0.570	1
25	0.372	0.451	0.523	1

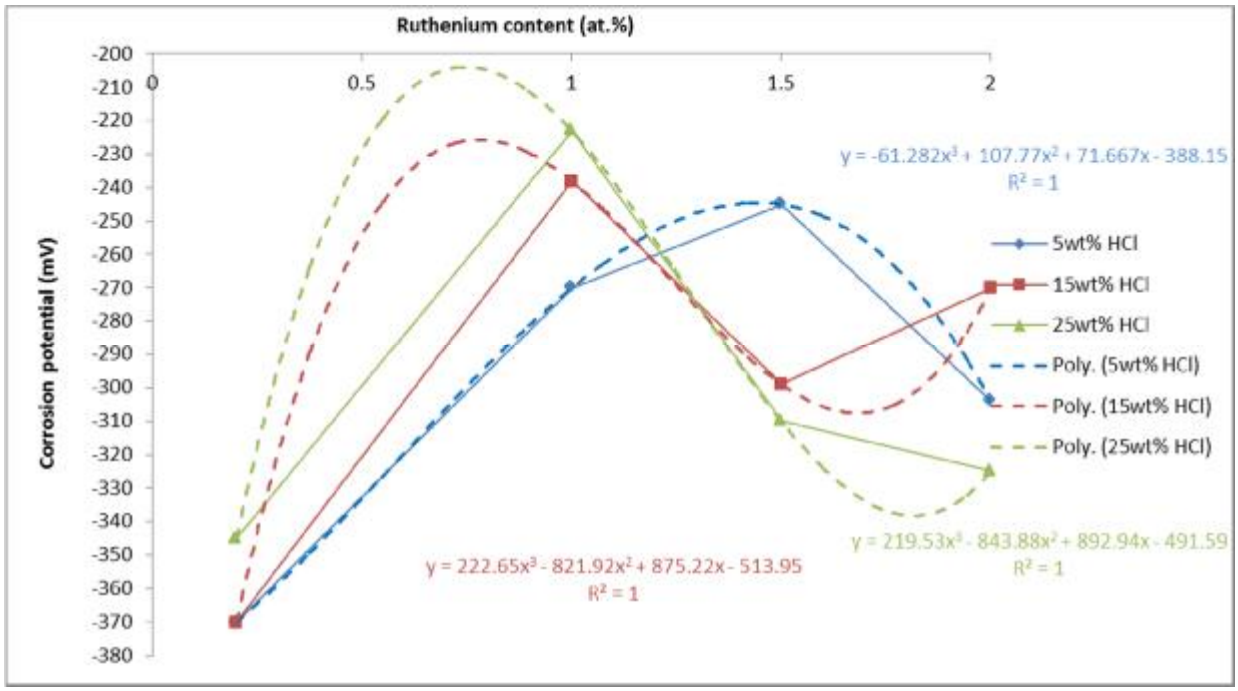


Figure 5.11. *TiAl corrosion potential evolution with different ruthenium additions.*

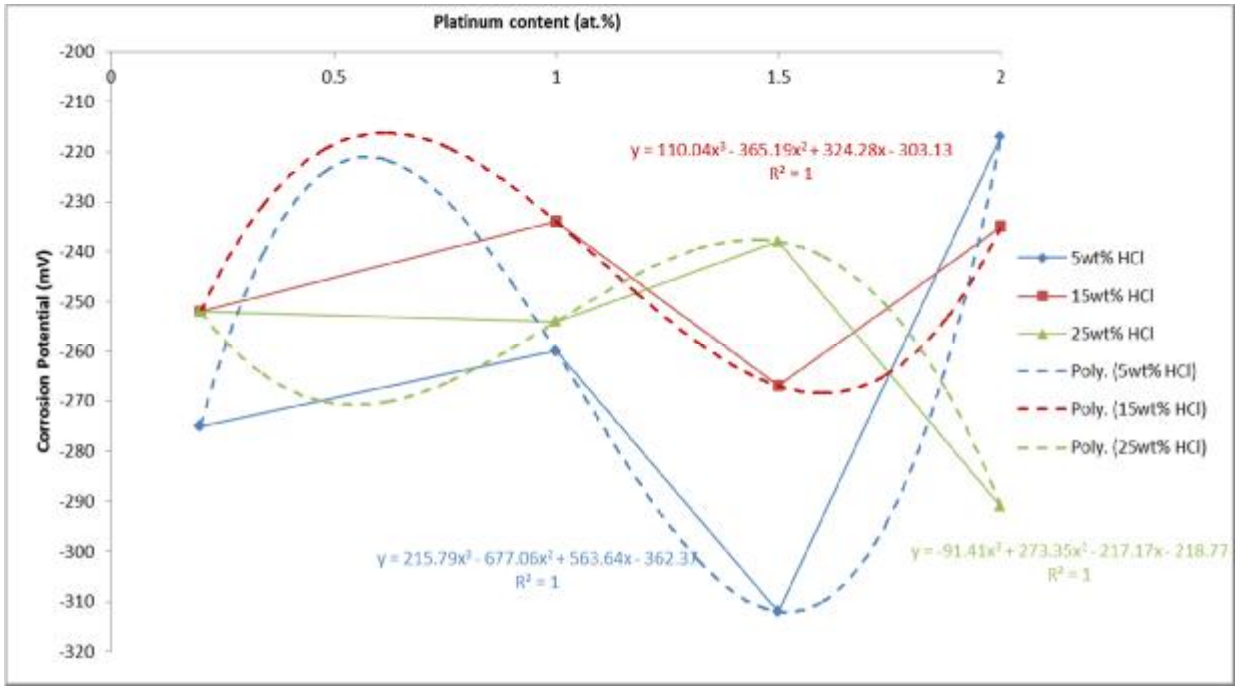


Figure 5.12. *TiAl corrosion potential evolution with different platinum additions.*

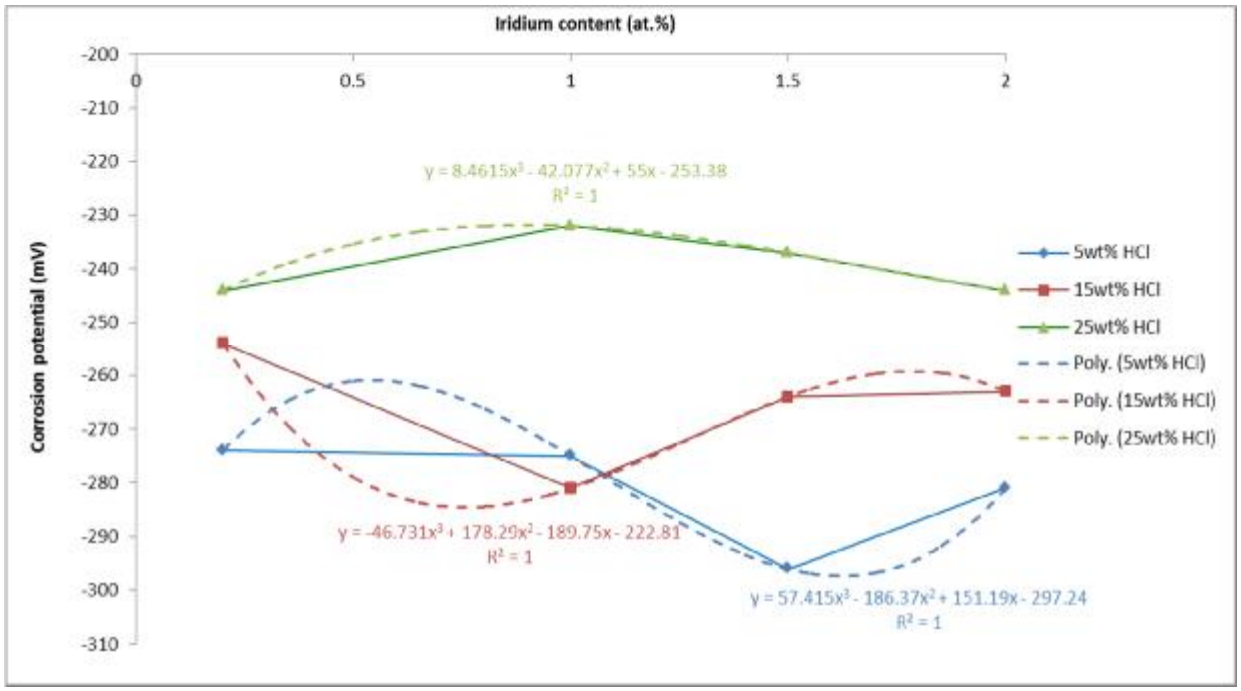


Figure 5.13. *TiAl corrosion potential evolution with different iridium additions.*

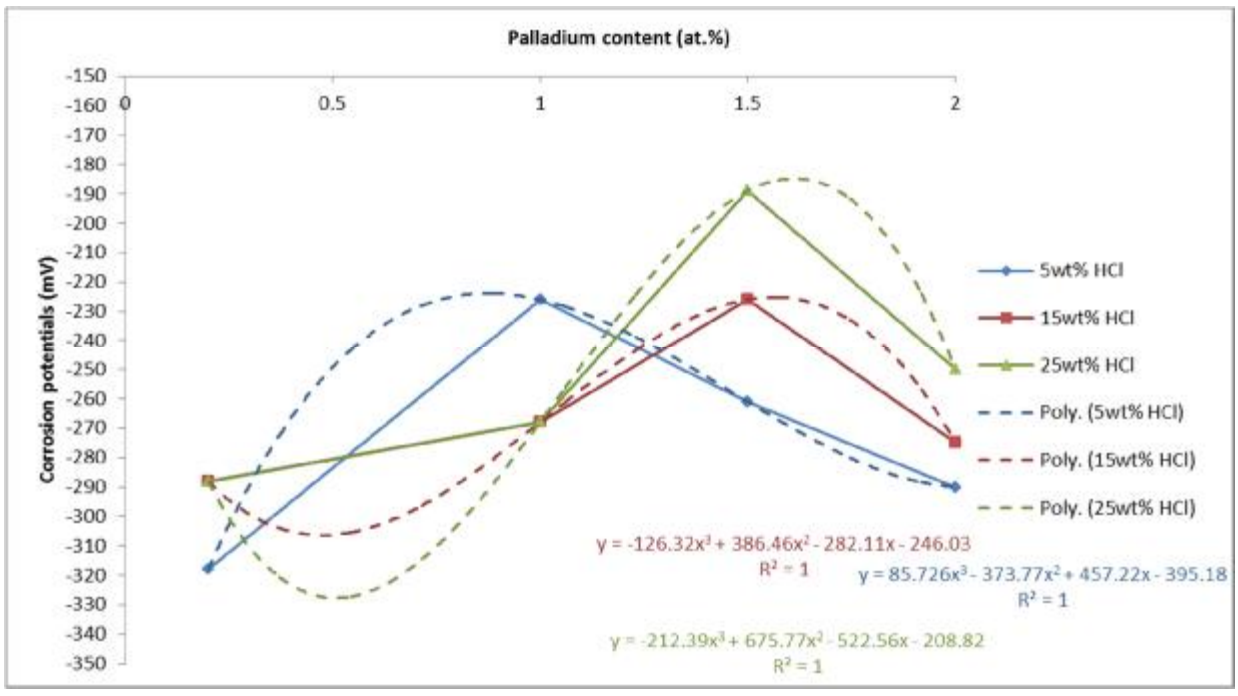


Figure 5.14. *TiAl corrosion potential evolution with different palladium additions.*

5.2.4 Corrosion rate and potential increase

From Tables 5.1 - 5.5, comparative corrosion rate histograms were drawn, and Figure 5.15 shows that in all solution concentrations, γ-TiAl alloys with additions of palladium, platinum and iridium had low corrosion rates, indicative of good corrosion resistance. The corrosion rate of γ-TiAl alloyed with ruthenium was higher than that for plain γ-TiAl, even though the addition of ruthenium to γ-TiAl, like other platinum group metals, shifted the corrosion potential to nobler values. This observation is strange, since it does not support ruthenium also promoting the cathodic modification. However, previous work (van der Lingen and Sandenbergh, 2001) also showed that ruthenium additions tended to shift the potentiodynamic curve towards high current density, resulting in high corrosion rates.

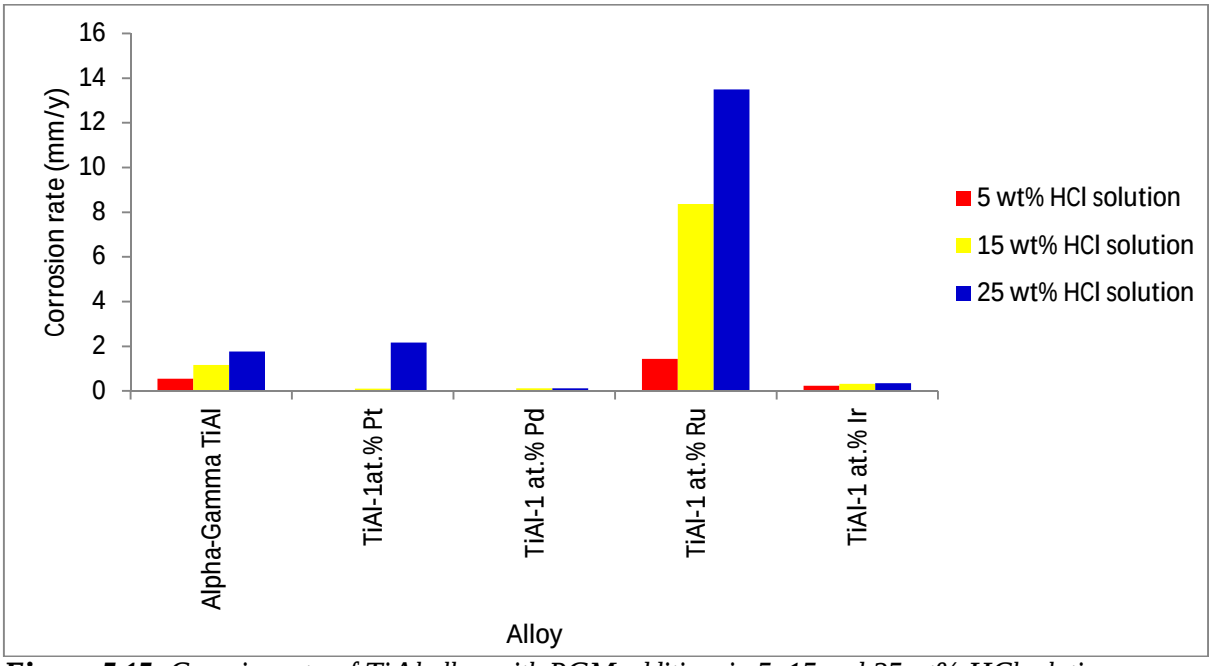


Figure 5.15. *Corrosion rates of TiAl alloys with PGM additions in 5, 15 and 25 wt% HCl solutions.*

5.2.5 Cathodic modification

Cathodic modification involves the passivation of a metal in a reducing acid in order to change the kinetics of the hydrogen evolution reaction by alloying the metal with a noble metal which has a higher exchange current density than the metal being passivated. The introduction of PGMs to the plain γ-TiAl resulted in a general improvement of corrosion resistance by shifting the corrosion

potentials to nobler values. However, the cathodic modification is achieved only (Potgieter *et al*., 1990):

1. When the plain γ-TiAl has a small critical current density (i_{crit}) which will be easily exceeded by the current of the hydrogen cathodic reaction on γ-TiAl with PGM addition at the given passivation potential (E_{pass}) (Figure 2.9).
2. If the passivation potential (E_{pass}) of plain γ-TiAl is sufficiently negative to allow the introduced cathodic component to change the corrosion potential (E_{corr}) of the γ-TiAl with PGMs to a value in the passive range that is more positive than E_{pass}, but less positive than the potential associated with the onset of transpassive processes (E_{trans}).
3. When the transpassive potential (E_{trans}) of plain γ-TiAl is sufficiently electropositive to allow a wide passivation region.

Table 5.8 shows the passivation regions obtained for the plain γ-TiAl scans in the three solutions. These regions decreased with increasing solution concentration and completely disappeared in 25 wt% HCl solution. Whether the cathodic process of the γ-TiAl alloyed with PGMs fell in the active, passive or transpassive region of the plain TiAl was verified by comparing the curves of PGM-alloyed γ-TiAl to the plain γ-TiAl scans. Figure 5.16 shows the potentiodynamic scans of γ-TiAl alloyed with PGMs superposed on the potentiodynamic scan of plain γ-TiAl in 5 wt% HCl. All the corrosion potentials of γ-TiAl alloyed with PGMs were in the passive region, suggesting that TiAl alloyed with PGMs would spontaneously passivate in the 5 wt% HCl solution, due to cathodic modification. A similar trend was observed in the 15 wt% HCl solution (Figure 5.17). However, in the 25 wt% HCl solution, the corrosion potentials of γ-TiAl alloyed with PGMs did not intersect the plain γ-TiAl curve in the passive region (Figure 5.18). While the cathodic process of γ-TiAl alloyed with platinum and iridium intersected the plain γ-TiAl curve in the transpassive region, the cathodic process of γ-TiAl alloyed with palladium intersected the plain γ-TiAl curve in the active region. In either case, this resulted in alloy dissolution. This behaviour in the 25 wt% HCl solution suggested that it would be very difficult to improve corrosion resistance of γ-TiAl alloys by cathodic modification, due to the fact that the passive region did not exist at all on the potentiodynamic scan of the plain γ-TiAl immersed in 25 wt% HCl solution (Table 5.8). These results showed that PGM-alloyed γ-TiAl could passivate spontaneously in 5 and 15 wt% HCl solutions, whereas corrosion

would take place in 25 wt% HCl. This was because a very large increase in corrosion potential (Table 5.6) resulted in the cathodic reaction of PGM-alloyed γ-TiAl intersecting the anodic reaction in the transpassive region of the plain γ-TiAl, and an increase in current density occurred. This gave higher corrosion rates in PGM-alloyed γ-TiAl than plain γ-TiAl, although the corrosion potential values were nobler, as was the case for TiAl-1.0 at.% Ru, TiAl-1.5 at.% Pt and TiAl-1.0 at.% Ir in 25 wt% HCl solutions. It is worth noting that if spontaneous passivation occurred in TiAl-1.0 at.% PGM in 5 and 15 wt% HCl solution, unstable behaviour (passivation or dissolution) was observed with TiAl-0.2 at.% PGM, TiAl-1.5 at.% PGM and TiAl-2.0 at.% PGM in 15 wt% HCl solutions, indicating a passive-active behaviour. Other similar potentiodynamic curves are shown in Figures 5.19 to 5.21.

Table 5.8*. Characteristic values of potentials and current density for plain TiAl.*

Characteristic values of potentials	**Solution concentration (wt% HCl)**		
	5	**15**	**25**
E_{pa} (mV)	-296	-251	-378
E_{pit} (mV)	-48	-138	-281
Passivation region	From -296 to -48	From -251 to -138	~0

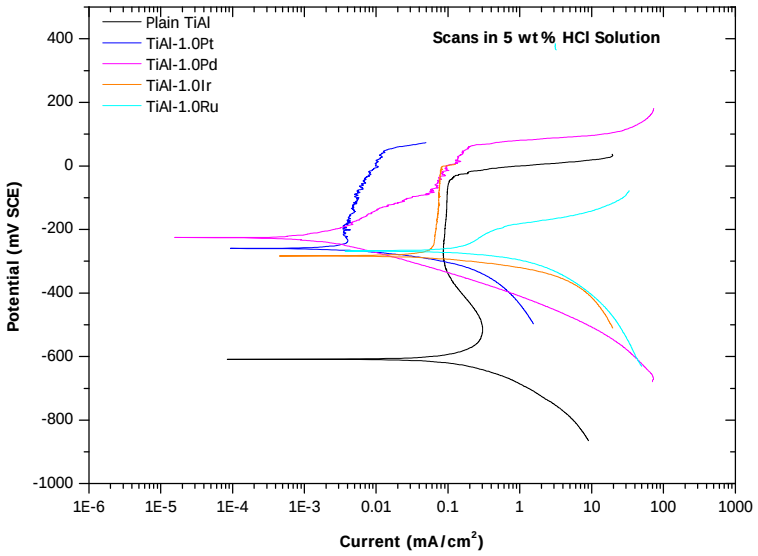


Figure 5.16. *Effect of PGM additions on the polarisation scans of TiAl-1.0 at.% PGM in 5 wt% HCl solution.*

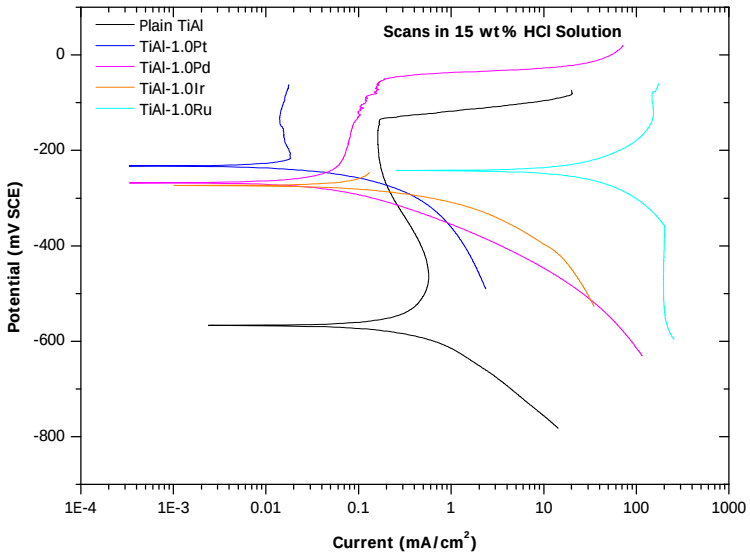


Figure 5.17. *Effect of PGM additions on the polarisation scans of TiAl-1.0 at.% PGM in 15 wt% HCl solution.*

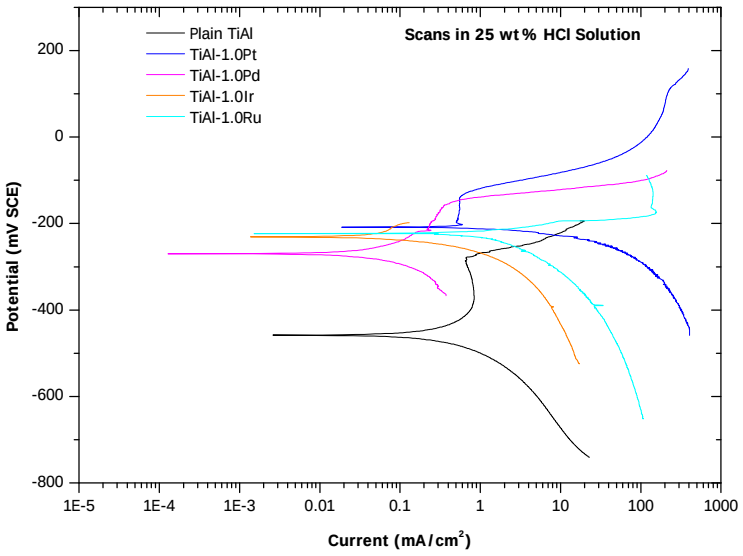


Figure 5.18. *Effect of PGM metal additions on the polarisation scans of TiAl-1.0 at.% PGM in 25 wt% HCl solution.*

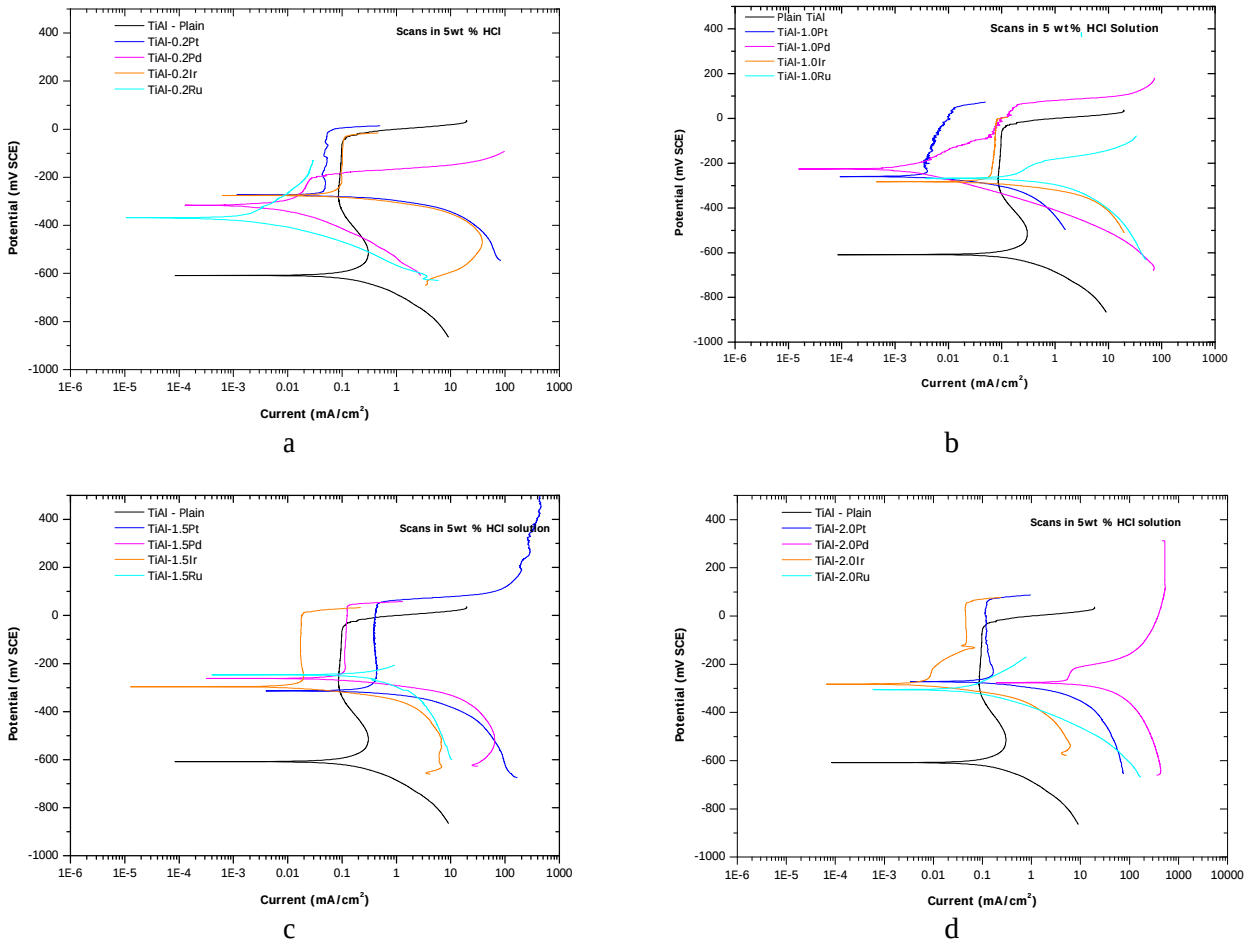


Figure 5.19. *Effect of PGM additions on the polarisation scans in 5 wt% HCl solution.*

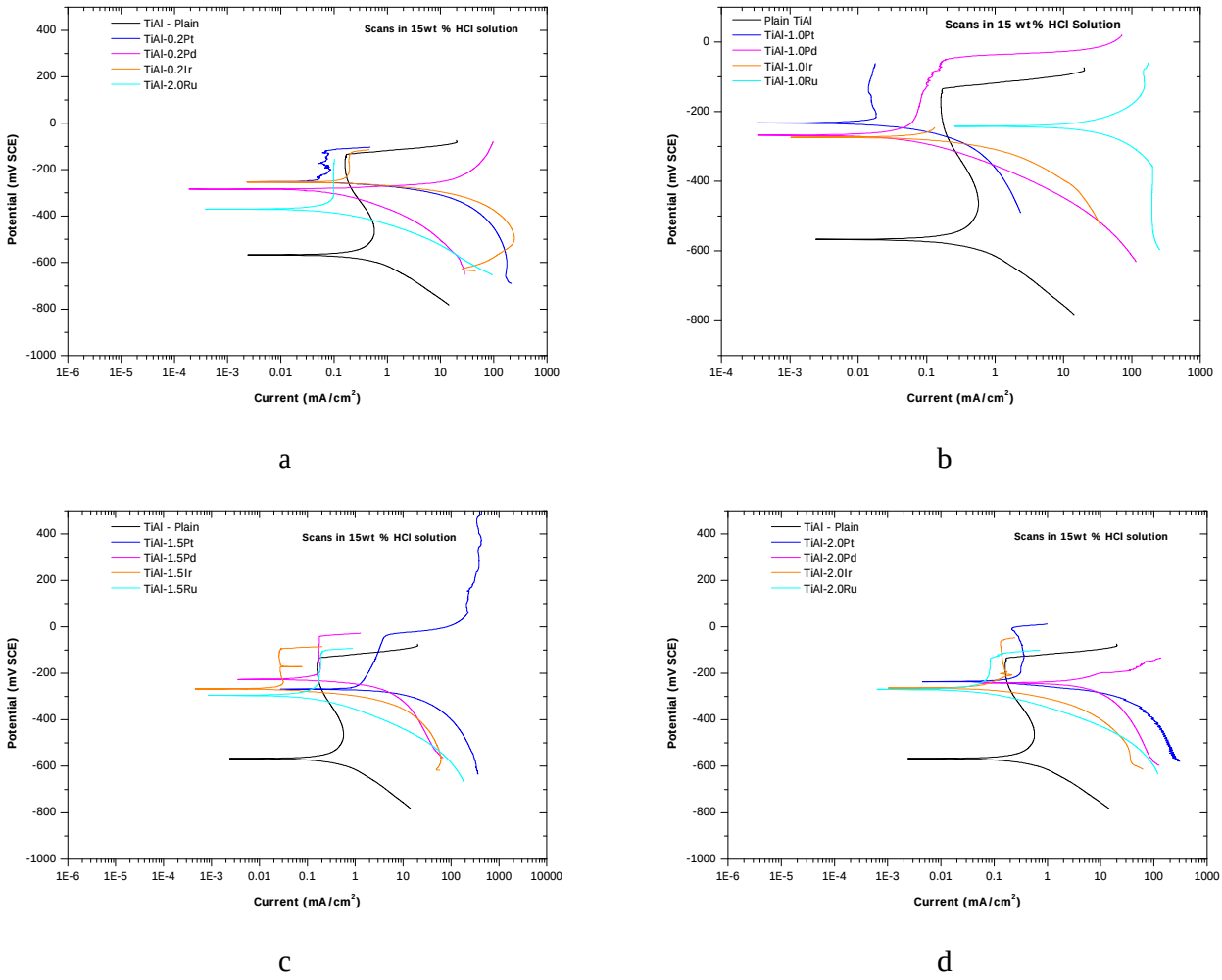


Figure 5.20. *Effect of PGM additions on the polarisation scans in 15 wt% HCl solution.*

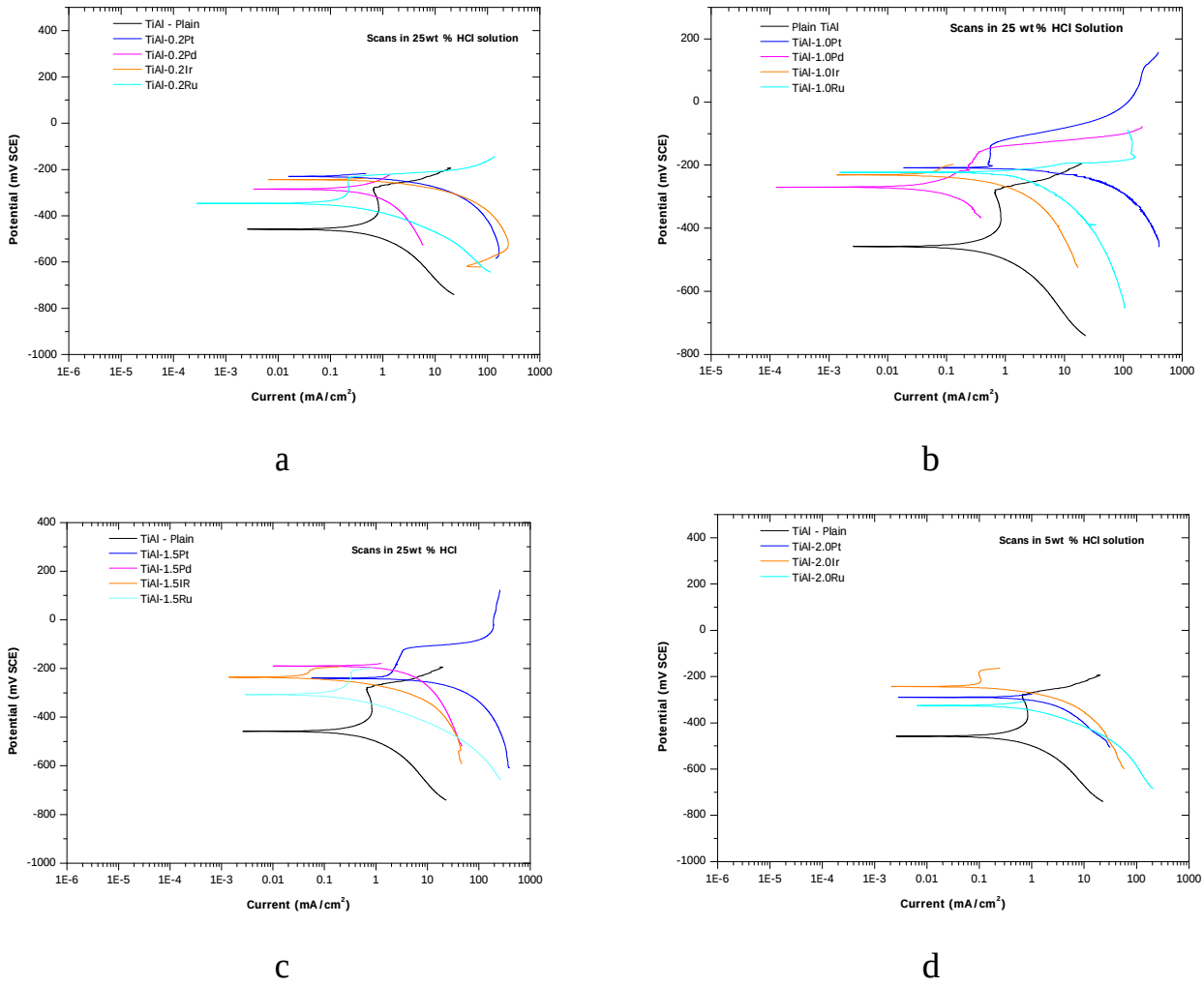


Figure 5.21. *Effect of PGM additions on the polarisation scans in 25 wt% HCl solution.*

TiAl-0.2 at.%PGM

Gamma-TiAl with 0.2 at.% Pd or Ir showed passivation with corrosion potentials above the passivation potential of plain γ-TiAl (-296 mV) and below the pitting potential of plain γ-TiAl (-48 mV) in 5 wt% HCl solution. Even though there was a shift of corrosion potentials towards more positive values, γ-TiAl with 0.2 at.% Pt or Ru showed corrosion potentials which were below the passivation potential of the plain γ-TiAl, suggesting an active or passive-active regime. In the 15 wt% HCl solution, the passivation behaviour was the same as in the 5 wt% HCl with γ-TiAl-0.2 at.% Pd and γ-TiAl-0.2 at.% Ir with passivation by cathodic modification, whereas γ-TiAl-0.2 at.% Pt and γ-TiAl-0.2 at.% Ru showed passive-active corrosion. In 25 wt% HCl, even though the

corrosion potentials shifted to more positive values, there was no corrosion resistance improvement by cathodic modification for all four alloys, as there was no passivation region on the potentiodynamic scan of the plain γ-TiAl.

TiAl-1.5 at.% PGM

In 5 wt% HCl solution, the corrosion potentials of γ-TiAl-1.5 at.% PGM were all above the passivation potential of the plain γ-TiAl (-251 mV) and lower than its pitting potential (-138 mV), indicating passivation by cathodic modification. In 15 wt% HCl solution, only TiAl-1.5 at.% Pd had the corrosion potential between the passivation and the pitting potentials of the plain γ-TiAl, indicating passivation by cathodic modification. Alloys TiAl-1.5 at.% Pt, TiAl-1.5 at.% Ru and TiAl-1.5 at.% Ir had corrosion potentials lower than the passivation potential of plain γ-TiAl, indicating a passive-active regime with possible passivation in the passive region or dissolution in the active region. In 25 wt% HCl solution, passivation by cathodic modification was not possible, because of the absence of any passive region.

TiAl-2.0 at.% PGM

Titanium aluminides with 2.0 at.% PGM showed passivation in 5 wt% HCl solution with the corrosion potentials of all PGM-alloyed γ-TiAl being between the passivation and pitting potentials of plain TiAl, indicating passivation by cathodic modification. In the 15 wt% HCl solution, the corrosion potentials of TiAl-2.0 at.% Pt alloy was in the passivation zone, while the corrosion potentials of TiAl-2.0 at.% Ru and TiAl-2.0 at.% Ir alloys were below the passivation potentials of plain γ-TiAl, indicating the passive-active regime with instability with respect to passivation or dissolution. In the 25 wt% HCl solution, all the corrosion potentials were in the transpassive zone, resulting in the dissolution of the alloys. There were no data for the TiAl-2.0 at.% Pd as the sample was completely consumed, due to the aggressive nature of the solution, and the lack of sufficient protection.

5.2.6 Analysis of different parameters affecting the corrosion behaviour

5.2.6.1 Solution concentration and corrosion rate

From Table 5.3, corrosion rates were drawn as a function of HCl concentration, Figure 5.22. These results show that in 5 and 15 wt% HCl solutions, γ-TiAl alloys with additions of 1.0 at.% palladium, platinum or iridium had low corrosion rates, indicative of a good corrosion resistance. In 25 wt% HCl solution, the corrosion rate of γ-TiAl alloyed with platinum was higher than the corrosion rate of plain γ-TiAl, even though the platinum addition, like other PGMs, shifted the corrosion potential to nobler values. This observation supported the fact that the high increase of the corrosion potential of the Pt-alloyed γ-TiAl resulted in the cathodic process falling in the transpassive zone on the potentiodynamic curve of the plain γ-TiAl (Figure 5.17). Figure 5.22 also shows that the best performance in corrosion improvement was achieved with the palladium additions. The apparent missing data in Figure 5.22 were negligible corrosion rates. The addition of iridium also resulted in a very low corrosion rate, not significantly affected by the variation of HCl concentration in the solution. The corrosion rate of γ-TiAl alloyed with ruthenium was higher than the corrosion rate of plain γ-TiAl, even though the addition of ruthenium to γ-TiAl, like other platinum group metals, shifted the corrosion potential to nobler values.

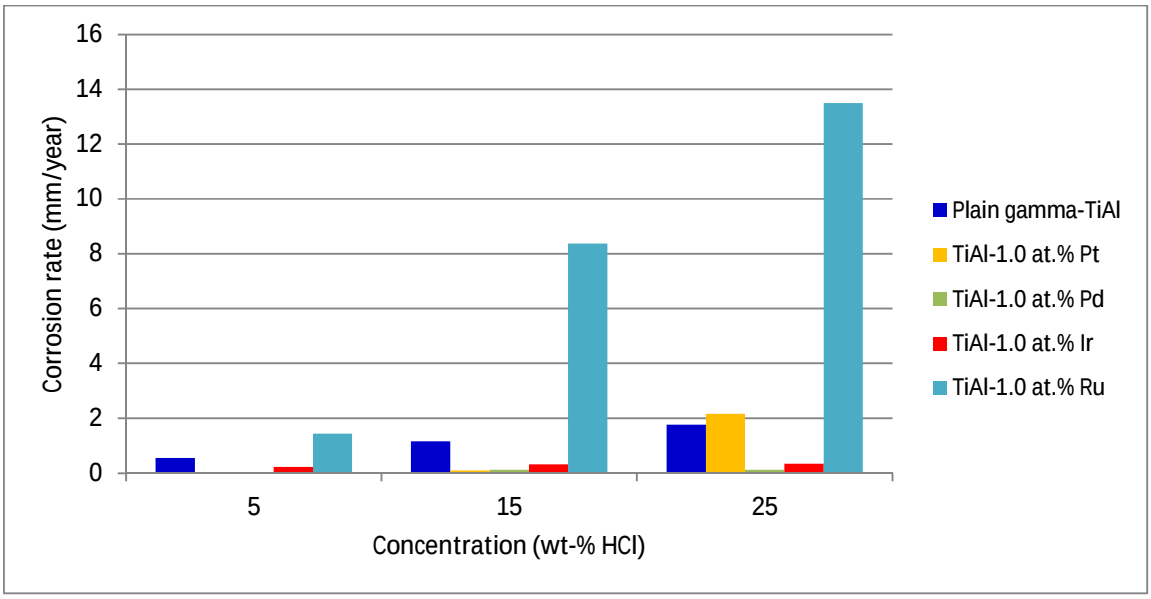


Figure 5.22*. Corrosion rates of TiAl alloys with 1.0 at.% PGM additions in 5, 15 and 25 wt% HCl solutions (Apparent missing data were negligible corrosion rates).*

Of all titanium aluminides, γ-TiAl with ruthenium showed more PGM containing phases at 0.2 at.% addition, indicating that galvanic corrosion typical of multiphase microstructure alloy would happen the most. As the Ru content was increased, more PGM containing phases appeared, although this occurred with the addition of other PGMs. The particularity of Ru is that, at 0.2 at.% addition, it was found to shift the titanium alloys to zones of high current density, a situation that promoted dissolution (van der Lingen and Sandenbergh, 2001). This was probably the case in this work, although there was much scatter, suggesting that the results were inconclusive, and ideally, there should be repeated.

5.2.6.2 Accumulation of PGMs on the surfaces of corroded TiAl alloys

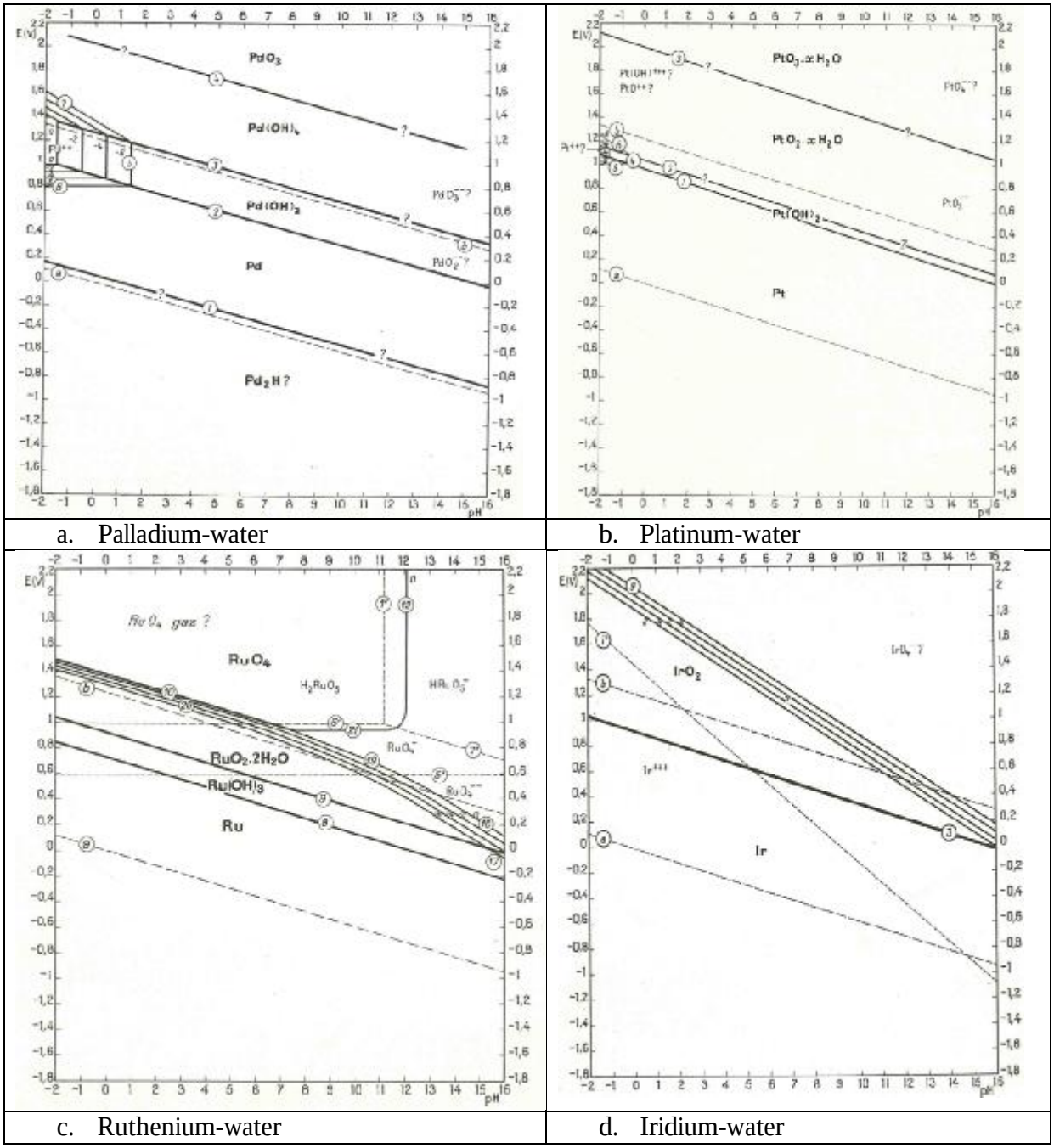
The accumulation of PGMs on the surface of TiAl can be explained by the corrosion behaviour of PGMs as presented by Pourbaix *et al.* (1963). Platinum, palladium, ruthenium and iridium are very noble metals, since in the potential-pH diagrams (Figure 5.23), their domains of stability cover most of the stability domain of water. According to their respective potential-pH diagrams, they are thermodynamically stable in the presence of aqueous solutions of any pH, with the exception of strong oxidising agents and complexing substances.

Platinum remains unaltered in the presence of water or in aqueous solutions of caustic alkalis at temperatures around 25°C (Pourbaix *et al.*, 1959 and 1963). It is not attacked by acids and is attacked only with difficulty by oxidising agents. The noncomplexing acids, sulphuric and nitric, do not attack platinum. Ferric chloride and hydrogen peroxide solutions also appear to not cause any reaction. The best known reagent for dissolving platinum, *aqua regia (*nitrohydrochloric acid), acts by means of a combination of oxidising action of nitric acid and complexing action of hydrochloric acid and dissolves platinum as H_2PtCl_6 (Pourbaix *et al.*, 1959; Freier, 1978). Hydrochloric acid, which does not attack platinum on its own, will attack when it contains chlorine in solution, because it then combines oxidising and complexing actions (Craig and Anderson, 1994).

Palladium is not attacked by water, except at high temperatures, and is not tarnished in moist air. Non-oxidising acids, acetic, hydrofluoric, oxalic and sulphuric acids are without effect at ordinary temperatures (Pourbaix *et al.*, 1963). Dilute nitric acid attacks palladium only slowly, but the metal is corroded quite rapidly by the concentrated acid. At 25°C, iridium is not attacked by water,

solutions of caustic alkalis, acids and oxidising agents including *aqua regia*. Ruthenium is less noble than the three other PGMs. Although ruthenium is not attacked by water or non-complexing acids, it is easily corroded by oxidising alkaline solutions, such as peroxides and alkaline hypochlorites.

The solutions used were 5 wt% HCl (pH = 0.11), 15 wt% HCl (pH = -0.52) and 25 wt% HCl (pH = -0.62). In these aggressive conditions, the titanium and aluminium of the matrix were expected to be dissolved, leaving behind phases of high PGM content on the surface (Figure 5.24). The EDX results indicated that the PGM contents of these particles were very high (Table 5.9), suggesting that dissolution did not affect the phase of high PGM content. The poor corrosion resistance of γ-TiAl with ruthenium agreed with Pourbaix *et al.* (1963) in that ruthenium was less noble than the other PGMs and hence more easily corroded. In terms of cathodic modification, even though the corrosion potential of Ti-47.5 at.% Al was shifted to the passive region by the ruthenium additions, the exchange current density was very high, explaining the high corrosion rate observed in TiAl-1.0 at.% Ru.



a. Palladium-water | b. Platinum-water

c. Ruthenium-water | d. Iridium-water

Figure 5.23*. Potential-pH diagrams for PGM-water system at 25°C (*Pourbaix *et al.*, 1963*).*

The shift of corrosion potentials to nobler values was attributed to the accumulation of precious metals on the surface of the γ-TiAl alloys, which simultaneously improved the hydrogen evolution efficiency and inhibited anodic dissolution (Potgieter and Brookes, 1995). To confirm this, SEM and EDX were conducted on the corroded surfaces to evaluate the PGM content after

potentiodynamic scans in 25 wt% HCl solution. The corrosion tests involved exposure of samples to 25 HCl wt% solutions for 180 minutes, 30 minutes of which were in open circuit potential. The EDX results are shown in Table 5.10 and the microstructures are shown in Figures 5.24. Overall, there was an increase of PGM contents of the surface of the different γ-TiAl alloys, from 1.0 at.%, in the as-cast alloys, to a maximum of 2.7 at.% for Ru-alloyed γ-TiAl, although the increase for Pt and Ir was negligible. The PGM contents of the surfaces of the different alloys in Table 5.10 show a clear increase, confirming that an effective accumulation of PGMs took place on the surfaces during corrosion. The HCl corroded away the rest of the matrix while PGM-containing phases were corroded to a lesser extent (Figure 5.24), thus exposing more of PGM-containing phases. Iridium-alloyed TiAl showed a negligible increase, which is in agreement with the moderate effect of the HCl concentration on its corrosion rate and the low number of pits observed on the corroded samples (Figure 5.24c).

Table 5.9*. EDX analyses of light particles on corroded surface of different alloys.*

Elements	**PGM content in light contrast phases of different alloys (at.%)**			
	TiAl-1.0 at.% Pt	TiAl-1.0 at.% Pd	TiAl-1.0 at.% Ir	TiAl-1.0 at.% Ru
Al	44.7	45.3	50.4	43.3
Pt	13.7	-	-	-
Pd	-	8.8	-	-
Ir	-	-	4	-
Ru	-	-	-	13
Ti	41.6	45.9	45.6	43.7
Total	100	100	100	100

Table 5.10*. EDX analyses of alloy surfaces after potentiodynamic tests in 25 wt% HCl solution.*

Alloy	**Surface composition after corrosion test (at.%)**					
	Al	Ti	Pd	Pt	Ir	Ru
TiAl-1.0 at.% Pd	52.6±1.7	45.0±1.4	2.4±0.3	-	-	-
TiAl-1.0 at.% Pt	49.9±0.1	48.9±0.1	-	1.2±0.1	-	-
TiAl-1.0 at.% Ir	50.1±0.5	48.8±0.4	-	-	1.2±0.1	-
TiAl-1.0 at.% Ru	39.3±3.6	58.0±3.1	-	-	-	2.7±0.6

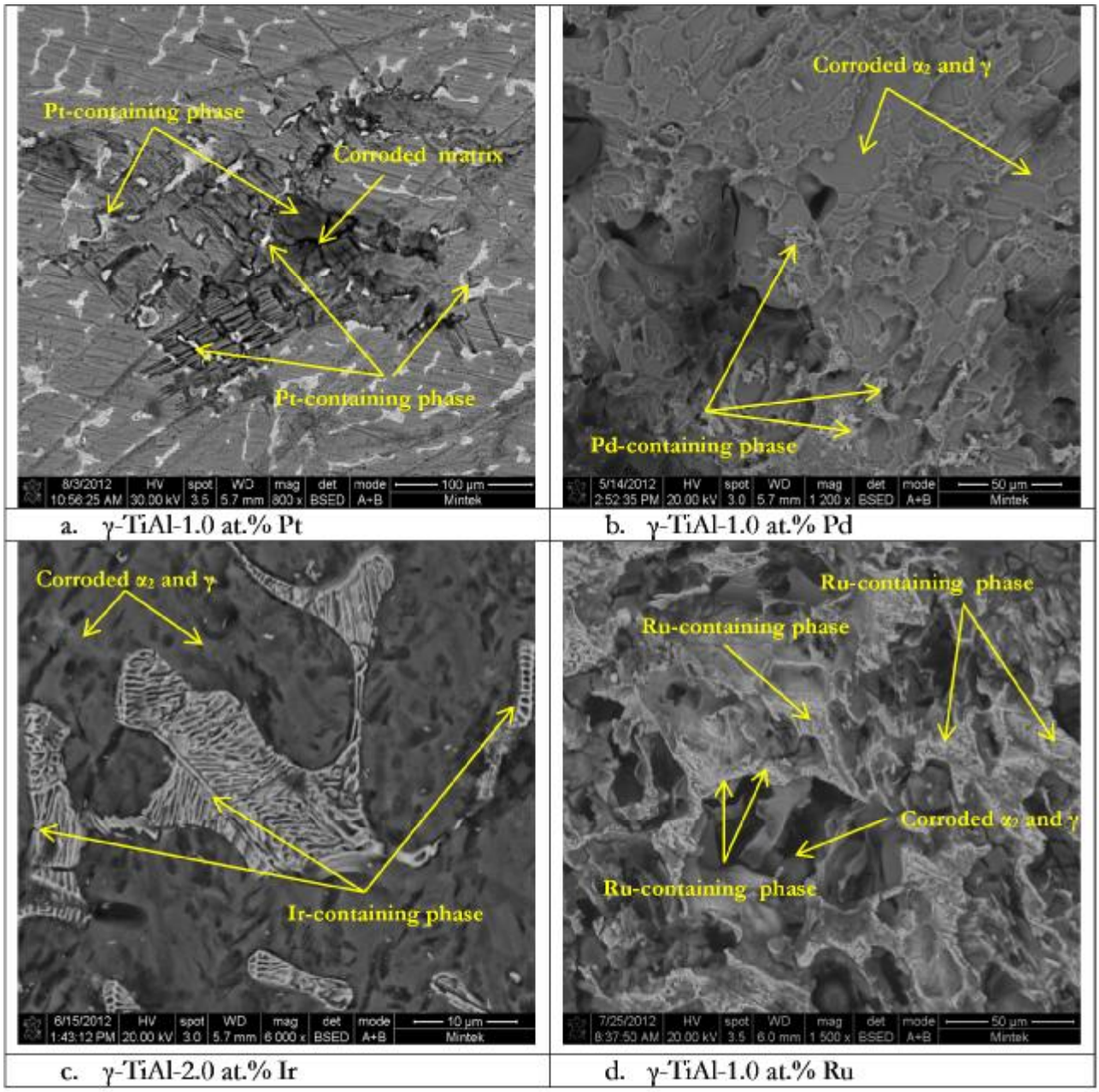


Figure 5.24*. SEM-BSE images of the corroded surface of TiAl-1.0 at.% PGM after potentiodynamic scanning in 25 wt% HCl solution showing PGM-containing phases on the surface.*

5.2.6.3 Open circuit potential measurements

Open circuit potential (OPC) tests were run for 15 hours, during which the samples were exposed to a 5 wt% HCl solution. The results of the tests are presented in Figure 5.25 and Table 5.11, where the corrosion potential (mV) is reported as a function of time in an open circuit. The general trend

was a continuous increase of the corrosion potential with time, to a value between -350 mV and -200 mV, suggesting that the samples became less active. Gamma-TiAl alloyed with palladium showed a large decrease of the corrosion potential in the first 30 minutes, indicative of an increase in activity, followed by a continuous increase up to the end of the test. This behaviour in the first minutes of the tests could explain the destruction of some of the Pd-containing samples.

Gamma-TiAl alloyed with platinum showed a very high increase in corrosion potential and was above -100 mV after 15 hours of exposure. This behaviour is in agreement with the high corrosion rate observed for this alloy during the potentiodynamic scan in 25 wt% HCl. An exposure to a less aggressive solution for a long time could give the same results as for a more aggressive solution for a short period of time. Gamma-TiAl alloyed with iridium and palladium showed small variations of the open circuit potential with time, indicating that these additions promoted long term stability in the solution. This observation is consistent with the low variations in corrosion rate observed in these alloys (Figure. 5.22). The shift of open circuit potential towards nobler or less active potentials before stabilising is usually attributed to the progressive formation of a passive oxide film on the sample surface during immersion (Zhao and Jerkiewicz, 2006). Stabilisation at active potentials is due to the breakdown of the passive film as dissolution takes place. The samples did not exhibit potential stabilisation, but rather a continuous increase in potential, which seemed to be due to the PGM accumulation on the surface, as was the case for γ-TiAl alloyed with Pd and Ru. However, the surface increase of Ir and Pt was negligible.

5.2.6.4 Effect of PGM content on the corrosion potential

The effect of PGM content on the corrosion potential was evaluated by plotting the corrosion potential as a function of the PGM content in 5, 15 and 25 HCl solutions. While it was established that the addition of PGM introduced a shift of the corrosion potentials toward more positive values (Figure 5.7), Figures 5.27 to 5.30 show that regardless of the solutions, the corrosion potentials remained within 200-300 mV range, indicating that there was no benefit in adding more PGM to the γ-TiAl, as the potential increase achieved with 2.0 at.% PGM additions could well be achieved with 0.2 at.% PGM additions. This behaviour was more noticeable in γ-TiAl with iridium additions. These figures also show that higher jumps occurred with increased PGM additions, but remained more or less in the 200-300 mV range, which was explained by the accumulation of PGM on the

surface. The higher the PGM content in the γ-TiAl alloy, the higher was the amount of the PGMs found on the surface of the alloy. It should be noted that at 2.0 at.% Pd, there was complete destruction of the sample, leading to the absence of data in Figure 5.27.

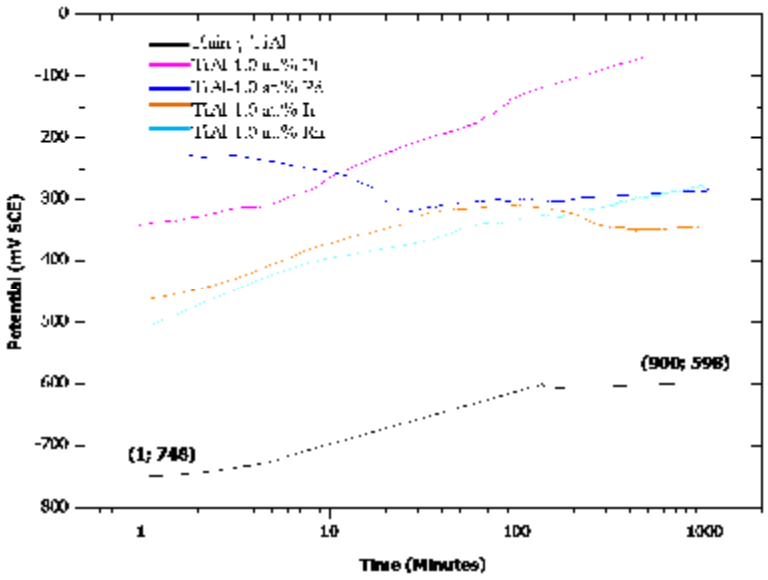


Figure 5.25*. Open circuit potential curves for Ti-47.5 at.% Al alloyed with various PGMs tested in 5 wt% HCl.*

Table 5.11*. Start and finish open circuit potentials.*

Alloy	**Potential [mV (SCE)]**		**Potential variation [mV (SCE)]**
	Start (1 min.)	**Finish (900 min.)**	
Plain TiAl	-748	-598	150
TiAl-1.0 at.% Pt	-341	-70	271
TiAl-1.0 at.% Pd	-214	-286	-72
TiAl-1.0 at.% Ru	-510	-285	225
TiAl-1.0 at.% Ir	-466	-340	126

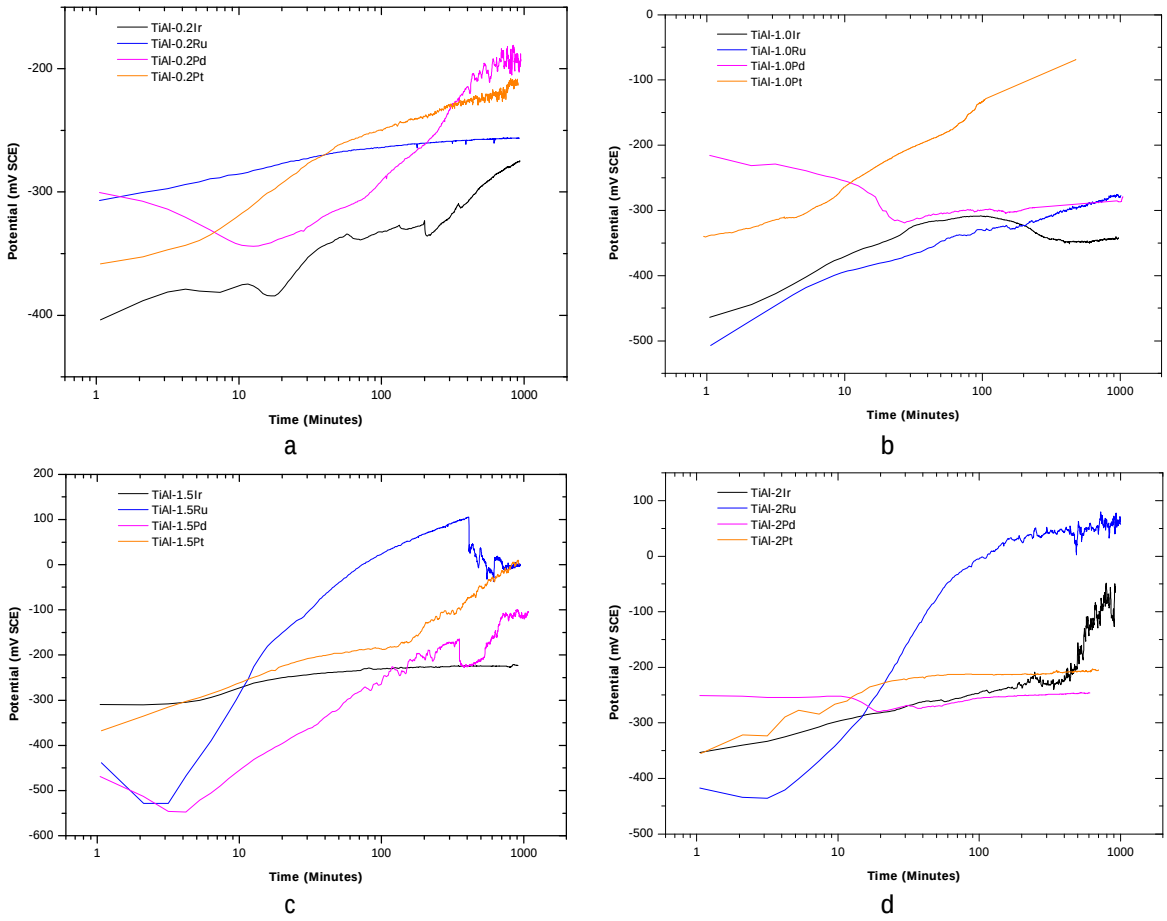


Figure 5.26*. Open circuit potential curves for Ti-47.5 at.% Al alloyed with various PGM additions tested in 5 wt% HCl.*

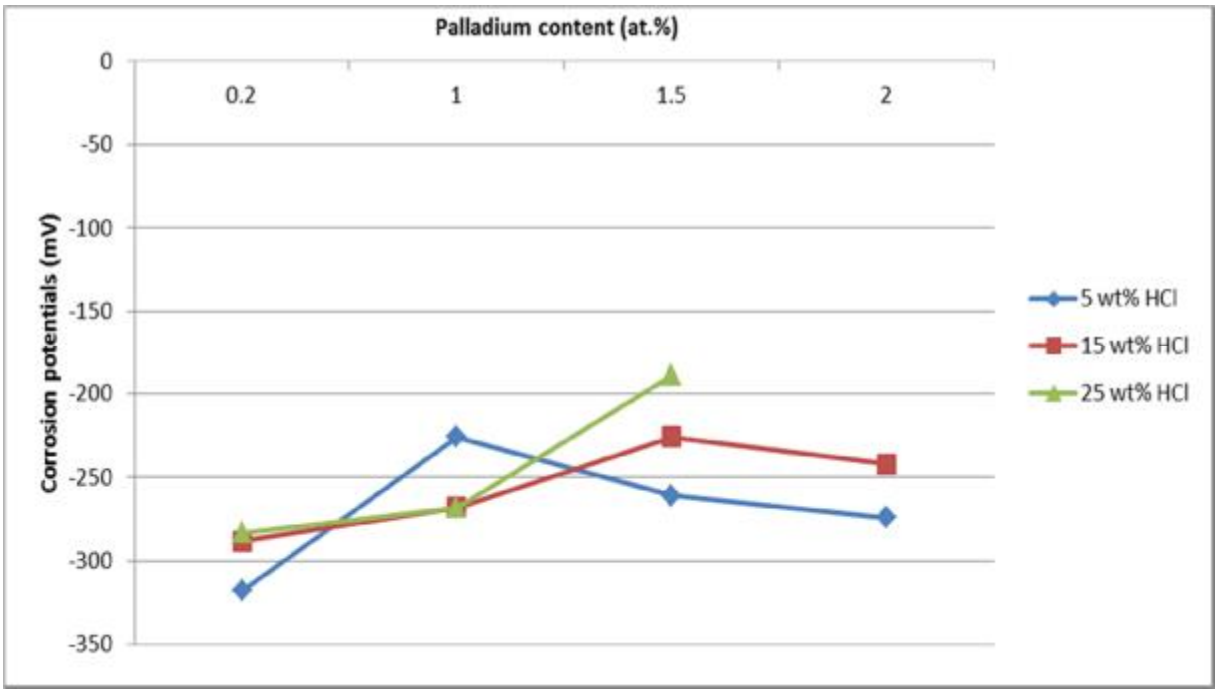


Figure 5.27. *Variation of corrosion potentials with Pd additions in 5, 15 and 25 wt% HCl solutions, where the γ-TiAl with 2.0 at.%Pd in 25 wt% HCl was totally destroyed.*

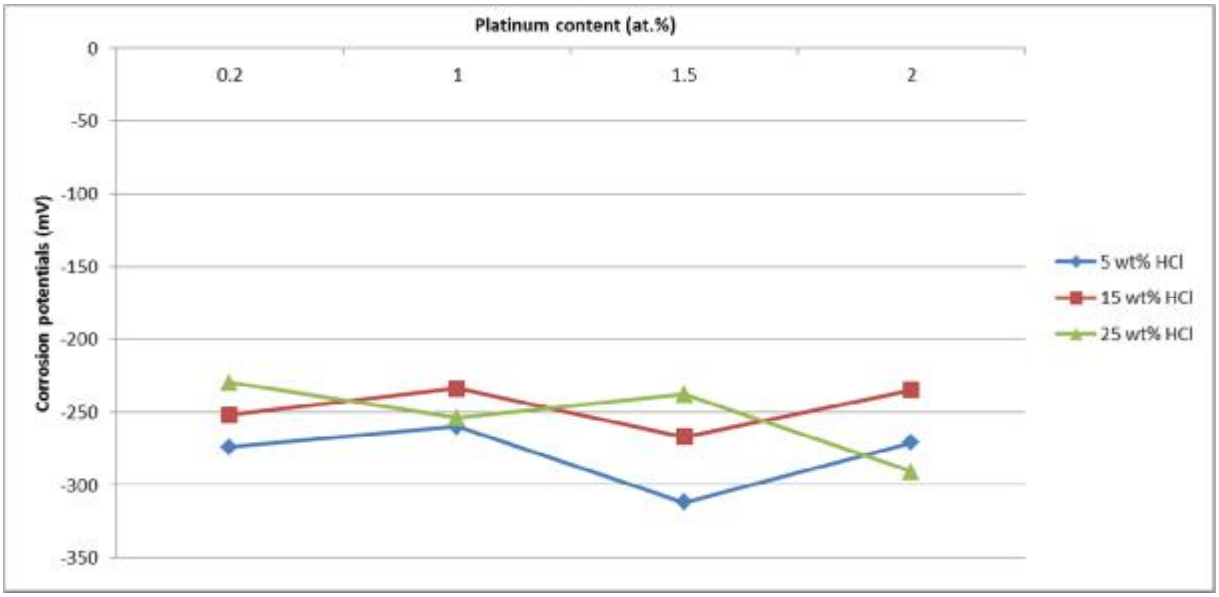


Figure 5.28. *Variation of corrosion potentials with Pt additions in 5, 15 and 25 wt% HCl solutions.*

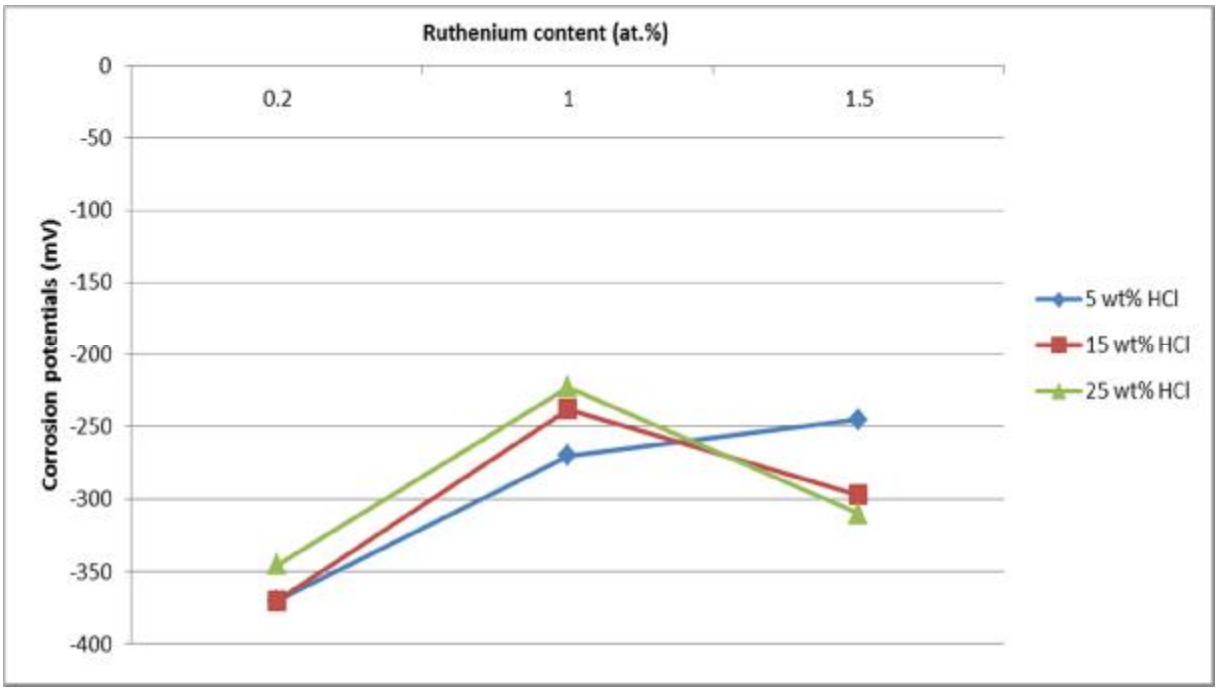


Figure 5.29. *Variation of corrosion potentials with Ru additions in 5, 15 and 25 wt% HCl solutions.*

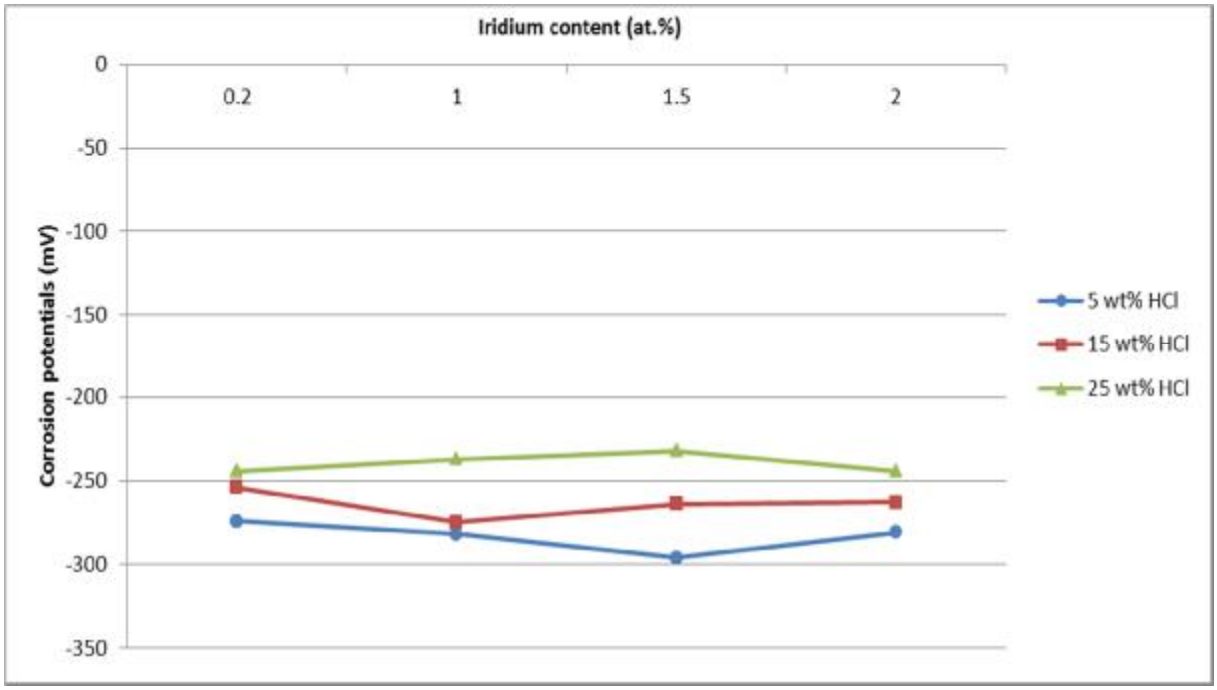


Figure 5.30. *Variation of corrosion potentials with Ir additions in 5, 15 and 25 wt% HCl solutions.*

5.3 Discussion

The results of the corrosion behaviour of plain TiAl alloy and TiAl alloys with PGMs showed that keeping added PGMs in solid solution was beneficial, as it improved the resistance of TiAl alloys to corrosion by cathodic modification.

Cathodic modification involves the passivation of a metal in a reducing acid in order to change the kinetics of the hydrogen evolution reaction by alloying the metal with a noble metal that has a higher exchange current density than the metal being passivated (Higginson, 1989). The observations made on γ-TiAl alloyed with PGMs indicated that alloy passivation by cathodic modification was achieved in the 5 wt% HCl solution. In this solution, the modification of the cathodic process occurred because the corrosion potentials of PGM-alloyed γ-TiAl were in the passive region, and suggested that PGM-alloyed γ-TiAl would spontaneously passivate. In 15 wt% HCl solution, the process was unstable, the corrosion potentials being either in the passive or active regions. This event corresponded to the passive-active regime and suggested that the effect of PGM addition to γ-TiAl could not be easily predicted. In the 25 wt% HCl solution, the corrosion potentials of γ-TiAl alloyed with PGMs did not intersect the plain γ-TiAl curve in the passive region, but fell either in the transpassive or the active region. In either case, this resulted in active dissolution of the alloys. This behaviour suggested that it was not possible to improve corrosion resistance of the γ-TiAl alloys by cathodic modification, due to the absence of the passive region on the potentiodynamic scan of the plain γ-TiAl. These results showed that PGM-alloyed γ-TiAl would passivate spontaneously in 5 wt% HCl solutions, and could passivate or corrode in 15 wt% HCl solutions, and alloy dissolution would surely occur in 25 wt% HCl solutions. Thus, there was a solution concentration limit beyond which the alloy passivation by cathodic modification could not be achieved.

While the Pd-alloyed γ-TiAl was protected in 5 wt% HCl solution, this alloy was completely dissolved in two cases (TiAl-0.2 at.% Pd and TiAl-2.0 at.% Pd in the 25 wt% HCl solution). There appeared to be no sediment left in the container. The complete dissolution in the 25 wt% HCl solution was promoted by the formation of soluble compounds of palladium with chlorine in very acidic and reducing solutions such as the hydrochloric acid (Pourbaix *et al.*, 1963; Williams-Jones *et al.*, 2004; Wojnicki *et al.*, 2011). This could have occurred in this work with Pd forming a soluble compound with titanium from the γ-TiAl.

The results suggested that the shift of corrosion potentials to more positive values by the addition of PGMs did not mean that passivation would necessary occur, as the existence of the passivation region depended on the nature of the alloy and the aggressiveness of the solution. The passivation zone of the plain γ-TiAl decreased with increasing acidity of the solution, completely vanishing in the 25 wt% HCl solutions. Thus, even though the addition of PGMs to γ-TiAl resulted in the corrosion potential being shifted to more positive values, this outcome would not necessarily be the passivation by cathodic modification. The corrosion potential shift could cause the corrosion potential to fall either in the active or transpassive region of unalloyed γ-TiAl, due to the shrinking of the passivation region, leading to active dissolution in both cases.

In addition to the corrosion potential, all other parameters affecting the corrosion behaviour of PGM-alloyed γ-TiAl needed to be analysed simultaneously. These parameters included the solution acidity, corrosion rate, accumulation of precious metal on the alloy surface during dissolution, open circuit potential and the PGM content of the alloys. In aqueous media, the corrosion behaviour of γ-TiAl depends on the titanium content (Saffarian *et al.*, 1996). Titanium aluminides are susceptible to pitting, and the pitting corrosion decreases with increasing aluminium content. For solutions of the same concentration, the pitting potential had the highest value for Ti_3Al, followed by TiAl, and the lowest value was found for $TiAl_3$ (Saffarian *et al.*, 1996). In this work, γ-TiAl had a fixed aluminium content, which could not be responsible for pitting potential variation. Plain γ-TiAl showed pitting potentials of -48 mV in 5 wt% HCl solution, -138 mV in 15 wt% HCl solution and -281 mV in 25 wt% HCl, showing a decreased pitting potential with increasing solution concentration. A decrease in pitting potential is detrimental to resistance to pitting corrosion, as its narrows the passivation zone and favour the occurrence of pitting corrosion and active dissolution in the transpassive regime at an early stage.

The addition of PGMs to γ-TiAl not only resulted in the shift of corrosion potentials towards more positive values, but also in an increase of the pitting potential, suggesting an improvement in resistance to pitting corrosion, as the passivation zone expanded and the pitting phenomenon was delayed. The shift of the corrosion potentials towards more positive values was attributed to the modification of the cathodic process. However, this shift alone was not enough to cause improved corrosion resistance as other aspects of the alloy electrochemistry, such as current density and long

term exposure to acid also played a part. Generally, the current density at the corrosion potential decreased with increasing PGM content, but in some alloys, there was a sharp increase in the current density, suggesting that, even though there was a shift of the corrosion potential to more positive values, observed high current densities resulted in high dissolution rates.

The open circuit potentials after 1000 minutes (Figure 5.26) and accumulation of Ru or Pd on the surface of corroded alloys also indicated the alloys' behaviour. Alloys showing high PGM content on the surface, such as γ-TiAl alloyed with 1.0 at% Ru or Pd, also showed high corrosion rates, suggesting a shift of the potentiodynamic curves towards high current density. The relatively large amount of Ru or Pd observed on the surface led either to the corrosion potential being in the transpassive region or a shift towards high current density, two situations which both favoured the dissolution of the alloys. Previous work also showed that ruthenium additions to titanium shifted the potentiodynamic scan towards high current density (van der Lingen and Sandenbergh, 2001).

As shown in Sections 4.2.1-4.2.2, adding more than 1.0 at.% Pt and more than 1.5 at.% Pd or Ir (Ru results were inconclusive) was not beneficial to the corrosion resistance, because it led to the precipitation of new phases with higher PGM contents. G phase in γ-TiAl with Ru (Khataee et al., 1989a, 1989b and 1989c, Grytsiv *et al.*, 2003), τ_1 phase in γ-TiAl with Pd (Zaikana *et al.*, 2011), τ_3 in γ-TiAl with Pt (Ding *et al.*, 2000), and similarly, γ-TiAl with Ir, which resulted in the higher corrosion rates generally observed in the multiphase alloys, since the matrix became depleted of PGM (Vaidya and Preece, 1978; Chawla, 1993; Davis, 1999; Ghali and Revie, 2010). This would result in an improvement not as good as it should be, because the individual phases possess different electrode potentials, depending on the PGM content of the different phases, resulting in one phase acting as an anode and being subject to corrosion (Scully, 1966). In this instance, the phases with high PGM contents acted as cathodes, and the matrix as the anode. The matrix was thus subjected to dissolution, even though the presence of the PGMs shifted the corrosion potentials to more positive values. In systems exposed to aqueous environments, the corrosion process is under cathodic control, which means that the size of the cathode will control the anode current density (Chawla, 1993; Landolt, 2007). The larger the cathode area compared to the anode area, the greater will be the anode current density. For γ-TiAl, this meant that as the amount of PGMs was increased from 0.2 at.% to 2.0 at.%, more areas of higher PGM content phases were introduced in the

microstructure, giving higher anodic current density to the matrix, increased matrix dissolution and more PGM-containing particles were left on the corroded surface. The general result in such a case is the surface enrichment of the less active elements (Landolt, 2007); here, there was surface enrichment in PGM-containing particles. This was confirmed by the high values of end potentials in the open circuit potential tests and the PGM content of corroded surfaces. To avoid this effect, lower PGMs than the solubility limits in γ and α_2, the main phase components, should be added to the γ-TiAl alloys, although there improvement with amounts higher than the solubility limits.

The PGM content of γ-TiAl was varied from 0.2 at.% to 2.0 at.% and assessed for its effect on the corrosion potential. For a given PGM, at each addition level and irrespective of the solution concentration, there was a shift of corrosion potential when the performance was compared to that of plain γ-TiAl. However, as shown in Figure 5.7 and Figures 5.27 to 5.30, irrespective of the solution concentration, the corrosion potentials remained in the -300 mV to -200 mV region, suggesting that increasing the PGM content did not significantly improve the resistance to pitting corrosion. A large shift of the corrosion potential to more positive values was not necessarily beneficial to the PGM-alloyed γ-TiAl, and could result in the corrosion potential falling in the transpassive region of the plain γ-TiAl, leading to active dissolution. This limitation in the achieved corrosion potential with increasing PGM additions is an indication that the corrosion potentials achieved after addition of 0.2 or 2.0 at.% PGM were very close to each other and show that there was no benefit in increasing the PGM content.

The solutions of 5 wt% HCl (pH = 0.11), 15 wt% HCl (pH = -0.52) and 25 wt% HCl (pH = -0.62) were very aggressive and showed that, at pH below 0, the improvement of the corrosion resistance became hard to achieve. This suggested that there is a limit, set at $pH \geq 0$, below which the improvement of corrosion resistance by PGM additions could not be achieved, and indicated that in less aggressive solutions with $pH \geq 1.0$, the γ-TiAl alloyed with PGMs should perform better.

5.4 Conclusions

When γ-TiAl alloyed with PGMs was tested in 5, 15 and 25 wt% HCl solutions, the corrosion potentials were shifted to more positive values, suggesting a corrosion resistance improvement by modification of the cathodic process. There was a decrease in pitting potential of the plain γ-TiAl

with increasing solution concentration. A decrease in pitting potential is detrimental to pitting corrosion resistance as its narrows the passivation zone and favours the occurrence of pitting corrosion and active dissolution in the transpassive regime. Additionally, there was an increase of the pitting potential, leading to improvements in pitting corrosion resistance, as the passivation zone expanded and pitting was delayed.

The corrosion resistance improvement by modification of the cathodic process was achieved in 5 wt% HCl solutions. Platinum, palladium, ruthenium or iridium additions to the γ-TiAl alloy modified the cathodic process, facilitating a spontaneous passivation. In 15 wt% HCl solutions, the results were unpredictable, corresponding to the passive-active regime. In 25 wt% HCl solutions, it was not possible to improve corrosion resistance of TiAl alloys by cathodic modification, due to the absence of the passive region on the potentiodynamic scan of the plain γ-TiAl. The resulting process fell in the transpassive or active regime, leading to active dissolution in either case. The absence of the passivation zone on the potentiodynamic scan of the plain γ-TiAl was attributed to the high aggressiveness of the solution.

Cathodic modification of PGM-alloyed γ-TiAl occurred as a result of increased PGM content, especially with Ru or Pd, on the surface of the TiAl alloys, which simultaneously improved hydrogen evolution efficiency and inhibited anodic dissolution. The new phases formed in γ-TiAl with additions of increasing amounts of PGMs (0.2, 1.0, 1.5 .0 and 2.0 at.% Pt, Pd, Ru or Ir) could give improved corrosion resistance. However, there was no benefit in increasing the PGM content, as the same performance was achieved at 0.2 at.% and 2.0 at.% PGM. Furthermore, increasing the PGM content in the γ-TiAl alloy beyond 1.0 at.% was not beneficial, as a more noble phase formed, and galvanic corrosion occurred, with the matrix acting as the anode and the PGM-containing phase as the cathode.

In terms of alloy performance, there was limit of the solution concentration beyond which the alloy passivation by cathodic modification could not be achieved. With pH between 0.1 and -0.6, the hydrochloric acid solutions were very aggressive.

CHAPTER 6

HIGH-TEMPERATURE OXIDATION BEHAVIOUR

6.1 Oxidation behaviour tests

6.1.1 Thermogravimetric analysis (TGA)

The effect of PGM content on the oxidation behaviour of TiAl alloy was assessed by TGA. Table 5.1 summarises the mass gains for the alloys with different PGM contents at 1185°C. The assessment of mass gain was done at 1185ºC because this was the temperature limit set for the equipment used, and there was no significant mass change from 900ºC to 1185ºC. Figure 6.1 shows the relative mass gain with increasing PGM content. Ruthenium-alloyed γ-TiAl showed the largest mass gain at 1.0 at.% Ru. The lowest mass gain was achieved with iridium and palladium additions.

Table 6.1. *Mass change as a function of precious metal content at 1185 °C.*

PGM content (at.%)	**Relative mass change in PGMs-alloyed TiAl (wt%)**			
	Ru	Pd	Pt	Ir
0.2	1.09±0.03	1.23±0.03	1.83±0.04	1.96±0.03
1.0	4.02±0.02	0.85±0.03	1.32±0.04	0.97±0.03
1.5	2.26±0.02	0.57±0.03	2.28±0.03	0.53±0.02
2.0	2.62±0.02	0.90±0.03	2.18±0.03	1.13±0.03

6.1.2 Microstructural characterisation of oxidised alloys

6.1.2.1 External appearance of oxidised alloys

The samples were loaded in a muffle furnace, heated to 950°C at 10°C/minute and held at 950°C for 120 hours in static air. At the end of the holding time, the samples were allowed to furnace cool. The oxidised samples were then removed from the furnace after cooling to room temperature. All the samples underwent oxidation during exposure to the oxygen in the air at 950°C, and exhibited beige oxide scales on the surface. There were cracks in all the scales, possibly because of different coefficients of thermal expansion of the metal substrates and the oxide scale. Under the beige oxide scale was a white oxide layer, which had good adhesion to the substrate. This was especially the

case in the alloys with platinum additions, which showed a complete loss of the beige scale and revealed, at all addition levels, a whiter surface after breakaway of the beige oxide.

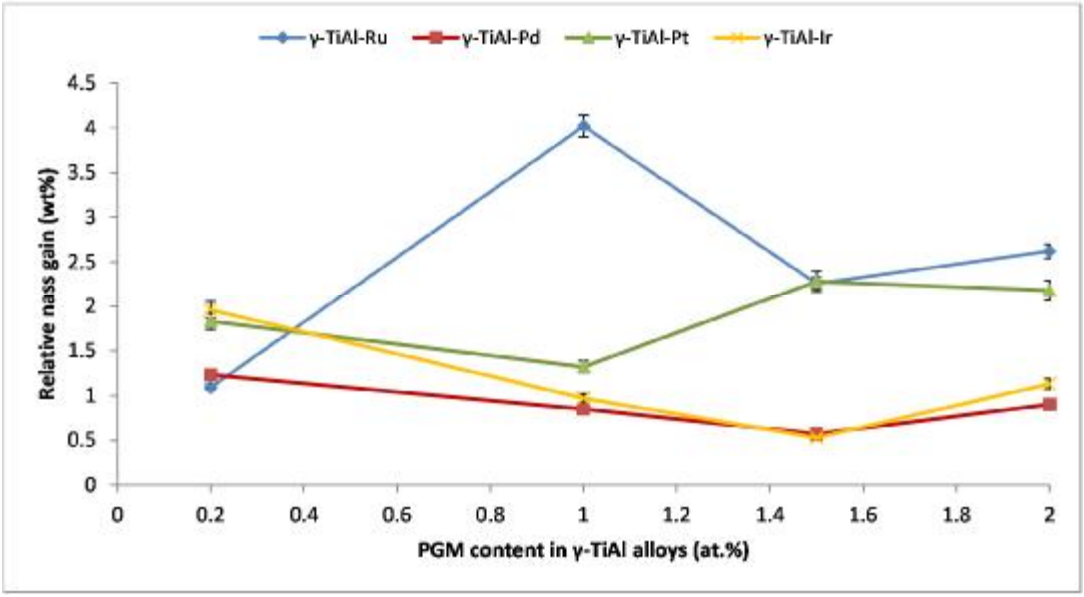


Figure 6.1. *Effect of PGM content on mass gain for TiAl alloys at 1185 °C.*

6.1.2.2 Phase transformation during oxidation of TiAl alloys

The microstructures of the oxidised samples are presented in Figures 6.2 to 6.5. The EDX analyses of TiAl alloys with additions of ruthenium, platinum, iridium and palladium are presented in Tables 6.2 to 6.5, and all the layers had ruthenium. In most cases, the small sizes of phases analysed resulted in large errors. The EDX results in Table 6.2 and Figure 6.2 show that the oxidised zone of Ru-alloyed γ-TiAl had a layer of TiO_2 (Area 1) on the surface, followed by a thick layer of mixed oxides (Al_2O_3 and TiO_2, in Areas 2 and 3) underneath. Under the oxide layers was a layer containing on average 50.8±1.5 at.%Ti, 31.0±0.5 at.% Al, 17.4±1.8 at.% O and 0.8±0.2 at.% Ru, a composition which agreed with the Z-phase, $Ti_5Al_3O_2$, of Copland *et al.* (1999). However, this layer was lighter in contrast than the substrate, and considering the average atomic number of the Z-phase, it should have been darker than the substrate. The light contrast of the layer could be explained by the Ru content, since in the substrate, most of the ruthenium was concentrated in the lighter regions, which were the ternary phase. This layer was not part of the oxide scale which was examined by XRD and it is assumed that the layer was the Z-phase. Under the Z-phase was the substrate with the as-cast

microstructure. The oxide scales were continuous, non-porous, without cracks, and an oxygen penetration of 188.0±2.5 µm.

Table 6.2. *EDX analyses of TiAl alloy with 1 at.% Ru shown in Figure 6.2.*

Areas analysed	**Composition (at.%)**				**Phases**
	Al	Ti	O	Ru	
Area 1	1.2±2.3	32.5±2.1	65.7±1.0	0.6±0.1	TiO_2
Area 2	25.3±1.1	11.8±0.7	62.5±0.6	0.4±0.1	Al_2O_3+TiO_2
Area 3	27.2±0.6	11.2±0.3	61.2±0.3	0.4±0.1	Al_2O_3+TiO_2
Area 4	31.0±0.5	50.8±1.5	17.4±1.8	0.8±0.2	$Ti_5Al_3O_2$+Ru
Area 5	48.6±1.6	49.6±2.2	-	1.8±0.7	~Ti_3Al+γ-TiAl+G-phase

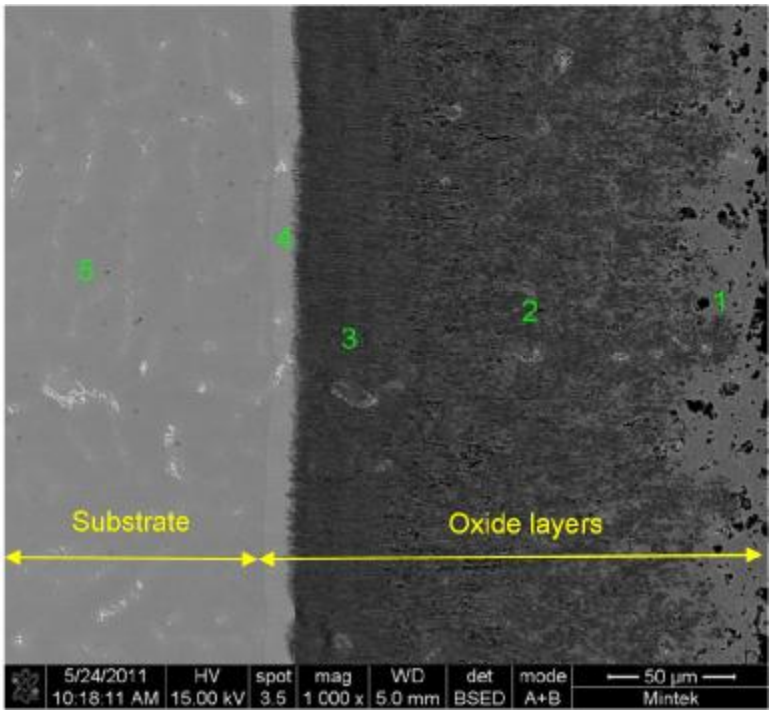


Figure 6.2. *SEM-BSE image of oxides in γ-TiAl with 1 at.% Ru, showing (1) TiO_2, (2-3) TiO_2+Al_2O_3, (4) $Ti_5Al_3O_2$ and (5) substrate after 120 hours at 950°C.*

Platinum-alloyed γ-TiAl (Table 6.3 and Figure 6.3) followed a different oxidation pattern, and TiO_2 layers alternated with mixed TiO_2+Al_2O_3 layers. The layer between the metal substrate and the oxidised layers contained Ti_3Al and platinum, and no oxygen. This layer was immediately adjacent to the TiO_2 layer. In the TiAl alloy containing 1.0 at.% Pt, the TiO_2 surface layer spalled, leaving an Al_2O_3 layer with some islands of TiO_2. The Al_2O_3 layer and the other layers underneath adhered very well to the substrate, as shown in Figure 6.3. PGM-rich phases (very light contrast particles)

were present in the oxidised zone in Figures 6.3 and 6.4, indicating that the presence of PGMs did not stop the oxidation front wave. The oxide scale here was also continuous, non-porous, without any cracks and an oxygen penetration depth of 155±14.5 µm. The wide variation on the oxygen penetration thickness was the result of a high irregularity of the surface caused by the peel-off of the external oxide layer. The composition of Area 5 showed large errors, because it was varying mixtures of phases within the substrate, due to a wavy oxidation front, where the dark phases were attacked more and the light phases were attacked less. The non-oxidised phases were analysed in Section 4.2.2.

Table 6.3. *EDX analyses of TiAl alloy with 1 at.% Pt shown in Figure 6.3.*

Areas analysed	**Composition (at.%)**				**Phases**
	Al	Ti	O	Pt	
Area 1	33.9±8.9	5.4±5.6	60.5±3.7	0.2±0.1	Al_2O_3+TiO_2
Area 2	0.4±0.3	33.2±0.6	65.9±0.8	0.5±0.3	TiO_2
Area 3	22.9±5.5	14.5±4.0	61.7±1.5	0.9±0.8	Al_2O_3+TiO_2
Area 3	0.5±0.3	33.9±2.5	64.9±5.4	0.7±0.3	TiO_2
Area 4	35.0±1.7	63.1±2.4	-	1.9±1.6	~Ti_3Al
Area 5 grey	41.9±10.6	57.8±11.0	-	0.3±0.3	~Ti_3Al+γ-TiAl
Area 5 bright	49.1±0.3	48.3±1.6	-	2.6±1.4	γ-TiAl

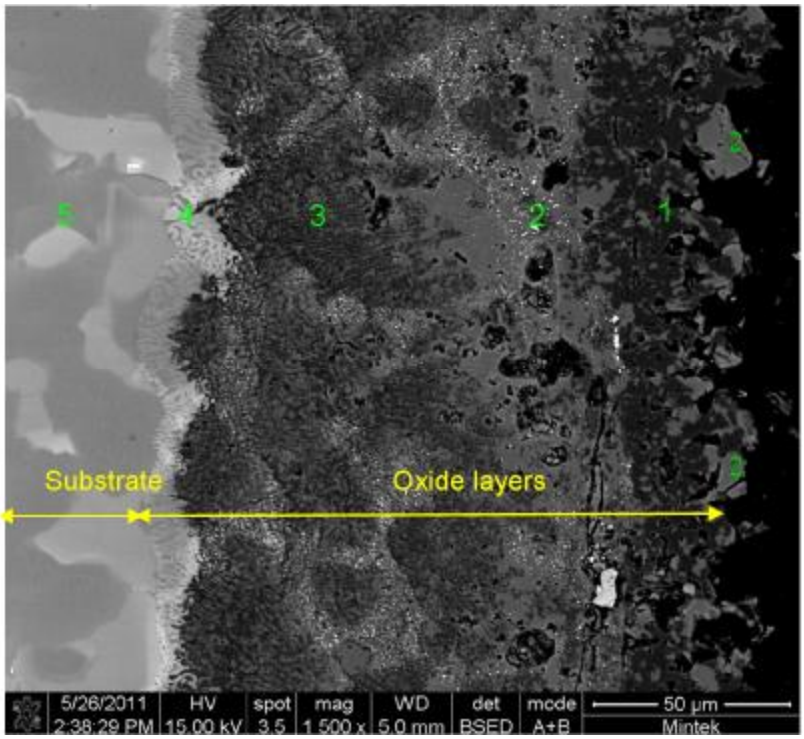


Figure 6.3. *SEM-BSE image of oxides in TiAl with 1 at.% Pt, showing (1) Al_2O_3, (2) TiO_2, (3) $TiO_2+Al_2O_3$, (4) Ti_3Al and (5) substrate after 120 hours at 950°C.*

The oxidation-affected zone in iridium-alloyed γ-TiAl (Table 6.4 and Figure 6.4) followed an oxidation pattern similar to that observed in Pt-alloyed γ-TiAl. This zone showed a TiO_2 layer (Area 1) on the surface, with isolated particles of Al_2O_3, followed underneath by a layer of thick mixed $TiO_2+Al_2O_3$ (Areas 2 and 3). Under the mixed oxide layer was a layer of composition corresponding to Ti_3Al, which contained iridium (Area 4). This layer was adjacent to the metal substrate.

The oxidation-affected zone in the palladium-alloyed γ-TiAl (Table 6.5 and Figure 6.5) showed a completely different oxidation pattern, with a TiO_2 layer on the surface, followed by a thick layer of mixed $TiO_2+Al_2O_3$, with some Pd. The mixed-oxide layer was followed by a layer of high titanium content, indicating a migration of titanium towards the oxidation-affected zone, leaving behind a high-palladium phase corresponding to the ternary compound τ_1 between the high-titanium content layer and the metal substrate. The large errors observed in the EDX analyses of different areas (Area 3, Table 6.5) were from the pick-up of the matrix surrounding the small areas (different proportion of small phases) analysed, smaller than 3 μm, so that the beam was interacting with these other phases. In the oxide scale, Area 1 (TiO_2) was continuous and non-porous, without any cracks. The area of mixed oxide (Areas 2, 3 and 4) were porous. The maximum oxygen penetration was 180 μm. Even though phases 5 and 6 did not appear to be continuous, this place of the sample gave the best contrast. Elsewhere, these phases were continuous, but with poorer contrast.

In most cases, there was breakaway of the oxide scales. The oxide scales were analysed by XRD and typical patterns are shown in Figures 6.6 and 6.7 for oxide scale obtained from TiAl alloys with palladium or iridium additions. Alumina and TiO_2 were confirmed. The oxide scales also showed Pd and Pd_2Al_3 peaks, indicating that the Pd was present in the oxidation-affected zone, either alone or bound to Al in an oxidation-resistant compound, leaving Ti to oxidise. There was also a small peaks of AlIr, with the others being coincident with the oxides, Figure 6.7. The results of XRD supported the observation that white particles in the oxidation-affected zone were PGMs that were left behind the oxidation front wave.

The effect of PGM content on the oxidation behaviour of γ-TiAl alloys was assessed by conducting oxidation tests on γ-TiAl alloys with 0.2, 1.5 and 2.0 at.% PGMs. Gamma-TiAl alloys with 0.2 at. % PGMs did not show internal oxidation. As the PGM content of the TiAl alloys was increased, more oxidation was observed in the samples, resulting in generalised internal oxidation at 2.0 at.% PGM. The oxidation followed the trend obtained in the thermogravimetric analyses, which showed that TiAl alloys with high PGM contents had the highest mass gain, indicative of a high level of oxygen intake and oxidation. Figure 6.8 shows SEM images of internal oxidation in TiAl alloys with 2.0 at.% Ru and Table 6.6 shows the EDX analyses of internal oxidised zones. These analyses might have errors, because it was not a flat surface. A similar trend was observed in TiAl alloys with 2.0 at.% Pd and 2.0 at.% Pt. The titanium aluminide alloy with 2.0 at.% Ir did not show extended internal oxidation.

Table 6.4. *EDX analyses of TiAl alloy with 1 at.% Ir shown in Figure 6.4.*

Areas analysed	**Composition (at.%)**				**Phases**
	Al	Ti	O	Ir	
Area 1	7.1±2.2	34.0±1.9	58.9±0.9	-	TiO_2+Al_2O_3
Area 2	38.4±1.3	-	61.6±1.5	-	Al_2O_3
Area 3	33.0±1.3	9.2±1.0	57.8±1.9	-	Al_2O_3+TiO_2
Area 4	37.0±0.8	62.2±0.7	-	0.9±0.2	~Ti_3Al
Area 5	48.5±3.5	51.7±1.5	-	1.1±0.2	γ-TiAl+Ti_3Al

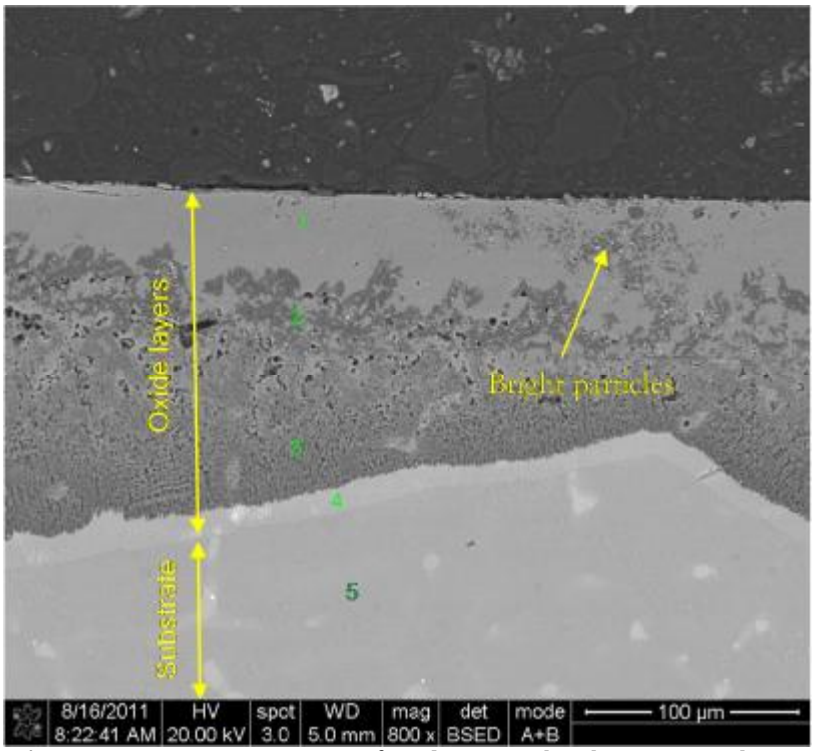


Figure 6.4. *SEM-BSE image of oxides in TiAl with 1 at.% Ir, showing (1) TiO_2 (2-3) TiO_2+Al_2O_3, (4) Ti_3Al and (5) substrate after 120 hours at 950°C.*

Table 6.5. *EDX analyses of TiAl alloy with 1 at.% Pd shown in Figure 6.5.*

Areas analysed	**Composition (at.%)**				**Phases**
	Al	Ti	O	Pd	
Area 1	-	41.2±0.4	58.8±0.4	-	TiO_2
Area 2	37.4±2.1	5.6±1.2	56.9±1.3	-	Al_2O_3+TiO_2
Area 3	28.3±7.8	11.5±4.7	59.6±3.5	0.6±0.1	Al_2O_3 +TiO_2
Area 4	38.4±3.6	7.1±3.0	54.7±3.1	0.8±0.5	Al_2O_3 +TiO_2
Area 5	14.1±4.0	76.7±6.0	5.3±2.4	3.9±1.1	α-Ti+Ti_3Al
Area 6	64.3±1.3	25.0±0.5	1.6±1.5	9.1±0.6	τ_1
Area 7	42.4±1.2	39.1±0.3	17.0±0.4	1.5±0.6	Ti_3Al+ γ-TiAl

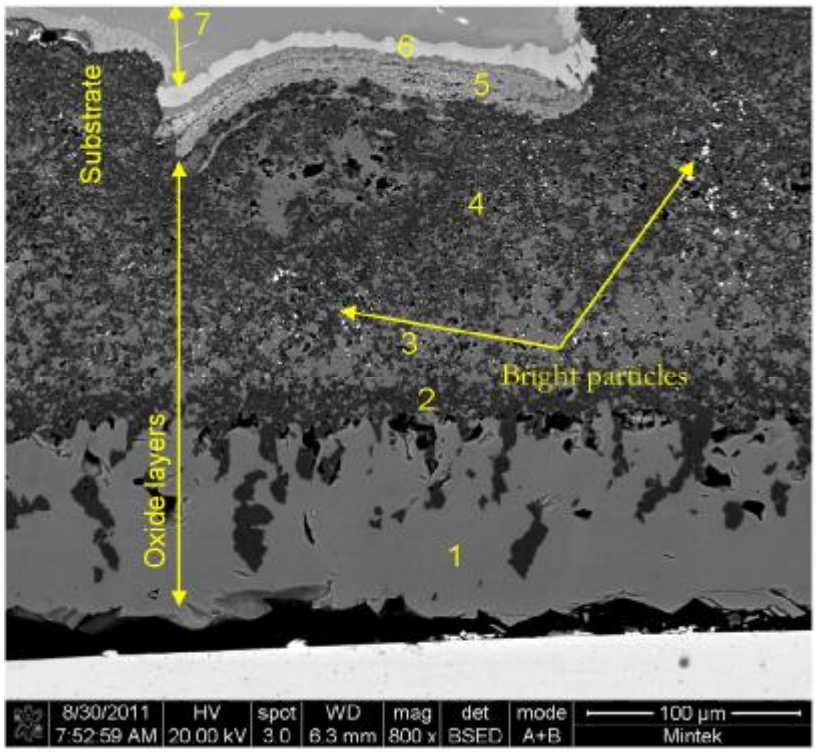


Figure 6.5. *SEM-BSE image of oxides on TiAl with 1 at.% Pd, showing (1) TiO_2, (2) Al_2O_3 (3-4), TiO_2+Al_2O_3, (5) Ti_3Al, (6) $Ti_{25}Al_{75-x}Pd_x$ and (7) substrate after 120 hours at 950°C.*

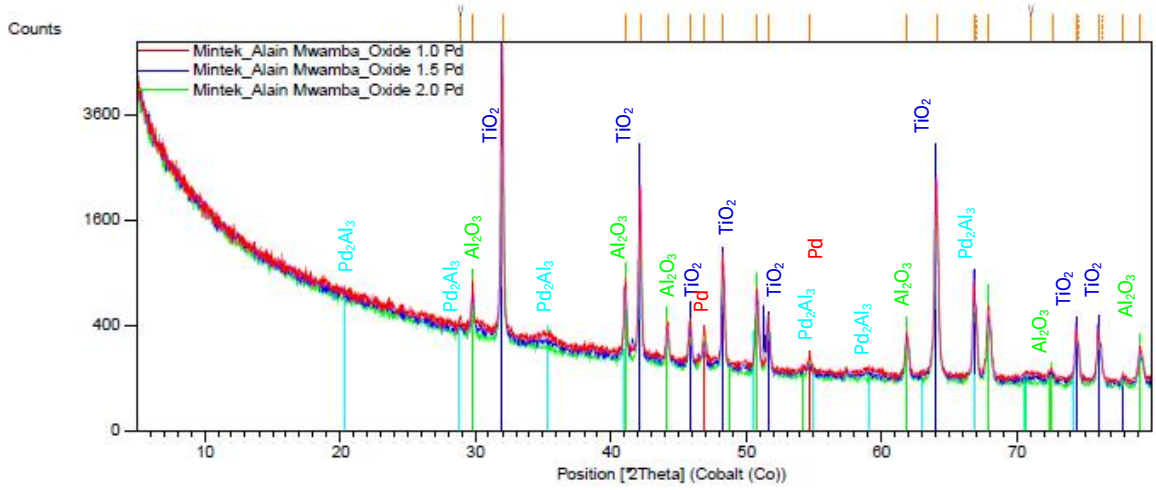


Figure 6.6. *XRD patterns of the oxide scales on TiAl with 1.0, 1.5 and 2.0 at.% Pd, showing TiO_2, Al_2O_3, Pd_2Al_3 and Pd peaks.*

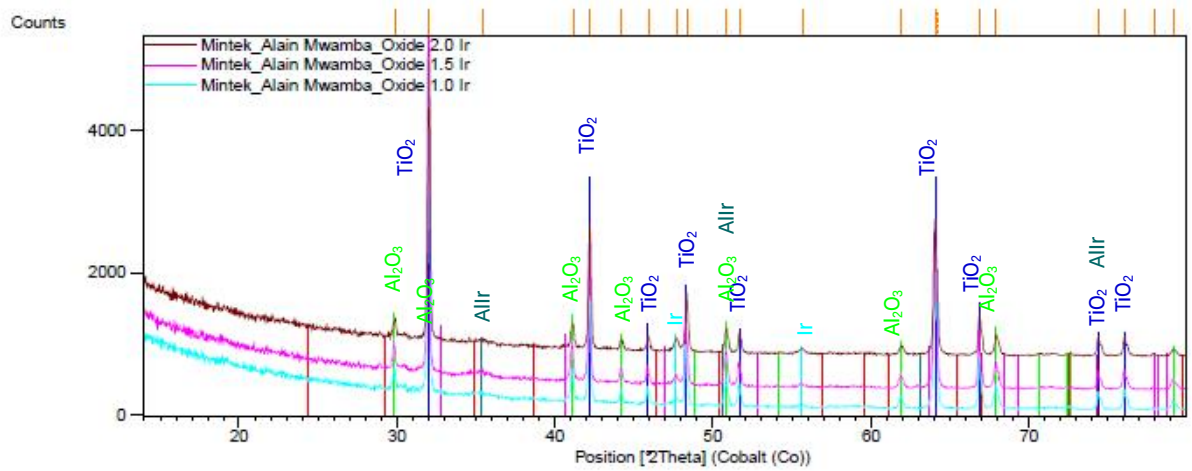
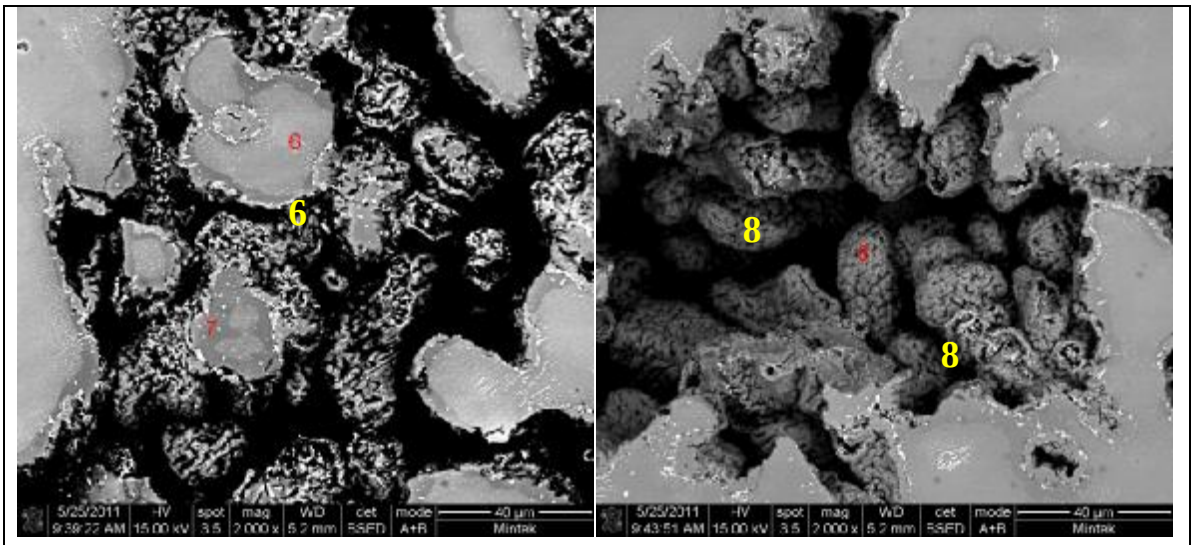


Figure 6.7. *XRD patterns of the oxide scales on TiAl with 1.0, 1.5 and 2.0 at.% Ir, showing TiO_2, Al_2O_3, AlIr and Ir peaks.*



TiAl -2.0 at.% Ru

Figure 6.8. *SEM-BSE images of internal oxidation in TiAl with 2 at.% Ru addition after 120 hours at 950°C.*

Table 6.6. *EDX analyses of internal oxidised zones in TiAl with 2 at.% Ru shown in Figure 6.8.*

Areas analysed	**Composition (at.%)**				**Phases**
	Al	Ti	Ru	O	
Area 6-7	63.1±08	33.3±0.7	0.5±0.1	3.1±0.7	$TiAl_2$+TiO_2+Al_2O_3+ (Ru)
Area 8	9.9±0.4	44.5±0.7	0.09±0.03	45.5±0.9	Al_2O_3+TiO_2+ (Ru)

6.2 Discussion

In most cases, the oxide scale spalled either partially or totally. Spallation is due to stresses set up by a mismatch between substrate metal and scale contractions on cooling to room temperature (Landolt, 2007). The oxidation behaviour of Ru-, Pt-, Ir- or Pd-alloyed γ-TiAl can be interpreted and understood from previous investigations (Becker *et al.*, 1992; Brady *et al.*, 1996; Jacobson *et al.*, 1999; Copland *et al.*, 1999). The effect of PGMs on the oxidation behaviour of two-phase TiAl was assessed with respect to the ability of the alloy to form the aluminium oxide and Z-phase ($Ti_5Al_3O_2$) that would stabilise the aluminium oxide phase and promote its continuity (Copland *et al.*, 1999). For oxidation resistance, the formation of Al_2O_3 is desired over TiO_2. The latter grows at a rapid rate and does not provide adequate protection above 600-700ºC (Jacobson *et al.*, 1999). Alumina scales, by virtue of their extremely slow, parabolic rates of growth, are protective at temperatures above 1200°C (Copland *et al.*, 1999). During the study of the thermodynamics of γ-TiAl oxidation based on the Al-Ti-O phase diagram, Rahmel and Spencer (1991) concluded that the formation of a continuous Al_2O_3 scale is not to be expected if the composition of the alloy is in the two-phase region Ti_3Al+TiAl, and that the formation of a continuous protective Al_2O_3 scale would be favored by:

- An increase in the aluminium content up to, or even above, the equilibrium composition between Ti_3Al and TiAl on the Ti-Al-O phase diagram, because the alloy is then in equilibrium with Al_2O_3. The selective oxidation of aluminium to form the protective scale could nevertheless decrease the aluminium content in the subsurface zone below the critical value of Al_2O_3 stability.
- Alloying TiAl with components which decrease the titanium activity and increase the aluminium activity.

Figure 6.9 is a vertical section of a pressure-composition Ti-Al-O phase diagram at 900°C, where the phases Ti_3Al, TiAl and $TiAl_3$ were treated as line compounds (Rahmel and Spencer, 1991). From studies of the oxidation of titanium, the main reaction product is TiO_2, and TiO, Ti_2O_3. The Magneli phases (Figure 6.10), with the general formula Ti_nO_{2n-1}, are oxidised rapidly to TiO_2, or the formation of these oxides is retarded due to slow phase-boundary reactions, so that TiO_2 and Al_2O_3 are the reaction products observed. However, for general conditions on the metal surface with the

oxygen content above 66.50 at.% (Figure 6.10), TiO_2 (rutile) is more likely to form, as it is the most stable titanium oxide at all temperatures and ambient pressure (Murray and Wreidt, 1986).

A continuous layer of Al_2O_3 can form on the surface of the alloy at high temperature which protects the alloy from further oxidation. As described in the next paragraph, the formation of Al_2O_3 on the surface leads to Al depletion on the sub-surface layer resulting in the formation of a new stoichiometric ternary phase, the Z-phase, in the sub-surface layer (Copland *et al.*, 1999; Shemet *et al.*, 2000; Locci *et al.*, 2001). Figure 6.11 shows the calculated isothermal phase diagram of Ti-Al-O system at 900°C, including the ternary Z-phase (Dettenwanger *et al.*, 1996). Dettenwanger *et al.* (1994) found that binary γ-alloys formed a continuous Al_2O_3 scale at temperatures up to 1000°C in pure oxygen, but did not form a continuous alumina scale in air.

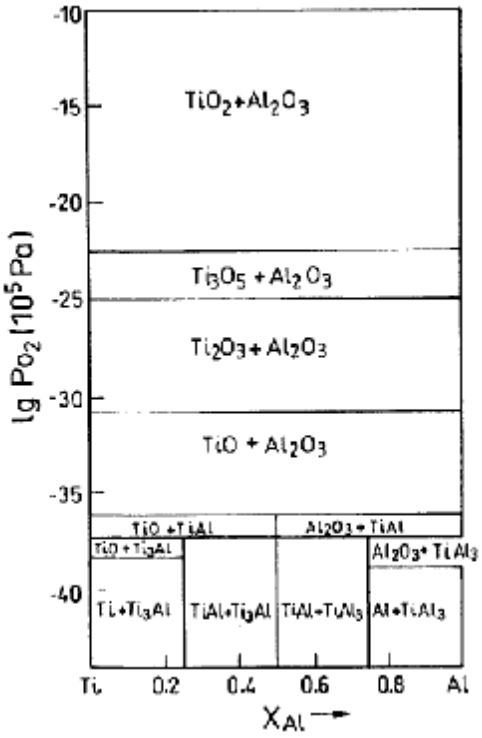


Figure 6.9. *Vertical section of the pressure-composition Ti-Al-O phase diagram at 900°C (Rahmel and Spencer, 1991).*

Approximately 60-70 at.% Al was needed for binary Ti-Al alloys to form a continuous Al_2O_3 scale in air, while only about 47-49 at.% Al was needed in pure oxygen. According to Copland *et al.*

(1999), γ-TiAl forms a subsurface zone of $Ti_5Al_3O_2$, or Z-phase, if the initial stage of oxidation at 1000°C is protective. A continuous layer of $Ti_5Al_3O_2$ forms directly under the Al_2O_3-rich scale, requiring very little titanium diffusion, oxygen enrichment and aluminium depletion. For equi-atomic single-phase γ-TiAl, the Z-phase formed according to the reaction (Copland *et al.*, 1999; Young and Gleeson, 2002):

$$Ti_{50}Al_{50} + 20O \rightarrow 10Ti_5Al_3O_2 + 20Al \qquad \text{(Equation 5.1)}$$

For two-phase α_2+γ-TiAl (~47 at.% Al) (Copland *et al.*, 1999):

$$Ti_{53}Al_{47} + 20O \rightarrow 10Ti_5Al_3O_2 + 17Al + 3Ti \qquad \text{(Equation 5.2)}$$

The aluminium released in these reactions diffuses outward to form more Al_2O_3 scale (Young and Gleeson, 2002). With continued oxidation, the Z-phase layer partially destabilised at the Z / γ-TiAl interface to form a mixture of oxygen-saturated α_2-Ti_3Al and Z. The precipitation of oxygen-saturated α_2-Ti_3Al coincides with the breakdown of the protective Al_2O_3-rich scale and the subsequent formation of a non-protective TiO_2 + Al_2O_3 scale. It is worth noting that the two equations show that single phase γ-TiAl releases only aluminium that can oxidise and form Al_2O_3, and the two-phase α_2+γ-TiAl releases both aluminium and titanium, which are likely to form mixed Al_2O_3+TiO_2 during oxidation.

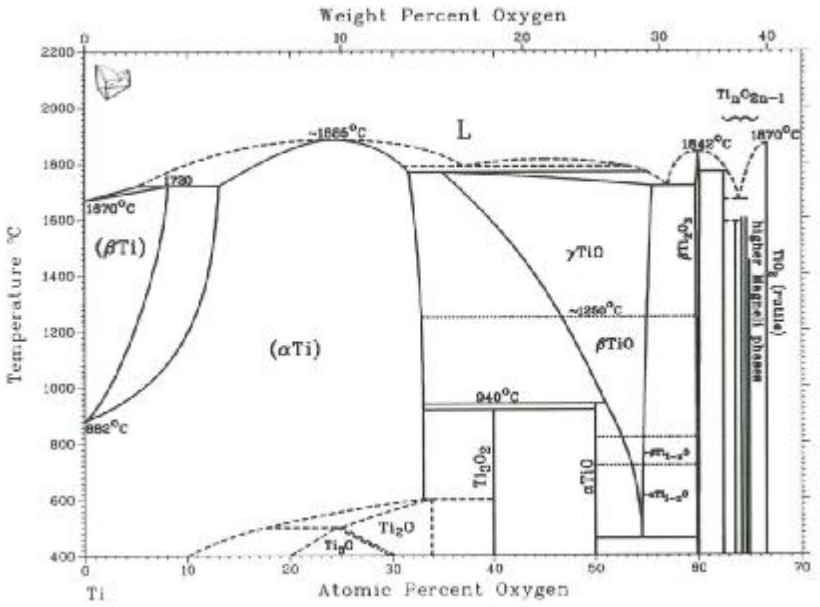


Figure 6.10. *Partial Ti-O binary phase diagram (Murray and Wreidt, 1986).*

The subscale formation in γ-TiAl during high-temperature oxidation is not in itself a cause of non-protective oxidation (Young and Gleeson, 2002). The development and maintenance of a continuous Z-phase layer supports the growth of a protective, Al_2O_3-rich scale. However, in the absence of an Al_2O_3-stabilising third element, such as silver (Shemet *et al.*, 2000), the Z-phase becomes unstable at the Z/γ-TiAl interface and precipitation of oxygen-saturated Ti_3Al (α_2) occurs as a result of preferential aluminium oxidation, particularly in the presence of oxygen (Becker *et al.*, 1992). About 2 at.% Ag addition promoted and stabilised the formation of an alumina scale on γ-TiAl up to the test time of 12000 h and probably beyond (Shemet *et al.*, 2000). The destabilisation of the Z-phase is believed to be the primary cause of the transition from protective to non-protective oxidation of γ-TiAl based alloys (Young and Gleeson, 2002). The presence of α_2 next to the $Ti_5Al_3O_2$ under the mixed $TiO_2+Al_2O_3$ scale was also found by Zheng *et al. (1995)*. They found that under the initially-formed protective alumina scale was the depleted layer consisting of the ternary phase $Ti_5Al_3O_2$ only, and Al_2O_3 was the oxide in equilibrium with it. On further exposure, the extent of aluminium consumption increased, leading to the formation of α_2 in the depleted layer. Due to the high solubility of oxygen in α_2, the aluminium would tend to oxidize internally, rather than form an external scale, leading to oxidation of titanium, which was accompanied by a strong increase in the scale growth rate.

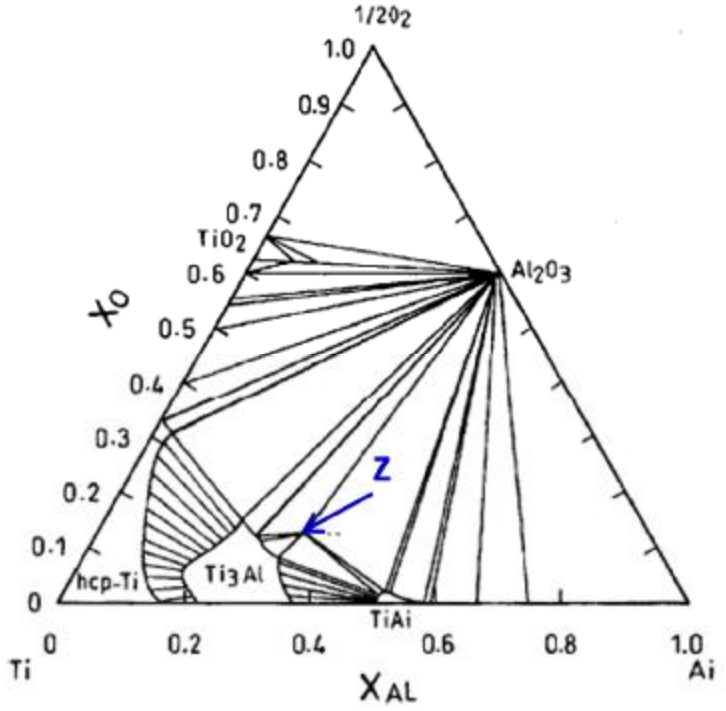


Figure 6.11. *Calculated isothermal section of the Ti-Al-O ternary system at 900°C including the ternary Z-phase (Dettenwanger, 1996).*

When the alloy was oxidised in air (Dettenwanger *et al.*, 1998; Appel *et al.*, 2011b), nitrogen played a significant part in promoting the formation of the non-protective mixed TiO_2+Al_2O_3, and significantly reduced the incubation period until the breakaway of the initially-formed alumina scale, and then enhanced the growth of mixed TiO_2+Al_2O_3 scale (Shemet *et al.*, 1997). Rakowski *et al.* (1995) showed that, when γ-TiAl was oxidised in air, the presence of nitrogen resulted in the formation of intermixed TiN and Al_2O_3 on the alloy's surface, which prevented the development of a continuous alumina layer. The resulting mixed oxide layers were permeable to nitrogen and promoted further nitriding. Titanium nitride formation during oxidation of γ-TiAl in air was also observed by Lang and Schütze (1996) and Dettenwanger *et al.* (1998).

Ruthenium (Grytsiv *et al.*, 2004) was also added to TiAl alloys and improved the oxidation resistance of γ-TiAl. This improvement was attributed to the formation of a protective layer of the ternary compound (G-phase) around the grains of the γ-TiAl (Grytsiv *et al.*, 2004). Other alloying elements such V, W, and Nb were added to TiAl for oxidation resistance improvement (McKee and Huang, 1992; Shida and Anada, 1996; Singheiser *et al.*, 2003; Lee, 2005). The mechanism by which they

improve oxidation resistance was different from that observed in γ-TiAl with silver and ruthenium additions. The addition of V and W was beneficial to the oxidation behaviour at 982°C by tying up oxygen vacancies (Kekare and Astwith, 1997).

In this work, after 120 hours at 950ºC in air, Ru-alloyed γ-TiAl showed a layer of TiO_2 on the surface, followed by a thick layer of mixed Al_2O_3+TiO_2 underneath. Under the oxide layers was a subscale layer of Z-phase, which is known to stabilise Al_2O_3 (Coppland *et al.*, 1999). This was supported by more Al_2O_3 than TiO_2 in the mixed layer. However, the progressive formation and growth of TiO_2 is believed to be the result of nitrogen in the air which prevented the formation of continuous Al_2O_3, even though ruthenium stabilised the Z-phase (Rakowski *et al.*, 1995; Shemet *et al.*, 1997; Lang and Schütze, 1996). The TiN formed would have decomposed, releasing nitrogen for further nitriding inward and giving rise to TiO_2 formation behind the reaction front. This could also explain the sole presence of TiO_2 on the surface and its progressive decrease towards the metal substrate and a dominance of Al_2O_3 near the Z-phase. Ruthenium as an alloying element in the two-phase γ-TiAl (Ti_3Al + TiAl) facilitated the stabilisation of the Z-phase and subsequent promotion of more protective Al_2O_3 away from the surface.

Platinum- and iridium-alloyed TiAl showed similar oxidation patterns, with alternating oxide layers. The TiO_2 layer on the surface was followed by a mixed TiO_2+Al_2O_3 layer, which was followed by an Al_2O_3 layer. The oxidation layer subscale was Ti_3Al in both cases, which indicated the transformation of the Z-phase and formation of Ti_3Al with high oxygen solubility and promotion of non-protective TiO_2 and TiO_2+Al_2O_3 layers. The reason for the TiO_2 layer on the surface is also believed to be due to the presence of nitrogen in the air. As alloying elements, platinum and iridium could also stabilise the Z-phase and promote the formation of Al_2O_3 in the early stages of oxidation. XRD conducted on the oxidation products showed the presence of AlIr, in addition to aluminium and titanium oxides.

Palladium-alloyed TiAl showed a TiO_2 layer on the surface, followed underneath by a thick layer of mixed TiO_2+Al_2O_3, a layer consisting of α-Ti(O), Ti_3Al(O) and Pd_2Al_3, with a ternary phase adjacent to the metal substrate, which had a composition corresponding to τ_1 in the Al-Pd-Ti phase diagram (Raghavan, 2011). The presence of the mixed oxide indicated that there was no protection against oxidation. The compound Pd_2Al_3 was identified by XRD on the oxidation products of γ-TiAl with

Pd. It is important to recognise that for both γ-TiAl with Pd and γ-TiAl with Ir, the AlIr and Pd_2Al_3 compounds were in the oxidation products, while Z-phase was on the substrate.

The major factors affecting the oxidation behaviour of the γ-TiAl alloy are composition of the alloy, atmosphere surrounding the workpiece, oxidation temperature and holding time. In this work, the base composition of the γ-TiAl alloy was Ti-47.5 at.% Al, in the Ti_3Al-γ-TiAl two-phase region. Such a composition does not favour the formation of Al_2O_3 because of the presence of Ti_3Al in the microstructure (Rahmel and Spencer, 1991). Two-phase α_2 + γ-TiAl oxidised between 900°C and 1080°C in air, forming the mixed TiO_2+Al_2O_3 with TiO_2 as the major component (Takasaki *et al.*, 1994; Roy *et al.*, 1996; Reddy *et al.*, 2001). The atmosphere surrounding the workpiece during oxidation was air, which promoted the formation of TiN in the early stage of oxidation, preventing the formation of a continuous Al_2O_3 layer on the surface of the alloy (Rakowski *et al.*, 1995; Shemet *et al.*, 1997; Lang and Schütze, 1996). The oxidation tests were conducted at 950°C, above the temperature range where the mixed oxide TiO_2+Al_2O_3 is protective. The Z-phase was found to be metastable and decomposed into oxygen-saturated Ti_3Al and Al_2O_3, on which the exclusive Al_2O_3 growth could not be sustained (Copland *et al.*, 1999).

During oxidation tests, the γ-TiAl alloys showed an increase in oxygen intake with increasing PGM content, with the highest oxygen intake occurring at 2.0 at.% PGM addition, apart from the value of the alloy with 1 at.% Ru. The oxidation of 2.0 at.% PGM alloys corresponded to internal oxidation. However, γ-TiAl alloys with 2.0 at.% iridium did not show extensive internal oxidation, indicating a high oxidation resistance. The high value for the 2 at.% Ru appears anomalous, although Chaston (1965) reported increasing partial pressure for RuO_3 at temperatures above a 1000°C. This should have given high values for the Ru-containing alloys, not just the 1 at.% alloy, so perhaps the value is anomalous and should be checked. Gamma-TiAl alloys with ruthenium, palladium and platinum exhibited higher susceptibility to internal oxidation. The oxidation resistance of γ-TiAl alloys is associated with the development of Z-phase beneath the oxidation subscale which promotes a continuous Al_2O_3 on the surface of the single-phase or γ-TiAl alloys. However, due to the discontinuous distribution of γ-TiAl in the two-phase γ-TiAl alloys in this work, a continuous Z-phase was not expected to form and withstand long term oxidation, as

observed by Copland *et al.* (1999). During extended exposure to air at 950°C, the Z-phase formed, was metastable and decomposed to give stable phases according to the following reaction:

$$3Ti_5Al_3O_2 \rightarrow 5Ti_3Al + 2Al_2O_3 \quad \text{(Equation 5.3)}$$

This corresponded to a precipitation of oxygen-saturated Ti_3Al and Al_2O_3, and Ti_3Al then acted as an oxygen reservoir for aluminium and titanium released from the reaction of $Ti_5Al_3O_2$ formation:

$$2Ti_{52.5}Al_{47.5} + 40O \rightarrow 20Ti_5Al_3O_2 + 5Ti + 35Al \quad \text{(Equation 5.4)}$$

Aluminium and titanium released from the above reaction reacted with oxygen to form Al_2O_3 and TiO_2:

$$Ti + 2O \rightarrow TiO_2 \quad \text{(Equation 5.5)}$$

$$2Al + 3O \rightarrow Al_2O_3 \quad \text{(Equation 5.6)}$$

The simultaneous formation of TiO_2 and Al_2O_3 near the Z-phase supported the observation of mixed Al_2O_3+TiO_2 in the oxide layer adjacent either to Z-phase or Ti_3Al, with predominance of Al_2O_3. Aluminium oxide could only be in higher amounts than titanium oxide, as it had two sources: the Al_2O_3 resulting from the precipitation of oxygen-saturated Ti_3Al and the reaction with oxygen of aluminium released by the formation of the Z-phase in the two-phase region. It is therefore believed that the effect of PGMs was to react with some of aluminium and titanium released to increase their content in the Ti-Al-PGM ternary phase (G-phase in the case of Ru-alloyed TiAl (Khataee *et al.*, 1989a and 1989b), τ_9 in the Pt-alloyed TiAl (Raghavan, 2012a) and τ_1 in the Pd-alloyed TiAl (Raghavan, 2012b). The high aluminium content (above 48 at.% Al) observed in the solid solution of Ti-Al phase with PGMs is due to the fact that in the as-cast condition, these phases developed in the γ-TiAl, a high-aluminium content phase at the expense of titanium.

The Ti-Al-PGM phases containing titanium, aluminium and PGM were more visible in the oxidised zone, with increased PGM content and did not contain oxygen, indicating that titanium and aluminium were tied to the PGM in more oxidation resistant phases. These PGM-containing phases, present in the as-cast microstructure, had either the same PGM content or higher in the oxide scales.

The analysis of the oxidised zone in internally-oxidised samples of Ru-γ-TiAl had $TiAl_2$+TiO_2+Al_2O_3+(Ru), which was a brittle combination, on the surface and mixed oxides with

high titanium contents underneath. The following reactions are proposed to explain the presence of $TiAl_2$, TiO_2 and Al_2O_3 in the oxidation-affected zone:

$$4TiAl + 14O \rightarrow 4TiO_2 + 2Al_2O_3 \quad \text{(Equation 5.7)}$$

$$2Ti_3Al + 10O \rightarrow 5TiO_2 + TiAl_2 \quad \text{(Equation 5.8)}$$

These reactions indicated that $TiAl_2$ was surrounded by mixed TiO_2+Al_2O_3 resulting from the reactions (Equations 5.7 and 5 8). The $TiAl_2$ was lost by peeling off or during metallographic preparation, leaving the mixed oxides which were dominant at areas where internal oxidation occurred.

Plain γ-TiAl exposed to oxygen at high temperature forms an Al_3O_2 scale due to the outward diffusion of aluminium, leaving behind an aluminium-depleted zone. Gamma-TiAl alloys were oxidised in air, an atmosphere where the Al_3O_2 scale formed on the surface was not expected to be continuous, due to the presence of nitrogen in air. This facilitated the diffusion of titanium outwards to form TiO_2, resulting in a mixed oxide. Except for γ-TiAl-2.0 at.% Ir, addition of 2.0 at.% Pd, Pt or Ru resulted in high concentrations of the PGM in γ-TiAl and during the exposure to oxygen of the air at 950°C, titanium from the γ-TiAl diffused outwards and reacted with oxygen, forming TiO_2. By continuously exposing the PGM-containing γ-TiAl alloys to air at 950°C, the titanium content of γ-TiAl significantly decreased. This resulted in formation of $TiAl_3$, which is the most stable titanium aluminide (Gauthier *et al.*, 2003). However, due to the presence of PGMs, there was formation of extended binary phases, $Al_{75-x}(PGM)_xTi_{25}$, where there was substitution of aluminium atoms by PGM atoms and the replaced aluminium atoms reacted with oxygen to form Al_2O_3, producing mixed oxides throughout the oxidised zone. The formation of such extended binary phases was clearly observed in γ-TiAl alloys with palladium (Table 6.5: Area 6). The relatively low melting point of palladium (~1550°C) may have played a part. The fact that the palladium atoms preferentially replaced aluminium atoms in $TiAl_3$ was attributable to higher aluminium affinity for oxygen than palladium (Ellingham, 1944; Marakusheva and Bezmena, 1971).

6.3 Summary

1. Platinum group metal additions of 1.0 at.% could not stop oxidation of the TiAl alloys after 120 hours at 950°C. The alloys underwent oxidation, irrespective of the PGM used, with different oxidation patterns and to different extents.

2. The microstructure of the oxidised alloys with 1 at.% PGMs had a very brittle oxidation-affected zone, consisting of many layers which included an external layer of TiO_2, followed underneath by a layer of mixed Al_2O_3 + TiO_2. In some cases, a layer of alumina formed above the mixed oxides. The layer under the oxide scale, adjacent to the alloy substrate, was $Ti_5Al_3O_2$ in the Ru-alloyed γ-TiAl or Ti_3Al in the Pt- and Ir-alloyed γ-TiAl with dissolved PGMs. In Pd-alloyed γ-TiAl, a substituted binary phase $Ti_{25}Al_{75-x}Pd_x$ ie. $Ti(Al,Pd)_3$ was observed between a high-titanium content layer and the metal substrate.
3. The oxide scale in Ru-, Ir- and Pt-alloyed γ-TiAl was continuous, non-porous and without cracks. In the Pd-alloyed γ-TiAl, the oxide scales were porous and had cracks.
4. Thermogravimetric analyses and isothermal oxidation tests both showed that the oxidation resistance of γ-TiAl alloys could be improved with PGM additions below 1 at.%. Platinum group metal additions ≥1 at.% were deleterious to the oxidation resistance, allowing extensive internal oxidation.
5. During oxidation, the substituted binary phases appeared to remain undisturbed in the oxidised region and were easily removed during metallographic preparation, leaving behind isolated lamellar grains deprived of γ phase.

CHAPTER 7

MECHANICAL ALLOYING AND CONSOLIDATION BY SPARK PLASMA SINTERING

7.1 Introduction

Bulk γ-TiAl was produced by melting commercially pure aluminium and titanium with additions of targeted amount of PGMs and characterised. This chapter reports and discusses the characterisation of γ-TiAl powder produced by milling together titanium hydride and aluminium of commercial purity with additions of 0.5 at.% platinum group metals (PGMs).

7.2 Powder characterisation of mechanically alloyed powders

7.2.1 Apparent density, particle size distribution and particle morphology

The apparent density of powder was about 1.06 g/cm^3, which was very low compared to the density of the bulk titanium aluminide (~4.0 g/cm^3) Low apparent densities are known to occur in powder with a very narrow size distribution, and high densities in powder with wide size distribution or a bimodal distribution (Sánchez *et al.*, 2003). For the different MA powders, the size distribution parameters of 5 measurements are given in Table 7.1 and the particle size distribution curves (ISO 13320) are given in Figures 7.1 to 7.4. With agglomeration of fine particles in big particles occurring, the particle size distribution was mono-, bi- and trimodal.

Table 7.1. *Statistical parameters of the particle size distribution in different MA powders.*

Statistical parameters	**Powder**			
	γ-TiAl-0.5 Pd	**γ-TiAl-0.5 Pt**	**γ-TiAl-0.5 Ir**	**γ-TiAl-0.5 Ru**
D[4,3], μm	97.9±6.50	17.12±0.06	27.82±0.47	12.98±0.05
D[3,2], μm	8.9±0.14	5.50±0.01	5.87±0.02	3.45±0.01
d_{10},μm	3.16±0.03	2.16±0.002	2.09±0.02	1.34±0.01
d_{50},μm	28.53±0.93	12.00±0.05	16.72±0.23	9.01±0.04
d_{90},μm	344.40±28	40.00±0.11	71.96±1.40	30.95±0.13
Specific surface area, m^2/g	0.676±0.001	1.094±0.002	1.022±0.004	1.730±0.002

Where:

- D[4,3]: Volume moment mean or De Brouckere Mean Diameter reflects the size of those particles which constitute the bulk of the sample volume. It is most sensitive to the presence of large particulates in the size distribution
- D[3,2]: Sauter mean diameter, defined as the diameter of a sphere which has the same volume/surface area ratio as a particle of interest.
- d_{10}: 10 wt% of the particles are smaller than d_{10} and 90 wt% are larger than d_{10}.
- d_{50}: Median diameter or medium value of particle diameter is a particle diameter or size value in case where a cumulative distribution percentage reaches 50%. 50 wt% of the particles are smaller than d_{50} and 50 wt% are larger than d_{50}.
- d_{90}: 90 wt% of the particles are smaller than d_{90} and 10 wt% are larger than d_{90}.

The larger errors observed on the D[4,3] and d90 are due to agglomeration which gives particles of widely varying sizes.

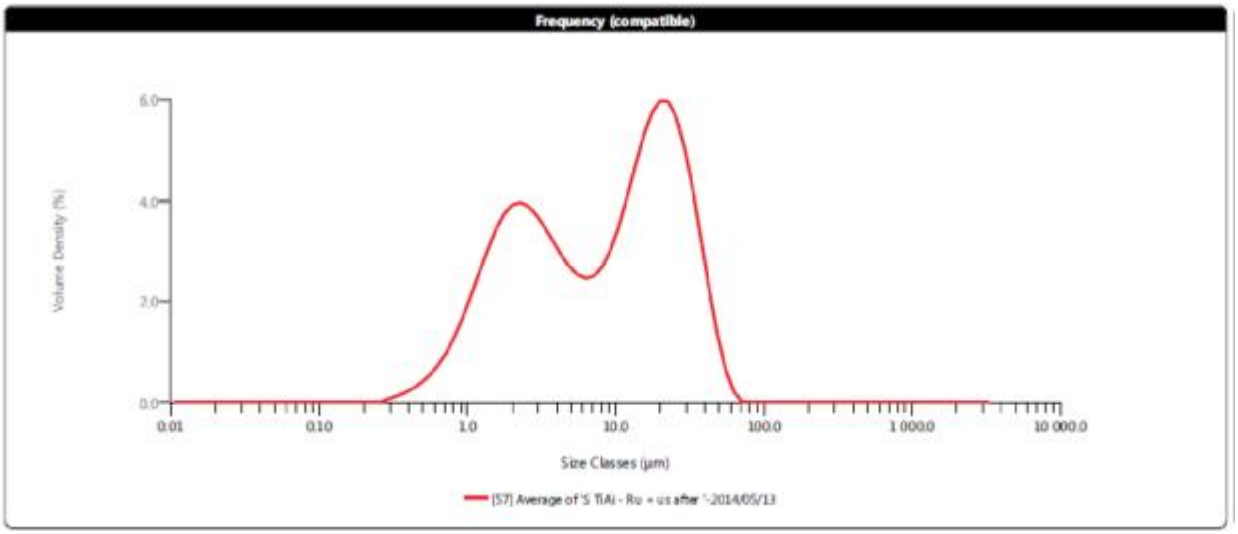


Figure 7.1. *Bimodal particle size distribution of MA powder γ-TiAl-0.5 at.% Ru.*

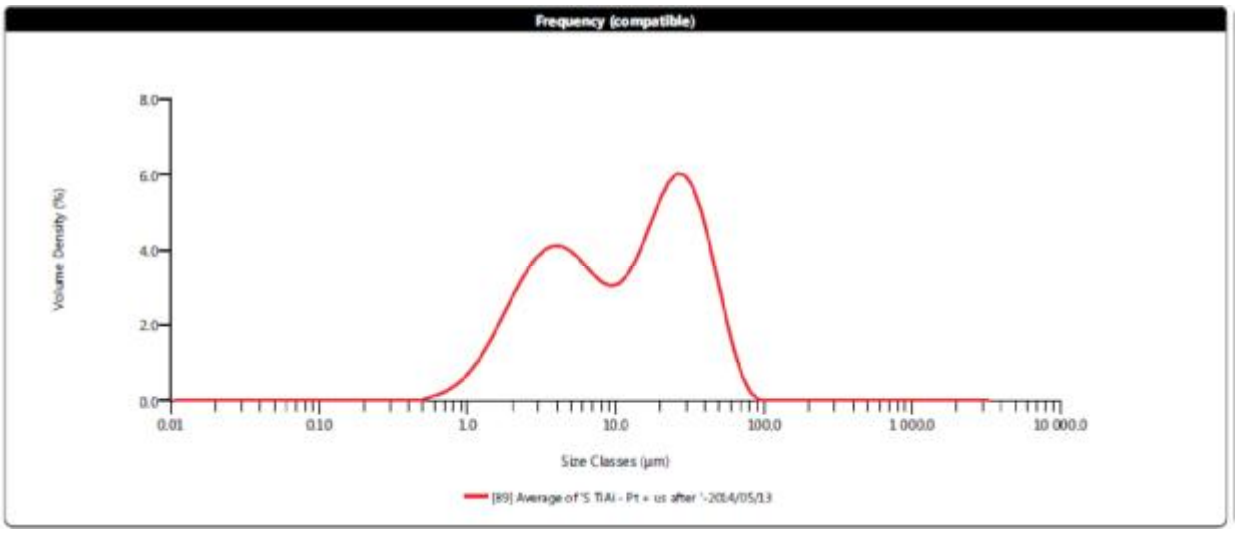


***Figure 7.2**. Bimodal particle size distribution of MA powder γ-TiAl-0.5 at.% Pt.*

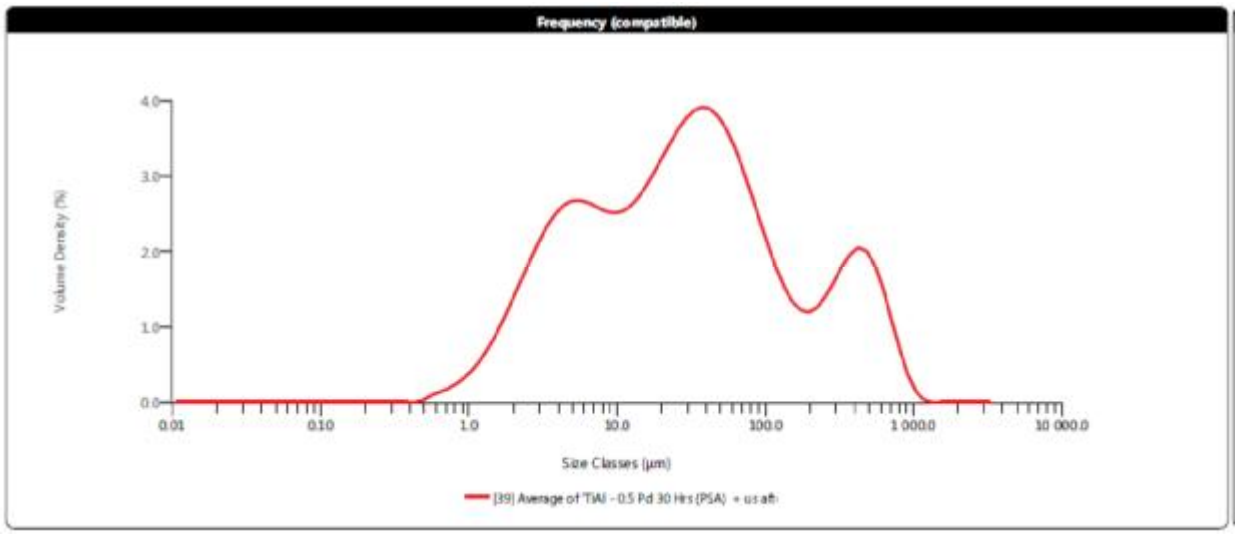


***Figure 7.3**. Trimodal particle size distribution of MA powder TiAl-0.5 at.% Pd.*

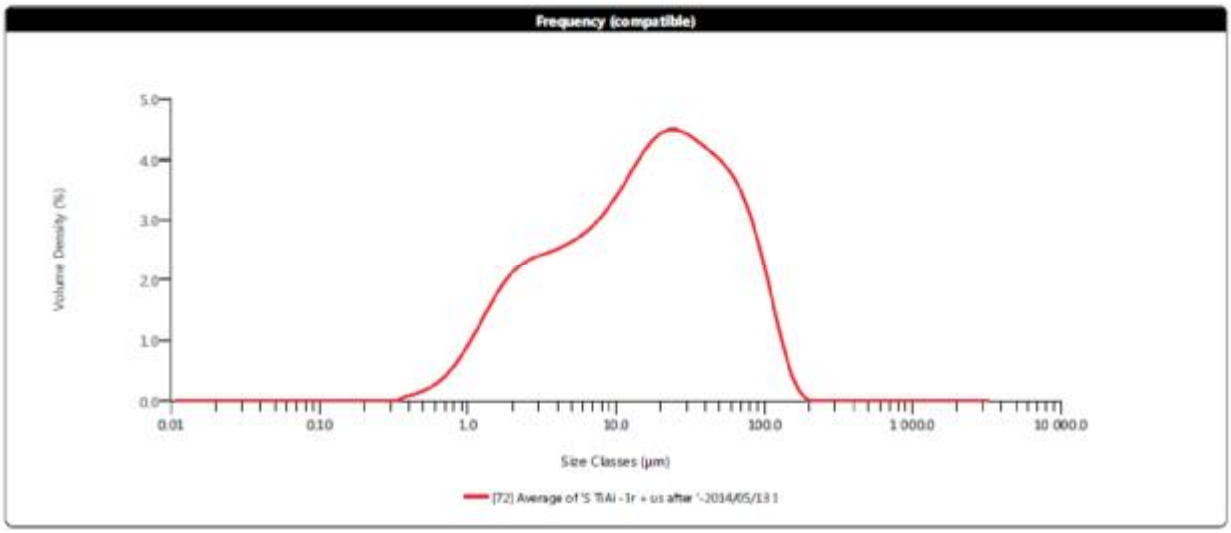
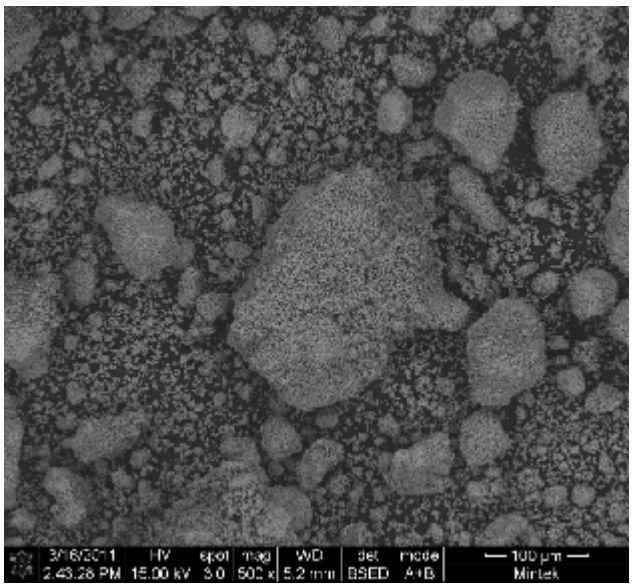


***Figure 7.4**. Slightly bimodal particle size distribution of MA powder TiAl-0.5 at.% Ir.*

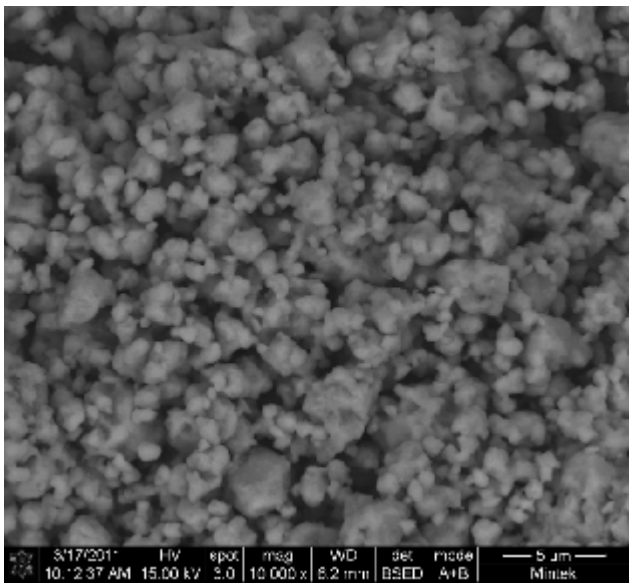
The shapes of curves indicated the trend of the particle size in the powders. The four powders showed a trend toward a bimodal or even multimodal distribution, due to the agglomeration of fine particles.

Three of the four powders gave very high specific surface areas, indicating the presence of more fine particles. The TiAl-0.5 at.% Pd powder showed the highest peak for coarse particles, indicating a large amount of agglomeration, because of its high ductility compared to the other PGMs added. With three peaks, this powder showed agglomeration around these particle sizes. The agglomeration effect was confirmed by the high value of the De Brouckere Mean Diameter and the low value of the specific surface area in the powder. This happened because the milling parameters were kept the same for all the powders. The iridium-containing powder gave a distribution which was less bimodal than the other powders.

The typical morphology of particles found in the four powders is shown in Figure 7.5. These micrographs indicate that the powders consisted of very fine particles of mostly rounded irregular shape. Angular shapes were also visible. Many individual particles were smaller than 1 µm. In the midst of the fine particles were large particles with sizes varying from 50 to 500 µm (Figure 7.5a). The large particles were agglomerates of fine particles, as shown by the microstructure in Figure 7.5b.



a. Agglomerates at low magnification



b. Agglomerate surface at high magnification

Figure 7.5*. Typical SEM-BSE micrographs of MA powder TiAl-0.5at.% Ru.*

7.2.2 Phase identification

Phases formed during mechanical alloying and heat treatment of mechanically alloyed (MA) powders were determined by a combination of XRD and EDX analyses. The results of XRD analyses are presented in Figure 7.6 to 7.13.

In all cases, before heat-treatment, the as-mechanically alloyed powders showed XRD patterns with expected broad peaks, indicative of small crystallites in the powder particles and possible tendency to amorphisation, as a result of the milling. The formation of the target alloy was difficult to observe as it was difficult to identify with accuracy any expected phases and other phases formed during milling. Overall, after milling, the phases present were TiH_2, PGMs and (Al). Aluminium and TiH_2 peaks were broadened.

After heat treatment at 600°C for 2 hours and furnace cooling, the XRD pattern of the TiAl-0.5 at.% Ru powder (Figure 7.7) showed TiAl and $TiAl_3$ which were absent in the powder XRD pattern

before heat treatment. The temperature of 600ºC and two hour holding time were chosen because they correspond to the complete dissociation of TiH_2 in Ti and gaseous hydrogen (Sandim *et al.*, 2005; Rasooli *et al.*, 2013).

The XRD pattern of heat-treated MA powder did not show any peak of ruthenium, indicating that the dissolution, started during milling, was completed with heat treatment. Broadened titanium peaks were visible on the patterns, indicating that Ti had aluminium in solid solution. This also suggested that the heat treatment resulted in the decomposition of residual TiH_2 into Ti and H_2, which would have been given off.

Carbon was expected to also be present in the powder, and was confirmed by EDX analyses of the powders after heat treatment (Table 7.2). Carbon had to be present as a result of contamination by the carbon of the stearic acid which was used as the process control agent (PCA). Stearic acid is a fatty acid with an 18 carbon chain, whose molecular formula is $C_{18}H_{36}O_2$ and the structural formula is $CH_3(CH_2)_{16}COOH$. The contamination by the PCA was inevitable, as milling could not be conducted without it. During milling, there was decomposition of stearic acid, resulting in carbon and oxygen being in the powder. Part of oxygen is also believed to have derived from air during powder handling.

EDX also showed the presence of Fe, Cr, and Ni in the powder, even though no peaks of phases containing those elements were visible on the XRD patterns. This was an indication that these elements were in solid solution, both in the as-mechanically alloyed and the heat treated powders. Iron, chromium and nickel originated from the grinding media used in the milling process. The grinding balls were made of nickel-chromium stainless steel and so contamination with Fe, Cr and Ni could be expected (Suryanarayana, 2004). The contamination by Fe, Cr and Ni of the grinding ball was inevitable and could only be prevented by using other type of grinding balls such as alumina ceramic balls. This could not be done as it was not in the scope of this work.

The XRD patterns of the MA γ-TiAl with additions of 0.5 at.% Pt, Pd and Ir were similar to the patterns of TiAl-0.5 at.% Ru powder after milling, and showed broadened TiH_2, Al and PGM peaks after milling (Figures 7.8 to 7.13), indicating that the crystal sizes decreased towards amorphisation and the processes of TiH_2 decomposition and aluminium-titanium diffusion were not completed after 30 hours of milling. After heat treatment, they showed Ti peaks and one of the peaks from

TiAl, Ti_3Al or $TiAl_3$ (Figures 7.7, 7.9, 7.11 and 7.13). The presence of Ti after heat treatment was a confirmation that the TiH_2 observed in the powder obtained from milling decomposed during heat treatment, released H_2 and gave Ti, which then dissolved aluminium to form (Ti). Studies on the kinetics of the thermal decomposition of titanium hydride powder have shown that above 500ºC, the decomposition of TiH_2 is completed in times shorter than 50 minutes (Sandim *et al.*, 2005; Rasooli *et al.*, 2013). In this work, TiH_2 was heat-treated at 600ºC for 2 hours. The absence of aluminium peaks in the XRD patterns after heat treatment was an indication that, at that stage, all aluminium was now bound in TiAl, Ti_3Al or $TiAl_3$ compounds or dissolved in titanium.

The presence of TiAl and Ti_3Al in the heat treated powders is in agreement with Neves *et al.* (2003) and Shao *et al.* (2015) who found Ti_3Al and TiAl and unreacted Ti, after heating the mechanically alloyed powder for 2 hours at 750ºC for 2 hours. Even though carbon was present in the EDX results (Table 7.2), no carbon-containing phase was visible on the XRD patterns, suggesting that, in each case, carbon was in solid solution. The XRD would only detect free carbon or a carbide if it was present in at least 4 Vol.%. This was not the case in this work.

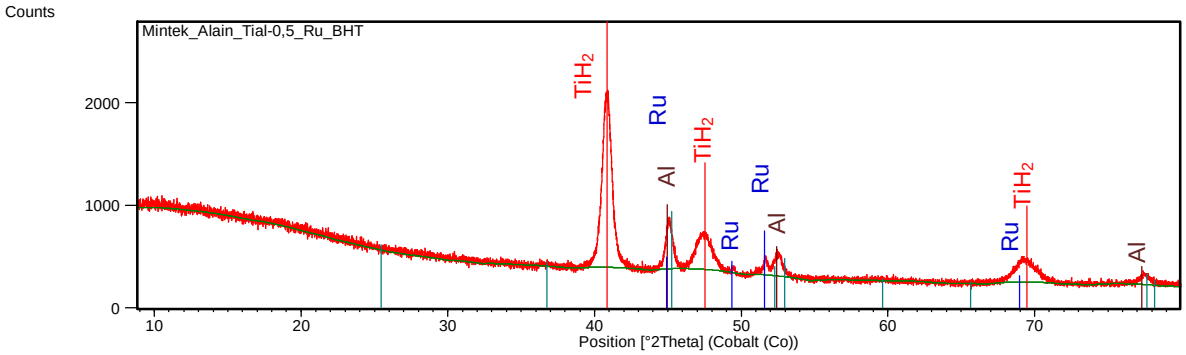


***Figure 7.6**. XRD pattern of mechanically alloyed TiAl-0.5 at.% Ru powder showing (Ru), (Al) and TiH_2 peaks.*

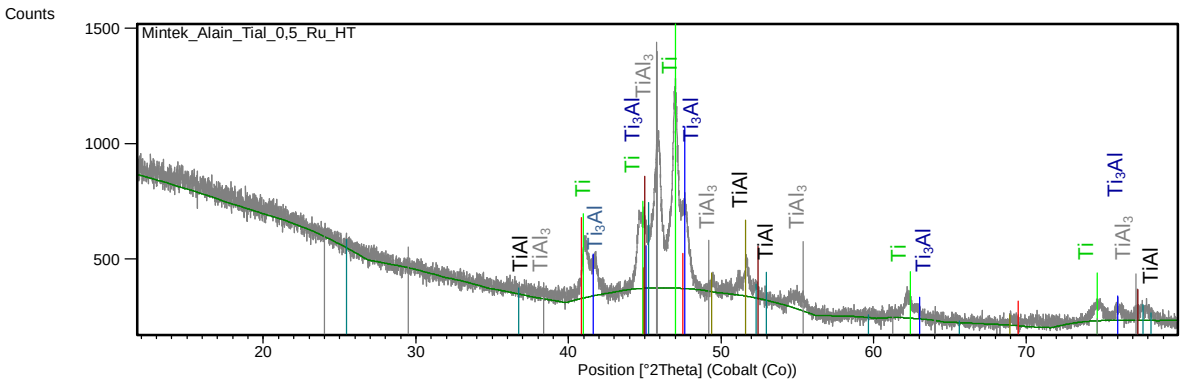


***Figure 7.7**. XRD pattern of TiAl-0.5 at.% Ru powder after heat treatment at 600°C for 2 hours showing TiAl, $TiAl_3$, and (Ti) peaks.*

Table 7.2. *EDX results of the MA and heat treated (HT) powders.*

MA Powder	PGM	Composition (at.%)							
		Ti	**Al**	**PGM**	**Fe**	**C**	**Cr**	**Ni**	**O**
γ-TiAl-0.5 at.% Ru MA	Ru	52.8±4.5	40.3±4.0	0.5±0.1	3.7±0.6	0.7±0.5	1.1±0.1	0.9±0.1	0.2±0.1
γ-TiAl-0.5 at.% Ru HT		51.2±3.9	41.6±1.4	0.5±0.0	3.6±0.2	1.5±0.5	1.0±0.3	0.6±0.1	-
γ-TiAl-0.5 at.% Ir MA	Ir	52.7±3.5	40.7±2.5	0.5±0.1	3.2±0.1	1.4±0.3	0.9±0.1	0.6±0.1	-
γ-TiAl-0.5 at.% Ir HT		53.2±2.5	40.4±3.2	0.6±0.1	3.5±0.3	0.9±0.7	0.9±0.2	0.6±0.1	-
γ-TiAl-0.5 at.% Pd MA	Pd	52.5±3.1	41.9±1.8	0.5±0.1	2.1±0.5	1.1±0.7	1.0±0.4	0.6±0.2	0.5±0.1
γ-TiAl-0.5 at.% Pd HT		52.1±2.7	42.0±0.7	0.6±0.2	2.3±0.3	1.6±0.4	0.8±0.2	0.4±0.1	0.3±0.2
γ-TiAl-0.5 at.% Pt MA	Pt	50.2±2.4	43.3±3.7	0.7±0.2	3.1±0.5	1.6±0.4	0.6±0.1	0.6±0.2	-
γ-TiAl-0.5 at.% Pt HT		51.0±2.6	42.3±2.4	0.6±0.2	3.6±0.3	1.3±0.5	0.8±0.3	0.5±0.1	-

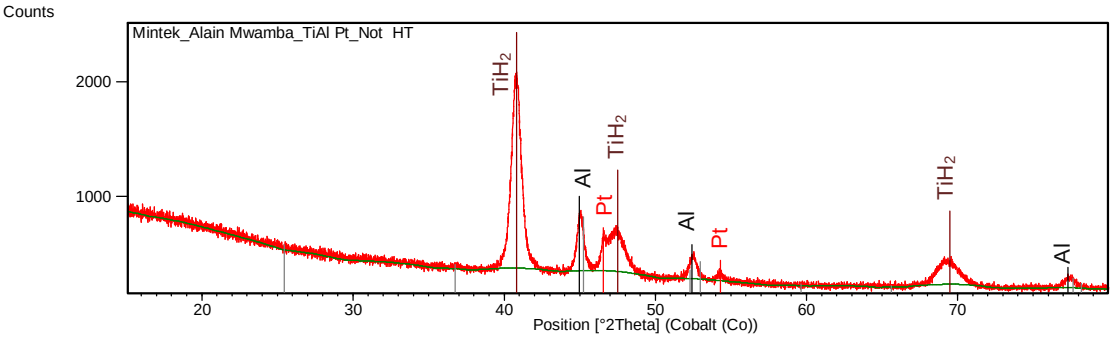


***Figure 7.8**. XRD pattern of mechanically alloyed TiAl-0.5 at.% Pt powder showing (Pt), (Al) and TiH_2 peaks.*

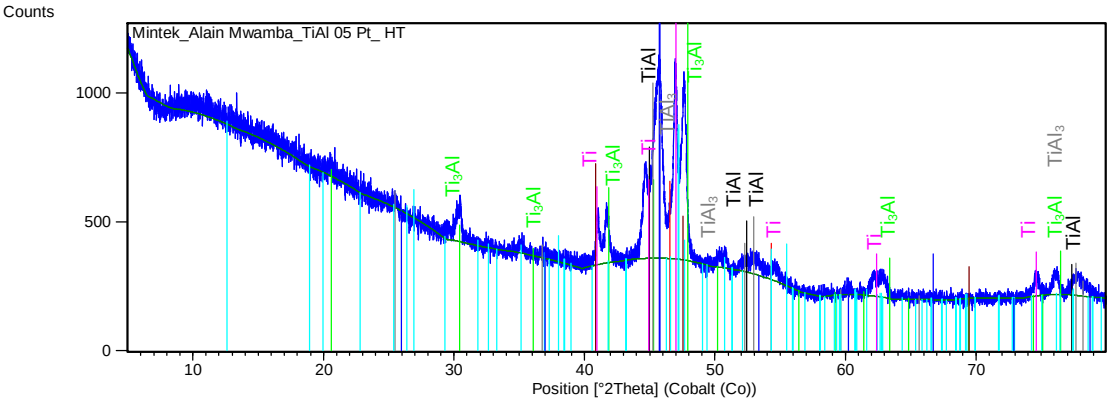


***Figure 7.9**. XRD pattern of TiAl-0.5 at.% Pt powder after heat treatment at 600°C for 2 hours showing TiAl, Ti_3Al, Ti_3Al, and (Ti) peaks.*

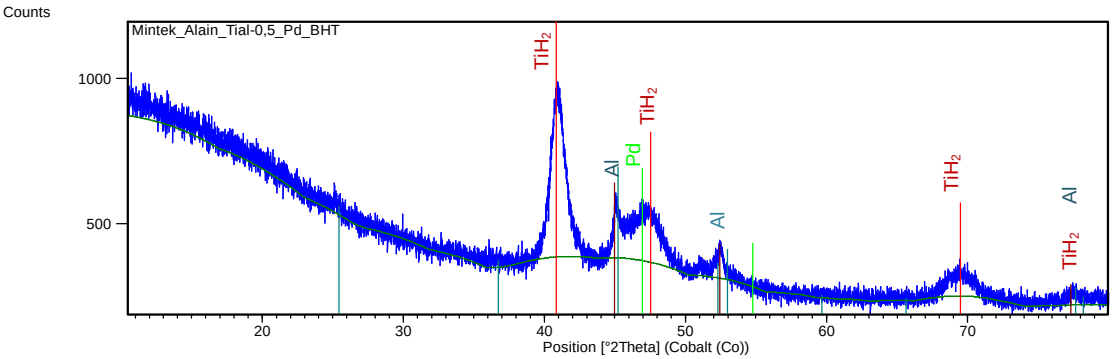


***Figure 7.10**. XRD pattern of mechanically alloyed TiAl-0.5 at.% Pd powder showing (Pd), (Al) and TiH_2 peaks.*

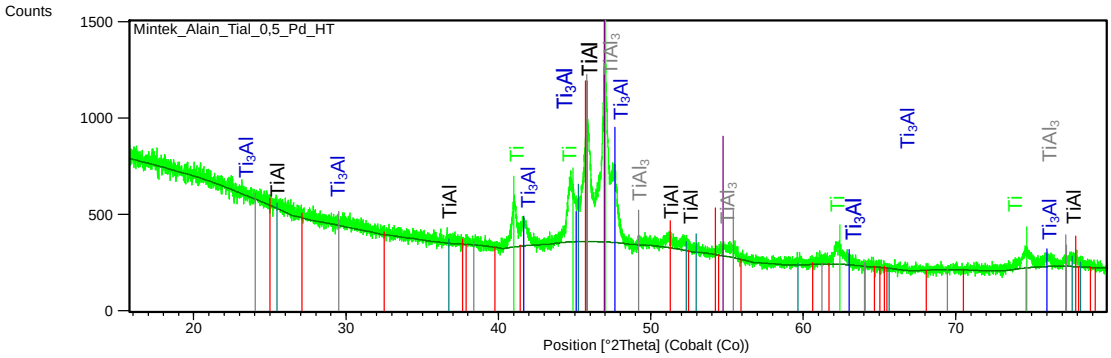


***Figure 7.11**. XRD pattern of TiAl-0.5 at.% Pd powder after heat treatment at 600°C for 2 hours showing TiAl, Ti_3Al, $TiAl_3$ and (Ti) peaks.*

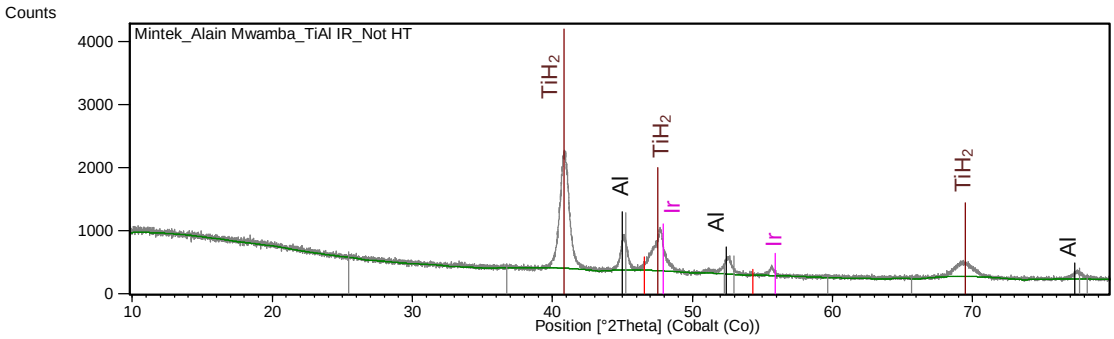


***Figure 7.12**. XRD pattern of mechanically alloyed TiAl-0.5 at.% Ir powder showing (Al), (Ir) and TiH_2 peaks.*

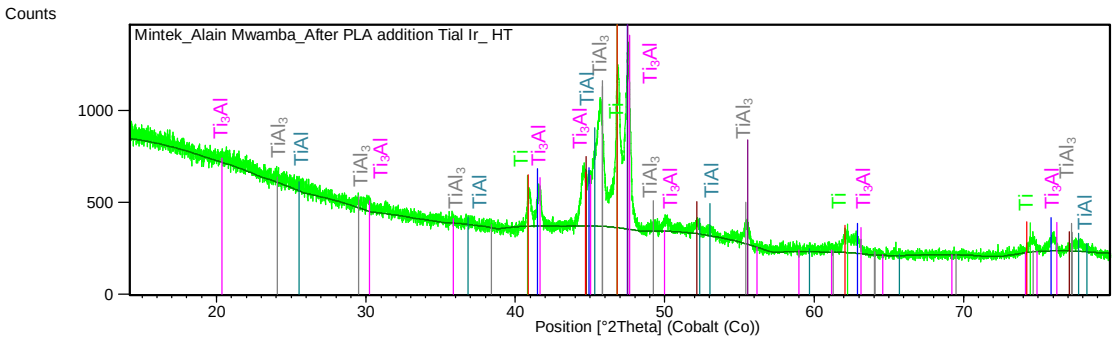


***Figure 7.13**. XRD pattern of TiAl-0.5 at.% Ir powder after heat treatment at 600°C for 2 hours showing TiAl, Ti_3Al, $TiAl_3$ and (Ti) peaks.*

7.3 Transformations upon heating and high-temperature oxidation behaviour

Transformations upon heating and high-temperature oxidation of the powders were examined by simultaneous differential scanning calorimetry (DSC) and thermogravimetric analysis (TGA). Figures 7.14 and 7.15 show the DSC and TGA curves of TiAl-0.5Ru (γ-TiAl-0.5 at.% Ru), TiAl-

0.5Ir (γ-TiAl-0.5 at.% Ir), TiAl-0.5Pd (γ-TiAl-0.5 at.% Pd) and TiAl-0.5Pt (γ-TiAl-0.5 at.% Pt) powders milled for 30 hours. These DSC curves showed narrow exothermic peaks in the temperature range 280-300°C (Figure 14). These peaks corresponded to the decomposition of the stearic acid (Jaw *et al*., 2001) used as PCA. The stearic acid decomposition was illustrated by slight mass losses observed on the TGA curve (Figure 7.15). Except for γ-TiAl-0.5 at.% Ir, the endothermic peaks for γ-TiAl with Pd, Pt and Ru were sharp and high.

Noticeable mass increase during aluminium oxidation started at ~300°C, corresponding to the exothermic peaks observed in Figure 7.14. This oxygen intake occurred in stressed powder particles. The powders under DSC analysis came from a mechanical alloying process, which imparted extensive deformation to the particles and initiated amorphisation. The heat input resulted in material relaxation, which explained the weak endothermic peaks observed between 310°C and 330°C.

As the temperature increased, each powder showed two broad exothermic peaks in the range of 550-600°C and 870-900°C. The exothermic reactions at 550-630°C were the decomposition of residual TiH_2, oxidation of some Ti resulting from the decomposition and the formation of $TiAl_3$, TiAl, Ti_3Al from (Al). This was consistent with the XRD results which showed the presence of these three phases after heat treatment of the powders at 600°C for 2 hours and were thought to have formed during heating of the powders. These exothermic peaks at 550-600°C also explained the absence of the endothermic peaks corresponding to the melting of aluminium between 650-700°C because Al was already bound in $TiAl_3$, TiAl and Ti_3Al or as Al_2O_3. The exothermic peak observed in the 750-950°C range corresponded to the oxidation of TiAl, Ti_3Al and $TiAl_3$ phases.

The γ-TiAl-0.5 at.% Ir showed another behaviour. First, it showed a shorter exothermic peak than other alloys in the temperature range 280-300°C and the occurrence of other peaks with increasing temperature was delayed and peaks were observed at slightly higher temperatures than for other alloys. It also showed an endothermic peak between 650°C and 700°C, which could be attributed to the melting of some residual aluminium. When the formation of a new compound takes place from mechanically alloyed powder during heating in a DTA or DSC cell, the heat released gives rise to an exothermic peak (Lü and Lai, 1998; Suryanarayana, 2004).

Figure 7.15 is TGA curve shows the mass changes that occurred with increasing temperature. As a general trend, the TGA graphs first showed mass losses, between 100°C and 300°C,

followed by mass increase for all samples up to 1050°C, when each run was stopped. This mass increase was due to a continuous oxidation of aluminium and titanium by the oxygen of the air.

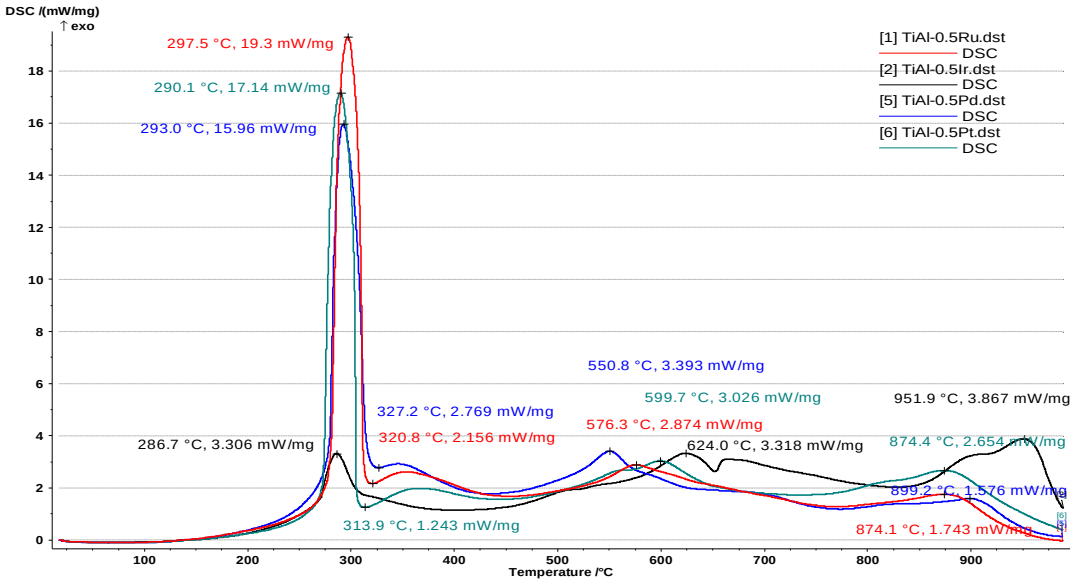


***Figure 7.14**. DSC curves for γ-TiAl-0.5 at.% PGM powders milled for 30 hours.*

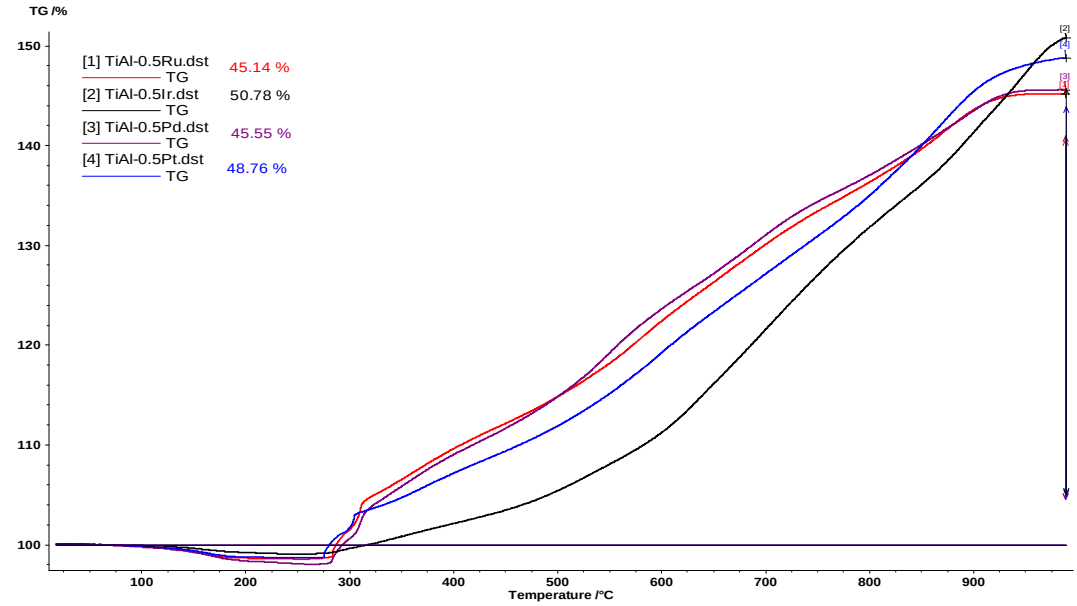


***Figure 7.15**. TGA curves for γ-TiAl-0.5 at.% PGM powders milled for 30 hours.*

7.4 Consolidation by spark plasma sintering (SPS)

After consolidation by spark plasma sintering, PGM-containing powder compacts showed a different microstructure and free elements which would be absent if the γ-TiAl alloys were cast.

These new features were expected to result in unpredictable behaviour of the alloys which could be beneficial or detrimental to the intended target use.

7.4.1 Microstructure

A typical microstructure of a compact obtained from the simultaneous plasma heating and pressing of mechanically alloyed powder is shown in Figure 7.16. The EDX analyses (Table 7.3) show that the compact microstructures contained α_2, γ phase, with dissolved C in γ and α_2, and Al_2O_3, with PGM addition (except Ir) Fe, Ni and Cr in solid solution, even though the sizes of the different phases were too small to analyse accurately, as shown by the higher errors.

The microstructures of the spark-plasma sintered compacts were all similar, except that γ-TiAl-0.5 at.% Ir showed limited iridium dissolution (Figure 7.17), with lighter particles containing Ir in a two-, or three-phase matrix with no Ir. The EDX analyses (Table 7.3) showed that the lightest particles (Area 4 in Figure 7.17) comprised Al (43.3±5.3 at.%), Ti (30.2±4.9 at.%), Ir(24.4±2.4 at.%), which is outside the partial Al-Ir-Ti isothermal section at 1650°C in Figure 2.9 (Raghavan, 2008). The sample were made at 1100°C, which not the same temperature as the isothermal section. The light particle also appeared to be two phase, which further make their identification difficult. However, due to the small size (the coarsest shown in Figure 7.17 was ~4 µm across) of the phases, there would have been some matrix pick-up during EDX analyses. Apart from the presence of these very light and coarse phases (Area 4 in Figure 7.17) in the matrix of γ-TiAl with iridium, the matrices were all similar and showed three areas, denoted on the micrographs as 1, 2 and 3 (Figures 7.16 and 7.17). These areas were impossible to analyse accurately because the different regions were well below 2 µm across, and resulted in very inaccurate analyses. Thus, the results presented here are just indicative. In γ-TiAl-0.5 at.% Pd, γ-TiAl-0.5 at.% Pt and γ-TiAl-0.5 at.% Ru, Area 1 was a phase of high aluminium content, indicating γ-TiAl and Area 2 was a region of high titanium content, which showed one phase, α_2 (Table 7.3). One would have expected to have the alternating lamellae ($\alpha_2+\gamma$) at these compositions, but the spark plasma sintered compacts showed α_2. This indicated that the presence of α_2 phase extended to high aluminium content and lamellae did not develop. Some black, cuboid phases were distributed in the matrix, with an average size of <1 µm across (Area 3 in Figures 7.16 and 7.17), and EDX results indicated much higher oxygen, although they were not determined.

It could be anticipated that the behaviour of the compacts would be different from the cast γ-TiAl alloys due to the presence of the unexpected Fe, Ni, Cr and C contamination (Table 7.3).

Iron, nickel and chromium came from the grinding balls, which consisted of steel containing Cr and Ni used in the mechanical alloying. Carbon came mainly from the stearic acid used as the PCA during mechanical alloying, as well as the carbon sleeves of the sintering furnace.

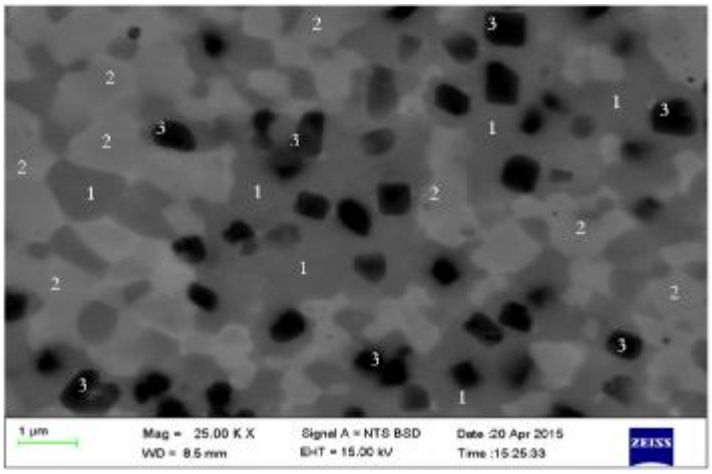


***Figure 7.16**. SEM-BSE image of spark plasma-sintered γ-TiAl-0.5 at.% Pt powders showing the three different phases.*

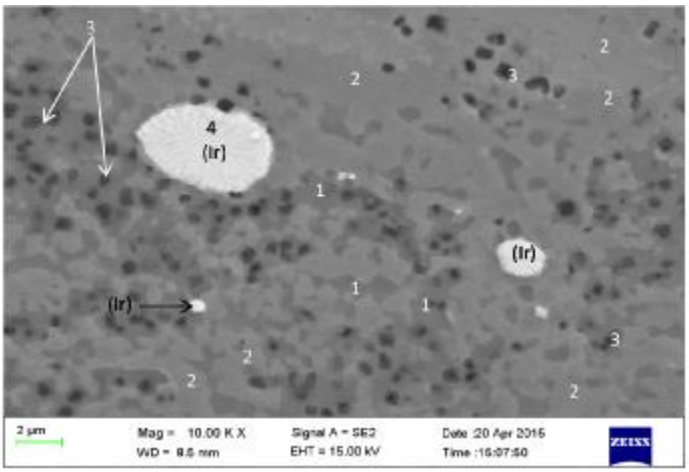


***Figure 7.17**. SEM-SE image of the spark plasma-sintered γ-TiAl-0.5 at.% Ir powders showing the iridium solid solution.*

7.4.2 Hardness

The hardness of the spark plasma sintered compacts is shown in Table 7.4, and the range was the same for the four alloys, with values almost three times the hardness of the cast alloys (~840 HV_5). The significant increase in hardness is believed to come from solid solution hardening due to the elements in solid solution (Fe, Cr, Ni and C) and the fine distribution of phases.

***Table 7.3**. EDX analyses of γ-TiAl-0.5 at.%Pd, γ-TiAl-0.5 at.%Ir and γ-TiAl-0.5 at.%Pt SPS compacts.*

Alloy	**Elements**			
γ-TiAl-0.5 at.% Pd		*Area 1*	*Area 2*	-
	C	0.2±0.1	0.7±0.2	-
	O	0	0	-
	Al	48.0±5.3	43.3±4.6	-
	Ti	44.7±4.9	46.5±5.7	-
	Cr	1.2±1.0	1.7±1.4	-
	Fe	4.6±2.2	6.3±4.7	-
	Ni	0.6±0.5	0.9±0.7	-

	Pd	0.7±0.4	0.6±0.3	-
	Total	100	100	-
	Phases	γ	α_2	-
γ-TiAl-0.5 at.% Ir		*Area 1*	*Area 2*	*Area 4*
	C	0.7±0.8	0.5±0.3	0.4±0.2
	O	0	0	0
	Al	48.8±1.7	45.1±3.3	43.3±5.3
	Ti	45.5±2.1	50.2±4.5	30.2±4.9
	Cr	0.6±0.1	0.6±0.2	0
	Fe	4.0±0.3	3.3±1.9	1.7±2.2
	Ni	0.4±0.03	0.3±0.1	0
	Ir	0	0	24.4±2.4
	Total	100	100	100
	Phases	γ	α_2	(Ir)
γ-TiAl-0.5 at.% Pt		*Area 1*	*Area 2*	-
	C	0.4±0.2	0.5±0.3	-
	O	0	0	-
	Al	47.0±4.3	45.1±3.6	-
	Ti	45.4±3.4	49.3±4.5	-
	Cr	1.3±0.8	0.7±0.2	-
	Fe	4.8±2.5	3.5±2.1	-
	Ni	0.5±0.3	0.4±0.1	-
	Pt	0.6±0.2	0.5±0.3	-
	Total	100	100	-
	Phases	γ	α_2	-
γ-TiAl-0.5 at.% Ru		*Area 1*	*Area 2*	-
	C	0.8±0.1	0.7±0.3	-
	O	-	-	-
	Al	45.8±0.7	43.4±0.9	-
	Ru	3.3±0.5	1.6±0.7	-
	Ti	38.3±1.2	48.1±1.5	-
	Cr	2.3±0.3	1.2±0.3	-
	Fe	9.4±0.8	4.5±1.0	-
	Ni	-	0.5±0.2	-
	Total	100	100	-
	Phase	γ	α_2	-

Table 7.4. *Vickers hardness of compacts obtained by SPS.*

Vickers hardness with 5 kg load				
Alloy	**TiAl-0.5 at.% Ru**	**TiAl-0.5at.% Pd**	**TiAl-0.5at.%Pt**	**TiAl-0.5 at.% Ir**
HV5	837±15	846±14	834±14	837±13

7.5 Discussion

The apparent density of the mechanically alloyed γ-TiAl powders was about 1.06 g/cm^3. The density of the cast γ-TiAl was ~4.5 g/cm^3 and the density of the spark plasma sintered compacts

was ~4.2 g/cm^3. The four γ-TiAl powders showed a trend toward a bimodal or even multimodal distribution, due to the agglomeration of fine particles.

The powders consisted of very fine particles of rounded irregular and angular morphology. Many individual particles were smaller than 1 μm. In the midst of the fine particles were large particles with sizes varying from 50 to 500 μm, as a result of high agglomeration. Particle agglomeration can occur after the size particle decreases, because of the increase of the surface area and energy, and subsequent increased reactivity between particles. Attraction between powder particles occurs when the sum of separation forces in the system is smaller than the attraction forces between the adhering particles (Pietsch, 2004).

The γ and α_2, phases were observed only after heat treatment, showing that both milling and heat treatment were necessary to form the phases. The Al peaks also broadened and shifted slightly towards smaller 2θ angles on the XRD pattern. The breaking of powder particles to very fine size during milling would cause broadening, but the shift was due to alloying. The broadening of TiH_2 peaks was also from particle size reduction to the nano-size during milling. TiH_2 is a very brittle material and readily broke during milling. Reaction of aluminium to form new phases only took place during heat treatment. The heat treatment was conducted at 600°C, a temperature where Al atoms actively diffuse. The appearance of TiAl, Ti_3Al and $TiAl_3$ peaks on the XRD patterns of the heat-treated powders was due to the diffusion and reaction of aluminium. All PGMs (Ir, Ru, Pd and Pt) disappeared in (Ti), (Ti_3Al), (TiAl), and ($TiAl_3$) solid solutions after heat treatment.

Carbon was expected to also be present in the powder as a result of contamination by the stearic acid ($C_{18}H_{36}O_2$) which was used as the process control agent (PCA). The contamination by the PCA was inevitable, as milling could not be conducted without PCA, and it was difficult to remove. During milling, there was decomposition of stearic acid resulting in carbon and oxygen being in the powder. Part of oxygen is also believed to have derived from air during powder handling.

Iron, chromium and nickel were present in the powder in solid solution, both in the mechanically alloyed and the heat treated powders. These elements originated from the grinding media used in milling, because the grinding balls were made of nickel-chromium stainless steel and so contamination with Fe, Cr and Ni occurred.

When the powders were heated in air, oxidation occurred as a result of aluminium and titanium reaction with oxygen of the air. Reactions started by a mass loss from the hydrogen release of

residual TiH_2, which was followed by a continuous oxidation of the powder expressed by a continuous mass increase up to the test end.

The compacts obtained by spark plasma sintering showed different hardnesses and microstructures from cast alloys and lower densities than cast γ-TiAl alloys. The hardness of the spark-plasma sintered compacts was higher than the hardness of the cast alloys. This sharp increase in hardness was due to the change in microstructure.

Instead of the lamellar and γ-TiAl grains of the cast γ-TiAl alloys, a homogeneous lamellar-free microstructure consisting of α_2 and γ-TiAl phases, Al_2O_3, PGMs (except Ir), Fe, Ni and Cr dissolved in γ-TiAl and Ti_3Al. There was no $TiAl_3$. The formation of carbides was unlikely, probably because of the low carbon content. The solubility limits are around 1 at.% C for α_2 and γ, which are higher than the value in Table 7.3, indicating that C was dissolved in these solids. Precipitates such as Ti_3AlC and Ti_2AlC and Ti_3AlC_2 can only exist at high temperature (Tian and Nemoto, 1999). They could form during spark plasma sintering which was carried out at 1200°C, especially given that there are phase fields of Ti_2AlC+TiAl+Ti_2Al and Ti_2AlC+Ti_3AlC+Ti_3Al in the isothermal sections of the Ti-Al-C system at 1000°C, 1100°C and 1300°C (Cam *et al.*, 1991; Okamoto, 1992; Bandyopadhyay *et al.*, 2000; Riaz *et al.*, 2000; Hayes *et al.*, 2009).

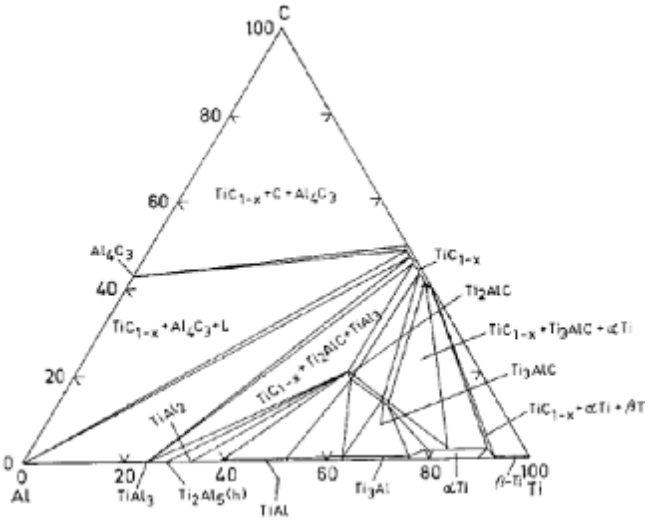


***Figure 7.18**. Isothermal section of Ti-Al-C system at 1000°C (Bandyopadhyay et al., 2000).*

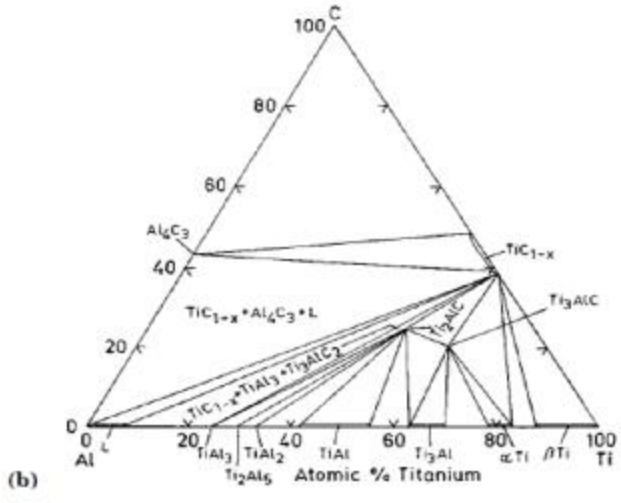


***Figure 7.19**. Isothermal section of Ti-Al-C system at 1100°C (Bandyopadhyay et al., 2000).*

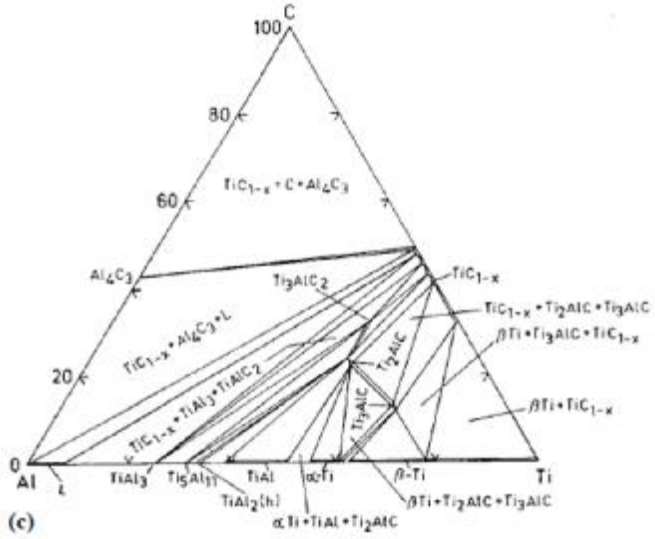


***Figure 7.20**. Isothermal section of Ti-Al-C system at 1300°C (Bandyopadhyay et al., 2000).*

CHAPTER 8

COLD SPRAY COATING

8.1 Process optimisation

The first step of the coating procedure was using the optimized parameters (Hussain, 2012; Jeandin *et al.*, 2013; King *et al.*, 2013; Mordi *et al.*, 2014) of the spray process, which included the temperature (T), pressure (P), powder feed rate (F) and gun nozzle-substrate inter-distance (d). In Table 8.1, P, F, and d were kept constant with a varying temperature. The substrates were Titanium Grade 2 and Ti-6Al-4V of mass m_1 before coating and mass m_2 after coating and mass change was Δm and, where $\Delta m = (m_2-m_1)$, and $\Delta m\ \% = [(m_2-m_1)/m_1] \times 100$. Although the results of TGA showed mass decrease up to 1.0 at.% Pt addition and up to 1,5 at.% Pd and 1.5 at.% Ir additions, the corrosion results showed that 1.0 at.% PGM additions or more was not beneficial. On that basis, and trying to minimise the amount of PGM added, an addition of 0.5 at.% PGM was chosen, also without introducing the more PGM-rich phases, which were deleterious. Thus, the coating materials were γ-TiAl a with 0.5 at.% PGM (Pt, Pd, Ru and Ir) additions.

The temperature and the feeding rate were optimised. Several runs with the conditions in Table 8.1 were conducted for temperature optimisation. In Table 8.2, T, P and d were kept constant with a varying feed rate. Tables 8.1 to 8.5 show the results of optimisation tests, run to determine the optimal conditions for coatings. These results showed that the optimal parameters for coating operations were:

- Temperature, T = 550 °C
- Pressure, P = 145 bars
- Working distance (distance between the gun nozzle and the substrate), d = 10 mm
- Feed rate, f = 20.

Table 8.1. *Coating parameters for Titanium Grade 2 substrate with γ-TiAl with 0.5 at.% Pt powder.*

Run number	T (°C)	P (bars)	Feed rate,	d (mm)	m_1 (g)	m_2 (g)	Δm (%)
1-1	450	145	10	10	6.675	6.685	0.15
1-2	500	145	10	10	6.672	6.700	0.12
1-3	550	145	10	10	6.679	6.689	0.15

Table 8.2. *Coating parameters for titanium Grade 2 substrate with γ-TiAl with 0.5 at.% Ru powder.*

Run number	T (°C)	P (bars)	Feed rate	d (mm)	m_1 (g)	m_2 (g)	Δm (%)
2-1	550	145	10	10	6.733	6.739	0.09
2-2	550	145	20	10	6.776	6.790	0.20
2-3	550	145	40	10	6.614	6.629	0.23

Table 8.3. *Coating parameters for titanium Grade 2 substrate with γ-TiAl with 0.5 at.% Ir powder.*

Run number	T (°C)	P (bars)	Feed rate	d (mm)	m_1 (g)	m_2 (g)	Δm (%)
3-1	550	145	10	10	14.032	14.072	0.29
3.2	550	145	20	10	14.035	14.090	0.39
3.2	550	145	40	10	14.043	14.078	0.25

Table 8.4. *Coating parameters for Ti-6Al-4V substrate with γ-TiAl with 0.5 at.% Ir powder.*

Run number	T (°C)	P (bars)	Feed rate,	d (mm)	m_1 (g)	m_2 (g)	Δm (%)
4-1	550	145	10	10	5.171	5.188	0.32
4-2	550	145	20	10	5. 376	5.401	0.47
4.3	550	145	40	10	5. 394	5.414	0.37

Table 8.5. *Coating parameters for Ti-6Al-4V substrate with γ-TiAl with 0.5 at.% Ir powder.*

Run number	T (°C)	P (bars)	Feed rate,	d (mm)	m_1 (g)	m_2 (g)	Δm (%)
5-1	550	145	20	10	5.522	5.538	0.29
5-2	550	145	20	10	4.925	4.947	0.45
5.3	550	145	20	10	5.573	5.591	0.32

8.2 Surface preparation

Surface preparation for coating was performed using alumina blasting. As surface preparation techniques for cold spraying, silica or alumina blasting are more efficient than chemical techniques (Jeandin *et al.*, 2013; Mordi *et al.*, 2014), not only because they break and remove the fine oxide layer but they also create on the substrate surface the irregularities needed for good adhesion of the coating powder particles. Surface preparation by alumina blasting was the only standard technique available for cold spraying.

8.3 Characterisation of the substrates and coatings

8.3.1 Chemical composition and hardness of the substrates

Two substrates were chosen for the coating with MA γ-TiAl, commercially pure Titanium Grade 2, referred to in this work as Titanium Grade 2 and Ti-6Al-4V. As per ASTM specification (ASTM B265-13ae1, 2013), the standard Titanium Grade 2 composition is shown in Table 8.6. The Vickers hardness of Titanium Grade 2 is about 200 HV_{10} when as-cast, and 145 HV_{10} when

annealed. In this work, the hardness of the Titanium Grade 2 was 222±5HV_{10}. The Titanium Grade 2 substrate was cast and rolled (rolled coupon). Tables 8.6 and 8.7 indicate that the itanium Grade 2 in this work had lower impurities than the standard Titanium Grade 2, and that the Ti-6Al-4V was within the specifications of the standard materials. Table 8.7 gives the composition of Ti-6Al-4V as provided by Carpenter and Arcam, ASM specification and this work (AAS).

Table 8.6. *Standard composition of Titanium Grade 2.*

Titanium grade 2 composition (wt%)		
Element	ASTM standard composition	AAS obtained composition
Ti	99.2	99.5±0.01
C	≤0.1	0.01±0.005
Fe	≤ 0.3	0.09±0.01
H	≤0.015	-
N	≤ 0.03	-
O	≤ 0.25	-

Table 8.7. *Composition of Ti-6Al-4V.*

	Ti-6Al-4V composition (wt%)		
Elements	Carpenter, Arcam (2016)	ASTM stand. composition	ASS composition
Ti	88.75-91.0	90.0	90.10
Al	5.50-6.75	6.0	6.05
V	3.50-4.50	4.0	3.56
C	0.10	-	-
Fe	0.40	0.25	0.14
H	0.015	-	≤ 0.20
N	0.05	-	≤ 0.03
O	0.020	0.2	≤ 0.25
Others	0.040	-	≤ 0.30

8.3.2 Microstructure of the substrate

8.3.2.1 Ti-6Al-4V alloy

Phases reported in the Ti-6Al-4V microstructure include α matrix, usually dark in contrast, and β phase, bright contrast, distributed in the matrix. Typical microstructures of annealed Ti-6Al-4V are shown in Figure 8.3 (Andrade *et al.*, 2010; Moskalewicz *et al.*, 2010).

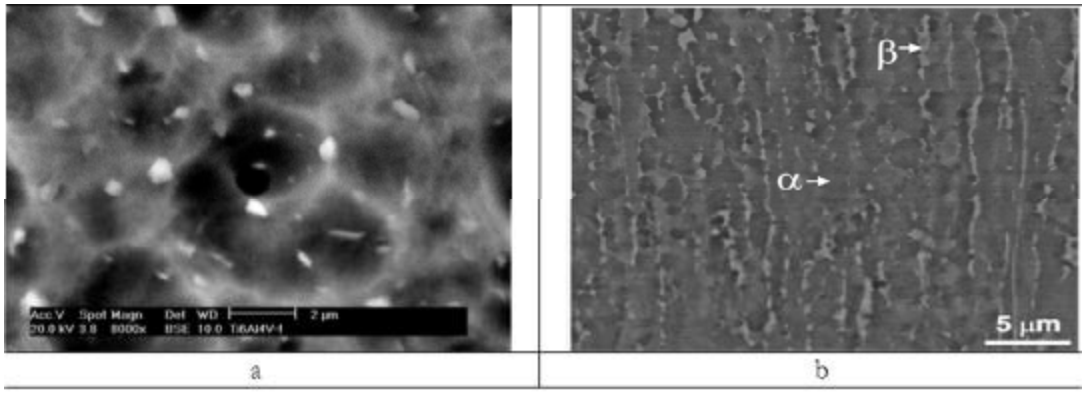


Figure 8.1*. SEM-BSE images of Ti-6Al-4V: (a) annealed at 800°C for two hours (Andrade et al., 2010) and (b) hot rolled and annealed 750°C for 2 hours (Moskalewicz et al., 2010).*

The microstructure of the Ti-6Al-4V substrate used in this work is shown in Figure 8.4. It consisted of a matrix of primary α phase (dark) with the β phase, bright and alingned in the matrix, typical of hot rolled and annealed alloys. The substrate was cut from a metal sheet, which went through a process of hot rolling and annealing. The overall composition of the substrate in Table 8.9 was 90.5±0.3 Ti-5.8±0.2 Al-3.7 V (wt%), typical of the Ti-6Al-4V alloy (Table 8.9: Area 1). The bright phase (Figure 8.4: Area 2) was too small to analyse by itself, and the result in Table 8.9 gives more Ti and Al from the surrounding matrix. The actual composition should be extrapolated away from the matrix. The contrast difference in areas 1 (dark matrix) and 2 (bright) was due to the V content, which was assumed to have been higher in area 2 than in area 1. Based on the BSE imaging mode, Area 2 with more V (heavier metal) and less Al (lighter metal) was expected to have a bright contrast, and the matrix (Area 1) with more aluminium and less V than Area 2 had a dark contrast. The hardness was 378±10 HV_{10}.

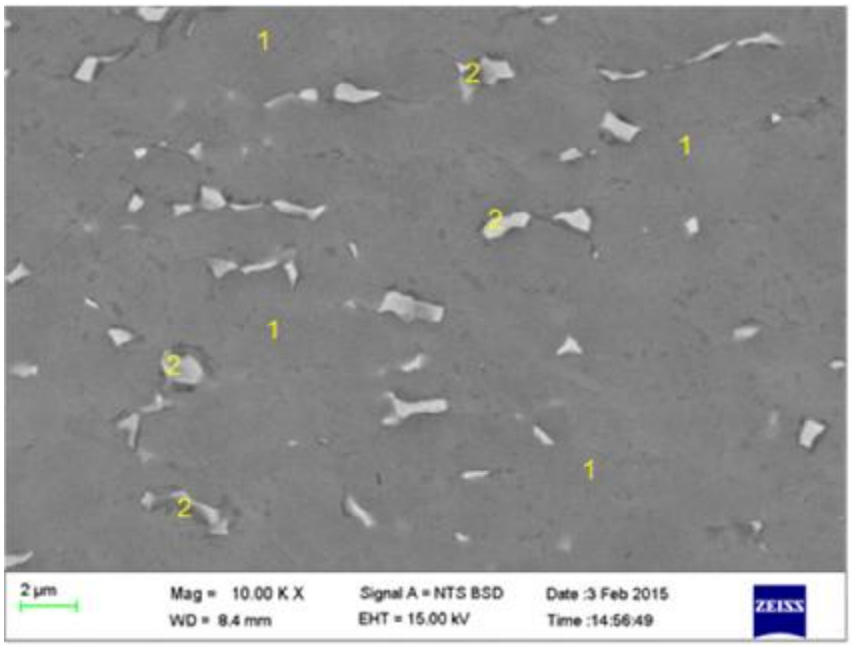


***Figure 8.2**. BSE image of the Ti-6Al-4V microstructure.*

***Table 8.8.** EDX analyses of Ti-6Al-4V substrate.*

Area	Contrast	Phases	Composition (at.%)		
			Ti	Al	V
Overall	-	α+β	86.8 ± 0.5	9.9 ± 0.3	3.3 ± 0.2
1	Matrix	α	87.2 ± 0.3	10.2 ± 0.1	2.5 ± 0.3
2	Bright	β	80.9 ± 1.9	7.2 ± 0.4	11.9 ± 2.3

8.3.3 Coating microstructure

The microstructure of the coating substrate and coating is shown in Figure 8.5 for titanium Grade 2 and Figure 8.6 for Ti-6Al-4V. The thickness of the coating was not constant. Ten measurements at different positions gave an average thickness of 19.1±7.4 µm. The large errors on thickness were due to process control issues. The adherence of successive coating layers onto the layer adjacent to the substrate was very difficult, resulting in material loss and high variation in coating thickness.

A typical microstructure of the the coating is shown in Figure 8.7, which is a higher magnification image of an area of the coating in Figure 8.6, showing the different phases. The results of EDX analyses of the coating are shown in Table 8.10. Similar microstructures were found for Pd-, Pt- and Ru-alloyed γ-TiAl coatings and are shown in Figure 8.8. Overall, the microstructures consisted of γ-TiAl, Al_2O_3, PGM particles with Al and Ti in solid solution, (Ti)

and (Al). This micrograph shows that regardless of the powder used, and apart from the PGM-containing phase, all phases mentioned above were present.

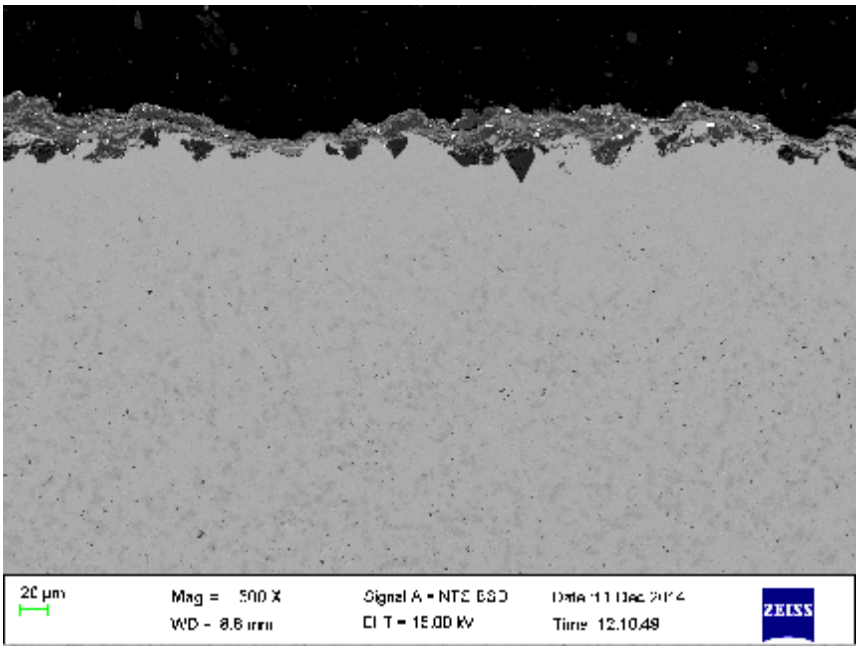


***Figure 8.3**. SEM-BSE image of the titanium Grade 2 substrate and the iridium-alloyed coating.*

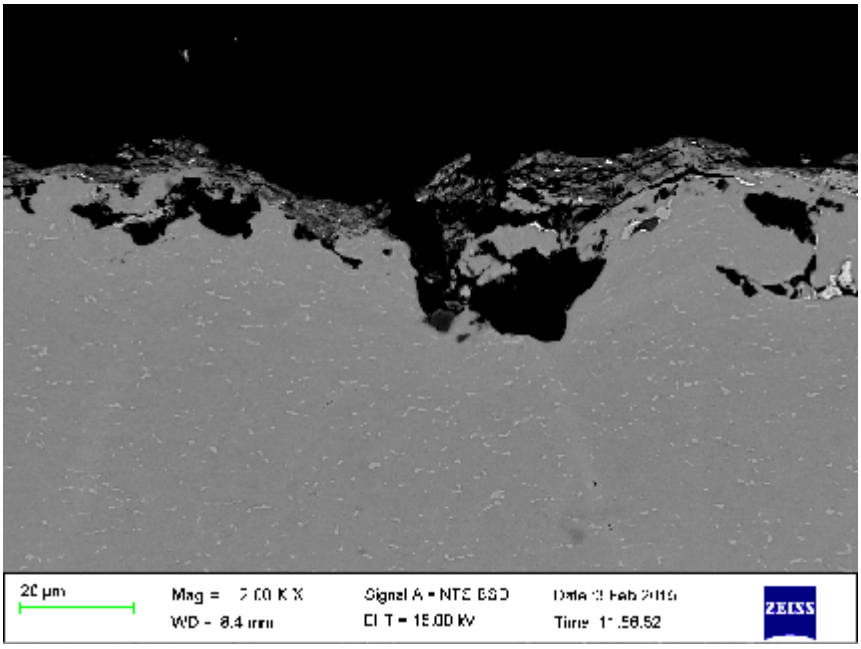


***Figure 8.4**. SEM-BSE image of the titanium Grade 2 substrate and the iridium-alloyed coating.*

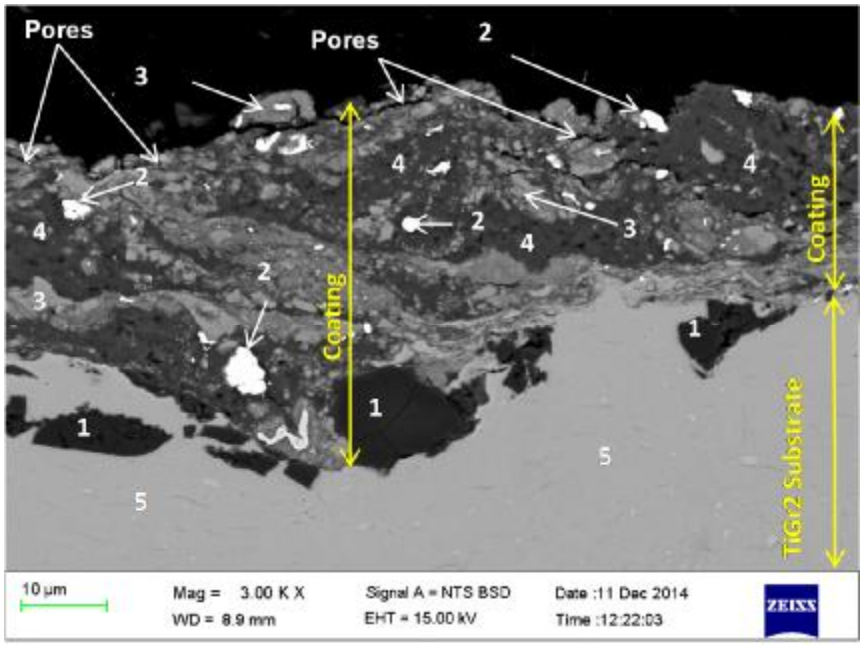


***Figure 8.5**. SEM-BSE image of the iridium-alloyed coating on titanium Grade 2 showing the different phases in Table 8.10.*

***Table 8.9.** EDX analyses of the titanium Grade 2 coating layer with Ir.*

Area	Element content (at.%)						Phases
	O	Al	Ti	Fe	Cr	Ir	
Overall	25.7±5.0	42.5±8.3	30.6±8.9	0.6±0.2	0.13±0.05	0.5±0.2	γ-TiAl + Al_2O_3
1	6.5±1.2	33.0±1.1	0.6±0.1	-	-	-	Al_2O_3
2	5.5±0.2	4.7±0.2	6.5±0.3	-	-	83.3±4.2	Ir (Al,Ti)
3	31.6±1.7	34.6±2.5	33.1±2.0	0.6±0.1	-	-	γ-TiAl + Al_2O_3
4	9.3±1.6	88.6±2.3	1.8±1.0	0.3±0.1	-	-	Al + Al_2O_3
5	-	-	100	-	-	-	(αTi)
6	-	-	-	-	-	-	Pores

8.3.3.1 Titanium Grade 2

The microstructure of the titanium Grade 2 substrate is shown in Figures 8.1 and 8.2. It consisted of a matrix of primary α phase (grey) with TiH_2 phase (dark) evenly distributed in the matrix. At high magnification in Figure 8.2, additional phases were visible (bright phase). The chemical composition of the different phases in the titanium Grade 2 is shown in Table 8.10. The EDX results showed that the grey matrix and dark phase distributed in the matrix were 100 at.% Ti and were assumed to be α (the matrix) and TiH_2 (hydrogen could not identified by the detector). The EDX results of the bright phase showed that it contained Fe in addition to Ti. However, these phases were too small to measure accurately and were assumed to be βTi. Due

to their small sizes, the dark phase could not be measured accurately, but the real value would have less Ti because the result was increased by the surrounding Ti.

Table 8.10. *EDX analyses of the titanium Grade 2 substrate.*

Area	**Elemental content (at.%)**					**Phases**
	Ti	Al	Fe	Cr	Si	
1 (Dark)	100	-	-	-	-	(αTi)
2 (Grey)	100	-	-	-	-	TiH_2
3 (Bright)	95.3±0.8	-	4.7±0.8	-	-	βTi

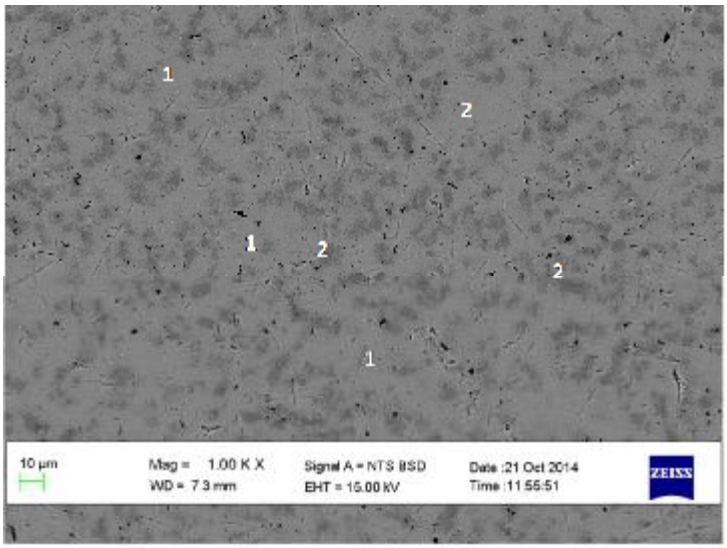


Figure 8.6*.SEM-BSE image of the titanium Grade 2 microstructure showing (1) (αTi) and (2)* TiH_2.

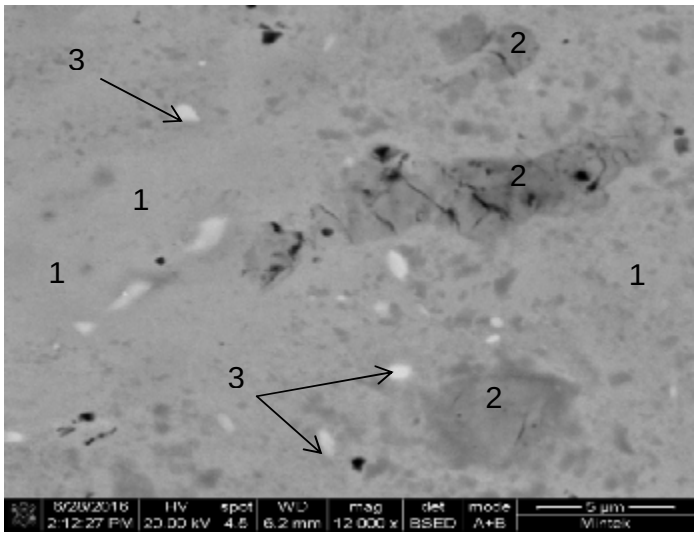


Figure 8.7*. SEM-BSE image of the titanium Grade 2 microstructure showing (1) (αTi), (2)* TiH_2 *and (3) bTi*

8.3.4 Interface analysis

The interface between the substrate and the coating layer was irregular and heterogeneous. In some places, there was direct contact between the coating and the substrate, and in other places there were Al_2O_3 particles from the alumina powder blasting, partly or completely embedded in the substrate. A typical interface is shown in Figures 8.9a for a titanium Grade 2 substrate. It shows particles of Al_2O_3 embedded in the substrate and the irregular curve of the interface. There was a coating-affected zone (CAZ) in Figure 8.9a, where all the dark contrasts identified in the titanium Grade 2 substrate before coating were no longer present, indicating that a phase dissolution took place during the coating process, due to the heat generated.

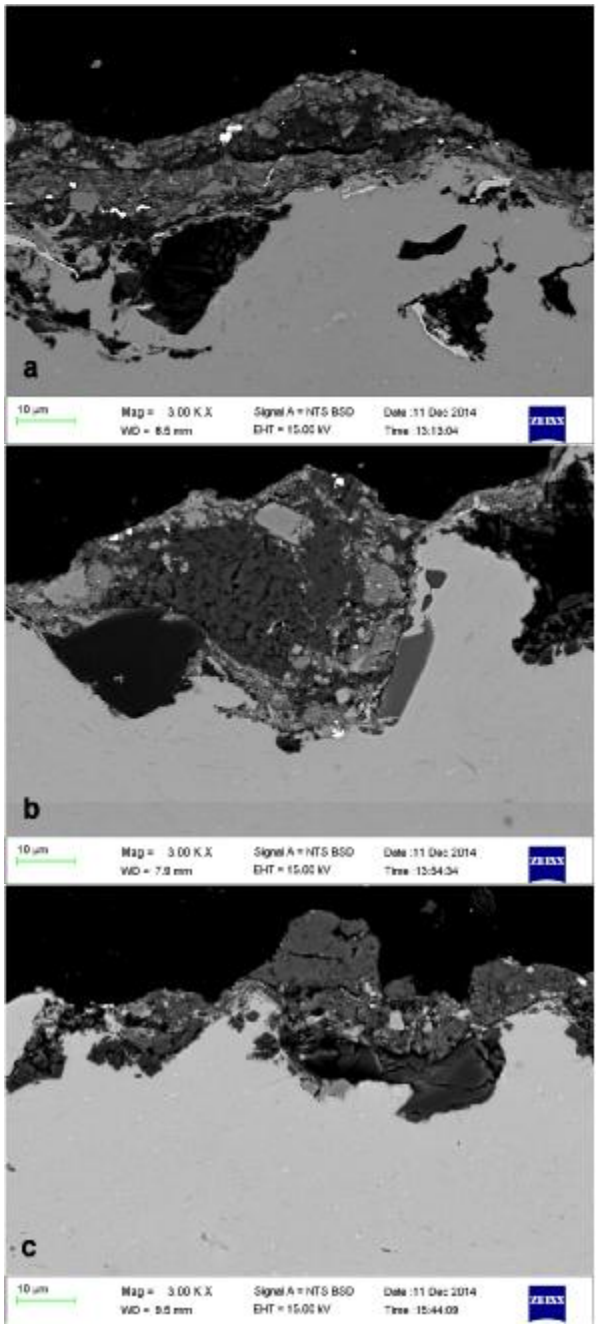


***Figure 8.8**. SEM-BSE images of γ-TiAl coating layer with 0.5 at% (a) Pt, (b) Pd and (c) Ru additions on titanium Grade 2 substrate.*

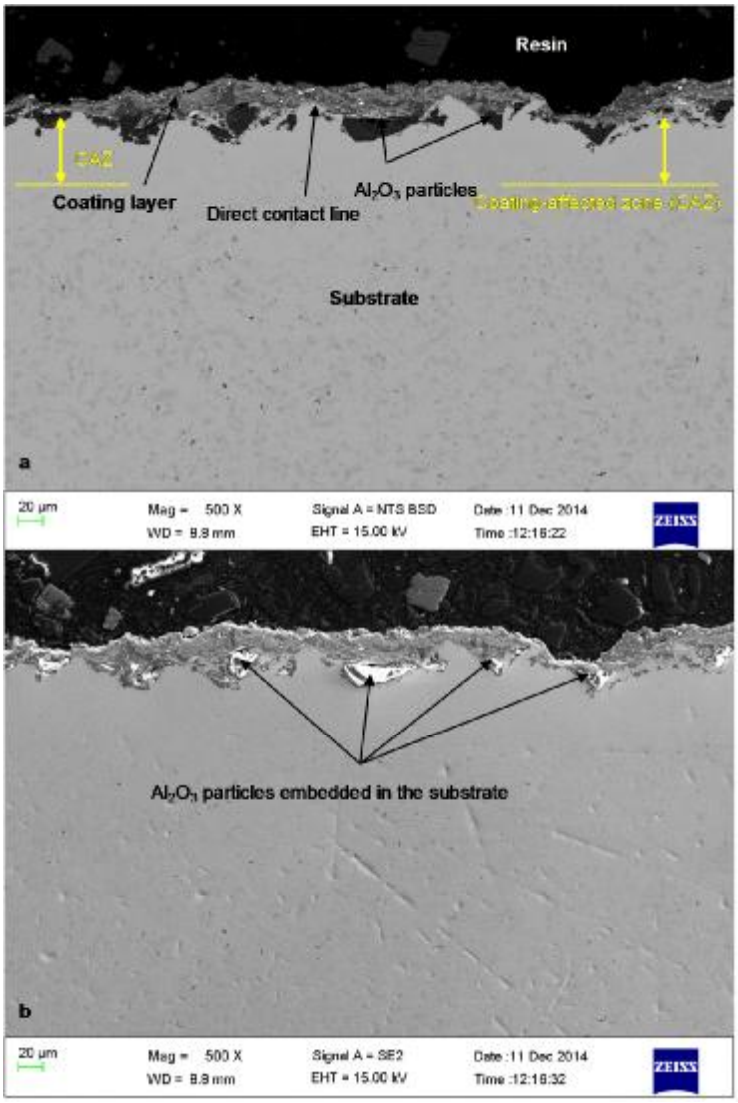


***Figure 8.9**. Titanium Grade 2 substrate-coating layer interface for coating of γ-TiAl with Ir: (a) SEM-BSE image and (b) SEM-SE image.*

8.4 Effect of heat treatment on the Ti-6Al-4V and titanium Grade 2 substrates

The effect of heat treatment was assessed on coated and uncoated surfaces of Ti-6Al-4V and titanium Grade 2 substrates. From the microstructural data available in the literature on phase compositions in Ti-6Al-4V (Peterson, 2011; Jha *et al.*, 2015), the average composition is shown in Table 8.11.

***Table 8.11.** EDX analyses of the α and β phases in Ti-6Al-4V (Peterson, 2011 and Jha et al., 2015).*

Ti-6Al-4V phase composition						
Phases	Ti		Al		V	
	wt%	at.%	wt%	at.%	wt%	at.%
(αTi)	92.8±0.8	88.7±0.9	6.1±0.8	10.3±0.7	1.1±0.5	1.1±0.5
(βTi)	89.8±0.8	88.9±0.7	4.8 ±0.8	8.2±0.8	5.4±2.3	4.9±2.7

The results of EDX analyses are shown in Tables 8.12 and 8.13 for the coated and uncoated surfaces of the Ti-6Al-4V substrates. The coated side showed some protection due to the presence of iridium-alloyed γ-TiAl coating (Figure 8.10 a: Area 1). A zone with only pure αTi was adjacent to the coating (Figure 8.10 a: Area 2), followed by a zone consisting of αTi+β (Area 3), (Table 8.12: Area 2). In addition, from the outer to inner position on the substrate (from bottom to top), the bright phases in Area 3 decreased in size, changed in morphology and were more dispersed compared to Area 4, which was the unchanged part of the substrate.

The uncoated side of the samples was oxidised, resulting in the formation of an oxide layer, with a total thickness of 10.2±0.5 μm. The microstructure of the oxide layer consisted of four areas. Area 1 consisted of mainly TiO_2, and aluminium oxide was present and no vanadium oxide. Below Area 1 was Area 2, a layer consisting of mixed oxide with TiO_2 being the main phase. Aluminium and vanadium were present, probably as oxides. Area 3 had the composition of Ti-6Al-4V (Table 8.13). The microstructure was different from that of the rolled Ti-6Al-4V described above. Area 4 had the composition and microstructure typical to Ti-6Al-4V.

Table 8.12. *EDX analyses of the different layers of the oxidation affected zone of the coated Ti-6Al-4V (Figure 8.10a).*

Elements	**Composition (at.%)**		
	Area 2	Area 3	Area 4
O	0	0	0
Al	23.9±3.2	10.9±0.5	10.6±0.5
Ti	73.5±3.4	85.8±0.5	85.5±0.5
V	2.7±0.8	3.6±0.1	3.9±0.1
Phases	(αTi)	(αTi)+(βTi)	(αTi)+(βTi)

Table 8.13. *EDX analyses of the different layers of the oxidation affected zone of the uncoated Ti-6Al-4V (Figure 8.10b).*

Elements	**Composition (at.%)**			
	Area 1	Area 2	Area 3	Area 4
O	71.0±0.7	65.5±5.0	0	0
Al	0.3±0.1	3.1±1.1	11.2±1.1	10.2±1.1
Ti	28.7±0.5	29.6±0.8	85.5±1.3	86.1±1.3
V	0	1.8±1.3	3.3±0.1	3.7±0.1
Phases	TiO_2, Al_2O_3	TiO_2, Al_2O_3, V	α+β	α+β

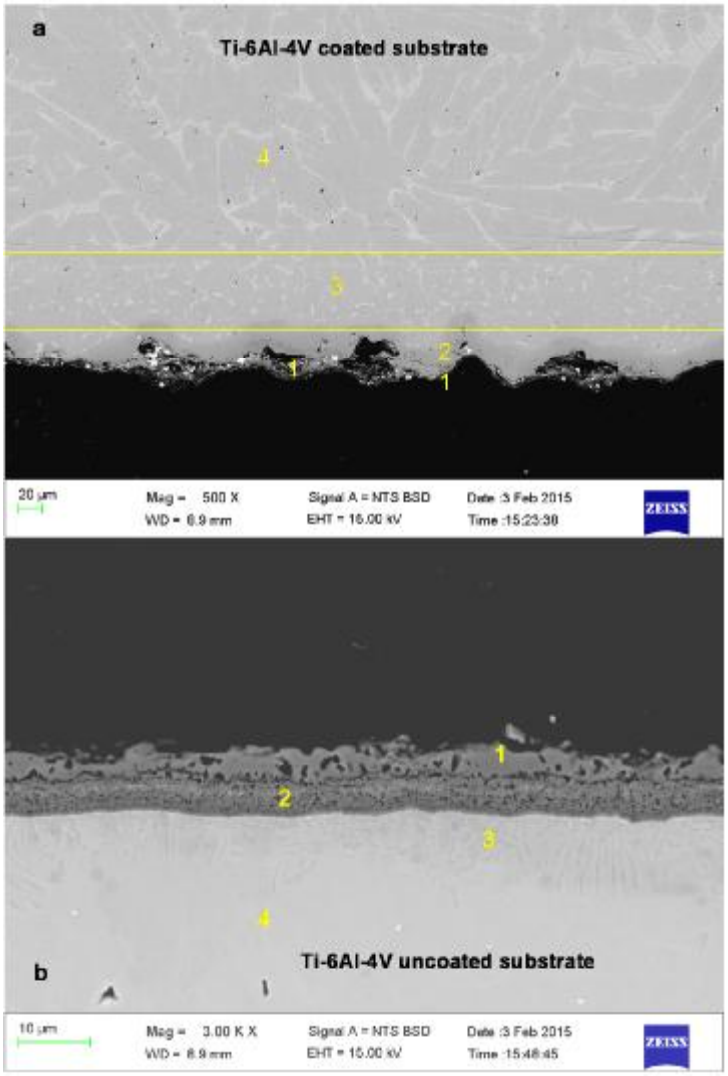


***Figure 8.10**. SEM-BSE images of cross-sections of: (a) coated, and (b) uncoated substrates of oxidised Ti-6Al-4V substrate.*

On the titanium Grade 2 substrate, the coated side did not show any oxidation under the Ir-alloyed γ-TiAl coating (Figure 8.11). A coating-affected zone was present, without the dark (β) phase. Below the coating-affected zone was the normal microstructure typical of titanium Grade 2 as shown in Table 8.8.

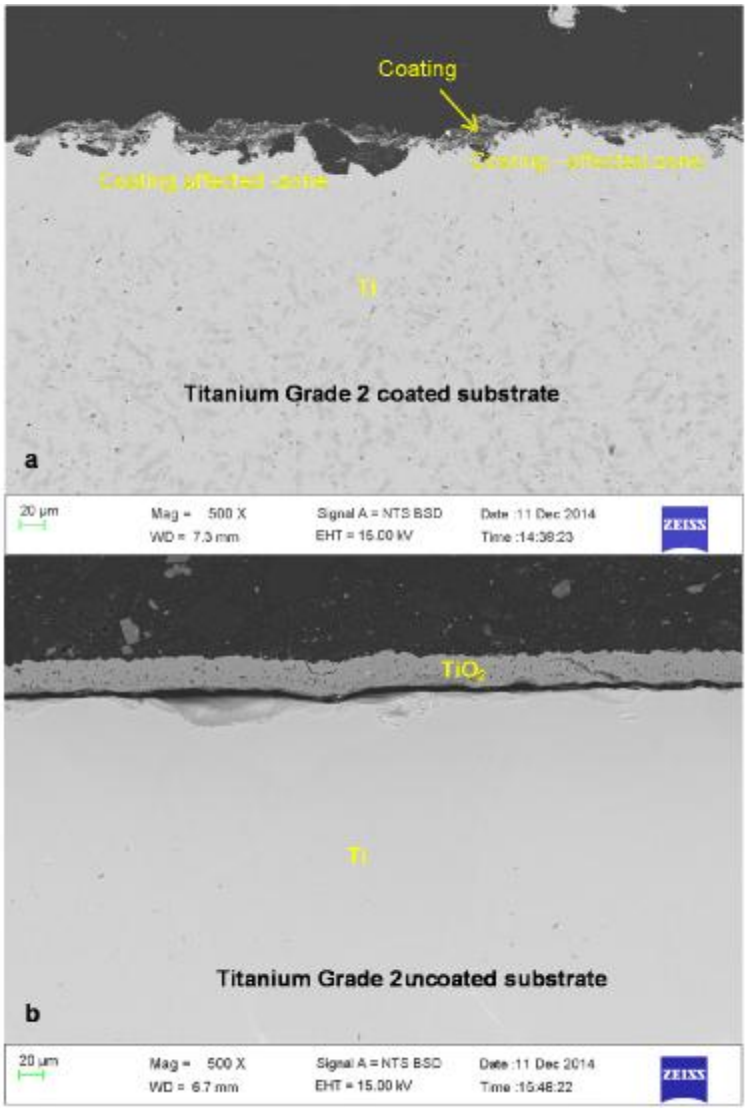


Figure 8.11*. SEM-BSE images of cross-sections of: (a) coated, and (b) uncoated of oxidised titanium Grade 2 substrates.*

8.5 Discussion

The substrates on which coatings were conducted were commercial Titanium Grade 2 and Ti-6Al-4V alloys. The analyses conducted on titanium Grade 2 showed Fe (Table 8.7), believed not to be in solid solution, as the EDX analyses conducted on selected areas showed precipitates (Figure 8.1), which were rich in Fe, indicating that the Fe amount was above the solubility limit. The hardness was $222 \pm 5HV_{10}$, suggesting an increase due to precipitation and rolling. The microstructure of Ti-6Al-4V was typical of the standard alloy (Peterson, 2011; Jha *et al.*, 2015),

and consisted of αTi matrix with aligned β phase, of high vanadium content, indicating rolling. The hardness was was 378±10HV_{10}, falling well in the range of γ-TiAl (Table 4.6).

The results of the EDX analyses indicated that the microstructure of the coating was very complex and consisted of many phases, including γ-TiAl, (Al), PGM-containing phases, Al_2O_3 and TiO_2. Gamma-TiAl was expected, as it was the target alloy during mechanical alloying by double diffusion of titanium and aluminium. PGM-containing phases were also the result of mechanical alloying. Diffusion of aluminium and titanium in PGM, and vice-versa, led to the formation of high-PGM content phases.

The Al_2O_3 particles of the coating had two origins. The Al_2O_3 within the coating layer came from the cold spray process itself. Even though the process is called "cold", it is conducted in air, at temperatures above 300°C. In this work, it was conducted in air at 550°C, and the diffusion rates of Al atoms would have been higher than Ti atoms because of Al's lower melting point. The aluminium atoms diffused out; some was the aluminium observed in the coating, and some oxidised with oxygen in the air, forming Al_2O_3. This was facilitated by the small size of the mechanically-alloyed particles. From the Ellingham diagram (Ellingham, 1944), with competition between aluminium and titanium to react with oxygen, oxygen would preferably react with aluminium first and form Al_2O_3, before reacting with titanium.

The Al_2O_3 particles at the substrate-coating interfaces were the result of prior cleaning by alumina blasting. The blasting was conducted using aluminium oxide powder to clean the surfaces of the titanium Grade 2 substrate and Ti-6Al-4V. By using the energy of the Al_2O_3 particles exiting the gun nozzles, the Al_2O_3 broke and removed any nano- or micro-sized titanium oxide that would have formed as a result of exposure of the substrate to the air oxygen over time. After the removal of the titanium oxide layer, the high-energy Al_2O_3 particles penetrated the substrate and became embedded.

The exposure of the substrate to atmosphere of oxygen-containing argon demonstrated the ability of the coating to protect the titanium Grade 2 and Ti-6Al-4V substrates. This was shown by comparing the cross-sections of the coated and uncoated substrates. For both substrates, the coating proved to be protective. However, immediately below the coating, in a coating-affected zone, the substrate experienced some heat and the βTi phase in the matrix dissolved. Since there was no change in composition in the coating-affected zone compared to the original substrate, the disappearance of the dark phases of the titanium Grade 2 substrate and the bright phase of Ti-6Al-4V substrate was from oxidation at 950°C.

The substrate-coating interface was not continuous on the two substrates, due to the Al_2O_3 from cleaning being embedded in the substrate and preventing direct contact between the substrate and the coating, and this could become the weakest part in the substrate-coating bonding. Nevertheless, after subjecting the samples to heat treatment, there seemed to be no weakening of the bonds where the Al_2O_3 particles were located. At this stage, the bend test was not undertaken because the first step was to assess the high-temperature behaviour of the coating layer in oxidising environments.

8.6 Summary

Mechanically alloyed powders of γ-TiAl with 0.5 at.% Pd, Pt, Ru or Ir additions were coated onto titanium Grade 2 and Ti-6Al-4V substrates using the cold spraying process. Titanium Grade 2 was softer than γ-TiAl alloys and Ti-6Al-4V had hardnesses in the range of γ-TiAl alloys. The optimal temperature to coat in the process was 550°C.

The coating layers adhered to the substrates. Alumina particles from the surface cleaning by alumina blasting were embedded in the substrate. The interface between the substrate and the coating layer was irregular and heterogeneous. Some alumina particles from the sandblasting were at the substrate-coating interface, occasionally interrupting the continuity of the substrate-coating contact. In the case of iridium-alloyed γ-TiAl, particles of high iridium content were observed, indicating that during mechanical alloying, aluminium and titanium atoms diffused into iridium.

The oxidation tests conducted on the coated substrates revealed that the coating layers provided some protection, as no oxide layer was observed under the coating layers. As expected, the uncoated side of the substrate showed oxide formation.

CHAPTER 9
GENERAL DISCUSSION

9.1 Introduction

Gamma-titanium aluminide (γ-TiAl) is an alloy with much potential for applications where light weight for energy saving, room temperature corrosion resistance in aqueous solutions, high-temperature oxidation resistance, or where the combination of all the performances above is needed. Through the literature survey conducted in this work, the superiority of high-temperature performance of titanium aluminides over conventional alloys such as nickel-based superalloys, titanium-, aluminium- and magnesium-based alloys was established (Lasalmonie, 2006). The weakness of the titanium aluminide alloys was also established. While titanium aluminides show potential at high temperatures, room temperature brittleness remains a challenge, hindering the widespread use of these alloys in applications where high toughness is required. The literature also shows that there is very limited knowledge on aqueous corrosion behaviour of titanium aluminide (Rivera-Denizard *et al.*, 2008; Long and Rack, 1998; Escudero *et al.*, 2004; Jafariana *et al.*, 2009; Bello *et al.*, 2010). Most investigations conducted on titanium aluminides were aimed at improving the room temperature ductility and the oxidation resistance above 800°C (Meier, 1989; Rahmel *et al.*, 1995; Reddy *et al.*, 2001; Chu and Wu, 2003; Yang and Wu, 2003; Chuprina and Shalya, 2007). Elements such as V, Mn and Cr were added to improve the room temperature ductility (Lapin, 2009), B and C to increase creep resistance (Huang and Chesnutt, 1994; Tetsui and Miura, 2002). Niobium (Nb), Ta, V, Si, Ag and P were added to improve oxidation (Schumacher *et al.*, 2000).

There were no data available on platinum group metal (PGM) additions to titanium aluminide alloys for aqueous corrosion and high-temperature oxidation resistance improvement prior to this investigation. Platinum group metal additions to titanium aluminide alloys have potential of improving the corrosion resistance in aqueous solutions and high-temperature oxidising media. Could coating titanium and titanium alloys with PGM-containing titanium aluminide alloys have the multiple benefits of improved corrosion resistance in aqueous solutions, good ductility at room temperature and high-temperature oxidation resistance? In an attempt to provide answers to this question, investigations were conducted on the γ-alloys with PGMs, as coating materials

for titanium Grade 2 and Ti-6Al-4V, including the plain γ-TiAl microstructure with PGMs, the effect of PGM addition on the corrosion behaviour of γ-TiAl alloys with PGMs in aqueous solutions, the effect of PGM addition on the high-temperature behaviour of γ-TiAl alloys with PGMs, γ-TiAl alloys with PGMs produced by mechanical alloying and consolidated by spark plasma sintering, and the coating of mechanically alloyed γ-TiAl powders with PGMs cold sprayed onto titanium Grade 2 and Ti-6Al-4V.

9.2 Microstructure of the γ-TiAl alloy

Previous investigations have established the microstructural features of the γ-TiAl alloy to be fully lamellar, consisting of alternating lamellae of TiAl (γ) and Ti_3Al (α_2), near lamellar with lamellar grains with isolated γ grains, duplex with lamellar and γ grains and near γ (Kim, 1989; Pu *et al.*, 1993; Wu, 2006; Imayev *et al.*, 2007) in the composition range 44-48 at.% Al, with the near γ microstructure occurring near 50 at.% Al. This was confirmed in this work, and the fast cooling, after melting was sufficient to retain conditions sufficiently close to equilibrium at the temperature of melting. Since cooling under true equilibrium conditions is very slow, and the work did not require it, it was sufficient to use the as-cast samples. If the microstructure of a particular temperature had been required, the samples would have been annealed at that temperature for a long period and quenched. The as-cast γ-TiAl alloy contained 47.5 at.% Al, which led to a volume fraction of 25 % α_2 and 75 % γ, which was close to values found after heat treatment by Ding *et al.* (1986), Murray (1988) and Yang and Hao (1999). These observations showed that the microstructure was duplex, consisting of lamellar and γ grains. The target composition in this work was 47.5 at.% Al, as this is the composition where a microstructure with more γ phase could be expected (Huang and Chesnutt, 1994; Schuster and Palm, 2006). However, due the high cooling rate in the button arc furnace, the γ phase did not fully develop, as its formation is sluggish (Kim, 1989), even when the alloy is heat-treated above 1200°C in the alpha region of the Ti-Al phase diagram. Thus, this allowed the development a microstructure consisting of γ and lamellar grains (α_2 and γ).

The crystal structures of the two phase components in the γ-TiAl alloy were established to be hexagonally close packed for α_2 (Appel *et al.*, 2011c) and face-centred tetragonal for γ (Duwez and Taylor, 1952; Kim, 1989; Djanarthany *et al.*, 2001). In the two-phase region, the γ-TiAl had hardnesses in a range around 300HV10 for the plain alloy. The hardness did not vary much with platinum group metal (Pt, Pd, Ru and Ir) addition. This suggested that there was not a crystal structure change leading to hardening.

Platinum, palladium, ruthenium and iridium were added at 0.2, 1.0, 1.5 and 2.0 at.% to improve the aqueous and hot-temperature corrosion resistance of γ-TiAl alloys, but were also expected to affect the microstructure. In most investigations (Shi *et al.*, 1992; Huang and Chesnutt, 1994; Kim, 1994b; Loria, 2000 and 2001; Schumacher *et al.*, 2000; Goral *et al.*, 2006; Moskal, 2007; Lapin, 2009), alloying of γ-TiAl aimed at improving the room temperature ductility and high-temperature oxidation and generally involved transition metals other than PGMs (Appel *et al.*, 2011d). Ruthenium is the only PGM extensively researched with regards to its effect on the microstructure of γ-TiAl (Kathaee *et al.*, 1989a, 1989b and 1989c; Kimura and Pope, 1997; Kim *et al.*, 1999; Grytsiv *et al.*, 2003). The ruthenium solubility limit in γ-TiAl is dictated by its solubility limit in α_2 and γ phases, and was established to be ~0.5 at.% Ru. in α_2 and 1 at.% Ru in γ by Kathaee *et al.* (1989c). Literature on the addition of Pt and Pd to γ-TiAl indicated that the maximum solubility in α_2 and γ was 2.5 at.% for Pd (Ding *et al.*, 2000; Raghavan, 2008 and Zaikina *et al.*, 2011a) and 5.5 at.% for Pt. For this work, it could be expected that, in the 0.2-2.0 at.% addition range, Pd and Pt were in solid solution. However, new phases were observed at all PGM addition levels (0.2; 1.0; 1.5 and 2.0 at.%). It is worth noting that in this work, new phases developed at Pd and Pt contents below the solubility limit of Zaikana *et al.* (2000) and Ding *et al.* (2000), which could suggest that the solubility limit of the two PGMs might be lower than indicated. Addition of Ru led to the formation of a two-phase microstructures γ+G. In the two-phase α_2+γ composition range, Pd addition formed the α_2+γ+B2 three-phase mixture (Zaikina *et al.*, 2011a) and Pt addition the α_2+γ+τ_3 three-phase mixture (Zaikina *et al.*, 2011b; Zaikina *et al.*, 2012). These ternary phase diagrams all have two- and three-phase regions, as well as single phase regions, so any alloy whose composition lies in one of these regions will thermodynamically have that number of phases.

9.3 Effect of PGM additions on corrosion behaviour of γ-TiAl in aqueous solutions

The only publications found on corrosion of γ-TiAl in aqueous solution were the work of Saffarian *et al.* (1996) and a more recent work by Seikh *et al.* (2015). In aqueous solutions, Saffarian *et al.* found that Ti_3Al and TiAl showed corrosion behaviour intermediate between pure Al and Ti, which depended on the aluminium content. The susceptibility to pitting corrosion decreased with increasing titanium content, shown by the increase of pitting potential with increasing titanium content. Results reported here are consistent with the observations by Saffarian *et al.* (1996) and it was also established that the passivation zone of the plain γ-TiAl decreased with increasing solution acidity. Saffarian *et al.* (1996) also found that there was a systematic decrease of the pitting potential with increasing Cl^- concentration, which corresponds

to the shrinking of the passivation zone with increasing acidity. Seikh *et al.* (2015) found that γ-TiAl alloy produced by electron beam melting (EBM) has excellent corrosion resistance highlighted by high polarization resistance values and low corrosion rate. They also found that increasing the temperature significantly increased the corrosion of the EBM γ-TiAl alloy.

Literature on PGM additions to alloys of the Ti-Al systems to resist pitting corrosion is restricted to the αTi field with minor additions of Ru or Pd (Stern and Wissenberg, 1959a and 1959b; Potgieter, 1990; van der Lingen and Sandenbergh, 2001). There are no data available on the corrosion behaviour of PGM-containing γ-TiAl alloys in aqueous solutions. In this work, PGMs (Pt, Pd, Ru or Ir) were added to γ-TiAl to improve the resistance to pitting, and the results suggested that the addition of PGMs to γ-TiAl alloy increased the resistance to pitting corrosion by shifting the corrosion potentials towards more positive values and increased the pitting potential, suggesting an improvement in resistance to pitting corrosion, as the passivation zone expanded and the pitting phenomenon was delayed. The shift of the corrosion potentials towards more positive values was attributed to the modification of the cathodic process. Cathodic modification (Figure 2.10c) involves the passivation of a metal in a reducing acid in order to change the kinetics of the hydrogen evolution reaction by alloying the metal with a noble metal which has a higher exchange current density than the metal being passivated (Higginson, 1989). This was the case when Pt, Pd, Ru or Ir was added to γ-TiAl alloy (Figures 5.16, 5.17, 5.18 and 5.19).

The resistance to pitting could not be improved in very aggressive solutions, with pH≤0. In these very acidic and aggressive solutions, the potentiodynamic scans of the plain γ-TiAl showed no passivation zone (Figure 5.21), indicating that corrosion resistance could not be improved by cathodic modification, as the corrosion potential of the PGM-containing γ-TiAl fell either in the transpassive region or the active-passive region on the potentiodynamic scan of the plain γ-TiAl and led to alloy dissolution in both cases. This meant that the corrosion potential shift to more positive values alone was not enough to improve corrosion resistance as other aspects of the alloy electrochemistry, such as solution acidity, current density, long term exposure to acid and galvanic couple also played a part (Hwang and Kim, 2002; Du *et al.*, 2014; Oguike, 2014) . Generally, the current density at the corrosion potential decreased with increasing PGM content (Figure 5.15), but in some alloys, there was a sharp increase in the current density, indicating that, even though there was a shift of the corrosion potential to more positive values, observed high current densities resulted in high dissolution rates (Figure 5.22).

Stern and Wissenberg (1959b) ranked the effect of the most remarkable alloying elements in improving the corrosion resistance of an alloy in a decreasing order as Ir>Rh>Ru>Pt>Pd>Os>Au>Re. Investigated alloying elements included Pt, Pd, Ru and Ir and Ir outperformed all other PGMs in improving the corrosion resistance by reducing the corrosion rate. Thus, from this work, the decreasing corrosion resistance ranking due to the PGMs as alloying elements of γ-TiAl alloy is Ir>Pt>Pd>Ru. A question remains for Pd, as in some cases, the γ-TiAl samples were completely destroyed. The high corrosion rate observed with Ru was due to Ru tendency to shift the potentiodynamic curve towards high current density, resulting in high corrosion rates (van der Lingen and Sandenbergh, 2001).

The new phases formed in γ-TiAl with increasing amounts of PGMs (0.2, 1.0, 1.5 .0 and 2.0 at.% Pt, Pd, Ru or Ir) might have been thought to give improved corrosion resistance by changing the kinetics of the hydrogen evolution reaction. However, there was no benefit in increasing the PGM content, as the same performance was achieved at 0.2 at.% and 2.0 at.% PGM.

Adding more PGMs was not beneficial to the corrosion resistance, because it led to the precipitation of new phase, with higher PGM content, which resulted in the higher corrosion generally observed in multiphase alloys, as the matrix was depleted of PGM (Vaidya and Preece, 1978; Chawla, 1993; Davis, 1999; Ghali and Revie, 2010). However, the PGM-rich phases would only precipitate because the PGM solubility in the matrix has been exceeded, thus would not deplete the matrix of PGMs. Additionally, there will be a difference between the two phases and the individual phases possess different electrode potentials, resulting in a galvanic corrosion with one phase acting as an anode and being subject to corrosion (Scully, 1966). In this instance, the phases with high PGM contents acted as cathodes, and the matrix as the anode. The matrix was thus subjected to dissolution, even though the presence of the PGMs shifted the corrosion potentials to more positive values. In systems exposed to aqueous environments, the corrosion process is under cathodic control, which means that the size of the cathode will control the anode current density (Chawla, 1993; Landolt, 2007). The larger the cathode area compared to the anode area, the greater will be the anode current density. For γ-TiAl, this meant that as the amount of PGMs was increased from 0.2 at.% to 2.0 at.%, more areas of higher PGM content phases were introduced in the microstructure, giving higher anodic current density to the matrix, increased matrix dissolution and more PGM-containing particles were left on the corroded surface. The general result in such a case is the surface enrichment of the less active elements (Landolt, 2007); here, there was surface enrichment in PGM-containing particles. This was

confirmed by the PGM content of corroded surfaces (Figure 5.24) and the high values of end potentials in the open circuit potential tests (Figures 5.25-5.26).

Through the open circuit potential tests, it also was possible to show that the shift of the γ-TiAl corrosion potential towards more positive values (Figures 5.7-5.10) was due to the accumulation of PGMs on the surface as corrosion occurred (Figure 5.24). Cathodic modification of PGM-alloyed γ-TiAl then occurred as a result of increased PGM content on the surface of the γ-TiAl alloys, which simultaneously improved hydrogen evolution efficiency and inhibited anodic dissolution.

9.4 Effect of PGM additions on high-temperature oxidation behaviour of γ-TiAl

The high temperature oxidation mechanism of intermetallic compounds in the Ti-Al system is well established and understood (Rahmel and Spencer, 1991; Li *et al.*, 1992; Meier *et al.*, 1993; Shida and Anada, 1993; Rahmel *et al.*, 1995; Das *et al.*, 2002). The oxidation behaviour of γ-TiAl based alloys is extremely complex, and depends on temperature and atmosphere composition. Protective alumina scales were formed in pure oxygen up to 1000°C (Dettenwanger *et al.*, 1994). In air, a critical temperature, above which a mixed TiO_2/Al_2O_3 scale forms and grows at rates which are orders-of-magnitude faster than that of Al_2O_3 (Meier *et al.*, 1993; Dettenwanger *et al.*, 1994; Rahmel *et al.*, 1995). This temperature was found between 700°C and 800°C (Chang, 2007; Mitoraj and Godlewska, 2013). Meier *et al.* (1993) found that continuous alumina did not form at temperatures above 750°C.

The effect of PGMs on the oxidation behaviour of γ-TiAl was assessed by the ability of the alloy to form an external aluminium oxide and Z-phase ($Ti_5Al_3O_2$) that would stabilise the aluminium oxide phase and promote its continuity (Copland *et al.*, 1999). For oxidation resistance, the formation of Al_2O_3 is desired over TiO_2. The latter grows at a rapid rate and does not provide adequate protection above 600-700ºC (Jacobson *et al.*, 1999). On the other hand, alumina scales, by virtue of their extremely slow, parabolic rates of growth, are protective at temperatures above 1200°C (Copland *et al.*, 1999).

The additions of 0.2 at.% PGMs led to the development of oxidation resistance by the formation of Z-phase ($Ti_5Al_3O_2$) which promoted the formation of an external Al_2O_3 layer. As the PGM content was increased to 1.0 at.%, the oxidation resistance significantly decreased.

The alloys underwent oxidation, irrespective of the PGM introduced, with different oxidation patterns and to different extents. These results indicated that, as alloying elements in the γ-TiAl, ruthenium, platinum and iridium could facilitate the stabilisation of the Z-phase and subsequent promotion of more protective Al_2O_3 away from the surface in the early stage of oxidation at contents below 1 at.% and the TGA data suggested an optimum at 0.5 at.% PGM (Figure 6.1).

At 1 at.% addition, platinum-, ruthenium- and iridium-alloyed γ-TiAl showed a layer of TiO_2 on the surface, followed by a thick layer of mixed Al_2O_3+TiO_2 underneath (Figures 6.2 to 6.4). Under the oxide layers was a subscale layer of Z-phase, which is known to stabilise Al_2O_3 (Coppland *et al.*, 1999). This was supported by more Al_2O_3 than TiO_2 in the mixed layer. However, the progressive formation and growth of TiO_2 is believed to be the result of nitrogen in the air, which prevented the formation of continuous Al_2O_3, even though the PGMS stabilised the Z-phase (Rakowski *et al.*, 1995; Lang and Schütze, 1996; Shemet *et al.*, 1997). The TiN formed would have decomposed, releasing nitrogen for further nitriding inwards and giving rise to TiO_2 formation behind the reaction front. This could also explain the sole presence of TiO_2 on the surface, its progressive decrease towards the metal substrate and a dominance of Al_2O_3 near the Z-phase (Figures 6.2 to 6.4).

The microstructure of the oxidised alloys with 1 at.% PGMs had a very brittle oxidation-affected zone, consisting of an external layer of TiO_2, followed underneath by a layer of mixed Al_2O_3 + TiO_2. In some cases, a layer of alumina formed above the mixed oxides. The layer under the oxide scale, adjacent to the alloy substrate, was $Ti_5Al_3O_2$ in the Ru-alloyed γ-TiAl, and Ti_3Al in the Pt- and Ir-alloyed γ-TiAl with dissolved PGMs. In Pd-alloyed γ-TiAl, a substituted binary phase $Ti_{25}Al_{75-x}Pd_x$ i.e. $Ti(Al,Pd)_3$ was observed between a high-titanium content layer and the metal substrate. This showed that oxidation resistance improvement was best achieved with Ru addition. The oxide scale in Ru-, Ir- and Pt-alloyed γ-TiAl was continuous, non-porous and without cracks (Figures 6.2 to 6.4). In Pd-alloyed γ-TiAl, the oxide scales were porous and had cracks (Figure 6.5) and the substituted binary phases remained undisturbed in the oxidised region and were easily removed during metallographic preparation, leaving behind isolated lamellar grains deprived of γ phase.

9.5 Mechanical alloying and consolidation by spark plasma sintering

No particular phase was clearly identifiable in the mechanically-alloyed powder, and heat treatment at 600°C for 2 hours resulted in the formation of γ-TiAl and Ti_3Al. Titanium solid solution (αTi) was visible in the XRD patterns of heat-treated powders. By milling elemental Ti

and Al powder mixture for 40 hours, Al-Dabbagh *et al.* (2015) formed Ti(Al) and subsequent heat treatement led to the formation of a mixture of Ti_3Al and γ-TiAl. Even though γ-TiAl and Ti_3Al phases were identified in the XRD patterns of the heat-treated MA powders (Figures 7.7, 7.9, 7.11 and 7.13) there was no lamellar structure in the microstructure of the powders (Figure 7.5).

The presence of Ti after heat treatment was a confirmation that the TiH_2 observed in the powder obtained from the milling decomposed during heat treatment, released H_2 and gave Ti, which then reacted with aluminium to form (αTi). Studies on the kinetics of the thermal decomposition of titanium hydride powder have shown that above 500ºC, the decomposition of TiH_2 is completed in less than 50 minutes (Sandim *et al.*, 2005; Rasooli *et al.*, 2013). In this work, TiH_2 was heat-treated at 600ºC for 2 hours. The absence of aluminium peaks on the powder XRD patterns after heat treatment was an indication that, at that stage, all aluminium was now bound in TiAl or Ti_3Al compounds or dissolved in titanium.

The presence of TiAl and Ti_3Al is in agreement with Neves *et al.* (2003) and Shao *et al.* (2015) who found Ti_3Al and TiAl and unreacted Ti, after heating the mechanically alloyed powder for 2 hours at 750ºC for 2 hours. Shao *et al.* (2015) summarised the formation of the three intermetallic compounds. The decomposition of titanium hydride with temperature was given by:

$$TiH_2 \rightarrow Ti + H_2 \qquad \text{(Equation 7.1)}$$

In this work, this is explained by Equations 7.1 to 7.3. The formation of $TiAl_3$ intermetallic phase was given by:

$$6Ti + 6Al \rightarrow 4Ti + 2TiAl_3 \qquad \text{(Equation 7.2)}$$

The formation of $TiAl_2$ and $TiAl_3$ intermetallic phase:

$$4TiAl + 2TiAl_3 \rightarrow Ti_3Al + TiAl + 2TiAl_2 \qquad \text{(Equation 7.3)}$$

The formation of TiAl intermetallic alloys through the reaction of the products of Equation 7.3:

$$Ti_3Al + TiAl + 2TiAl_2 \rightarrow 6TiAl \qquad \text{(Equation 7.4)}$$

In this work, given the target composition in the two-phase region (Ti-47.5 at.% Al), Ti was in excess and the following reactions are proposed for the formation of Ti_3Al:

$$TiAl + 2Ti \rightarrow Ti_3Al \qquad \text{(Equation 7.5)}$$

$$TiAl_2 + 5Ti \rightarrow 2Ti_3Al \qquad \text{(Equation 7.6)}$$

$TiAl_3 + 8Ti \rightarrow 3Ti_3Al$ (Equation 7.7)

The result was the presence of TiAl and Ti_3Al from Equations 7.4 to 7.7. $TiAl_3$ was present because of its high stability (Sujata *et al.*, 1997). Many investigations have shown that $TiAl_3$ is the first intemetallic compound to form at the interface Ti/molten Al under equilibrium conditions (Kattner *et al.*, 1992; Sujata *et al.*, 1997; Fu *et al.*, 2001; Khoshhal *et al.*, 2010; Jiangping *et al.*, 2011; Sina and Iyengar, 2015). Under non-equilibrium conditions, such as rapid heating (Fu *et al.*, 2001), or under solid-state reactions by diffusion (Sina and Iyengar, 2015), Ti_3Al, TiAl and $TiAl_2$ formed. $TiAl_3$ and $TiAl_2$ then reacted with Ti to form Ti_3Al (Equations 7.6 and 7.7).

When the powders were heated in air, oxidation occurred as a result of aluminium and titanium reacting with oxygen in the air. Reactions started by a mass loss from the decomposition of the stearic acid, which was followed by a continuous oxidation of the powder expressed by a continuous mass increase (Figure 7.15). Heating the powder in air completed the formation of Ti_3Al, TiAl and $TiAl_3$, which started during milling, but the air was also a source of oxygen and nitrogen. From Lavoisier mass conservation laws (Lavoisier, 1789; Whitaker, 1975; Dickerson *et al.*, 1978), the formation of the three compounds did not introduce mass increase, which came either from the oxidation of Al and Ti, or formation of nitride by reactions with oxygen or nitrogen in the air. There was no nitrogen observed, indicating that mass increase was due to Al_2O_3 and TiO_2 formation. The initial temperature for oxide formation was not determined. It is assumed that, as temperature increased, Al_2O_3 must have formed first, given its lower standard free energy of formation (which is negative) as shown by the Ellingham diagram (Ellingham, 1944; Smeltzer, 1956; Jeurgen *et al.*, 2002), taking into account the temperature and the pressure variation. At at 25°C and 1 atm when formed from their elements in their stable form, the heat of formation are -400,00±0.15 kCal for Al_2O_3 (Kabuschewski and Alcock, 1979) and -225.52 ± 0.23 Kcal/mole for TiO_2 (Humphrey, 1951; Kabuschewski and Alcock, 1979).

The compacts obtained by spark plasma sintering showed different microstructures and hardnesses from the γ-TiAl obtained by conventional melting and casting, consisting of a homogeneous lamellar-free microstructure of evenly distributed α_2, γ and Al_2O_3 with Pd, Pd, Ru, Fe, Ni and Cr in solid solution. Iridium did not go into solid solution. Alumina in the microstructure of the spark plasma sintered γ-TiAl was also observed by Liu and Liu (2007). There is no information in the literature on the behaviour of PGMs or Fe, Ni and Cr in spark plasma sintered γ-TiAl alloys.

The presence of γ and α_2 was in agreement with Liu and Liu (2007) and Guyon *et al.* (2013), who made similar observations after spark plasma sintering at 1100°C, but did not agree with Mei and Miyamoto (2001), Shu-long *et al.* (2009) and Couret *et al.* (2008), who showed the formation of a lamellar structure after spark plasma sintering at the same temperature. Mei and Miyamoto (2001) also found a duplex microstructure consisting of α_2 and γ grains, after spark plasma sintering at 1100°C Ti-48 at.% Al derived from blending Ti and Al elemental powder. They obtained a lamellar microstructure after heat treating the sintered alloy at 1200°C for 2 hours. This indicated that spark plasma sintering carried out at 1100°C in this work could not give a lamellar structure. This was attributed to the sintering temperature (1100°C) before the alloy was cooled to room temperature. According to the Ti-Al phase diagram, at 1100°C, the sintering was conducted at a temperature where α_2 and γ are equilibrium and stable phases. It is also believed that the added PGMs, Fe, and Cr may have contributed in increasing the transformation temperature. Only reheating the alloy above 1120°C could lead to fully lamellar structure by the reaction $\alpha+\gamma \rightarrow \alpha_2+\gamma$ during the cooling process.

The hardness of 850 HV was above the range of hardness (700-750 HV) found in previous investigations (Liu and Liu, 2007; Chen *et al.*, 2009). This increased hardness is believed to come from the solid solution hardening due to the solubility of Fe, Ni and Cr in the γ and α2 phases. These elements were identified by EDX in both γ and α_2 phases.

9.6 Coating of MA γ-TiAl powder onto titanium Grade 2 and Ti-6Al-4V

From a material deposition perspective, factors indicating the coating quality on a substrate include good adhesive strength, constant thickness and the absence of porosity, which depend on the powder particle size distribution and the impact velocity, as well as the powder material (Klinkov *et al.*, 2005; Grigoriev *et al.*, 2015, Gurrapa, 2001b). Gamma-TiAl powders mechanically alloyed with 0.5 at.% Pd, Pt, Ru or Ir were cold sprayed onto titanium Grade 2 and Ti-6Al-4V substrates and gave a coating of irregular thickness, with minimal porosity and good adhesion to the substrate (Figures 8.9 to 8.11). The powder used during coating was a non-heat treated mechanically alloyed powder, deposited at 550°C. For both substrates, the couple particle/substrate was of the hard particle/hard substrate type, as defined by Bae *et al.* (2008), which could not make an easy coating. This hard/hard coupling was the reason why the coating thickness was very irregular, as in some areas, the particles could not stick to the substrate at the first spray gun pass.

The Al_2O_3 particles embedded in the substrates came from the alumina powder used to clean up the surface. During surface clean-up by alumina powder blasting, the Al_2O_3 particles, with Vickers hardness higher than $1500HV_{200}$ (Ćurković *et al.*, 2007; Figiel *et al.*, 2011), the Al_2O_3/Ti-6Al-4V or Al_2O_3/titanium Grade 2 as particle/substrate couples were of a hard/soft type and led to super-deep penetration of alumina particles due to the high-velocity of particles (Klinkov *et al.*, 2005), and extensive material removal which rendered the surface irregular and facilitated material deposition, in spite of a hard/hard coupling between the mechanically alloyed powder and the two substrates (Bae *et al.*, 2008). This resulted in the good adhesions of the mechanically alloyed powder particles to the titanium Grade 2 and Ti-6Al-4V substrates, but also in several alumina particles embedded in the substrates and at interfaces.

There is no information in the literature about the behaviour of platinum group metals used as alloying elements in the mechanically alloyed γ-TiAl powder cold sprayed onto substrates. In these investigations, cold spraying was conducted at 550°C, a temperature that left the PGMs in an incomplete alloying stage, which is in agreement with the XRD results of the mechanically alloyed powder and confirmed by the particles of high PGM content observed in the coating of titanium Grade 2 or Ti-6Al-4V substrates (Figures 8.5-8.7; 8.10-8.11).

Coatings on both substrates were dense near the coating/substrate interfaces. This was because the tests were conducted at a temperature (550°C) which softened the mechanically alloyed particles, allowing the tamping effect of successive particles during the subsequent passes of the gun to easily occur, once the first layer particles were bonded to the substrates, thus creating a dense coating. Li and Li (2003) have shown that the densification of the layer resulted from successively impacting particles which took place during powder spraying, leading to a top region presenting a porous structure, while the inner region was dense. The top region of the coatings investigated here showed some porosity (Figure 8.7). Due to the high density at the base of the coating, the oxidation tests of the coated substrates revealed that the coatings provided some protection, as no oxidation was observed on the substrate surface immediately adjacent to the coating.

The high amount of contaminants (Fe, Ni and C) picked up during milling should not be overlooked in evaluating the properties of the mechanically alloyed powders as contaminant contents were higher than the PGM contents. Thus, any property observed was not due to the sole presence of PGM, but would include the effect of these contamination elements. Therefore, the beneficial effect observed by coating could be considered as due not only to PGMs, but also

to Fe, Ni and C. It would have been beneficial to use alumina balls instead of stainless steel balls, but a suitable mill was not available.

This discussion shows that cast γ-TiAl of composition Ti-47.5 at.% Al with addition of PGMs had the typical microstructure obtained in the cast alloy, with new PGM-containing phases. PGM additions were more beneficial for aqueous corrosion resistance than for high-temperature oxidation resistance. The optimum addition was 0.5 at.% PGM addition, with iridium giving the best aqueous corrosion and high-temperature oxidation resistance. Mechanical alloying gave a powder with a different microstructure from the cast alloys, when spark plasma sintered or coated on to titanium Grade 2 or Ti-4Al-4V substrates. The coatings showed good adhesion and no porosity near the substrate, two performance qualities sought in coatings.

CHAPTER 10

CONCLUSIONS AND RECOMMENDATIONS

In the Ti-Al alloy system, Ti_3Al, γ-TiAl and $TiAl_3$ have attracted interest for their mechanical, physical and corrosion properties as suitable material for corrosion and oxidation resistance applications at room and elevated temperatures. Gamma-TiAl alloys of composition Ti-47.5Al (at.%) with addition of platinum group metals (PGMs) was investigated as coatings on titanium Grade 2 and Ti-6Al-4V for corrosion protection in aqueous solutions at room temperature and oxidation protection in air at elevated temperatures.

The microstructure of γ-TiAl was duplex, consisting of grains of alternating lamellae of α_2 and γ phases, and γ grains. PGM additions did not affect the microstructure significantly and the hardness. The hardness before and after PGM addition was between 300 and 400 HV_{10}.

PGM additions significantly improved the corrosion resistance properties of γ-TiAl alloys by cathodically modifying its properties in aqueous solutions. Corrosion resistance improvement occurred by PGM accumulation on the surfaces during long term exposure to the reducing aqueous solutions. Improvement of γ-TiAl corrosion resistance by PGM additions was investigated in very aggressive solutions with pH<1 and indicated that better results would be expected in acidic environments of pH>1. An optimum in corrosion resistance improvement was chosen at PGM addition of 0.5 at.%, and PGM additions beyond 0.5 at.% did not give further corrosion resistance improvement. Thus, PGMs are appropriate to add as alloying elements for corrosion resistance improvement in aqueous solutions when dealing with reducing media.

PGM additions did not significantly improve the oxidation resistance at elevated temperatures and, as for corrosion resistance, the oxidation resistance decreased with increasing PGM contents. While some oxidation resistance improvement could be observed at low PGM additions, with an optimum at 0.5 at.% PGM, oxidation resistance deteriorated beyond this value. This was due to the inability of PGM additions to promote the formation of the continuous Al_2O_3 layer, responsible of γ-TiAl protection at high temperatures in the presence of oxygen. However, oxidation resistance improvement can be achieved if PGMs are added below the solubility limits in α_2 and γ, the two main components of the γ-TiAl microstructure.

When γ-TiAl was produced by mechanical alloying, the microstructure of the mechanically alloyed powder which was spark plasma sintered (SPS) was different from the benchmark alloy produced by melting and casting and consisted of continuous α_2 and γ, and no alternating lamellae of the two phases. Except for iridium, other PGMs dissolved in α_2 and γ of the powder. The hardness of the SPS alloys was three times higher than the cast γ-TiAl.

Coating titanium Grade 2 and Ti-6Al-4V with mechanically alloyed powders containing 0.5 at.% PGMs using cold spraying gave some oxidation protection of substrates, even though the coatings had different thicknesses. Thus, the mechanically alloyed γ-TiAl powders can be used as coatings on other titanium-based alloys for oxidation protection. However, optimisation is still needed on coating parameters to give controllable coating thickness, oxide formation and reduced porosity. Particle morphology of the powders should be spherical (by spheroidisation for example), for better flow in the spray gun and better deposition onto the substrate. Finally, other coating techniques, such as high velocity oxygen fuel (HVOF) and plasma coatings also need to be investigated for coating of γ-TiAl alloys onto titanium-based alloys.

REFERENCES

Agarwal, A., Akhtar, M.J. and Balasubramaniam, R. (1996), Effect of alloying on aqueous corrosion and mechanical behaviour of iron aluminide Fe_3Al, *Journal of Materials Science*, Vol. 31, No. 19, pp. 5207-5213.

Albiter, A., Espinosa-Medina, M.A., Casales M. and Gonzalez-Rodriguez, J.G. (2004), Corrosion performance of NiAl intermetallic with Mo, Ga and Fe in neutral and alkaline media, *Journal of Applied Electrochemistry*, Vol. 34, pp. 1141-1145.

Al-Dabbagh, J.B., Tahar, R.M., Ishak, M. and Harun, S.A. (2015), Structural and phase formation of TiAl alloys synthesized by mechanical alloying and heat treatment, International *Journal of Nanoelectronics and Materials*, Vol. 8, pp. 23-32.

Amin, M.A. (2011), Influence of the alloying elements on uniform and pitting corrosion events induced by SCN- anion on Al-6061 and Al-Cu alloys surfaces, *Jordan Journal of Chemistry*, Vol. 6, No. 1, pp. 91-105.

Andrade, A., Morcelli, A. and Lobo, R. (2010), Deformation and fracture of an alpha/beta titanium alloy, *Revista Materia*, Vol. 15, No. 2, pp. 364-370.

Appel, F., Paul, J.D.H. and Oehring, M. (2011a), Gamma titanium aluminide alloys, *Science and Technology*, John Wiley-VCH Verlag & Co. KGaA, Weinheim, Germany, pp. 433-463.

Appel, F., Paul, J.D.H. and Oehring, M. (2011b), Gamma titanium aluminide alloys: *Science and Technology*, John Wiley-VCH Verlag GmbH & KGaA, Weinheim, Germany, pp. 729-738.

Appel, F., Paul, J.D.H. and Oehring, M. (2011c), Gamma titanium aluminide alloys: *Science and Technology*, John Wiley-VCH Verlag GmbH & KGaA, Weinheim, Germany, pp. 5-23.

Appel, F., Oehring, M., Paul, J.D.H and Lorenz, U. (2011d), Design, properties, and processing of a novel TiAl alloy, Structural intermetallics, pp. 139-148, *The Mineral, Metals & Materials Society*, Warrendale, PA, USA.

Arockiasamy, A., Eliezer, D., Wang, P.T., Horstemeyer M.F. and King, R.L. (2010), Electrochemical hydrogenation and corrosion studies of Ti-48Al-2Cr-2Nb alloy in acidic solution, *Anti-Corrosion Methods and Materials*, Vol. 57, No. 6, pp. 280-289.

ASTM B265:13ae1, Standard Specification for Titanium and Titanium Alloy Strip, Sheet, and Plate, Book of Standards Vol. 02.04, *ASTM International*, West Conshohocken, PA, 2013, www.astm.org

Bae, G., Xiong, Y., Kumar, S., Kang, K. and Lee, C. (2008), General aspects of interface bonding in kinetic sprayed coatings, *Acta Materialia*, Vol. 56, pp. 4858-4868.

Balasubramaniam, R. (2002), Hydrogen in iron aluminides, *Journal of Alloys and Compounds*, Vol. 330-332, pp. 506-510.

Bandyopadhyay, D., Sharma, R.C. and Chakraborti, N. (2000), The Ti-Al-C System (Titanium-Aluminum-Carbon), *Journal of Phase Equilibria*, Vol. 21, No. 2, pp. 195-198.

Banerjee, D. (1994), Ti_3Al and its alloys, *Intermetallic compounds, Principles and Practice*, Vol. 2, Westbrook, J.H. and Fleischer, R.L. (Eds.), pp. 91-131, John Wiley & Sons Ltd., Sussex, U.K.

Barret, C.S. and Massalski, T.B. (1980), *Structure of Metals*, 3rd revised edition, pp. 270-305, Pergamon Press, Oxford, U.K.

Batalu, D., Coşmeleaţă, G., Aloman, A. (2006), Critical analysis of the Ti-Al phase diagrams, *U.P.B. Science. Bulletin*, Series B, Vol. 68, No. 4, pp.77-90.

Becker, S., Rahmel, A., Schorr, M. and Schütze, M. (1992), Mechanism of isothermal oxidation of the intermetallic TiAl and TiAl alloys, *Oxidation of Metals*, Vol. 38, pp. 425-464.

Bello, S.A., Maldonado, I., Rosim-Fachini, E., Sundaram, P.A. and Diffoot-Carlo, N. (2010), In vitro evaluation of human osteoblast adhesion to a thermally oxidized γ-TiAl intermetallic alloy of composition Ti-48Al-2Cr-2Nb (at.%), *Journal of Materials Science: Materials in Medicine*, Vol. 21, pp. 1739-1750.

Benedek, R., van de Walle, A., Gerstl, S.S.A., Asta M. and Seidman, D.N. (2005), Partitioning of solutes in multiphase Ti-Al alloys, *Physical Review B71*, pp. 094201-1-094201-11.

Bertocci, U., Fink, J.L., Hall, D.E., Madsen, P.V. and. Ricker, R.E (1990), Passivity and passivity breakdown in nickel aluminide, *Corrosion Science*, Vol. 31, pp. 471-478.

Birbilis, N. and Buchheit, R. G. (2005), Electrochemical characteristics of intermetallic phases in aluminum alloys: An experimental survey and discussion, *Journal of the Electrochemical Society*, Vol. 152, pp. 140-151.

Bogner, A., Jouneau, P.H., Thollet, G., Basset. D. and Gauhier, C. (2007), A history of scanning electron microscopy developments: Towards "wet-STEM" imaging, *Micron*, Vol. 38, pp. 390-401.

Brady, M.P., Brindley, W.J., Smialek, J.L. and Locci, I. E. (1996), The oxidation and protection of gamma-titanium aluminides, *Journal of Oxidation of Metals*, Vol. 48, pp. 46-50.

Brandt, O.C. (1996), Mechanical properties of HVOF coatings, *International Journal of Fatigue*, Vol. 18, No. 6, pp. 417-417.

Brass, A.M. and Chêne, J. (1998), Hydrogen absorption in $\alpha_2+\gamma$ titanium aluminides during mechanical grinding, *Scripta Materialia*, Vol. 39, No. 11, pp. 1569-1575.

Braun, R., Rovere, F., Mayrhofer, P.H. and Leyens, C. (2010), Environmental protection of γ-TiAl based alloy Ti-45Al-8Nb by CrAlYN thin films and thermal barrier coatings, *Intermetallics*, Vol. 18, pp. 479-486.

Brossia, C.S. and Cragnolino, G.A. (2001), Effects of environmental and metallurgical conditions on the passive and localised dissolution of Ti-0.15%Pd, *Corrosion*, Vol. 9, pp. 768-779.

Buchanana, R.A. and Kim, J.G. (1990), Chloride-induced localized corrosion of Fe_3Al-type iron aluminides: Beneficial effects of Cr and Mo additions, *Materials Research Society Proceedings*, Vol. 213, pp. 945-951.

Buchheit, R.G. (1995), A Compilation of corrosion potentials reported for intermetallic phases in aluminium alloys, *Journal of Electrochemistry Society*, Vol. 142, No. 11, pp. 3994-3996.

Buchheit, R.G., Zavadil, K.R., Scully, J.R. and Knight, T.O. (1995), The electrochemical behaviour of the Al_3Ta intermetallic compound and pitting in two-phase Al_3Ta alloys, *Journal of the Electrochemistry Society*, Vol. 142, No. 1, pp 51-58.

Burleigh, T.D., Bovard, F.S. and Rennick, R.C. (1993), Corrosion potential for aluminium alloys measured by ASTM G. 69, *Corrosion*, Vol. 49, pp. 683-685.

Cam, G., Flower, H.M. and West, D.R.F. (1991), Solid state phase transformations in titanium-aluminum-carbon and titanium-aluminum-niobium-carbon alloys, *Materials Science and Technology*, Vol. 7, No 7, pp. 587-591.

Campbell, F.C. (2008), Elements of Metallurgy and Engineering Alloys, pp. 41-52, *ASM international*, Materials Park, Ohio 44073-0002, USA.

Cannon, W.R., Danforth, L S.C., Haggerty, J.S. and Marra, R.A. (1982), Sinterable ceramic powders from laser-driven reactions: Powder characteristics and process variables, *Journal of the American Ceramic Society*, Vol. 65, No. 7, pp. 330-335.

Černý, M. and Filípek, J. (2011), Anodic-modified anticorrosive coatings, *Acta Universitatis Agriculturae Mendelianae Brunensis*, Vol. 59, No. 5, pp. 23-30.

Chalker, P.R. (1991), Characterisation of coatings and interfaces, Advanced Surface Coatings: *A Handbook of Surface Engineering*, D.S. Rickerby and A. Mathews (Eds.), pp. 278-314, Blackie & Son Ltd., London, UK.

Champagne, V. K. (2007), *The Cold Spray Materials Deposition Process: Fundamentals and Applications*, pp. 105-116, Woodhead Publishing, Cambridge, UK.

Chang , S.Y. (2007), The Isothermal and Cyclic Oxidation Behavior of a Titanium Aluminide Alloy at Elevated Temperature, Journal of Materials Engineering and Performance, Vol.16, No 4, pp.508-514.

Chang, Y.W., Kim, N.J. and Lee, C.S. (2007), Aqueous corrosion characteristics of iron aluminides, *Advanced Materials Research*, Vol. 26-28, pp. 23-26.

Chaston, J.C. (1965), Reactions of Oxygen with the Platinum Metals : II-oxidation of ruthenium, rhodium, Iridium and osmium, *Platinum Metals Review*., Vol. 9, No 2, pp. 56-57.

Chaston, J.C. (1975), The Oxidation of the Platinum Metals: A descriptive survey of the reactions involved, *Platinum Metals Review*, Vol. 19, No 4, pp. 135-140.

Chawla, S.L. and Gupta, R.K. (1993), *Materials Selection for Corrosion Control*, Haddad, M.T. (Ed.), pp.30-63, ASM International, Materials Park, Ohio 44073-0002, USA.

Chen, C.C. (2014), Phase Equilibria at Ti-Al Interface under low oxygen pressure, *Atlas Journal of Materials Science*, Vol. 1, No 1, pp. 1-11.

Chen, G. and Wang, K.(1993), Preparation of amorphous $Ti_{50}Al_{50}$ by mechanical alloying and effects of milling atmosphere, *Proceedings of the 2nd Conference on Structural Applications of Mechanical Alloying*, Vancouver, British Columbia, Canada, 20-22 September 1993, pp. 149-155.

Chen, Y.Y., Yu, H.B., Zhang, D.L. and Chai, L.H. (2009), Effect of spark plasma sintering temperature on microstructure and mechanical properties of an ultrafine grained TiAl intermetallic alloy, *Materials Science and Engineering A*, Vol. 525, pp.166-173.

Choi, Y. and Kim, J.G. (2002), Investigation of passivity and its breakdown on Fe_3Al-Cr-Mo intermetallics in thiosulfate-chloride solution, *Materials Science and Engineering A*, Vol. 333, No. 1, pp. 336-342.

Chu, M.S. and Wu, S.K. (2003), The improvement of high temperature oxidation of Ti-50Al by sputtering Al film and subsequent interdiffusion treatment, *Acta Materiala*, Vol. 51, pp. 3109-3120.

Chuprina, V.G. and Shalya, I.M. (2007), Oxidation of TiAl intermetallics, *Powder Metallurgy and Metal Ceramics*, Vol. 46, No. 11-12, pp. 582 -588.

Connway, J.J. and Rizzo, F.J.(1998), Hot Isostatic Pressing, *Powder Metal Technologies and Applications*, Lee, P.W., Ed., ASM Handbook, Vol. 7, pp. 605-620, ASM International, Ohio, USA.

Colin, J., Serna, S., Campillo, B., Florez, O. and Gonzalez-Rodriguez, J.G. (2007), Corrosion performance of a rapidly solidified NiAl intermetallic macroalloyed with Fe in 0.5M H_2SO_4, *International Journal of Electrochemical Science*, Vol. 2, pp. 947-957.

Copland, E.H., Gleeson, B., and Young, D.J. (1999), Formation of Z-$Ti_{50}Al_{30}O_{20}$ in the sub-oxide zones of γ-TiAl-based alloys during oxidation at 1000°C, *Acta Materialia*, Vol. 47, pp. 2937-2949.

Cotton, J.B. (1967), The role of palladium in enhancing corrosion resistance of titanium, *Platinum Metals Review*, Vol. 11, No. 2, pp. 50-52.

Couret, A., Molénat, G., Galy, J. and Thomas, M. (2008), Microstructures and mechanical properties of TiAl alloys consolidated by spark plasma sintering, *Intermetallics*, Vol. 16, pp. 1134-1141.

Craig, B.D. and Anderson, D.S. (1994), *Handbook of Corrosion data: Materials data series*, J.R. Davis (Ed.), pp. 73-79, ASM International, Materials Park, Ohio 44073-0002, USA.

Crawmer, D.E. (2005), Thermal Spray Process, *Handbook of Thermal Spray Technology*, J.R. Davis (Ed.), pp. 54-76, ASM International, Materials Park, Ohio 44073-0002, USA.

Ćurković, L., Rede, V., Grilec, K. and Mulabdić, A. (2007), Hardness and fracture toughness of alumina ceramics, *Conference on Materials, Processes, Friction and Wear*, MATRIB '07, Vela Luka, 21-23 June 2007, pp. 40-45.

Das, K., Choudhury, P. and Das, S. (2002), The Al-O-Ti system, *Journal of Phase Equilibria*, Vol. 23, No. 6, pp. 525-536.

Datta, B.K. (2012), *Powder Metallurgy-An advanced technique of processing engineering materials*, Eastern Economy Edition, pp. 8-63, PHI Learning Private Limited, M-97, Connaught Circus, New Delhi-110001, India.

Davis, J.R. (1990), Properties and selection: Nonferrous alloys and special purpose materials, *Metals Handbook 2*, pp. 586-591, ASM International, Metals Park, Ohio, USA.

Davis, J.R. (1999), Corrosion of aluminum and aluminum alloys, *Metals Handbook 13*, pp. 86-97, ASM International, Metals Park, Ohio, USA.

De Graef, M. and McHenry, M.E. (2007), *Structure of Materials: an Introduction to Crystallography, Diffraction, and Symmetry*, pp. 425-465, Cambridge University Press, UK.

Deevi, S.C. and Zhang, W.J. (2003), Intermetallic applications, *Encyclopedia of Materials: Science and Technology*, Second Edition, Buschow, K.H.J., Cahn, R.W., Fleming, C., Ilschner, B., Kramer, E.J., Mahajan, S. and Veyssière, P. (Eds.), pp. 4165-4173, Elsevier, Amsterdam, Netherlands.

Delgado, C., Sundaram, P.A. (2007), A study of the corrosion behaviour of gamma titanium aluminide in 3.5 wt% NaCl solution and seawater, *Corrosion Science*, Vol. 49, No. 9, pp. 3732-3741.

Desch, C.H. (1914), Intermetallic compounds, *Monographs on Inorganic Chemistry*, A. Findlay Edition, pp. 37-78.

Dettenwanger, F., Schumann, E., Ruhle, M., Rakowski, J. and Meier, G.H. (1994), The effect of nitrogen on the oxidation of TiAl, *Material Research Society Symposium Proceedings*, North-Holland,

New-York, USA, Vol. 364, pp. 981-986.

Dettenwanger, F., Schumann, E., Rakowski, J., Meier, G.H. and Ruhle, M. (1996), Development and microstructure of the Al-depleted layer of oxidized TiAl, *Materials and Corrosion*, Vol. 48, pp. 23-27.

Dettenwanger, F., Schumann, E., Rühle, M., Rakowski, J. and Meier, G.H. (1998), Microstructural study of oxidised γ-TiAl, *Oxidation of Metals*, Vol. 50, pp. 269-307.

Dickerson, R.E., Gray, H.B., Haight, G.P. (1978), *Chemical Principles*, Forkner, M. and Rhame, B. (Eds), pp.46-92, Third edition Benjamin Cummings Publishing Company, California USA.

Dimiduk, D.M., Miracle, D.B and Ward, C.H. (1992), Development of intermetallic materials for aerospace systems, *Material Science Technology*, Vol. 8, pp. 367-375.

Dimiduk, D.M. (1999), Gamma titanium aluminide alloy: An assessment within the competition of aerospace structural materials, *Materials Science & Engineering* A, Vol. 263, No. 2, pp. 281-288.

Dimitrov, O. (1994), Ordering and disordering processes, *Intermetallic Compounds*, Principle and Practice1, Westbrook, J.H. and Fleischer, R.L. (Eds.), pp. 771-790, John Wiley & Sons Ltd., West Sussex, U.K..

Dinesh Kumar, A., Sathyanarayanan, S., Datta Gupta, S.D. and. Nageswara, M., Gas turbine materials- Current status and its developmental prospects-A critical review https://www.academia.edu/864980/Gas_Turbine_Materials-_Current_status_and_its_Developmental_Prospects-A_Critical_Review (Accessed 13 January 2015).

Ding, J.J., Qin, Q.W., Hao, S.M., Wang, X.T. and Chen, L. (1996), Partial phase diagram of the Ti-Al binary system, *Journal of Phase Equilibria*, Vol. 17, No. 2, pp. 117-120.

Ding, J.J., Rogl, P., Chevalier, B. and Etourneau, J. (2000), Structural chemistry and phase relations in intermetallic systems Ti-{Pd,Pt}-Al, *Intermetallics*, Vol. 8, No. 12, pp. 1377-1384.

Djanarthany, S., Viala, J-C., Bouix, J. (2001), An overview of monolithic titanium aluminides based on Ti_3Al and TiAl, *Materials Chemistry and Physics*, Vol. 72, pp. 301-319.

DMI Global (2012), http://www.dmiglobal.com/downloads/Turbochargers.pdf (Accessed 7 March 2012).

Donachie, M.J. (1989), *Titanium: A Technical Guide*, 2nd Edition, pp. 8-12, ASM International, Metals Park, Ohio, USA.

Draper, S.L., Krause, D., Lerch, B., Locci, I.E., Doehnert, B., Nigam, R., Das, G., Sickles, P., Tabernig, B., Reger, N and Rissbacher, K. (2015), Development and evaluation of TiAl sheet structures for hypersonic applications

http://ntrs.nasa.gov/archive/nasa/casi.ntrs.nasa.gov/20070034923.pdf (Accessed 13 January 2015).

Du, X.Q., Yang, Q.S., Chen, Y., Yang, Y. and Zhang, Z. (2014), Galvanic corrosion behaviour of copper/titanium galvanic couple in artificial seawater, *Transactions of Nonferrous Metals Society of China*, Vol. 24, pp. 570-581.

Duarte, A., Viana, F. and Santos, H.M.C.M. (1999), As-cast titanium aluminides microstructure modification, *Materials Research*, Vol. 2, No. 3, pp. 191-195.

Dunfee, W., Gao, M., Wei, R. P. and Wei, W. (1995), Hydrogen enhanced thermal fatigue of γ-titanium aluminide, *Scripta Metallurgica et Materialia*, Vol. 33, No. 2, pp. 245-250.

Duquette, D.J. (1994), Corrosion of intermetallic compounds, *Intermetallic compounds, Principles and Practice*, Vol. 1, pp. 965-975, John Wiley & Sons Ltd., West Sussex, U.K..

Duwez, P. and Taylor, J.L. (1952), Crystal structure of TiAl, *Journal of Metals*, pp.70-71.

Dykhuizen, R.C. and Smith, M.F. (1998), Gas dynamic principles of cold spray, *Journal of Thermal Spray Technology*, Vol. 7, No. 2, pp. 205-212.

Ebach-Stahl, A., Fröhlich, M. and Leyens, C. (2008), Influence of different annealing processes on the oxidation behaviour of γ-TiAl, *7th International Conference on Microscopy of Oxidation*, Chester, UK, 15-17 September 2008.

Ebach-Stahl, A., Fröhlich, M. and Leyens, C. (2009), Influence of different annealing processes under various atmospheres on the oxidation behaviour of γ-TiAl, *Materials at High Temperatures*, Vol. 26, No. 1, pp. 91-97.

Egerton, R. F. (2005), *Physical Principles of Electron Microscopy: An Introduction to TEM, SEM, and AEM*, pp. 125-151, Springer Science & Business Media, Inc.

Eliezer, D., Froes, F.H. and Suryanarayana, C. (1991), The effects of hydrogen on titanium aluminides, *Journal of Metals*, Vol. 43, No. 3, pp. 59-62.

Eliaz, N., Shemesh, G. and Latanasion, R.M. (2002), Hot corrosion in gas turbine components, *Engineering Failure Analysis*, Vol. 9, pp. 31-43.

Ellingham, H.J.T. (1944), Reducibility of oxides and sulphides in metallurgical processes, *Journal of the Society of Chemical Industry*, Vol. 63, No. 5, pp. 125-160.

Escudero, M.L., Muñoz-Morris, M.A., Garcıa-Alonso, M.C. and Fernandez-Escalante, E. (2004), In vitro evaluation of a γ-TiAl intermetallic for potential endoprothesic applications, *Intermetallics*, Vol. 12, pp. 253-260.

Fensin, S.J., Cerreta, E.K., Gray, G.T and. Valone, S.M (2014), Why are some interfaces in

materials stronger than others?, *Scientific Reports*, Vol. 4, pp. 1-5.

Figiel, P., Rozmus, M. and Smuk, B. (2011), Properties of alumina ceramics obtained by conventional and non-conventional methods for sintering ceramics, *Journal of Achievement in Materials and Manufacturing Engineering*, Vol.48, No. 1, pp. 29-34.

Freier, R.K. (1978), Supplements: Aqueous solution, Vol. 2, pp. 368-370, *Walter de Guyter publisher*, Berlin, Germany and New York, USA.

Froes, F.H., Suryanarayana, C. and Eliezer, D. (1992), Synthesis, properties and applications of titanium aluminides, *Journal of Materials Science*, Vol. 27, pp. 5113-5140.

Froes, F.H. (1994) Titanium aluminides: Science, technology, applications and synthesis by mechanical alloying, *Journal of Materials Science Technology*, Vol. 10, pp. 251-262.

Fu, E.K.Y., Rawlings, R.D. and. McShane, H.B. (2001), Reaction synthesis of titanium aluminides, *Journal of Materials Science*, Vol. 36, pp. 5537-5542.

Gao, K.W., Jin, J.W., Qiao, L.J., Chu, W.Y. and Hsiao, C.M. (1996), Effect of hydrogen on cathodic corrosion of titanium aluminide, *Journal of Corrosion*, Vol. 52, No. 1, pp. 3-7.

Garima, S., Singh, P.R., Sharma, R.K., Gaonkar, K.B. and Ramanujan, R.V. (2007), Aqueous corrosion behaviour of iron aluminide intermetallics, *Journal of Materials Engineering and Performance*, Vol. 16, No. 6, pp. 779-783.

Gauthier, V., Dettenwanger, F., Schutze, M., Shemet, V. and Quadakkers, W. J.(2003), Oxidation-resistant aluminide coatings on γ-TiAl, *Oxidation of Metals*, Vol. 59, No. 3-4, pp. 233-255.

Gauvin, R., Bernier, M.A., Joy, D.C. and. Schmidt, M. (1993), Characterisation of microstructural evolution of TiAl during mechanical alloying, *Proceedings of the 2nd Conference on Structural Applications of Mechanical Alloying*, pp. 93-100, Vancouver, British Columbia, Canada, 20-22 September 1993.

Gerling, R. Clemens, H., Schimansky, F and Wegmann, G. (2001), PM-processing of an advanced γ-TiAl alloy: Technologies, microstructures and mechanical properties, *Structural Intermetallics*, pp. 139-148, The Mineral, Metals & Materials Society, AIME, Warrendale, PA, USA.

German, R.M. and Bose, A. (1997), *Injection moulding of metals and ceramics*, pp.11-99, MPIF Publication, 105 College Road East, Princeton, New Jersey, USA.

German, R.M. (2005), *Powder Metallurgy and Particulate materials Processing*, pp. 400-401, MPIF Publication, 105 College Road East, Princeton, New Jersey, USA.

Ghali, E. and Winston Revie, R. (2010), *Corrosion resistance of aluminum and magnesium alloys:*

Understanding, performance, and testing, Vol. 12, pp. 459-463, John Wiley & Sons, West Sussex, UK.

Ghelichi, R and Guagliano, M. (2009), Coating by the cold process: a state of the art, *Frattura ed Integrita Strutturale*, Vol. 8, pp. 30-44.

Goral, M., Moskal, G. and Swadzba, L. (2006), The influence of Si on oxidation resistance of aluminide coatings on TiAl alloy, *Journal of Achievement in Materials and Manufacturing Engineering*, Vol. 18, pp. 459-462.

Govender, K., Scenini, F., Lyon, S.B. and Sherry, A.H. (2012), The influence of Pd and Ru additions on stress corrosion cracking of austenitic stainless steels, *Corrosion Engineering Science and Technology*, Vol. 47, No. 7, pp. 507-515.

Grigoriev, S., Okunkova, Sova, A., Bertrand, P. and Smurov, I. (2015), Cold spraying: From process fundamentals towards advanced applications, *Surface and Coatings Technology*, Vol. 268, pp. 77-84.

Grytsiv, A., Rogl, P. Schmidt, H. and Giester, G. (2003), Constitution of the ternary system Al-Ru-Ti (Aluminium-Ruthenium-Titanium), *Journal of Phase Equilibria*, Vol. 24, No. 6, pp. 511-527.

Grytsiv, A., Rogl, P. and Schmidt, H. (2004), Influence of 2 at.% ruthenium addition on the oxidation of γ-TiAl at 900°C in air, *Oxidation of Metals*, Vol. 62, pp. 15-28.

Gubicza, J. (2014), *X-ray line profile analysis in materials science*, pp.15-170, Engineering science Reference (IGI Global), Hershey PA, USA.

Gurrapa, I. (2001a), Platinum aluminide coatings for oxidation resistance of titanium alloys, *Platinum Metals Review*, Vol. 45, No. 3, pp. 124-129.

Gurrapa, I. (2001b), High-performance coatings for titanium alloys to protect against oxidation, *Surface Coatings Technology*, Vol. 139, pp. 216-221.

Guyon, J., Hazotte. A., Monchoux, J.P. and Bouzy, E. (2013), Effect of powder state on spark plasma sintering of TiAl alloys, *Intermetallics*, Vol. 34, pp.94-100.

Hanaor, D.A.H. and Sorrell, C.C. (2011), Review of the anatase to rutile phase transformation, *Journal of Materials Science*, Vol. 46, pp. 855-874.

Haasen, P. (1978), *Physical Metallurgy*, pp. 141-165, Cambridge University Press, Cambridge, UK.

Haruna, T., Shibata, T., Iwatam, T. and Sund Ararajan, T. (2000), Potential-pH region for environment-assisted cracking of gamma titanium aluminide, *Intermetallics*, Vol. 8, No. 8, pp. 929-935.

Hayes, F. H. (2009) updated by Cacciamani, G., Cornish, L., Cupid, D.M. and De Keyzer, J., Aluminium-Carbon-Titanium, in Landolt-Boernstein, Numerical data and functional

relationships in *Science and Technology (New Series).* Group IV: *Physical Chemistry*, Martiensen, W. (Ed), "Ternary Alloy Systems. Phase Diagrams, Crystallographic and Thermodynamic Data", Vol. 11E1, Effenberg, G. and Ilyenko, S. (Eds.), Springer-Verlag, Berlin, Heidelberg, pp. 41-71.

Higginson, A. (1989), Passivation of cathodically modified alloys, *British Corrosion Journal*, Vol. 24, No. 4, pp. 297-302.

Hoar, T.P. (1960), Increasing the resistance of titanium to non-oxidising acids, influence of addition of platinum metals, *Platinum Metals Review*, Vol. 4, No. 2, pp. 59-64.

Horiba Scientific (2014), A guidebook to particle size analysis, on https://www.horiba.com/fileadmin/uploads/Scientific/Documents/PSA/PSA_Guidebook.pdf (Accessed on 9 January 2014).

Huang, S.C. and. Chesnutt, J.C. (1994), Gamma TiAl and its alloys, *Intermetallic Compounds, Principle and Practice*, Westbrook, J.H. and Fleischer , R.L. (Eds.), Vol. 2, pp. 73-89, John Wiley & Sons Ltd., Sussex, U.K.

Hui-Ren, J.g-Lei, W., Wen-Shuai, M., Xiao-Ran, F., Zi-Qiang, D., Liang Z. and Yong, L. (2008), Effects of Nb and Si on high temperature oxidation of TiAl, *Transactions of Non-ferrous Metals Society of China*, Vol. 8, pp. 512-517.

Hume-Rothery, W. (1963), *Electrons, atoms, metals and alloys*, Dover Publications, 3rd edition, California, USA.

Humphrey, G.L. (1951), The Heats of Formation of TiO, Ti_2O_3, Ti_3O_5 and TiO_2 from combustion calorimetry, *Journal of the American Chemical Society*, Vol. 73, No 4, pp 1587-1590.

Hung, J.H., Chiu, Y.L. and Liang, J. (2008), Reciprocating wear properties of thermal sprayed titanium aluminide-alumina composite coating, *Surface and Coating Technology*, Vol. 202, pp. 5599-5602.

Hussain, T. (2013), Cold spraying of titanium: A review of bonding mechanisms, microstructure and properties, *Key Engineering Materials*, Vol. 533, pp. 53-90.

Hwang, W.S. and Kim, H.W. (2002), Galvanic coupling effect on corrosion behaviour of Al alloy-matrix composites, *Metals and Materials International*, Vol. 8, No. 6, pp. 571-575.

Imayev, R.M., Imayev, V.M., Oehring, M., Appel, F. (2007), Alloy design concepts for refined gamma titanium aluminide based alloys, *Intermetallics*, Vol. 15, pp. 451-460.

Jacob, V., Baccino, R., Moret, F., Suryanarayana, C., Froes, F.H., Mishurda, J. and Frefer, A. (1993), Microstructural transformation during mechanical alloying of Ti-47.5Al-3Cr titanium aluminium powder, *Proceedings of the 2nd Conference on Structural Applications of Mechanical Alloying*, pp. 33-39, Vancouver, British Columbia, Canada, 20-22 September 1993.

Jacobson, N.S., Brady, M.P. and Mehrotra, G.M. (1999), Thermodynamics of selected Ti-Al and Ti-Al-Cr alloys, *Oxidation of Metals*, Vol. 52, pp. 537-555.

Jafariana, H., Saebnooria, E., Sabour-Rougaghdama, A. and Shahrabia, T. (2009), Electrochemical corrosion of oxidized gamma-titanium aluminide in Ringer's solution, *Iranian Journal of Pharmaceutical Sciences*, Vol. 5, No. 1, pp. 51-54.

Jaw, K.S., Hsu, C. and Lee, J. (2001), The thermal decomposition behaviors of stearic acid, paraffin wax and polyvinyl butyral, *Thermochimica Acta*, Vol. 367-368, pp. 165-168.

Jeandin, M., Koivuluato, H and Vezzus, S. (2013), Coating properties, *Modern Cold Spray: Materials, Process, and Applications*, Villafuerte, J (Ed), pp. 107-224, Springer International Publishing AG, Switzerland.

Jeurgens, L.P.H., Sloof, W.G., Tichelaar, F.D. and Mittemeijer, E.J. (2002), Structure and morphology of aluminium-oxide films formed by thermal oxidation of aluminium, *Thin Solid Films*, Vol. 418, pp. 89-101.

Jiangping, L., Yanqing, S., Yanjin, X., Liangshun, L., Jingjie, G. and Hengzhi, F. (2011), First phase selection in solid Ti/Al diffusion couple, *Rare Metal Materials Engineering*, Vol. 40, No. 5, pp. 753-56.

Jillavenkatesa, A., Dapkunas, S.J. and. Lum, L.H. (2001), Particle size characterisation, *US National Institute of Standards and Technology, Special Publication*, Vol. 960, No. 1, pp. 125-137.

Jha, B.B., Sahoo, R. and T.K. Sahoo, T.K. (2015), Microstructural characterization of Ti-6Al-4V using ultrasonic attenuation and its correlation with mechanical behavior, *25th National Seminar & International Exhibition on Non Destructive Evaluation*, Hyderabad, India, 26-28 November 2015

Jovanović, M.T., Dimčić, B., Bobić, I., Zec, S. and Maksimović, V. (2004), Microstructure and mechanical properties of precision cast TiAl turbocharger wheel, *Materials Processing Technology*, Vol. 167, pp. 14-21.

Kainuma, R., Palm, M. and Inden, G. (1994), Solid-phase equilibria in the Ti-rich part of the Ti-Al system, *Intermetallics*, Vol. 2, No. 4, pp. 321-332.

Kattner, U.R., Lin, J.C., Chang, Y.A., (1992), Thermodynamic assessment and calculation of the Ti-Al system, *Journal of Metallurgical and Materials Transactions A*, Vol. 23, pp. 2081-2090.

Kekare, S.A. and Aswath, P.B. (1997), Oxidation of TiAl based intermetallics, *Journal of Material Science*, Vol. 32, pp. 2485-2499.

Khataee, A., Flower, H.M. and West, D.R.F. (1989a), The alloying of titanium aluminides with ruthenium, *Platinum Metal Review*, Vol. 33, No. 3, pp. 106-113.

Khataee, A. Flower, H.M. and West, D.R.F. (1989b), Constitution of Ti-Al-Ru system, *Materials Science and Technology*, Vol. 5, No. 7, pp. 632-643.

Khataee, A., Flower, H.M. and West, D.R.F. (1989c), Solid state transformation in Ti-Al-Ru system, *Materials Science and Technology*, Vol. 5, No. 7, pp. 873-881.

Khor, K.A., Murakoshi, Y., Takahashi, M. and Sang, T. (1996), Microstructure changes in plasma sprayed TiAl coating after isostatic pressing, *Journal of Materials Science Letters*, Vol. 15, No. 20, pp. 1801-1804.

Khoshhal, R., Soltanieh, M. and Mirjalili, M. (2010), Formation and growth of titanium aluminide layer at the surface of titanium sheets immersed in molten aluminum, *Iranian Journal of Materials Science and Engineering*, Vol. 7, No. 1, pp. 24-31.

Kim, H.B., Ahn, S., Jang, H.J., Sim, S.B. and Kim, K.W. (2007), Evaluation of corrosion behaviour and surface profiles of platinum-coated electrodes by electrochemistry and complementary microscopy: Biomedical implications for cancer therapy, *Micron*, Vol. 38, pp. 747-753.

Kim, Y. and Dimiduk, D.M. (1991), Progress in the understanding of gamma titanium aluminides, *Journal of Metals*, pp. 40-47.

Kim, S., Larson, D.J. and Smith, G.D.W. (1999), Alloying element partitioning in TiAl-Ru intermetallic alloys, *Intermetallics*, Vol. 7, No. 11, pp. 1283-1290.

Kim, Y.W. (1989), Intermetallic alloys based on gamma titanium aluminides, *The Journal of The Minerals, Metals & Materials Society (TMS)*, Vol. 41, No. 7, pp. 24-30.

Kim, Y.W. (1994a), Ordered intermetallic alloys, part III: Gamma titanium aluminides, *The Journal of The Minerals, Metals & Materials Society (TMS)*, Vol. 46, No. 7, pp. 30-39.

Kim, Y.W. (1994b), Gamma titanium aluminides, *The Journal of The Minerals, Metals & Materials Society (TMS)*, Vol. 46, No. 7, pp. 127-135.

Kim, Y.H. and Frankel, G.S. (2007), Effect of noble metal alloying on passivity and passivity breakdown of nickel, *Journal of the Electrochemical Society*, Vol. 154, pp. 36-42.

Kimura, Y. and Pope, D. (1997), Ductility and toughness considerations, *Structural Intermetallics*, The Minerals, Metals & Materials Society, Nathal, M.V., Darolia, R., Liu, C.T., Martin, P.L., Miracle, D.B., Wagner, R. and Yamaguchi M. (Eds.), pp. 99-106, TMS, Warrendale, PA, USA.

King, P., Yandouzi, M. and Jodoin, B. (2013), The physics of cold spray, *Modern Cold Spray: Materials, Process, and Applications*, Villafuerte, J (Ed), pp. 31-72, Springer International Publishing AG, Switzerland.

Klinkov, S.V., Kosarev, V.F. and Rein, M. (2005), Cold spray deposition: Significance of particle impact phenomena, *Aerospace Science and Technology*, Vol. 9, pp. 582-591.

Korb, L.J. and Olson, D.L. (1987), *Corrosion*, *ASM Handbook*, Vol. 13, No. 9, pp. 375-498, ASM International, Metals Park, Ohio 44073-0002, USA.

Krasicka-Cydzik, E., Kierzkowska, A. and Glazowska, I. (2007), Behaviour of anodic layer in Ringer's solution on Ti-6Al-4V ELI alloy after bending, *Archives of Materials Science and Engineering*, Vol. 28, No. 4, pp. 231-237.

Krienke, R.D. (1969), Plating wear-resistant coatings on titanium, *Metal Progress*, Vol. 95, No. 6, pp. 89-90.

Krishna Reddy, L (2008), *Principles of Engineering Metallurgy*, pp. 78-86, New Age Publisher, New Delhi, India.

Kubascheswski, O. and Alcock, C.B. (1979), Metallurgical Themochemistry, *International Series on Materials Science and Technology*, Raynor, G.V. and Phil, D. (Eds.), Vol. 24, No 5, pp. 267-317.

Lagos, M.A and Agote, I. (2013), SPS synthesis and consolidation of TiAl alloys from elemental powders: Microstructure evolution, *Intermetallics*, Vol. 36, pp. 51-56.

Lan, H. (2011), Microstructural evolution of (TiAl)+Nb+W+B alloy, *Transactions of Nonferrous Metals Society of China*, Vol. 21, pp. 2192-2198.

Landolt, D. (2007), Corrosion and Surface Chemistry of Metals, *Engineering Sciences Materials*, pp. 292-300, EPFL Press, Lausanne, Switzerland.

Lang, C. and Schütze, M. (1996), TEM investigation of the early stage of TiAl oxidation, *Oxidation of Metals*, Vol. 46, pp. 255-285.

Lapin, J. (2009), TiAl-based alloys: present status and future perspective, *Journal of Metals*, Vol. 5, pp. 19-25.

Lasalmonie, A. (2006), Intermetallics: why is it so difficult to introduce them in gas turbine engines? *Intermetallics*, Vol. 14, pp. 1123-1129.

Lavoisier, A. (1789), Traité élémentaire de chimie, Cuchet (Ed), Paris.

Lee, C.P., Chen, Y.Y., Hsu, C.Y., Yeh, J.W. and Shih, H.C. (2008), Enhancing pitting corrosion resistance of AlxCrFe1.5MnNi0.5 high-entropy alloys by anodic treatment in sulphuric acid, *Thin Solid Films*, Vol. 517, pp. 1301-1305.

Lee, D. (2005), Effect of Cr, Mn, V, W, and Si on high-temperature oxidation of TiAl alloys, *Metallic Materials International*, Vol. 11, pp. 141-147.

Leyens, C., Peter, M. and Kaysser, W.A. (1997), Intermetallic Ti-Al coatings for titanium alloys:

oxidation and mechanical behaviour, *Surface and Coating Technology*, Vol. 94-95, pp. 34-40.

Leyens, C., Peters, M., Hovsepian, P.E., Lewis, D.B., Luo, Q. and Munz, W.D. (2002), Novel coating systems produced by the combined catholic arc/unbalanced magnetron sputtering for environmental protection of titanium alloys, *Surface and Coatings Technology*, Vol. 155, pp. 103-111.

Leyens, C. and Peters, M. (2003), *Titanium and its alloys: Fundamentals and applications*, pp. 231-244, Wiley-VCH, Weinhein, Germany.

Leyens, C. and Braun, R. (2004), Environment and thermal protection of γ-TiAl alloys, *Materials Science Forum*, Vol. 461-464, pp. 223-230.

Li, C., Yang, W.H., Frefer, A. and Froes, F.H. (1993), Compaction of mechanically alloyed gamma titanium aluminide, *Proceedings of the 2nd Conference on Structural Applications of Mechanical Alloying*, pp. 83-91, Vancouver, British Columbia, Canada, 20-22 September 1993.

Li, C. and Li, W. (2003), Deposition characteristics of titanium coating in cold spraying, *Surface and Coatings Technology*, Vol. 167, pp. 278-283.

Li, X.L., Hillel, R., Teyssandier, F., Choi, S.K. and Van Loo, F.J.J. (1992), Reactions and phase relations in the Ti-Al-O system, *Acta Metallurgica et Materialia*, Vol. 40, No. 11, pp. 3149-3157.

Liu, C.T. and Kim, Y.W. (1992), Room-temperature environmental embrittlement in a TiAl alloy, *Scripta Metallurgica et Materialia*, Vol. 27, pp. 599-603.

Liu. Q. and Nash, P. (2011), The effect of ruthenium addition on the microstructure and mechanical properties of TiAl alloys, *Intermetallics*, Vol.19, No 9, pp. 1282-1290.

Liu, Y. and Liu, W. (2007), Mechanical alloying and spark plasma sintering of the intermetallic compound Ti50Al50, *Journal of Alloys and Compounds*, Vol. 440, pp. 154-157.

Liu, Z. and Narita, T. (2003), The effect of water vapour on the oxidation behaviour of γ-TiAl–Ag coatings at 1073 K in air, *Intermetallic*s, Vol. 11, pp. 795-805.

Locci, I.E., Brady, M.P. and Smialek, J.L. (2001), Long term oxidation of model and engineering TiAl Alloys, *Materials Research Society Symposium Proceeding*, Vol. 646, pp. 501-506.

Long, M. and Rack, H.J. (1998), Titanium alloys in total joint replacement: A materials science perspective, *Biomaterials*, Vol. 19, No. 18, pp. 1621-1639.

Loria, E.A. (2000), Gamma titanium aluminides as perspective structural materials, *Intermetallics*, Vol 8, pp. 1339-1345.

Loria, E.A. (2001), Quo vadis gamma titanium aluminide, *Intermetallics*, Vol. 9, No. 12, pp. 997-1001.

Lozitskii, L.P., Karpov, E.N., Kudryashov, B.Y. and Motrii, N.N. (1974), Corrosion resistance of gas turbine tested in a high-temperature gas flow, *Problemy Prochnosti* (English translation), Vol. 9, pp. 87-90, Kiev Institute of Civil Aviation, Ukraine.

Lloyd, G.E. (1987), Atomic number and crystallographic contrast images with the SEM: A review of backscattered electron techniques, *Mineralogical Magazine*, Vol. 51, pp. 3-19.

Lü, L. and Lai, M.O. (1998), *Mechanical alloying*, Kluwer Academic, Massachusetts, USA.

Lütjering, G. and Williams, J.C. (2007), *Titanium-Engineering Materials and Processes*, Derby, B. (Ed.), pp. 33-35, Springer Berlin Heidelberg, New-York, USA.

Ma, H., Wang, M. and Wu, W. (2004), Oxygen permeation behaviours and hardening of titanium at high temperatures, *Journal of Material Science and Technology*, Vol. 20, No 6, pp. 719-723.

Marakusheva, A.A., and Bezmena, N.I. (1971), Chemical affinity of metals for oxygen and sulfur, *International Geological Review*, Vol. 13, pp. 1781-1794.

Martin, P.L. and Hardwick, D.A. (1994), Synthesis and Processing techniques, *Intermetallic compounds, Principles and Practice*, Vol. 1, Westbrook, J.H. and Fleischer, R.L. (Eds.), pp. 637-659, John Wiley & Sons Ltd., West Sussex, UK.

McCullough, C. Valencia, J.J., Levi, C.G. and Mehrabian, R. (1989), Phase equilibria and solidification in Ti-Al alloys, *Acta Metallurgica*, Vol. 37, No. 5, pp. 1321-1336.

McGill, I.R. (1990), Platinum metals in stainless steels, *Platinum Metals Review*, Vol. 34, No. 3, pp. 144-154.

McKee, D.W. and Huang, S.C. (1992), The oxidation behaviour of gamma-titanium aluminide alloys under thermal cycling conditions, *Corrosion Science*, Vol. 33, pp. 1899-1914.

Meier, G.H. (1989), A review of advances in high-temperature-corrosion, *Materials Science and Engineering A*, Vol. 120, pp. 1-11.

Meier, G., Pettit, F and Hu, S. (1993), Oxidation behaviour of titanium aluminides, *Journal de Physique*, IV Colloque C, Vol. 3, No. 9, pp.395-402.

Mei, B. and Miyamoto, Y. (2001), Preparation of Ti-Al intermetallic compounds by spark plasma sintering, *Metallurgical and Material Transactions A*, Vol. 32, pp. 843-847.

Mikli, V., Käerdi, H., Kulu P. and Besterci, M. (2001), Characterization of powder particle morphology, *Proceedings of the Estonian Academy of Sciences*, Vol. 7, No. 1, pp. 22-34.

Minkoff, I. (1967), Applications of the scanning electron microscope in materials science, *Journal of Materials Science*, Vol. 2, pp. 388-394.

Mitoraj, M. and Godlewska, E.M. (2013), Oxidation of Ti-46Al-8Ta in air at 700°C and 800°C under thermal cyclic conditions, *Intermetallics*, Vol. 34, pp. 112-121.

Moridi, A., Hassani-Gangaraj, S. M., Guagliano, M. and Dao, M. (2014), Cold spray coating: Review of material systems and future perspectives, *Surface Engineering*, Vol. 36, No 8, pp. 369-392.

Morris, J.W. Jr., (2001), Dislocation Plasticity: an Overview, *Encyclopedia of Materials Science and Technology*, pp. 1-36, Elsevier Science, Amsterdam.

Moskal, G. (2007), Microstructure and oxidation behaviour of TiAlSi coatings on TiAlCrNb alloys, *Journal of Achievements in Materials and Manufacturing Engineering*, Vol. 20, pp. 263-266.

Monnartz, P. (1911), The study of the Fe-Cr alloys with particular regard to their solubility toward acids, *Metallurgie*, Vol. 8, pp. 161-176.

Mordi, A., Hassani-Gangaraj, S.M., Guagliano, M. and Dao, M. (2014), Cold spray coating: review of material systems and future perspectives, *Surface Engineering*, Vol. 36, No. 6, pp. 369-395.

Moskalewicz, T., Wendler, B., Zimowski, S., Dubiel, B. and Czyrska-Filemonowicz, A. (2010), Microstructure, micro-mechanical and tribological properties of the nc-WC/a-C nanocomposite coatings magnetron sputtered on non-hardened and oxygen hardened Ti-6Al-4V alloy, *Surface & Coatings Technology*, Vol. 205, pp. 2668-2677.

Mridha, S., Ong, H.S., Poh, L.S. and Cheang, P. (2001), Intermetallics coatings produced by TIG surface melting, *Materials Processing Technology*, Vol. 113, pp. 516-520.

Murata, Y., Morinaga, M., Shimamura, Y., Takeda Y. and Miyaza, S. (1993), Mechanical properties and oxidation resistance of high purity TiAl Intermetallic compounds, *International Symposium on Structural Intermetallics Conference Proceedings*, pp. 247-256, Warrendale, Pennsylvania, USA, The Minerals, Metals & Materials Society, 26-30 September 1993.

Murray, J.L. and Wreidt, H.A. (1986), Oxygen-Titanium, *Binary Phase Diagrams*, Massalski et al. (Eds.), Vol. 2, pp. 1789-1794, ASM International, Ohio, USA.

Murray, J.L. (1988), Calculation of the titanium-aluminium phase diagram, *Metallurgical Transactions A*, Vol. 19, pp. 243-247.

Mwamba, A. and Chown, L. (2007a), Progress on development of water atomisation technique for platinum powders, *Mintek External Report 4725*.

Mwamba, A. and Chown, L. (2007b), Platinum-based super alloy components via powder metallurgy: Atomisation trials of platinum, *Mintek External Report 4726*.

Mwamba, A. (2008), Atomisation trials of copper, nickel, and iron for leaching applications,

Mintek Internal Report 40240.

Mwamba, A. and L.H. Chown, L.H. (2011), The use of titanium hydride in blending and mechanical alloying of Ti-Al alloys, *The Journal of The Southern African Institute of Mining and Metallurgy*, pp.159-165.

Nakagawa, M., Matono, Y., Matsuya, S., Udoh, K. and Ishikawa, K. (2005), The effect of Pt and Pd alloying additions on the corrosion behaviour of titanium in fluoride-containing environments, *Biomaterials*, Vol. 26, pp. 2239-2246.

Narita, T., Izumi, T., Yatagai, M. and Yoshioka, T. (2000), Sulphidation processing and Cr addition to improve oxidation resistance of TiAl intermetallics in air at 1173 K, *Intermetallics*, Vol. 8, pp. 371-379.

Neves, F., Carvalho, M.H. and Trindade, B. (2003), Production and consolidation of nanostructured mechanically alloyed Ti-Al-Ag intermetallics, *Materials Technology*, Vol.18, No 4, pp. 224-229.

Niewolak, L., Shemet, V. Thomas, C., Lersch, P., Singheiser, L. and Quadakkers, W.J. (2004), Oxidation behaviour of Ag-containing TiAl-based intermetallics, *Intermetallics*, Vol. 12, pp. 1387-1396.

Nordtest (2012), Nordtest methods, on: http://nordtest.info/images/documents/nt-methods/materials/NT%20mat%20001_Combustion%20by-products,%20corrosion_Corrosivity%20of%20combustion%20by-products%20used%20as%20fill%20around%20carbon%20steel%20structures_Nordtest%20Method.pdf (Accessed 7 March 2012).

Oguike, R.S. (2014), Corrosion studies on stainless steel (FE6956) in hydrochloric acid solution, *Advances in Materials Physics and Chemistry*, Vol. 4, pp. 53-163.

Okafor, I.C.I. and Reddy, R.G. (1999), The oxidation behaviour of high-temperature aluminides, *Journal of Metals*, Vol. 51, No. 6, pp. 35-40.

Okamoto, H. (1992), Aluminium-Carbon, *Journal of Phase Equilibria*, Vol. 13, No. 1, pp. 97-98.

Oliker, V.E. and Kresanov, V.S. (2000), Structure and properties of detonation coatings based on γ-TiAl, *Poroshk. Metall*., Vol. 11-12, pp. 82-88.

Oliker, V.E. and Kresanov, V.S. (2003), Scandium-containing gamma titanium aluminide alloys and coatings for aerospace structural parts, *Advanced Materials and Processes for Gas Turbines*, pp. 293-300, The Minerals, Metals and Materials Society, Warrendale, USA.

Oliker, V.E., Sirovatka, V.L., Grechishkin, E.F., Kostenko, A.D., Lashneva, V.V., Maksyuta, I.I., Anikin, Y.F., Goncharenko, A.F. and Derkach, V.M. (2005), Tribological properties of

detonation coatings based on titanium aluminides and aluminium titanate, *Powder Metallurgy and Metal Ceramics*, Vol. 44, No. 11-12, pp. 531-536.

Olubambi, P.A., Potgieter, J.H. and Cornish, L.A. (2009), Corrosion behaviour of superferritic stainless steels cathodically modified with minor additions of Ru in sulphuric and hydrochloric acid solutions, *Materials and Design*, Vol. 30, No. 5, pp. 1451-1457.

Osorio, J.D., Giraldo, J., Hernandez, J.C., Toro, A. and Hernández-Ortiz, J.P. (2014), *Heat Mass Transfer*, Vol. 50, pp.483-492.

Padmini, B.V., Rajani S. and Niranjan, H.B. (2014), Kinetic spray: the future art of coating, *Journal of Mechanical Engineering Research and Technology*, Vol. 2, No. 1, pp. 239-245.

Peterson, B. (2011), Energy dispersive spectroscopy characterization of solute segregation in Ti-6Al-4V, *MSc Thesis*, pp. 17-27.,Graduate Program in Materials Science and Engineering, The Ohio State University, USA.

Pietsch, W. (2004), Agglomeration in Industry: Occurrence and applications, *John Wiley & Sons*, Weinhein, Germany, Vol 1, pp. 37-45.

Pollock, T.M. (2006), Nickel-based superalloys for advanced turbine engines: chemistry, microstructure, and properties, *Journal of Propulsion and Power*, Vol. 22, No. 2, pp. 361-374.

Potgieter, J.H., Heyns, A.M. and Skinner, W. (1990), Cathodic modification as a mean of improving the corrosion resistance of alloys, *Journal of Applied Electrochemistry*, Vol. 20, pp. 711-715.

Potgieter, J.H. (1991), Alloys cathodically modified with noble metals, *Journal of Applied Electrochemistry*, Vol. 241, pp. 471-482.

Potgieter, J.H. and Brookes, H. (1995), The corrosion behaviour of a high chromium duplex stainless steel with minor additions of Ru in sulphuric acid, *Corrosion*, Vol. 51, No. 4, pp. 312-320.

Potgieter, J.H. (2010), Corrosion of Passive Alloys: The effect of noble metal additions, *Shreir's Corrosion*, Richardson, T.J.A. (Ed.), Elsevier Science, Vol. 3, pp. 2224-2249.

Pourbaix, M.J.N., Van Muylder, J. and de Zoubov, N. (1959), *Platinum Metals Review*, Vol. 3, No. 2, pp. 47-53.

Pourbaix, M. and de Zoubovan, N. (1963), *Etablissement et interprétation de diagrammes équilibres tension-pH*, *Atlas d'équilibres électrochimiques*, van Muylder, J. (Ed.), pp. 343–383, Publication du Centre Belge d'Etude de la Corrosion, Paris, France (in French).

Price, P.E. (1998), Cold isostatic pressing, *Powder Metal Technologies and Applications, ASM Handbook, Vol. 7*, Lee, P.W. (Ed.), pp. 382-388, ASM International, Metals Park, Ohio, USA.

Pu, Z., Shi, J., Zou, D. and Zhong, Z. (1993), Microstructure and mechanical properties of TiAl-based alloys, *Journal of Materials Science and Technology*, Vol. 9, pp. 449-457.

Rahmel, A. and Spencer, P.J. (1991), Thermodynamic aspects of TiAl and $TiSi_2$ oxidation: The Al-Ti-O and Si-Ti-O phase diagrams, *Oxidation of Metals*, Vol. 35, pp. 53-68.

Rahmel, A., Quadakkers, W.J. and Schutze, M. (1995), Fundamentals of TiAl oxidation: A critical review, *Materials and Corrosion*, Vol. 46, pp. 271-285.

Raghavan, V. (2005), Aluminium-Titanium, *Journal of Phase Equilibria and Diffusion*, Vol. 26, No. 2, pp. 171-172.

Raghavan, V. (2008), Al-Ir-Ti, *Journal of Phase Equilibria and Diffusion*, Vol. 29, No 4, pp. 371-372.

Raghavan, V. (2011), Al-Pd-Ti, *Journal of Phase Equilibria and Diffusion*, Vol. 32, pp. 251-252.

Raghavan, V. (2012a), Al-Pd-Ti (Aluminum-Palladium-Titanium), *Journal of Phase Equilibria and Diffusion*, Vol. 33, pp. 145-146.

Raghavan, V. (2012b), Al-Pt-Ti (Aluminum-Platinum-Titanium), *Journal of Phase Equilibria and Diffusion*, Vol. 33, pp. 147-148.

Rakowski, J.M., Pettit, F.S., Meier, G.H., Dettenwanger, F., Schumann, E. and Ruble, M. (1995), The effect of nitrogen on the oxidation of γ-TiAl, *Scripta Metallurgica et Materialia*, Vol. 33, pp. 997-1003.

Ramanujan, R.V (2000), Phase transformations in γ-based titanium aluminides, *International Materials Reviews*, Vol. 45, No. 6, pp. 217-240.

Rao, V.S. (2004), A review of the electrochemical corrosion behaviour of iron aluminides, *Electrochimica Acta*, Vol. 49, pp. 4533-4542.

Rasooli, A., Boutorabi, M.A., Divandari M. and Azarniyabull, A. (2013), Effect of high heating rate on thermal decomposition behaviour of titanium hydride (TiH_2) powder in air, *Materials. Science*, Vol. 36, No. 2, pp. 301-309.

Reddy, R.G., Wen, X. and Divakar, M. (2001), Isothermal oxidation of TiAl alloys, *Metallurgical and Materials Transactions A*, Vol. 32, pp. 2357-2361.

Reed, R.C. (2006), *The Superalloys: Fundamentals and applications*, pp. 18-25, Cambridge University Press, UK.

Riaz, S., Flower, H.M., West and D.R.F. (2000), Phase relationships involving TiC and Ti_3AlC (P Phase) in Ti-Al-C system, *Materials Science and Technology*, Vol. 16, pp. 984-992.

Ricker, R.E., Hall, D.E. and Fink, J.L. (1990), The effect of aqueous environments on the fracture behaviour of ductile nickel aluminide, *Scripta Metallurgica et Materialia*, Vol. 24, pp. 291-

296.

Riggs, W. and Couch, K. (2013), Metallography and image analysis, *Handbook of Thermal Spray Technology*, Davis, J.R. (Ed.), pp. 224-259, ASM International, Metals Park, Ohio, USA.

Rivera-Denizard, O., Diffoot-Carlo, N., Navas, V. and Sundaram, P.A. (2008), Biocompatibility studies of human foetal osteoblast cells cultured on gamma titanium aluminide, *Journal of Materials Science: Materials in Medicine*, Vol. 19, pp. 153-158.

Rybalka, K.V., Beketaeva, L.A., Bukhan'ko, N.G. and Davydov, A.D. (2011), Electrochemical behaviour and the rate of general corrosion of NiAl intermetallic compound in the unbuffered sodium chloride solutions, *Corrosion Science*, Vol. 53, pp. 630-636.

Roy, T.K., Balasubramaniam, R. and Ghosh, A. (1996), High-temperature oxidation of Ti_3Al-based titanium aluminides in oxygen, *Metallurgical and Materials Transactions*, Vol. 27A, pp. 3993-4002.

Saffarian, H.M., Gan, Q., Hadkar, R. and Warren, G.W. (1996), Corrosion behaviour of binary titanium aluminide intermetallics, *Corrosion Science*, Vol. 52, No. 8, pp. 626-633.

Salman, A., Gabbitas, B., Li, J. and Zhang, D.(2009), Tribological properties of thermally sprayed TiAl-Al_2O_3 composite coating, *Materials Science and Engineering*, Vol. 4, pp. 1-5.

Sánchez, F. Bolarín, A.M., Molera, P., Mendoza, J.E. and Ocampo, M. (2003), Relationship between particle size and manufacturing processing and sintered characteristics of iron powders, *Revista Latinoamericana de Metalurgia y Materiales*, Vol. 23, No. 1, pp. 35-40.

Sandim, H.R.Z., Morante, B.V. and Suzuki, P.A. (2005), Kinetics of Thermal Decomposition of Titanium hydride powder using in situ high-temperature X-ray Diffraction (HTXRD), *Materials Research*, Vol. 8, No. 3, pp. 293-297.

Sandvik (2015), on http://www.smt.sandvik.com/en/products/metal-powder/list-of-materials/ (Accessed 8 April 2015).

Satoh, H., Shimagori, K. and Kamikubo, F. (1987), The crevice corrosion resistance of some titanium materials: A review of the beneficial effects of palladium, *Platinum Metal Review*, Vol. 31, No. 3, pp. 115-121.

Savitsky, E., Polyakova, V, Gorina, N. and Roshan, P. (1978), *Physical Metallurgy of Platinum Metals*, pp. 84-85, MIR Publishers, Russia.

Schimansky, F.P., Liu K.W. and Gerling, R. (1999), Spray forming of gamma titanium aluminides, *Intermetallics*, Vol. 7, No. 11, pp. 1275-1282.

Schmitz-Niederau, M. and Schutze, M. (1999), The oxidation behaviour of several Ti-Al alloys at 900°C in air, *Oxidation of Metals*, Vol. 52, No. 3-4, pp. 225-240.

Schumacher, G. Dettenwanger, F., Schütze, M., Iberl, A. and Reil, D. (2000), XRD Investigations of the phosphorus effect on the oxidation of TiAl alloys by high-resolution methods, *Oxidation of Metals*, Vol. 54, No. 3-4, pp. 317-337.

Schuster, J.C. and Palm, M. (2006), Reassessment of the binary aluminum-titanium phase diagram, *Journal of Phase Equilibria and Diffusion*, Vol. 27, No. 3, pp. 255-277.

Schutz, R.W. (1996), Ruthenium enhanced titanium alloy: Minor ruthenium additions produce cost effective corrosion resistant commercial titanium alloys, *Platinum Metals Review*, Vol. 40, No. 2, pp. 54-61.

Schütze, M., Malessa, M, Rohr, V. and Weber, T. (2006), Development of coatings for protection in specific high temperature environments, *Surface and Coating Technology*, Vol. 201, pp. 3872-3879.

Scully, J.C. (1966), Fundamentals of corrosion, Owen, W.S., D.W. Hopkins and H.M. Finniston (Eds), pp. 85-92, *Pergamon Press*, UK.

Seikh, A.H., Mohammad, A. and Sherif, E.M. (2015), Corrosion behaviour in 3.5% NaCl solutions of γ-TiAl processed by electron beam melting process, *Metals*, Vol. 5, No 4, pp.2289-2302.

Shankar Rao, V. (2004), Some observations on the hydrogen embrittlement of Fe_3Al–Fe_3AlC intermetallic compounds, *Materials Research Bulletin*, Vol. 39, pp. 169-174.

Shao, H-P., Wang, Z., Lin, T. Ye, Q. and Guo, Z-M. (2015), Preparation of TiAl alloy powder by high-energy ball milling and diffusion reaction at low temperature, *Rare Metal*, pp. 1-5.

Shemet, V., Karduck, P., Hoven, H., Grushko, B., Fischer, W. and Quadakkers, W.J. (1997), Synthesis of the cubic Z-phase in the Ti-Al-O system by a powder metallurgical method, *Intermetallics*, Vol. 5, pp. 271-280.

Shemet, V., Tyagi, A.K., Becker, J.S., Lersch, P., Singeheiser, L., and Quadakkers, W.J. (2000), The formation of protective alumina-based scales during high-temperature air oxidation of γ-TiAl alloys, *Oxidation of Metals*, Vol. 54, pp. 211-235.

Sherif, E.M., Potgieter, J.H., Comins, J.D., Cornish, L., Olubambi, P.A. and Machio, C.N. (2009), The beneficial effect of ruthenium additions on the passivation of stainless steel corrosion in sodium chloride solutions, *Corrosion Science*, Vol. 51, pp. 1364-1371.

Shi, J.D., Pu, Z., Zhong, Z., and Zou, D. (1992), Improving the ductility of γ (TiAl) based alloy by introducing disordered β phase, *Scripta Metallurgica et Materialia*, Vol. 27, pp. 1331-1336.

Shida, Y. and Anada, H. (1993), Oxidation behaviour of binary Ti-Al alloys in high temperature air environment, *Materials Transactions, JIM*, Vol. 34, No.3, pp. 236-242.

Shida, Y. and Anada, H. (1996), The effect of various ternary additives on the oxidation behaviour of TiAl in high-temperature air, *Oxidation of Metals*, Vol. 45, pp. 197-219.

Shiue, R.K., Wu, S.K., Chen, Y.T. and Shiue, C.Y. (2008), Infrared brazing of Ti50Al50 and Ti-6Al-4V using two Ti-based filler metals, *Intermetallics*, Vol. 16, pp. 1083-1089.

Shu-Long, X., Jing, T., Li-Juan, X., Yu-Yong, C., Hong-Bao Y. and Jie-Cai, H. (2009), Microstructures and mechanical properties of TiAl alloy prepared by spark plasma sintering, *Transactions of Nonferrous Metals Society of China*, Vol. 19, pp. 1423-1427.

Sina, H. and Iyengar, S. (2015), Reactive synthesis and characterization of titanium aluminides produced from elemental powder mixtures, *Journal of Thermodynamics and Analytical Calorimetry*, Vol. 122, pp.689-698.

Singh, H., Sidhu T.S. and Kalsi, S.B.S. (2012), Cold spray technology: future of coating deposition processes, *Frattura ed Integrita Strutturale*, Vol. 22, pp. 69-84.

Singheiser, L., Niewolak, L., Fesch, U., Shemet, V. and Quadakkers, W.J. (2003), Fundamental considerations for the development of oxidation-resistant alloys and coatings based on γ-TiAl, *Metallurgical and Materials Transactions A*, Vol. 34, pp. 2247-2251.

Smeltzer, W.W. (1956), Oxidation of aluminium in the temperature range 400-600°C, *Journal of Electrochemical Society*, Vol. 103, No 4, pp. 209-214.

SST (2014), http://www.supersonicspray.com/en/cold_spray_full?pg=SE22000&rp=3 (Accessed 8 December 2014).

Stern, M. and Wissenberg, H. (1959a), The electrochemical behavior and passivity of titanium, *Journal of the Electrochemical Society*, Vol. 106, No. 9, pp. 755-759.

Stern, M. and Wissenberg, H. (1959b), The Influence of noble metal alloy additions on the electrochemical and corrosion behavior of titanium, *Journal of the Electrochemical Society*, Vol. 106, No. 9, pp. 759-764.

Streicher, M.A. (1977), Alloying stainless steel with the platinum metals increased resistance to corrosion in acids, *Platinum Metals Review*, Vol. 21, No. 2, pp. 51-55.

Stoloff, N., Shea, M. and Castagna, A. (1991), *Environmental Effects on Advanced Materials*, pp. 3-19, The Metallurgical Society, Warrendale, Pennsylvania, USA.

Sujata, M., Bhargava, S. and Sangal, S. (1997),On the formation of $TiAl_3$ between solid Ti and liquid Al, *Journal of Materials Science Letters*, Vol. 16, pp. 1175-78.

Sulka, G.D. and Jóźwik, P. (2011), Electrochemical behaviour of Ni_3Al-based intermetallic alloy in NaOH, *Intermetallics*, Vol. 19, pp. 974-981.

Sun, Z.M. and Hashimoto, H. (2003), Fabrication of TiAl alloys by MA-PDS process and the mechanical properties, *Intermetallics*, Vol. 11, pp. 825-834.

Suryanarayana, C. (2004), *Mechanical Alloying and Milling*, Marcel Dekker (Ed.), New York, USA.

Supersonicspray (2014), on http://www.supersonicspray.com/en/cold_spray_full?pg=SE22000&rp=3 (Accessed 8 December 2014).

Supersonicspray (2015), on http://www.supersonicspray.com/en/products_ full.php? pg=SE45000&rp=14 (Accessed 9 April 2015).

Szklarska-Smialoska, Z. (1999), Pitting corrosion of aluminium, *Corrosion Science*, Vol. 41, pp. 1743-1767.

Takasaki, A., Ojima, K. and Taneda, Y. (1994), High-temperature oxidation of cathodically hydrogen-charged two-phase (Ti_3Al, TiAl) titanium aluminides, *Metallurgical and Materials Transactions A*, Vol. 25, pp. 2491-4231.

Takasugi, T. (1988), Controlling embrittlement at grain boundaries in intermetallic compounds, *Journal de Physique*, Colloque C5, Supplément au numéro 10, Vol. 49, pp. 811-820 (in French).

Takayama, I. (1994), Development of oxidation coating for titanium, *Nippon Steel Technical Report*, Vol. 6, pp. 57-63.

Tang, Z., Wang, F. and Wu, W. (1997), Effect of a sputtered TiAlCr coating on the oxidation resistance of TiAl intermetallic compound, *Oxidation of Metals*, Vol. 48, pp. 511-525.

Tang, H.G., Ma Zhao, X.F.W., Yan, X.W. and Hong, R.J. (2002), Preparation of γ-TiAl alloys by mechanical alloying, *Journal of Alloys and Compounds*, Vol. 347, pp. 228-230.

Tetsui, T. (1999), Gamma Ti aluminides for non-aerospace applications, *Current Opinion in Solid State and Materials*, Vol. 4, No. 3, pp. 243-248.

Tetsui, T. and Miura, Y. (2002), Heat-resistant cast TiAl alloy for passenger vehicles, Mitsubishi Heavy Industries, Ltd., *Technical Review*, Vol. 39, No. 1, pp. 1-5.

Tetsui, T. (2002), Development of a TiAl turbocharger for passenger vehicles, *Materials Science and Engineering A*, Vol. 329-331, pp. 582-588.

Tetsui, T., Shindo, K., Kobayashi, S. and Takeyama, M. (2002), A newly developed hot worked TiAl alloy for blades and structural components, *Scripta Materialia*, Vol. 47, No. 6, pp. 399-403.

Tian, W.H. and Nemoto, M. (1999), Precipitation behaviour of $(Al, Ag)_3Ti$ and Ti_3AlC in $L1_0$-TiAl in Ti-Al-Ag system, *Intermetallics*, Vol. 7, pp. 1261-1269.

Tomashov, N.D. (1990), Cathodic Modification with Platinum Metals, *Platinum Metals Review*, Vol. 34, p. 154

Tonneau, A. Hénaff, G., Mabrua, C. and Petit, J. (1998), Environmentally-assisted fatigue crack propagation in aluminides at room temperature, *Scripta Materialia*, Vol. 39, No. 11, pp. 1503-1508.

Trufanov, A.A., Katsov, K.B. and Chervonyi, M.V. (1989), Effect of Ni and Mo additions on the corrosion-mechanical properties of Ti-Al alloy, Khlorvinil Production Organisation, Kaluga, *Fiziko-khimicheskaya Mekhanika Materialov*, Vol. 25, No. 3, pp. 28-32 (English translation).

Turns, E.W., Browning, J.W. and Jones, R.L. (1975), Electroplated titanium: properties and effects, *Plating and Surface Finishing*, Vol. 63, pp. 443-451.

Upadhyaya, G.S. (1997), *Powder Metallurgy Technology*, pp. 18-116, Illustrated Edition, Cambridge International Science Publishing, UK.

Valiente Bermejo, M A. and Zhang, Z. (2015), Relevance and limitations of arc furnace casting in welding research, *International Journal of Cast Metals Research*, Vol. 28, No 2, pp. 97-104.

Vaidya, S. and Preece, C.M. (1978), Cavitation erosion of age-hardenable aluminium alloys, *Metallurgical Transactions A*, Vol. 9, pp. 299-307.

Van der Lingen, E. and Sandenbergh, R.F. (2001), The cathodic modification behaviour of ruthenium additions to titanium in hydrochloric acid, *Corrosion Science*, Vol. 43, pp. 577-590.

Vernon-Parry, K.D. (2000), Scanning Electron Microscopy: An introduction, *III-Vs Review*, Vol. 13, No. 4, pp. 40-44.

Von Mises, R. (1913), Mechanik der festen Körper im plastisch-deformablen Zustand, Nachrichten von der Gesellschaft der Wissenschaften zu Göttingen, *Mathematisch-Physikalische Klasse*, Vol. 1, pp. 582–592 (In German).

Wang, Y, Lin, D and Law, C.C. (1999), Brittle-to-Ductile transition temperature and its strain rate sensitivity in a two-phase titanium aluminide with near lamellar microstructure, *Journal of Materials Science*, Vol. 34, pp. 3155-3159.

Westbrook, J.H. and Fleischer, R.L. (1994), Historical sketch, *Intermetallic Compounds, Principles and Practice*, Vol. 1, pp. 3-18, West Sussex, UK.

Whitaker, R. D. (1975), An historical note on the conservation of mass, *Journal of Chemical Education*, Vol. 52, No. 10, pp. 658-659.

Williams-Jones, A.E., Migdisov, A. and Normand, C. (2004), Experimental investigation of Pd solubility and speciation in H_2O-HCl liquids: Implications for the formation of hydrothermal palladium deposits, on http://www.divex.ca/projets/doc/SC5-Williams-Jones-2004.pdf (Accessed 12 May 2015).

Witusiewicz, V.T., Bondar, A.A., Hecht, U., Rex S. and Velikanova, T.Y. (2008), The Al-B-Nb-Ti system III: Thermodynamic re-evaluation of the constituent binary system Al-Ti, *Journal of Alloys and Compounds*, Vol. 465, pp. 64–77.

Wolff, I.M., Iorio, L.E., Scheers, P.V.T. and Potgieter, J.H. (1998), Oxidation and corrosion behaviour of Fe-Cr and Fe-Cr-Al alloys with minor additions, *Materials Science and Engineering A*, Vol. 241, pp. 264-276.

Wojnicki, M., Pacławski, K., Rudnik, E. and Fitzner, K. (2011), Kinetics of palladium (II) chloride complex reduction in aqueous solutions using dimethylamine borane, *Hydrometallurgy*, Vol. 110, pp. 56-61.

Wu, X. (2006), Review of alloy and process development of TiAl alloys, 2006, *Intermetallics*, Vol. 14, pp. 1114-1122.

Wu, Y.N. (2007), Hot corrosion behaviour of Pt-Ir modified aluminide coatings on the nickel-base single crystal superalloy TMS-82, *Journal of Materials Research*, Vol. 1, No. 22, pp. 206-216.

Xin, L., Shao, G., Wang, F., Tsakiropoulos P. and Li, T. (2003), Improving high-temperature oxidation resistance of TiAl-based alloys by $MnCl_2$ surface treatment, *Intermetallics*, Vol. 11, pp. 651-660.

Xiu-Feng, W., Mo, M., Xue-Bin, L., Xue-Quing, W., Chao-Gui, T., Rong-Kai, S. and Jiang-Guo, L. (2006), Diffusion bonding of γ-TiAl alloy to Ti-6Al-4V alloy under hot pressure, *Transactions of Nonferrous Metals Society of China*, Vol. 16, pp. 1059-1063.

Yamaguchi, M., Inui, H. and Ito, K. (1999), High-temperature structural intermetallics, *Acta Materialia*, Vol. 48, pp. 307-322.

Yang, R. and Hao, Y.L. (1999), Estimation of ($\gamma+\alpha_2$) equilibrium in two-phase Ti-Al-X alloys by means of sublattice site occupancies of X in TiAl and Ti_3Al, *Scripta Materialia*, Vol. 41, No. 3, pp. 341-346.

Yang, M.R. and Wu, S.K. (2003), Oxidation resistance improvement of TiAl intermetallics using surface modification, *Bulletin of the College of Engineering*, N.T.U., Vol. 89, pp. 3-19.

Young, D.J. and Gleeson, B. (2002), Alloy phase transformations driven by high-temperature corrosion processes, *Corrosion Science*, Vol. 44, No. 2, pp. 345-357.

Yule, A. and Dunkley, J. (1994), *Atomisation of melts for powder production and spray deposition*, pp. 47-87, Clarendon Press, Oxford, UK.

Zaikina, O.V., Khorujaya, V.G., Pavlyuchkov, D., Grushko, B. and Velikanova, T.Y.(2011a), Investigation of the Al-Ti-Pd Alloy system at 930 and 1100° C, *Journal of Alloys and Compounds*, Vol. 509, No. 9, pp. 43-51.

Zaikina, O.V., Khorujaya, V.G., Pavlyuchkov, D., Grushko, B. and Velikanova, T.Y.(2011b), Investigation of the Al-Ti-Pt Alloy system at 1100°C, *Journal of Alloys and Compounds*, Vol. 509, No. 9, pp. 7565-7571.

Zaikina, O.V., Khoruzha, V.G., Kornienko, K.E. and Velikanova, T.Y. (2012), Liquidus surface and melting diagram of the Al-Ti-Pd system in the Al-AlPd-TiPd-Ti region, *Powder Metallurgy and Metal Ceramics*, Vol. 51, No. 7-8, pp. 463-473.

Zhang, W.J., Reddy, B.V. and Deevi, S.C. (2001), Physical properties of TiAl-base alloys, *Scripta Materialia*, Vol. 45, pp. 645-651.

Zhao, B. and Jerkiewicz, G. (2006), Electrochemically formed passive layers on titanium - preparation and biocompatibility assessment in Hank's balanced salt solution, *Canadian Journal of Chemistry*, Vol. 84, No. 9, pp. 1132-1145.

Zheng, N., Fischer, W., Grübmeier, H., Shemet, V. and Quadakkers, W.J. (1995), The significance of sub-surface depletion layer composition for the oxidation behaviour of γ-titanium aluminides, *Scripta Metallurgica et Materialia*, Vol. 33, pp. 47-53.

APPENDIX: LIST OF JOURNAL AND CONFERENCE PAPERS PUBLISHED IN THE COURSE OF THE PhD WORK

Journal Papers

- I.A. Mwamba, L.A. Cornish, and E. van der Lingen (2012), Microstructure, mechanical and oxidation property evolution of γ-TiAl with addition of precious metals, *The Journal of Southern African Mining and Metallurgy*, Vol. 7A, pp. 517-526..
- I.A. Mwamba, L.A. Cornish, and E. van der Lingen (2013), A comparative assessment of TiAl-47.5 at.% Al cathodically modified by precious metal addition, *The Journal of Southern African Mining and Metallurgy*, Vol. 113, pp. 97-104.
- I.A. Mwamba, L.A. Cornish, and E. van der Lingen (2014), Effect of platinum group metal addition on microstructure and corrosion behaviour of Ti–47.5 at-%Al, *Corrosion Engineering, Science and Technology*, Vol. 49, pp.180-188.

Conference Proceedings

- Mwamba I.A. and Cornish, L.A. (2013), Milling of titanium hydride powder and aluminium for the production of TiAl with ruthenium additions, *SAIMM-PMDN 2013 Conference Proceedings*, pp.289-306.
- Mwamba, I.A., Cornish, L.A., Moema, J.S. and Papo, J.M. (2015), Assessment of coatings obtained by cold spraying mechanically alloyed powder onto Titanium Grade 2 and Ti-6Al-4V, *Microscopy Society of South Africa Proceeding*, Vol.45, p.36



Microstructural, mechanical, and oxidation property evolution of gamma-TiAl alloy with addition of precious metals

by I.A. Mwamba*†, L.A. Cornish†, and E. van der Lingen*

Transaction Paper

Synopsis

Titanium aluminide of composition Ti-47.5 at.% Al was prepared by melting titanium and aluminium of commercial purity with additions of precious metals of 0, 0.2, 1, 1.5 and 2 at.% content. The microstructure, hardness and oxidation properties were assessed. It was found that at 47.5 at.% Al, the microstructure of plain TiAl alloys was duplex, consisting of duplex lamellar grains and γ grains. The lamellar grains consisted of alternating lamellae of γ (TiAl) and α_2 (Ti_3Al), with overall aluminium content in the range of 43–47 at.%. The γ grains had a aluminium content above 50 at.%. The addition of precious metals to the TiAl alloy resulted in the formation of a new phase, with a high precious metal content, occurring mostly in the γ phase, without any major change to the microstructure. Increasing the amount of precious metals resulted in an increase of the new phase amount, at the expense of the γ phase. The hardness of the different alloys was around $300HV_{10}$. Overall, the research has shown that addition of precious metals to TiAl resulted in a slight increase in hardness and a significant improvement of the oxidation resistance. This shows that alloying TiAl with precious metals, at the addition levels investigated, does not alter the mechanical properties very much, but improves oxidation resistance.

Keywords
Titanium aluminide, TiAl, precious metals, ternary alloys, microstructure, properties.

Introduction

TiAl is one of the titanium aluminides found in the Ti-Al system, which exists over a range of compositions. Titanium aluminides represent an important class of alloys, providing a unique set of mechanical and physical properties with high potential in the automotive industry, power plant turbines, and aircraft engines. Intensive research efforts over the past three decades have matured the knowledge on TiAl-based alloys, and this state of progress is currently encouraging the consideration of this class of materials for structural, automotive, and aerospace applications. The outstanding thermo-physical properties of these alloys result mainly from a strongly ordered structure, which confers the following beneficial properties: high melting point, low density in the range 3.9–4.2 g/cm^3, high elastic modulus, low diffusion coefficient, good structural stability, and high ignition temperature when compared to conventional titanium alloys[1]. TiAl-based alloys show superior specific strength-temperature properties compared to classical titanium alloys, steels, and nickel-based superalloys in the temperature range from 500 to 900°C. With all these advantages over conventional high-performance alloys, TiAl alloys have been seen as promising for high-temperature structural applications. However, the lack of room-temperature ductility is still the main obstacle to their utilization as engineering materials[2]. The rigid bond structure restricts the ability to accommodate plastic deformation, thus reducing ductility.

TiAl-based alloys display dramatically different microstructures depending on the composition near a 50:50 Ti:Al atomic ratio. While γ-TiAl is found in the aluminium-rich region alloys, titanium-rich alloys exhibit a two-phase microstructure, consisting of layers of ordered face-centred tetragonal TiAl with a $L1_0$ structure and close-packed hexagonal Ti_3Al with $D0_{19}$[3-4].

The γ-TiAl ($L1_0$, tP4) phase is an ordered, equiatomic compound of the light elements Ti and Al. The high aluminium content of this compound increases the resistance to oxidation and burning, two critical concerns in the use of titanium-based materials. Gamma TiAl remains ordered to melting at ~1 440°C. The strong Ti-Al bond leads to high activation energy for diffusion, which helps retain strength and resist creep at high temperatures when diffusion becomes the rate-controlling process.

* *Advanced Materials Division, Mintek.*
† *School of Chemical and Metallurgical Engineering and DST/NRF Centre of Excellence in Strong Materials, University of the Witwatersrand.*

© *The Southern African Institute of Mining and Metallurgy, 2012. SA ISSN 2225-6253.* *This paper was first presented at the ZrTa2011 New Metals Development Network Conference, 12–14 October 2011, Mount Grace Country House & Spa, Magaliesburg.*

TiAl has a low resistance to oxidation at temperatures above 800°C. To date, many attempts have been made to improve the high-temperature oxidation resistance of stoichiometric TiAl, which include the sputtering of an Al film and subsequent interdiffusion treatment at 600°C for 24 hours in a high vacuum[5], sputtering of an Ag-containing TiAl coating[6], and insertion of silicon in the coating material of TiAl[7]. The beneficial influence of the coatings on the heat resistance of the alloy is a result of the presence of an aluminium-rich silicon-modified $TiAl_3$ phase, which is the most oxidation-resistant phase in the TiAl system[8].

A number of refractory metals have been found to significantly improve the oxidation resistance of γ-based materials, and these include Nb, W, and Cr[9]. Silver was also added to TiAl with a significant improvement of the oxidation resistance by promoting the formation of a continuous external alumina based scale[10,11]. In this work, precious metals including ruthenium, palladium, platinum, gold, and silver were added to TiAl-based alloy and the alloy was characterized in terms of microstructural evolution, hardness, and oxidation behaviour.

Experimental procedure

Preparation of TiAl compound

The TiAl alloy was prepared by melting titanium grade 2 and aluminium of commercial purity in a button arc furnace under argon. The target composition was Ti-47.5 at.% Al. Two types of alloys were prepared: plain TiAl and precious metals-containing TiAl. The compositions of the first set of melts at 0.2 at.% PMs (precious metals) are given in Table I. In the second set of melts, the amount of precious metals was increased to 1.0, 1.5, and 2.0 at.% at the expense of the titanium content, the aluminium content remaining 47.5 at.%.

Characterization of the benchmark alloys

The samples from the melting were cut, prepared metallographically, and observed with optical and scanning electron microscopes (SEM). SEM imaging and energy dispersive X-ray spectroscopy (EDX) were conducted with the FEI Nova NanoSEM®, a high-resolution scanning electron microscope (HR-SEM). The chemistry of the samples and the phases were determined using a combination of X-ray diffraction (XRD) and EDX.

For XRD, the samples were analysed with a PANalytical X'Pert Pro powder diffractometer with an X'Celerator detector and variable divergence with fixed receiving slits and Fe-filtered Co-Kα radiation. Phase identification was conducted using X'Pert Highscore plus software.

The plain TiAl and precious metals-containing compounds were heat treated in a tube furnace under argon flow. The samples were heated at a rate of 10°C/min to 1 000°C, then held for 1 hour and furnace-cooled. After heat treatment, the samples were characterized in terms of microstructure and hardness.

The oxidation behaviour of samples was determined by thermogravimetric analysis (TGA) using a NETZSCH STA instrument. TGA was conducted in air on the samples and the weight gain was deducted. The TGA has also allowed the determination of the onset of weight increase, corresponding to the onset of oxidation. Samples of 10 mg were loaded in the STA and heated from room temperature to 1 050°C under a flow of air.

Results and discussion

Microstructural characterization of cast alloys

Microstructure of TiAl with addition of 0.2 at.% precious metals

XRD analysis was conducted to evaluate the phase formation after melting of precursor materials in the button arc furnace. Titanium and aluminium were melted together and then remelted with ruthenium, platinum, palladium, gold, or silver addition. For comparison purposes, commercial TiAl in powder form was also scanned.

Typical XRD results are presented in Figures 1 to 3. For commercial TiAl powder (Figure 1), only TiAl peaks were clearly defined as the powder consisted of TiAl particles only. In the case of melted plain TiAl (Figure 2), there were TiAl peaks (γ) as well as Ti_3Al (α_2) peaks. These two phases were expected, as the composition was selected to produce a TiAl alloy with a duplex structure, consisting of lamellar and γ-TiAl grains. No titanium or aluminium peaks were observed, indicating complete alloying.

In the case of precious metals-containing TiAl at an addition of 0.2 at.% PMs (Ru, Pt, Pd, Au, or Ag), TiAl peaks appeared with a slight shift towards smaller Bragg angles, indicative of solid solution. Ti_3Al peaks were also visible on the XRD patterns. Again, no Al, Ti, or elemental precious metal peaks were visible. Peaks of elemental precious metals were not expected, given the low additions. The duplex

Table I

Elemental composition of the alloys

Compound	Composition (at.%)							
	Ti	Al	Ru	Pd	Pt	Ir	Ag	Au
Plain TiAl	52.5	47.5	-	-	-	-	-	-
Ru-containing TiAl	52.3	47.5	0.2	-	-	-	-	-
Pd-containing TiAl	52.3	47.5	-	0.2	-	-	-	-
Pt-containing TiAl	52.3	47.5	-	-	0.2	-	-	-
Ir-containing TiAl	52.3	47.5	-	-	-	0.2		-
Ag-containing TiAl	52.3	47.5	-	-	-	-	0.2	-
Au-containing TiAl	52.3	47.5	-	-	-	-	-	0.2

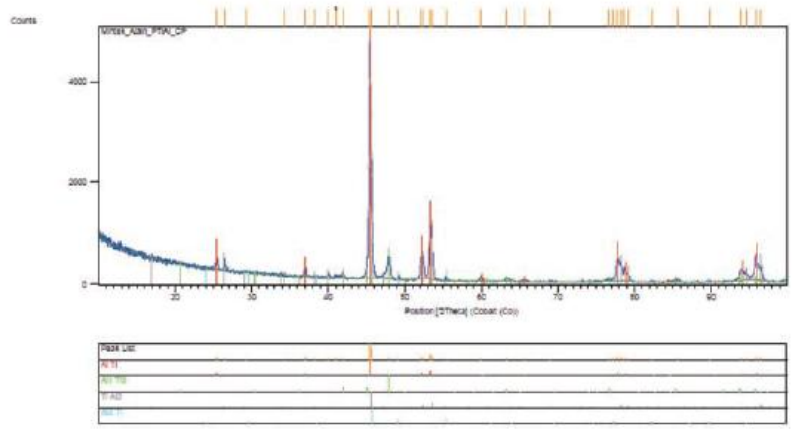


Figure 1—XRD pattern of commercial TiAl powder

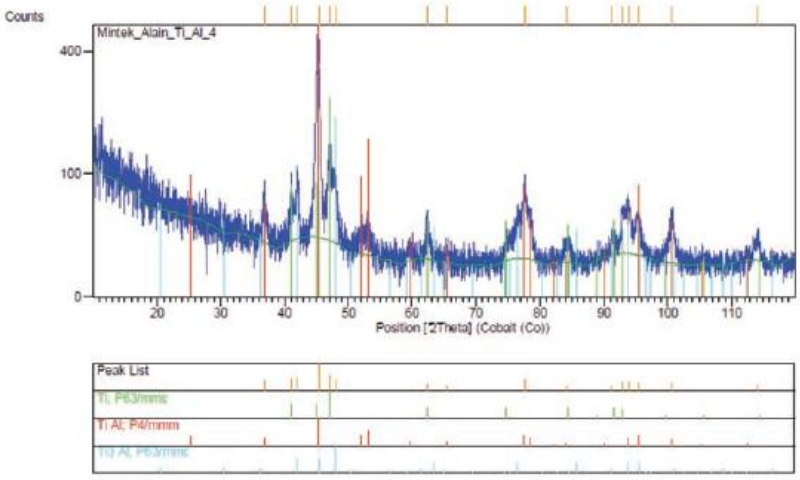


Figure 2—XRD pattern of as-cast plain TiAl

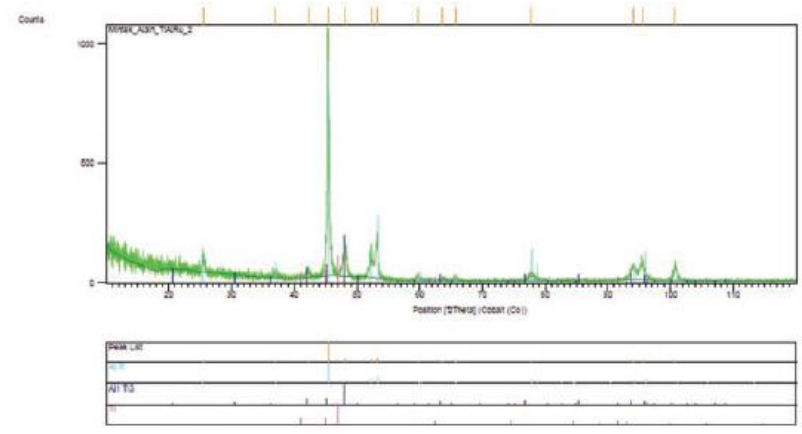


Figure 3—XRD pattern of as-cast TiAl with 0.2 at.% Ru

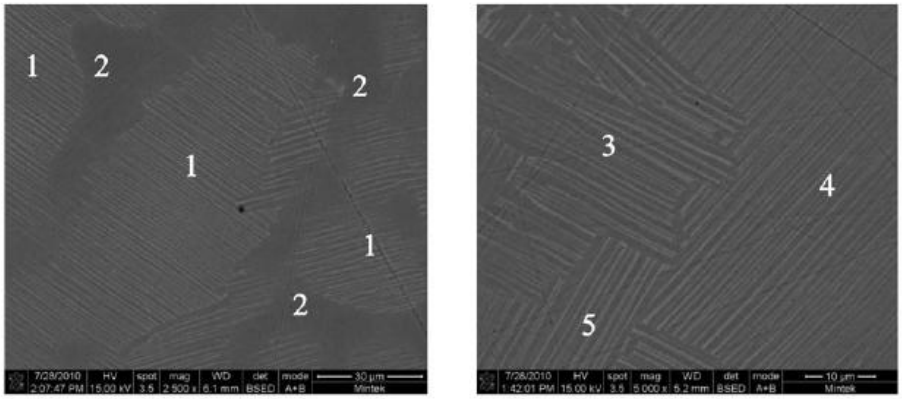


Figure 4—SEM mode micrograph of plain TiAl showing Ti_3Al and γ-TiAl phases

microstructure in the plain TiAl alloy is shown in Figure 4. The XRD patterns of Pt, Pd, Ag, and Au-containing TiAl alloys, which are not presented, showed similar peak trends, with Ti_3Al and γ-TiAl peaks.

Figure 4a shows that the microstructure obtained in plain TiAl at a target composition of Ti-47.5 at.% Al was duplex, consisting of lamellar grains (areas 1) with single-phase regions between them (areas 2). The grains identified in areas 1 comprised alternating light and dark lamellae.

In some parts, lamellar grains were adjacent. Figure 4b shows, at higher magnification, such an area which appears to be lamellar only. This figure also shows that different grains could be identified by the orientation of their lamellae (Areas 3 to 5).

Typical results obtained from EDX are reported in Table II. The overall composition indicates the formation of a duplex TiAl compound. After melting, the samples were furnace-cooled (a fairly slow cooling). The elemental composition showed that areas 1 in Figure 4a comprised alternating Ti_3Al (α_2) and γ-TiAl. According to the Ti-Al phase diagram[12], shown in Figure 5, Ti_3Al has an aluminium content of between 22 and 35 at.% at 400°C. From 35 to 49 at.% Al is the composition range of a two-phase field of Ti_3Al and TiAl, which was the case in these samples, with the lamellar region having a composition of 47.7 at.% Al. In the single-phase regions (areas 2 in Figure 4a), the aluminium content was above 50 at.%, showing the presence of only γ-TiAl. These observations indicated that the microstructure was a mixture of lamellar grains (with alternating α_2 and γ parallel phases) and γ-TiAl grains between the lamellar grains, typical of duplex microstructure[9].

Table II
EDX analysis of plain TiAl

Plain TiAl	Area	Elemental composition (at.%)			
		Ti	Std. dev.	Al	Std. dev.
	Overall	51.5	1.2	48.5	1.3
	Duplex 1	52.0	0.4	48.0	0.4
	Plain 2	47.7	1.1	52.3	1.2

SEM and EDS were also conducted on the TiAl compounds containing 0.2 at.% precious metals. Typical results are presented in Figure 6 and Table III respectively. SEM showed (Figure 6a) that the duplex structure was maintained in all samples in spite of the ruthenium addition. In addition, the precipitation of a light phase was observed in all samples doped with precious metals, mainly between the interfaces of the single-phase and duplex regions. The shape of these precipitates was irregular with no particular trend. No light phase was observed in the α_2/γ lamellar grains.

EDS results (Table III) showed that the light phases contained a higher precious metal content than the lamellar and γ phases. From Table III, the typical Ru content observed in the lamellar grains and γ-TiAl was below 1 at.%, which is in the range reported by Khataee *et al.*[13]. In a constitutional study of the Ti-Al-Ru system, they concluded that the solubility of ruthenium in γ is higher than in the lamellar phase, with reported values of about 0.5 at.% Ru in α_2 (Ti_3Al) and less or equal to 1 at.% in γ-TiAl.

The Al-Ru-Ti isothermal section in Figure 7 shows that the light phase reported in Table III (6.3 at.% Ru) is located in the zone containing γ-TiAl and the G-phase although the analysis of this small phase would have been affected by the surrounding phases. The G-phase is the $Al_{16}Ru_8Ti_6$ ternary

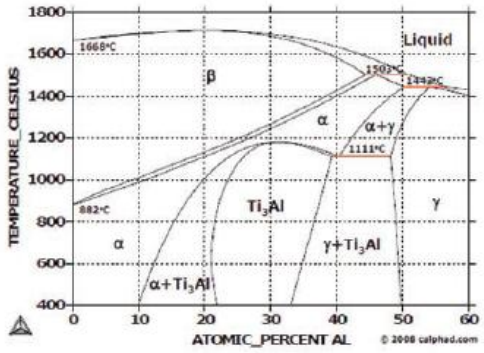


Figure 5—Ti-Al phase diagram[13]

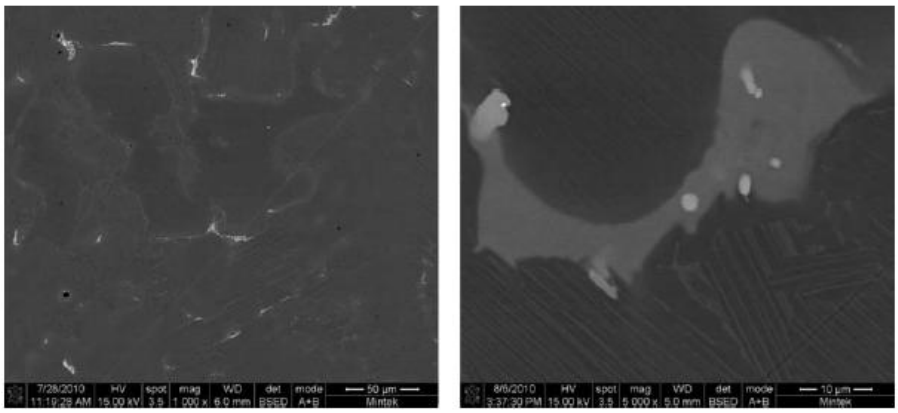


Figure 6—SEM mode micrographs of TiAl alloy with 0.2 at.% Ru

Table III

Typical EDX analysis of PMs-containing TiAl (5 analyses)

Alloy	Area	Elemental composition (at.%)					
TiAl-Ru		Ti	Std. dev.	Al	Std. dev.	Ru	Std. dev.
	Overall	51.8	1.1	47.8	1.3	0.4	0.08
	Plain -1	46.9	1.5	52.4	1.7	0.7	0.08
	Striped -2	49.5	1.0	50.1	1.2	0.4	0.07
	Light phase -3	45.0	1.7	48.6	1.3	6.4	1.0
TiAl-Pt		Ti	Std. dev.	Al	Std. dev.	Pt	Std. dev.
	Overall	51.3	1.1	47.3	1.1	1.4	0.4
	Plain- 1	50.1	1.2	47.8	1.1	2.1	1.5
	Striped -2	52.0	1.0	45.9	0.7	2.1	0.8
	Light phase-4	45.2	1.7	49.3	2.0	5.6	1.2
TiAl-Ir		Ti	Std. dev.	Al	Std. dev.	Ir	Std. dev.
	Overall	51.8	1.2	47.4	1.1	0.8	0.5
	Plain 1	48.7	0.9	50.4	1.3	0.9	0.5
	Striped 2	52.6	0.8	47.1	0.4	0.3	0.1
	Light phase-3	47.3	1.5	48.9	1.5	3.8	1.0
TiAl-Ag		Ti	Std. dev.	Al	Std. dev.	Ag	Std. dev.
	Overall	52.0	0.8	47.7	0.6	0.3	0.2
	Plain 1	46.3	0.7	53.5	0.6	0.7	0.2
	Striped 2	52.0	0.8	47.6	0.8	0.4	0.3
	Light phase-3	47.6	0.4	44.3	1.3	10.42	2.0

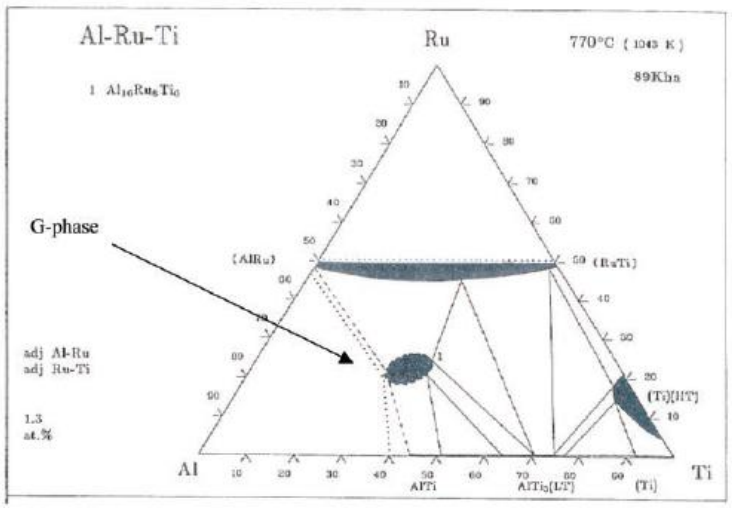
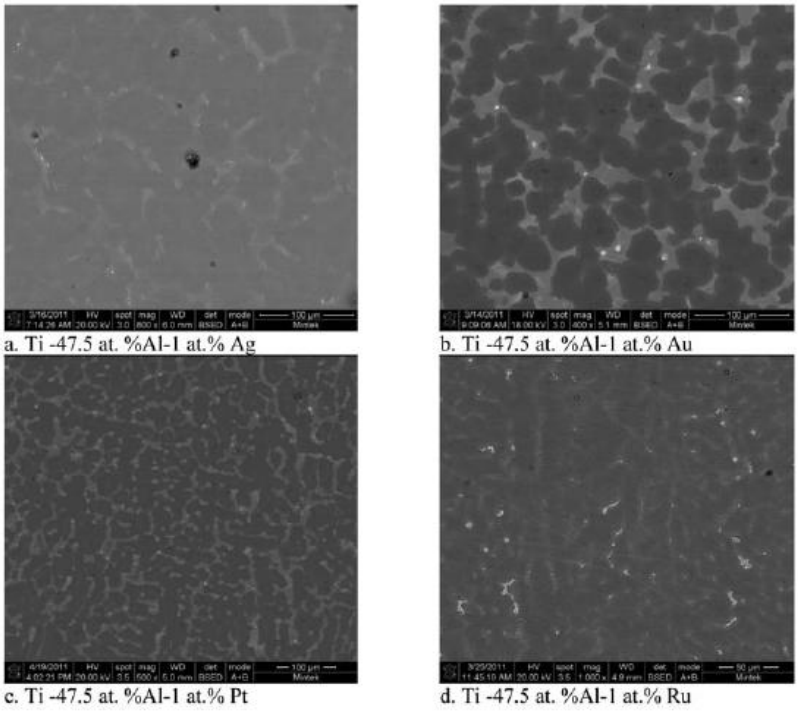


Figure 7—Isothermal section of the ternary Ti-Al-Ru phase diagram[14]

compound with the $Mn_{23}Th_6$ structure, a *D*8a-type crystal structure with a complex unit containing 116 atoms based on a bcc structure[12].

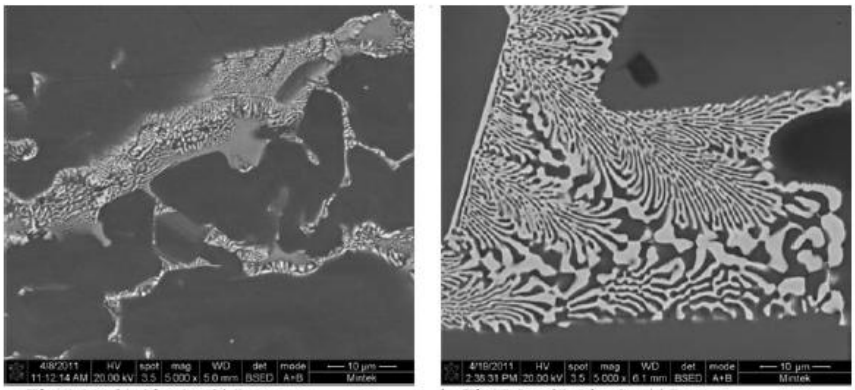
Effect of precious metal content on the microstructure of TiAl compounds

The increase of PM content led to an increase in the precipitation of the new phase at grain boundaries. This precipitation progressed more in the γ grains as shown in Figure 8. The new phase developed between lamellar grains in the γ phase, resulting in a complete separation of lamellar grains. As the content of PMs increased, white phases of higher PM content formed at the centre (Figure 8b). At 2 at.% PM addition, the white phase, viewed at high magnification, showed a eutectic morphology (Figure 9).



a. Ti -47.5 at. %Al-1 at.% Ag
b. Ti -47.5 at. %Al-1 at.% Au
c. Ti -47.5 at. %Al-1 at.% Pt
d. Ti -47.5 at. %Al-1 at.% Ru

Figure 8—SEM mode micrographs of TiAl alloys with 1.0 at.% precious metal



a. Ti-47.5 at.% Al – 2at.% Ru
b. Ti-47.5 at.% Al – 2at.% Pt

Figure 9—SEM mode micrographs of TiAl alloys with precious metals showing eutectic-like structures

Hardness evaluation

Hardness of TiAl alloys with 0.2 at.% precious metals

The Vickers hardness of the as-cast and heat-treated samples was evaluated and the results are reported in Table IV. The Vickers hardness of the plain TiAl was around 300, and the introduction of PMs resulted in a slight increase. However, the addition of silver resulted in a significant increase of the hardness, about $400HV_{10}$ in the as-cast condition. More investigation is needed to understand the sudden hardness increase observed in the Ag-containing TiAl alloys.

In general, the heat treatment at 1 000°C for 1 hour resulted in a slight softening of the alloys. Samples that had the highest hardness in the as-cast condition, TiAl-Pd and TiAl-Ag, showed the largest decrease. The decrease in hardness was expected, as the heat treatment was to soften the TiAl-based alloys while keeping the as-cast microstructure. To ensure that, the heat treatment temperature was set to correspond to annealing, without phase change, using the Ti-Al phase diagram[12,15].

Effect of precious metal content on the hardness of the TiAl alloys

The increase of PM content was assessed for its effect on the hardness, and the results are given in Table V. The macro-hardness of the TiAl alloys showed a general decreasing trend with increasing PM content (Figure 10), although it remained in the same range observed at the addition level of 0.2 at.% PMs, that is, $280\text{-}380HV_{10}$. However, TiAl alloys with Pd and Ir showed an inverse trend.

Oxidation behaviour of plain and precious metals-containing TiAl at high temperatures

TiAl with addition of 0.2 at.% precious metals

The high-temperature behaviour of the alloys was assessed by thermogravimetric analysis (TGA) with the results shown in Figures 11 and 12 together with those from a TiAl powder obtained by mechanical alloying. At 1 185°C in air, the weight gain in TiAl alloys containing 0.2 at.% PMs varied between 1 and 2 percent, with Ir- and Pt-containing TiAl alloys showing the highest weight gain (~2 percent) and Ru- and Pd-containing TiAl the lowest weight gain (~1 percent). This is illustrated in Figure 12, which is an expansion of the curves in Figure 11. In general, as the temperature increased, the TiAl alloys with PMs showed an abrupt weight increase from around 950°C, below which the weight gain was less than 1 percent in almost all cases. When compared to the weight gain in plain TiAl (Figure 11), the weight gains in TiAl alloys containing precious metals were significantly small. The weight gain in plain TiAl started earlier (~36 percent at 950°C), and showed an abrupt increase at about 480°C.

These results indicated that the presence of 0.2 at.% precious metals in the alloys retarded oxygen pick-up and therefore oxidation, and demonstrated that by adding

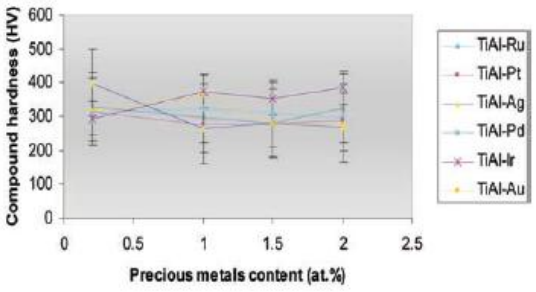


Figure 10—TiAl alloy macrohardness-precious metal content relationship

Table IV

Vickers macro-hardness of TiAl alloys with 0.2 at.% precious metals

Condition	Parameter	Compound						
		TiAl	TiAl-Ru	TiAl-Pd	TiAl-Pt	TiAl-Ir	TiAl-Ag	TiAl-Au
As-cast	Macro-hardness HV_{10}	281	314	328	314	293	399	318
	Standard deviation	23	28	23	10	17	13	22
Heat Treated	Macro-hardness HV_{10}	269	303	311	298	300	375	308
	Standard deviation	25	11	18	14	12	9	19

Table V

Vickers macro-hardness of as-cast plain and PMs-containing TiAl alloys

P.M. content (at.%)	Parameter	Compound					
		TiAl-Ru	TiAl-Pd	TiAl-Pt	TiAl-Au	TiAl-Ag	TiAl-Ir
1	Macro-hardness HV_{10}	324	296	276	362	264	373
	Standard deviation	17	16	11	14	9	15
1.5	Macro-hardness HV_{10}	309	280	281	280	281	353
	Standard deviation	33	21	15	14	10	11
2	Macro-hardness HV_{10}	298	326	289	277	268	385
	Standard deviation	27	14	16	13	8	16

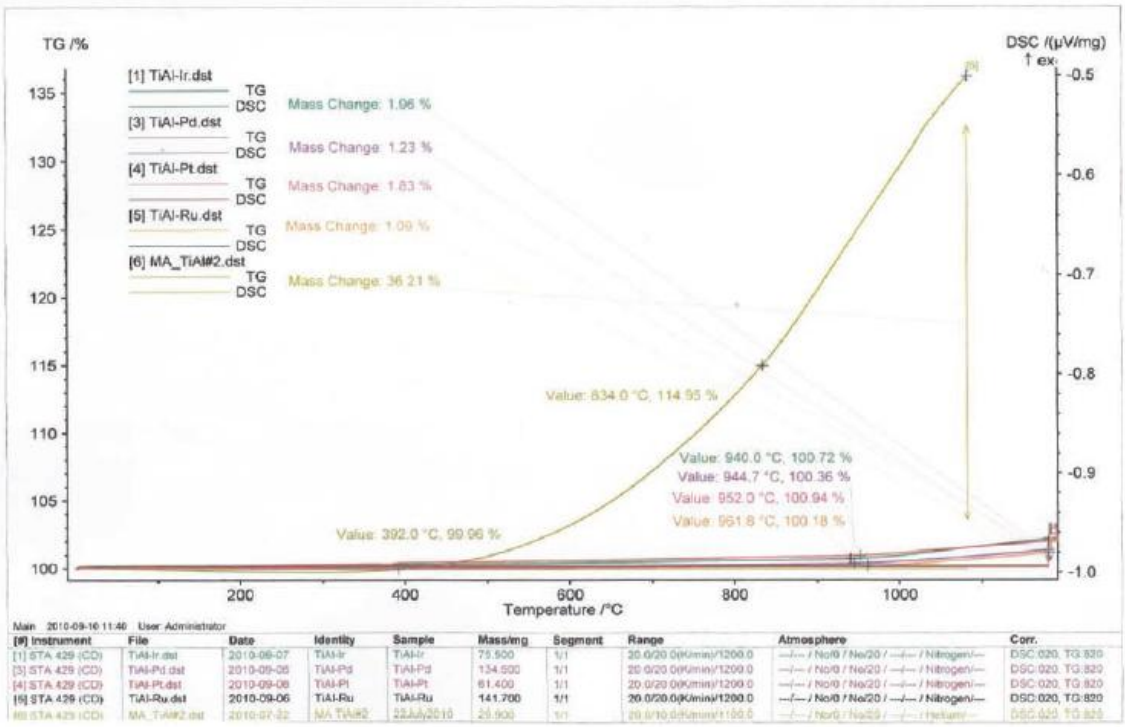


Figure 11—TGA curves of plain and TiAl alloys with 0.2 at.% PMs, including mechanically alloyed powder

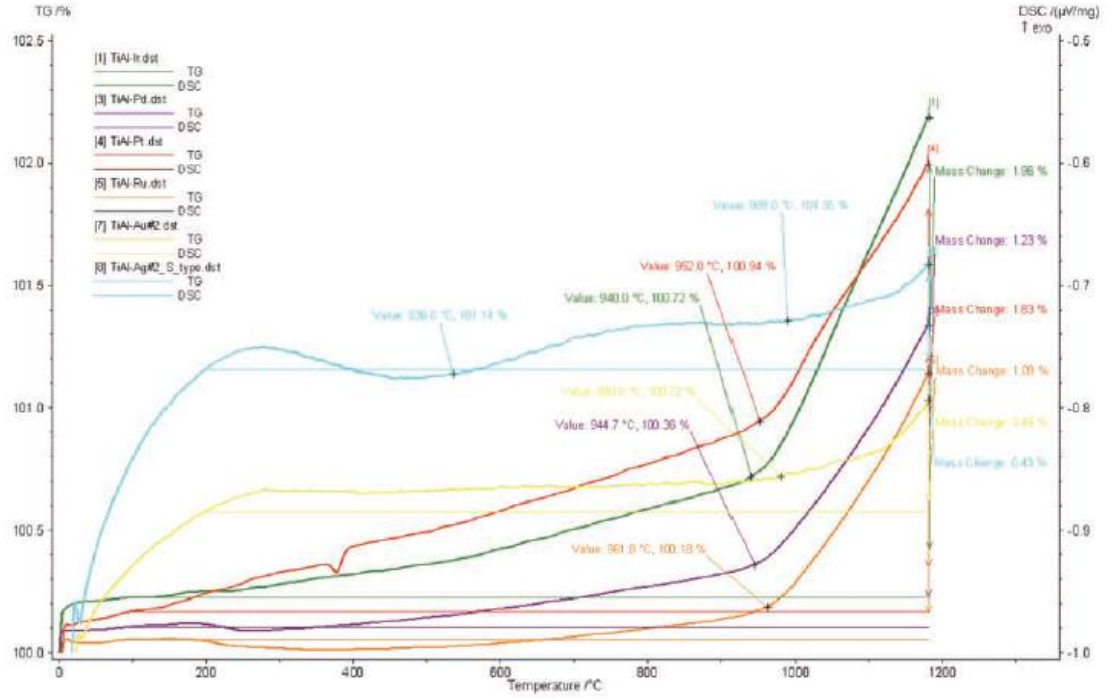


Figure 12—Typical TGA curves of TiAl alloys with 0.2at.% precious metals

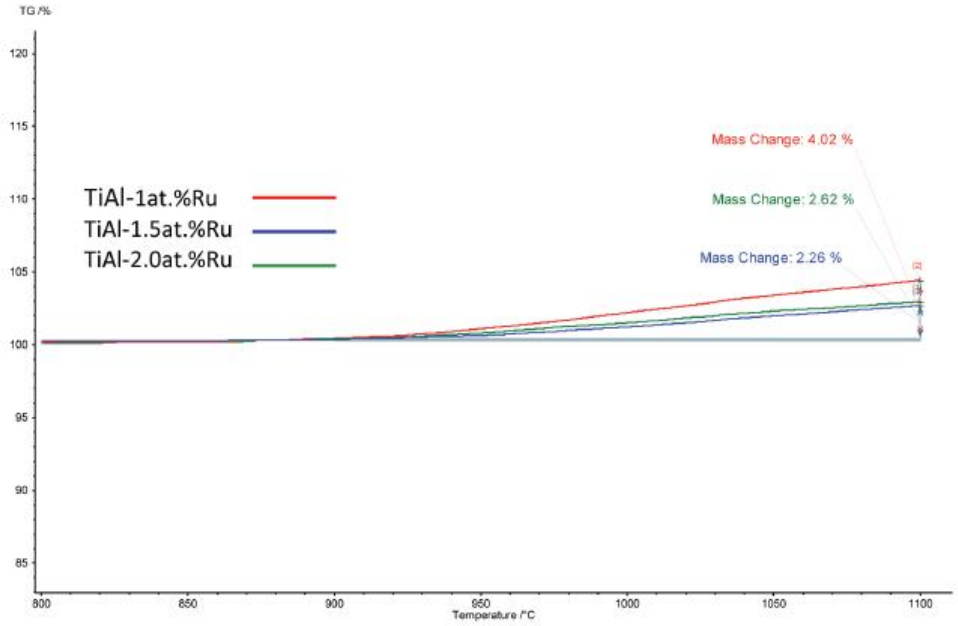


Figure 13—Typical TGA curves of TiAl alloys containing 1, 1.5 and 2 at.% Ru

Table VI

Mass change as a function of PM content at 1 185°C

PM content (at.%)	Relative mass change in TiAl compound doped with precious metal (%)					
	Ru	Pd	Pt	Ag	Au	Ir
0.2	1.09	1.23	1.83	0.93	0.45	1.96
1.0	4.02	0.85	1.32	2.84	2.14	0.97
1.5	2.26	0.57	2.28	1.42	4.65	0.53
2.0	2.62	0.90	2.18	1.41	9.44	1.13

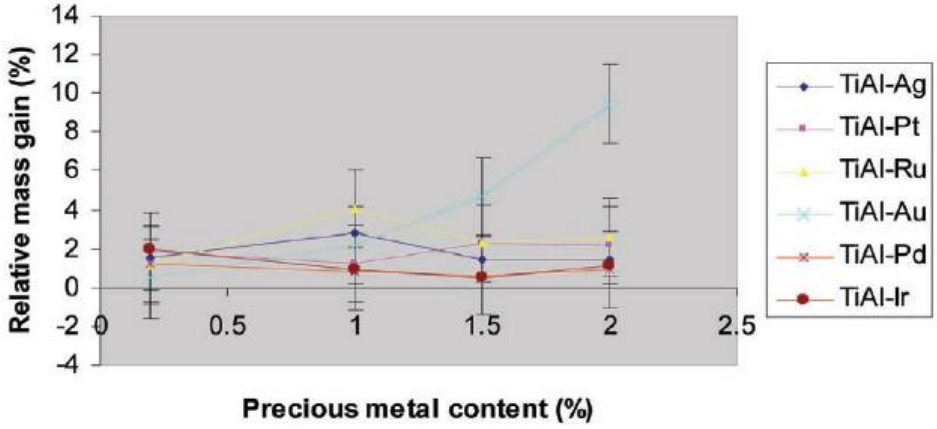


Figure 14—Typical curves of mass gain as functions of PM contents in TiAl alloys at 1 185°C

precious metals, the oxidation resistance of the TiAl can be significantly improved.

Effect of precious metal content on the oxidation behaviour of the TiAl alloys

The effect of PM content on the oxidation behaviour of TiAl was also assessed by a thermogravimetric analysis (TGA) of samples with 1, 1.5 and 2 at.% PMs. A typical TGA curve is shown in Figure 13 for the Ru-containing TiAl alloy. Table VI summarizes the mass gains for different PM contents. The mass gain at higher PM content (1–2 at.%) was either the same or higher than the mass gain observed with TiAl containing only 0.2 at.% PM, and is shown in Figure 14, for the mass gain at 1 185°C. For the gold-containing TiAl alloy, which showed a mass gain of about 9.5 percent at an addition level of 2 at.% Au, the increase was greater. These observations indicated that increasing the content of PMs in the TiAl alloy did not give better oxidation resistance than TiAl containing 0.2 at.% PMs, and the best results should be achieved below 1 at.% PM addition.

Conclusion

Plain and precious metals-containing TiAl alloys were produced by melting commercial aluminium and titanium together to the composition of Ti-47.5 at.% Al with additions of precious metals (PMs) at 0.2, 1, 1.5, and 2 at.%. The TiAl alloys were characterized in as-cast and heat-treated conditions in terms of their microstructure, hardness, and oxidation behaviour.

It was found that at Ti-47.5 at.% Al, the microstructure of plain TiAl alloy was duplex, consisting of lamellar and γ grains. The lamellar grains consisted of lamellae of γ (TiAl) and α_2 (Ti_3Al), with an overall composition of Ti-(43-47) at.% Al. The γ grains consisted of γ phase with an aluminium content above 50 at.%.

The addition of PMs to TiAl alloys at 0.2 at.% resulted in the formation of a new phase, mainly at the grain boundaries and in the γ grains, without major change in the matrix.

The hardness of the plain alloy was around $300HV_{10}$. Addition of PMs at 0.2 at.% to TiAl alloys resulted in a slight increase in hardness, and significant improvement of the oxidation resistance.

Increasing the PM content from 0.2 at.% to 1, 1.5 and 2 at.% resulted in increased precipitation of the whiter phase with high content of PMs, with no significant change to the hardness and no improvement to oxidation resistance. Instead, the addition of PMs above 1 at.% appeared to be deleterious to the oxidation resistance. Precious metal addition above 1 at.% resulted in the precipitation of the new phase at grain boundaries, which developed subsequently in the γ phases and isolated lamellar grains.

Acknowledgement

This paper is published with the permission of Mintek. The DST-AMI-PMDN, Mintek, Mr Edson Muhuma and Mr. Mokae Bambo at Mintek are thanked. L.A. Cornish thanks the National Research Foundation and the department of Science and Technology.

References

1. Tetsui, T. and Miura, Y. Heat-resistant cast TiAl alloy for passenger vehicles. *Mitsubishi Heavy Industries Ltd., Technical Review*, vol. 39, no. 1, 2002. pp. 1–9.
2. Duarte, A., Viana, F., and Santos, H.M.C.M. As-cast titanium aluminides microstructure modification, *Materials Research*, vol. 2–3, 1999. pp. 191–195.
3. Kimura, Y. and Pope, D. Ductility and toughness considerations in intermetallics, Structural intermetallics. The *Minerals, Metals & Materials Society*. 1997. pp. 99–106.
4. Jovanović, M.T., Dimčić, B., Bobić, I., Zec S. and Maksimović, V. Microstructure and mechanical properties of precision cast TiAl turbocharger wheels, *Materials Processing Technology*, 2004. 167. pp.
5. Chu, M.S. and Wu, S.K. The improvement of high temperature oxidation of Ti-50Al by sputtering Al film and subsequent interdiffusion treatment, *Acta Materialia*, vol. 51, 2003. pp. 3109–3120.
6. Ramanujan, R.V. Phase transformations in γ-based titanium aluminides, *International Materials Reviews*, vol. 45, no. 6, 2000. pp. 217–240.
7. Goral, M., Moskal, G., and Swadzba, L. The influence of Si on oxidation resistance of aluminide coatings on TiAl alloy, *Journal of Achievement in Materials and Manufacturing Engineering*, vol. 18, 2006. pp. 459–462.
8. Moskal, G. Microstructure and oxidation behaviour of TiAlSi coatings on TiAlCrNb alloy, *Journal of Achievements in Materials and Manufacturing Engineering*, vol. 20, 2007. pp. 263–266.
9. Huang, S.C. and Chesnutt, J.C. Gamma TiAl and its alloys, *Intermetallic compounds*, vol. 2, John Wiley & Sons Ltd, 1994. pp. 73–89.
10. Niewolak, L., Shemet, V., Thomas, C., Lersch, P., Singheiser, L., and Quadakkers, W.J. Oxidation behaviour of Ag-containing TiAl-based intermetallics, *Intermetallics*, vol. 12, 2004. pp. 1387–1396.
11. Calaphad. The titanium-aluminum (Ti-Al) phase diagram calculated with Thermo-Calc software, coupled with SSOL2 thermodynamic database, http:// www.calphad.com/titanium-aluminum.html. (Accessed 22 June 2011).
12. Khataee, A., Flower, H.M., and West, D.R.F. The alloying of titanium aluminides with ruthenium, *Platinum Metals Review*, vol. 33, no. 3, 1989. pp. 106–113.
13. Villars, P., Prince, A., and Okamoto, H. Handbook of Ternary Alloy Phase Diagrams. ASM International, vol. 4. pp 4273–4278
14. Murray, J.L. Calculation of the titanium-aluminium phase diagram. *Metallurgical Transactions A*, vol. 19A, 1988. pp 243–247. ◆



A comparative assessment of Ti-47.5 at.%Al cathodically modified by precious metal addition

by I.A. Mwamba*†, L.A. Cornish†, and E. van der Lingen*

Synopsis

Plain and alloyed titanium aluminides of composition Ti-47.5 at.% Al were prepared by melting commercial-purity titanium and aluminium with additions of 1 at.% precious metal. The as-cast alloys were subjected to potentiodynamic scans in 5, 15, and 25 wt% HCl aqueous solutions at room temperature and compared for their abilities to spontaneously passivate.

Addition of precious metals resulted in a general improvement of corrosion resistance by increasing the open circuit potential to more noble values. Addition of 1 at.% gold or silver to titanium aluminide did not significantly increase the corrosion potential (E_{corr}) above that of the plain titanium aluminide alloy, indicating that gold and silver are not sufficient cathodic modifiers to improve the corrosion resistance of titanium aluminide in all the solutions tested. However, platinum, palladium, and iridium additions shifted the corrosion potentials to the position of the passive region of plain TiAl for all solution concentrations. This indicated that TiAl alloyed with these platinum group metals would passivate spontaneously by cathodic modification. TiAl alloyed with palladium performed the best in 5 wt% HCl solution with the most positive corrosion potential. In 15 wt% HCl solution, alloys with platinum exhibited the most positive corrosion potentials, while alloying with iridium or palladium revealed more negative corrosion potentials. Thus, palladium alloying led to the best cathodic modification of titanium aluminide in low concentration HCl solution, whereas platinum and iridium alloying additions resulted in the best cathodic modification of titanium aluminide in high-concentration HCl solutions.

Keywords
cathodic modification, precious metals, titanium, corrosion.

Introduction

Titanium aluminides are alloys with high potential for elevated temperature applications in turbine components due to their strength at high temperatures, light weight, and good oxidation properties[1-5]. Much work has been dedicated to the investigation of the high-temperature oxidation properties of titanium aluminides, resulting in much available data. Although much work was done on the corrosion behaviour of pure titanium and titanium-based alloys, very limited information is available on the room-temperature or near room-temperature aqueous corrosion properties of titanium aluminides. This is due to the fact that most investigations conducted to date on the titanium aluminide alloys were aimed at high-temperature performance, and therefore, high-temperature properties such as oxidation and corrosion resistances were investigated. Gamma titanium aluminide, originally designed for high-temperature applications, appears to have excellent potential for bone repair and replacement, with the biological response expected to be similar to other titanium-base biomaterials[6]. These observations from early tests have triggered recent research activities on γ-TiAl as implants for the human body[7]. In the process, recent years have seen a growing interest in assessing the corrosion properties of γ-TiAl in aqueous media simulating human body fluids, which justify the need to generate a database on the corrosion properties of titanium aluminide in aqueous solutions[8].

Some catastrophic structure failures have occurred in various alloys due to lack of room-temperature corrosion resistance resulting in stress corrosion cracking[9-10]. Investigations of many alloy systems were triggered by corrosion-induced failure of structures in daily life. For instance, crevice corrosion studies of titanium and its alloys in sodium chloride in chemical industries where this metal and its

* Advanced Materials Division, Mintek and School of Chemical and Metallurgical Engineering and DST/NRF Centre of Excellence in Strong Materials, University of the Witwatersrand.
† School of Chemical and Metallurgical Engineering and DST/NRF Centre of Excellence in Strong Materials, University of the Witwatersrand.
© The Southern African Institute of Mining and Metallurgy, 2015. ISSN 2225-6253. This paper was first presented at the, Ferrous and Base Metals Development Network Conference 2012, 15–17 October 2012, Mount Grace Country House and Spa, Magaliesburg, South Africa..

alloys are extensively used. In most aqueous environments, titanium and titanium alloys show good corrosion resistance, due to the stable oxide films that form spontaneously on the surface. However, in chloride and/or fluoride solutions, titanium alloys are susceptible to attack, showing pitting and crevice corrosion[1]. Alloying elements, including nickel and molybdenum, have been added to titanium and titanium alloys to improve the corrosion resistance to pitting[2–13]. Precious metals were added to titanium to increase the corrosion resistance in non-oxidizing acids[14–15].

Addition of precious metals as alloying elements to improve corrosion resistance was not limited to titanium and its alloys. Precious metals were also used to increase the corrosion resistance of other alloys, such as stainless steel[16–17]. Their use for corrosion resistance improvement originated in 1911, when Monnartz reported that the rapid corrosion of iron-chromium alloys in certain acids could be suppressed by winding a platinum wire around the corrosion test specimen or by adding platinum as an alloying element to steel[18]. Stainless steel and nickel-based alloys were alloyed with other elements in order to improve their corrosion resistance[19–21].

Several methods for controlling or improving corrosion resistance of metals and alloys have been reported[22]. Corrosion resistance can be controlled and/or improved by cathodic modification[23–24]. For some metals and their alloys, such as aluminium, modification of anodic layers has been also used to improve corrosion resistance[25–27]. Beneficial alloying elements mostly used in cathodic modification include platinum group metals, and nickel and/or molybdenum[13,28]. When present in stainless steel, molybdenum led to better corrosion resistance by cathodic modification than molybdenum-free stainless steel[20].

Platinum group metal (PGM), nickel, or molybdenum additions facilitate cathodic depolarization by providing sites of low hydrogen overvoltage, which shifts alloy potential in the positive direction where oxide film passivation is possible[24,29]. A comprehensive description of the cathodic modification mechanism was given by Potgieter[15,25]. Relatively small concentrations of certain precious metals, of the order of 0.1 wt%, are sufficient to expand significantly the corrosion resistance of titanium in reducing acid media.

For alloys used in critical engine components, such as turbine blades and turbocharger casings, fuel combustion results in the formation of by-products, which form corrosive solutions once in contact with a moisturizing environment, leading to pitting and crevice corrosion[30–31] in addition to the hot corrosion usually observed in gas turbine components[32–33]. Alloying plays an important role in the corrosion resistance of materials in such environments, as the microstructural components of the alloy have different responses if subjected individually to the same environment. It is also difficult to predict the response of the alloy to the corrosive medium, as the presence of new phases, compounds, and structures can lead to pitting and/or galvanic corrosion. In this work, titanium aluminide alloys of $\alpha_2+\gamma$ and γ compositions with 1 at.% precious metal additions were prepared and assessed for pitting corrosion resistance. The precious metals were assessed for their ability to cathodically modify the titanium aluminide alloys.

Experimental procedure

Production of samples

TiAl alloys were prepared by melting Grade 2 titanium and CP aluminium in a button arc furnace under an argon atmosphere. The target composition was Ti-47.5 at.% Al ($\alpha_2+\gamma$) for the plain TiAl alloys. Plain TiAl and TiAl alloyed with precious metals (PMs), e.g. silver, gold, platinum, palladium, and iridium, were prepared containing 1 at.% PM substituting for titanium, with the aluminium content remaining at 47.5 at.%. Hereafter, precious metal(s) are referred to as PM(s). A plain γ-TiAl alloy made with 52.5 at.% Al was included in the study for comparison.

Electrochemical tests

Potentiodynamic scans were conducted with an ACM AutoTafel potentiostat/galvanostat system using a conventional three-electrode system with a saturated calomel electrode (SCE). For each alloy system, tests were done in 5, 15, and 25 wt% HCl at room temperature to assess the effect of solution concentration on the corrosion rate. Scans were conducted with Grade 2 titanium, CP aluminium, plain aluminides ($\alpha_2+\gamma$-TiAl), and aluminides with addition of precious metals.

The surfaces of the samples were ground to a 1200 grit SiC paper finish, degreased with methanol, rinsed with distilled water, and dried. The surface was prepared just prior to starting the polarization experiment to limit long-term oxidation. Before conducting the scan, each sample was immersed in the solution for approximately 60 minutes to obtain a stable corrosion potential. Potentiodynamic scans were done by scanning from -350 mV to +1000 mV versus the corrosion potential at a scanning rate of 10 mV.min-1.

Results and discussion

Electrochemical behaviour

The results of the different tests are shown in Table I, and the scans at different solution concentrations are shown in Figures 1 to 10. Table II shows the potential increase jump observed with increasing solution concentration (5, 15, 25 wt% HCl) after 60 minutes' exposure with reference to plain TiAl, and was established with the following calculations:

$$\Delta E_5 = E_5 - E_{TiAl} \quad [1]$$

$$\Delta E_{15} = E_{15} - E_{TiAl} \quad [2]$$

$$\Delta E_{25} = E_{25} - E_{TiAl} \quad [3]$$

where:

ΔE = Potential increase difference
E_5 = Corrosion potential in 5 wt% HCl solution
E_{15} = Corrosion potential in 15 wt% HCl solution
E_{25} = Corrosion potential in 25 wt% HCl solution
E_{TiAl} = Corrosion potential of plain TiAl alloy

Effect of alloying addition on corrosion potential

Corrosion of Grade 2 titanium and CP aluminium

Table I

Test parameters and resulting corrosion potentials, current densities and corrosion rates

Samples	HCl (wt %)	i_{corr} (mA/cm²)	Corr rate (mm/y)	E_{corr} (mV SCE)
Ti grade 2	5	0.001	0.010	-381
Ti grade 2	15	0.086	0.864	-611
Ti grade 2	25	0.300	2.700	-611
Aluminium	5	6.700	62.700	-909.000
Aluminium	15	62.000	578.100	-892.00
Aluminium	25	-	-	-
Alpha-gamma TiAl	5	0.061	0.548	-505
Alpha-gamma TiAl	15	0.130	1.161	-566
Alpha-gamma TiAl	25	0.200	1.764	-482
Gamma TiAl	5	1.400	12.00	-677
Gamma TiAl	15	1.200	10.530	-686
Gamma TiAl	25	1.000	9.960	-625
TiAl-1%Au	5	1.400	12.600	-508
TiAl-1%Au	15	1.900	17.10	-493
TiAl-1%Au	25	2.200	19.80	-353
TiAl-1%Ag	5	0.062	0.558	-636
TiAl-1%Ag	15	0.073	0.657	-579
TiAl-1%Ag	25	0.370	3.330	-515
TiAl-1%Pt	5	0.003	0.030	-260
TiAl-1%Pt	15	0.011	0.099	-234
TiAl-1%Pt	25	0.240	2.160	-254
TiAl-1%Pd	5	0.001	0.009	-228
TiAl-1%Pd	15	0.013	0.117	-286
TiAl-1%Pd	25	0.018	0.167	-268
TiAl-1%Ru	5	0.160	1.440	-270
TiAl-1%Ru	15	0.330	5.970	-238
TiAl-1%Ru	25	1.500	13.500	-223
TiAl-1%Ir	5	0.035	0.334	-282
TiAl-1%Ir	15	0.035	0.324	-275
TiAl-1%Ir	25	0.040	0.342	-232

Table II

Corrosion potential variation with precious metal addition

Metal/alloy	Corrosion potential (mV)			Potential increase (mV)		
	E_5	E_{15}	E_{25}	ΔE_5	ΔE_{15}	ΔE_{25}
Ti	-381	-611	-611	244	-66	-149
Al	-909	-892	-	-284	636	-
(α_2 + γ) TiAl	-505	-556	-462	0	0	0
TiAl (γ)	-677	-668	-625	-72	-112	-163
TiAl-Au	-508	-493	-353	97	63	109
TiAl-Ag	-636	-579	-515	-31	-23	-53
TiAl-Pd	-228	-268	-286	379	288	184
TiAl-Pt	-260	-254	-254	845	822	208
TiAl-Ru	-270	-238	-223	835	816	288
TiAl-Ir	-282	-275	-232	323	291	230

Results for Grade 2 Titanium are shown in Table II and Figures 1. Aluminium (Figure 2) was less noble than titanium, suggesting that aluminium was more susceptible to corrosion than titanium. In 25 wt % HCl solution, the sample was completely destroyed. Such a response was expected, because aluminium and its alloys are known to be susceptible to higher corrosion rates than steel and titanium in chloride solutions. Aluminium shows a pitting potential lower than the H^+/H_2 equilibrium in neutral electrolytes at 1 M concentration[34].

Corrosion of plain TiAl

TiAl with α_2 + γ phases in the microstructure

In the 5 wt% HCl solution, duplex titanium aluminide (Table I and Figure 3) had a lower corrosion potential than Grade 2 titanium and higher than CP aluminium, indicating that titanium aluminide was nobler than aluminium and less noble than Grade 2 titanium. Titanium aluminide gave the most positive E_{corr} values in 15 wt% and 25 wt% HCl solutions. It appeared that in high-concentration solutions, duplex TiAl had a better resistance to corrosion. The high corrosion potential observed with titanium aluminide in the 25 wt% HCl solution was due to the combined contribution of titanium and aluminium, a result of passivation of the alloy surface, as was demonstrated in previous work on aluminides[35]. There is no data available for aluminium in 25 wt% HCl solution, because it could not stand the aggressiveness of the solution and was completely destroyed. The primary passivation zone range decreased with increasing

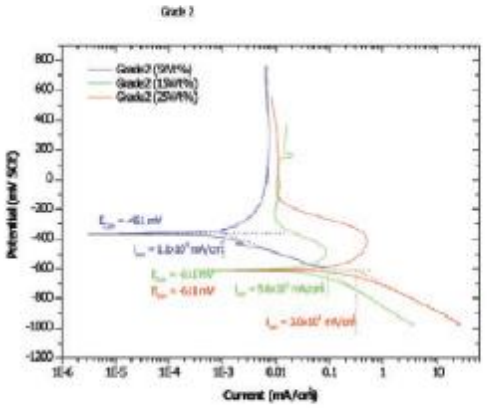


Figure 1—Potentiodynamic scans for Grade 2 titanium in HCl solution of different concentrations

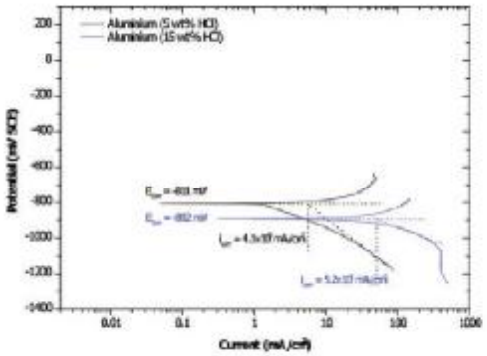


Figure 2—Potentiodynamic scans for CP aluminium in HCl solution of different concentrations

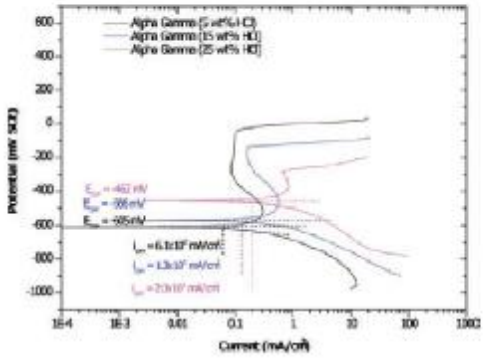


Figure 3—Potentiodynamic scans for plain TiAl ($\alpha_2+\gamma$) in HCl solution of different concentrations

concentration of HCl in solution. At all solution concentrations, the potentiodynamic scans indicated that there was pitting at potentials that decreased with increasing acid concentration. Alloy pitting was followed by a transpassive region that ended with a secondary passivation at current densities that were very close, irrespective of solution concentrations.

The increase of corrosion potential with increasing solution concentrations is believed to be the result of a strong and fast passivation reaction of the TiAl alloy in a more and more aggressive solution.

Plain TiAl with only γ phase in the microstructure

The potentiodynamic scan of single-phase titanium aluminide is shown in Figure 4. There was a high variation of corrosion potential as the solution concentration increased from 5 wt% HCl to 15 wt% HCl, and a small potential variation between the 15 wt% and 25 wt% HCl solutions, indicating that at higher solution concentrations, the corrosion potential was not influenced by the change in concentration. Overall, the scans gave corrosion potentials that were less noble than the corresponding potentials observed with duplex TiAl in solutions of the same concentration, suggesting that $\alpha_2+\gamma$-TiAl was more corrosion resistant than γ-TiAl. The low potentials observed with the γ-TiAl seemed to be the contribution of aluminium content, which was higher than in the duplex TiAl. Alloying of titanium with aluminium in a given solution was expected to result in a corrosion potential lower than the titanium corrosion potential and higher than the aluminium corrosion potential in the same solution. Lowering of corrosion potential with alloying is well documented for aluminium when it is alloyed with less noble elements, such as magnesium and zinc[36].

The passivation region for γ-TiAl decreased with increasing solution concentration. The pitting potential also decreased with increasing solution concentration, and transpassivity occurred at potentials that decreased with increasing solution concentrations. Secondary passivation occurred at a current density that was almost the same,

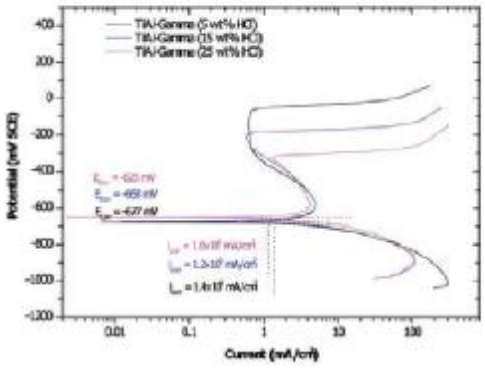


Figure 4—Potentiodynamic scans for plain γ-TiAl in HCl solution of different concentrations

irrespective of the solution concentration.

Corrosion of duplex TiAl alloyed with precious metals

Overall, the addition of 1 at.% precious metals to duplex TiAl resulted in an increase of corrosion potentials, compared to plain duplex TiAl in solutions of same concentration. The results are discussed further.

TiAl alloyed with silver and gold

The potentiodynamic scans for TiAl-1.0 at.% Ag and TiAl-1.0 at.% Au at different solution concentrations are given in Figures 5 and 6. Overall, there was no improvement of the corrosion resistance by addition of silver compared to the plain TiAl alloy. Instead, the addition of silver shifted the corrosion potential to less noble values (Table II), indicating that modification of the cathodic process could not be achieved with silver addition to TiAl alloy. There was an increase in the corrosion potentials for TiAl alloyed with gold (Table II). As the solution concentration increased, the corrosion potential increased as well. The corrosion potential

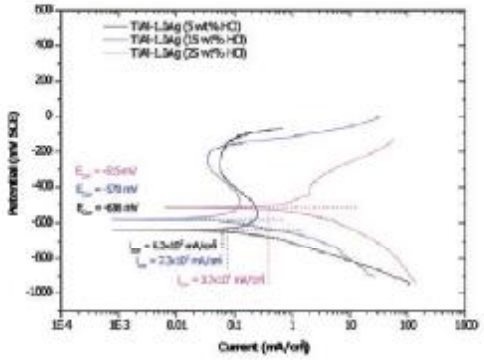


Figure 5—Potentiodynamic scans for TiAl-1.0 at.% Ag in HCl solution of different concentrations

increase with increasing solution concentration occurred at

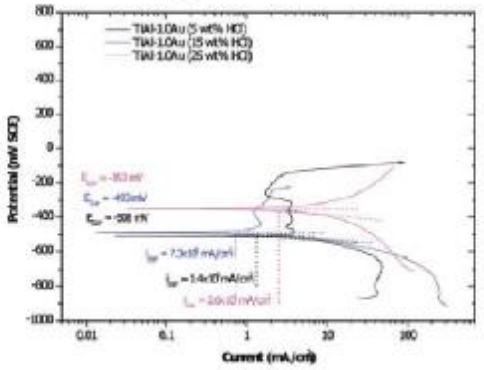


Figure 6—Potentiodynamic scans for TiAl-1.0 at.% Au in HCl solution of different concentrations

higher values than for the plain TiAl in solutions of the same concentration. The increase of corrosion potential with increasing solution concentrations is believed to be the result of a combined action of a strong and faster passivation reaction of the TiAl alloy in an increasingly aggressive solution, and an increase in gold content on the surface. The values of E_{corr} in the TiAl with gold suggested that the change in concentration from 5 wt% HCl to 15 wt% HCl impacted little on the corrosion potential (Table II).

TiAl alloyed with PGMs

The addition of PGMs to duplex TiAl resulted in an increase of the corrosion potential (Table I). Typical potentiodynamic scans are shown in Figure 7 for duplex TiAl alloyed with 1.0 at.% Pt. The addition of platinum shifted the corrosion potential to nobler values. These results showed that TiAl-1 at.% Pt will passivate spontaneously in 5, 15, and 25 wt % HCl solutions.

The corrosion potential in 25 wt% HCl was lower than in 15 wt% HCl owing to platinum being removed from the exposed surface of the TiAl samples and the relative amount of the two phases α and γ changing, resulting in a decrease of the corrosion potentials. There was more γ-TiAl phase than α_2 (Ti_3Al), resulting in a higher aluminium content, although this explanation needs to be verified by conducting EDX and XPS on the surface of the samples and potentiodynamic scans on the α_2-phase samples. From the data available, it is speculated that the corrosion potential of α_2 (Ti_3Al) was higher than that of γ (TiAl), because of the higher titanium content.

However, a very large increase in corrosion potential (Table III) could result in the cathodic process falling in the transpassive region of the plain TiAl, and an increase in current density, corresponding to alloy dissolution. Whether the cathodic process of the TiAl alloyed with PGMs fell in the active, passive, or transpassive region of the plain TiAl was verified by comparing the corresponding addition scans together with the plain TiAl scans.

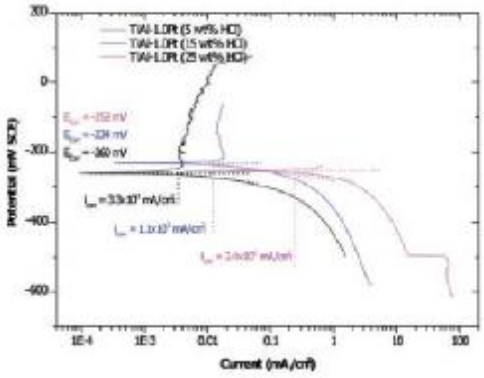


Figure 7—Potentiodynamic scans for TiAl-1.0 at.% Pt in HCl solution of different concentrations

Table III

Characteristic values of potentials and current density for plain TiAl

Characteristic values of potential or current density	Solution concentration (wt% HCl)		
	5	15	25
E_{pr} (mV)	-525	-484	-378
E_{pa} (mV)	-296	-251	-378
E_{pp} (mV)	-48	-138	-281
I_{cr} (mA/cm²)	3.0E-001	5.5E-01	8.2E-01
Passivation region	From -296 to -48	From -251 to -138	~0

Cathodic process modification

The analysis of the results has shown that aluminium, with a very negative dissolution potential, was more susceptible to pitting corrosion than Grade 2 titanium. For other alloy systems[36], alloying titanium with aluminium was expected to lead to a corrosion potential between the corrosion potentials of titanium and aluminium. The value of that corrosion potential will depend on the aluminium content in the TiAl alloy. From the data gathered with duplex TiAl ($\alpha_2 + \gamma$) and single-phase γ-TiAl, it appeared that the corrosion potentials of the duplex $\alpha_2 + \gamma$-TiAl were higher than those for single-phase γ-TiAl at all solution concentrations, indicating that γ-TiAl, with high aluminium content, would give lower corrosion potentials. It was also observed that the passivation region of plain duplex TiAl decreased with increasing solution concentration.

Thus, the introduction of precious metals in TiAl alloy resulted in a general improvement of corrosion resistance by shifting the corrosion potentials to nobler values. However, the cathodic modification will be achieved only:

1. When the plain duplex TiAl has a small critical current density (i_{cr}) that will be easily exceeded by the current of the hydrogen cathodic reaction on TiAl with precious metal addition at the given passivation potential (E_p)
2. If the passivation potential (E_p) of plain duplex TiAl is sufficiently negative to allow the cathodic component that has been introduced to change the corrosion potential (E_{corr}) of the TiAl with precious metal to a value in the passive range that is more positive than E_p but less positive than the potential associated with the onset of transpassive processes (E_p)
3. When the transpassive potential (E_{tr}) of TiAl is sufficiently electropositive to allow a wide passive range.

Figures 8 to 10 are the potentiodynamic scans of TiAl alloyed with precious metals superimposed on the potentiodynamic scans of plain duplex TiAl. Table III shows the extension of the passive region in the 5 wt% HCl, indicating that the corrosion potentials of TiAl alloyed with PGMs fell in that range, and none of the scans intersected the scan of plain TiAl in the transpassive region (Figure 8), suggesting that TiAl alloyed with PGMs would spontaneously passivate in the 5 wt% HCl solution by modification of the cathodic process, except for Ru. A similar trend was observed in the 15 wt% HCl solution, where all the cathodic processes of TiAl alloyed with PGMs fell within the passivation region, without intersecting the scan of the plain TiAl scan in the active or transpassive regions (Figure 9). However, in the 25 wt% HCl solution, corrosion potentials of TiAl alloyed with precious metals all fell outside the passivation region (Figure 10). The cathodic scan of TiAl alloyed with silver, gold, and palladium intersected the plain TiAl scan in the active region, indicating that alloy dissolution would occur. The cathodic process of TiAl alloyed with platinum, and iridium intersected the plain

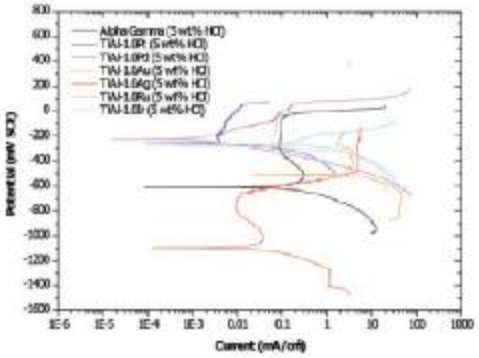


Figure 8—Effect of precious metal addition on the cathodic process in 5 wt% HCl solution

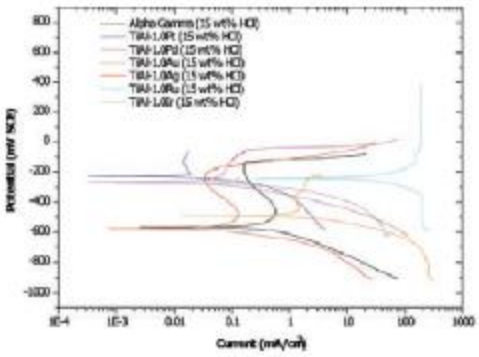


Figure 9—Effect of precious metal addition on the cathodic process in 15 wt% HCl solution

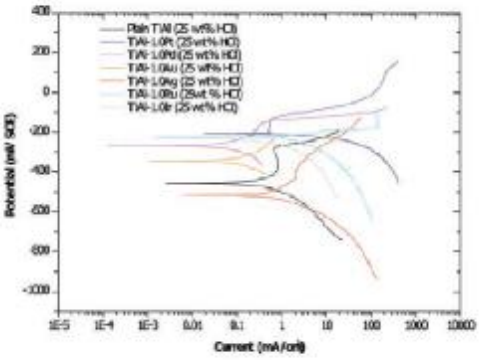


Figure 10—Effect of precious metal addition on the cathodic process in 25 wt% HCl solution

TiAl scan in the transpassive region, indicating that alloy dissolution would occur. This behaviour of alloys in the 25 wt% HCl solution suggested that it would be very difficult to improve corrosion resistance of TiAl alloys by cathodic modification with some precious metals.

Conclusion

Titanium aluminide of composition Ti-47.5 at.% Al was prepared by melting Grade 2 titanium and CP aluminium with 1 at.% additions of gold, silver, platinum, palladium, ruthenium, and iridium. The corrosion behaviour of the alloyed titanium aluminide was investigated by conducting potentiodynamic scans in 5, 15, and 25 wt% HCl aqueous solution at room temperature and compared to CP aluminium, Grade 2 titanium, and plain titanium aluminide of duplex microstructure ($\alpha_2 + \gamma$-TiAl).

CP aluminium was very susceptible to corrosion and Grade 2 titanium did not exhibit any significant susceptibility to pitting. Plain titanium aluminide ($\alpha_2 + \gamma$) - TiAl was nobler than CP aluminium and less noble than titanium Grade 2 in all solution concentration.

Silver addition to titanium aluminide did not bring the corrosion potential Ecorr above that of plain titanium aluminide for all solution concentrations, indicating that silver addition could not improve the corrosion resistance. Gold addition to TiAl alloy brought a slight improvement, resulting in the active-passive state.

Overall, addition of platinum group metals improved corrosion resistance by increasing the open circuit potential to nobler values. Platinum, palladium, and iridium additions shifted the corrosion potential to the passive region of plain TiAl in 5 wt% and 15 wt% HCl solutions, suggesting that TiAl alloyed with these platinum group metals will passivate spontaneously by modification of the cathodic process. In 25 wt% HCl solution, the new corrosion potentials fell in the transpassive region as a result of the shift of the TiAl passivation region to lower potentials, leading to alloy dissolution by some of the platinum group metal alloys.

References

1. Lasky, H.A. Titanium aluminides - An overview. *Materials Research Society Proceedings*, vol. 39, 1984. pp. 351–365.
2. Banerjee, D. Ti_3Al and its Alloys. *Intermetallic Compounds, Principles and Practice*, vol. 2. Westbrook, J.H and Fleischer, R.L. John Wiley, Chichester, England, 1995. pp. 91–131.
3. Huang, S. and Chesnutt, J.C. Gamma TiAl and its Alloys. *Intermetallic Compounds, Principles and Practice*, vol. 2. Westbrook., J.H and Fleischer, R.L. John Wiley, Chichester, England, 1995. pp. 73–90.
4. Yamaguchi, M. and Inui, H. Al_3Ti and its L12 variation. *Intermetallic compounds, Principles and Practice*, vol. 2. Westbrook., J.H and Fleischer, R.L.John Wiley & Sons Ltd, Chichester, England, 1995. pp. 73–90.
5. Dimiduk, D., Viala, J.-C., and Bouix, J. An overview of monolithic titanium aluminides based on Ti_3Al and TiAl. *Materials Chemistry and Physics*, vol. 72, no. 3, 2001. pp. 301–319.
6. Rivera-Diberard, O., Depoot-Carlo, N., Nappa, V., and Subramani, P.A. Biocompatibility studies of human foetal osteoblast cells cultured on gamma titanium aluminide. *Journal of Materials Science: Materials in Medicine*, vol. 19, no. 1, 2008. pp. 153–158.
7. Zhang, B.B., Zheng, Y.F., and Liu, Y. Effect of Ag on the corrosion behaviour of Ti-Ag alloys in artificial saliva solutions. *Dental Materials*, vol. 25, 2009. pp. 672–677.
8. Bello, S.A., Maldonado, L., Rossi-Fattima, E., Subramani, P.A., and Depoot-Carlo, N. In vitro evaluation of human osteoblast adhesion to a thermally oxidized γ-TiAl intermetallic alloy of composition Ti–48Al–2Cr–2Nb (at.%). *Journal of Materials Science: Materials in Medicine*, vol. 21, 2010. pp. 1739–1750.
9. Vervoort, D.P., Darwin, R.L., and Williams, F.W. Assessment of aircraft collateral damage from dry chemical fire extinguishing agents. US Navy Halon 1211 Replacement Program, Naval Research Laboratory, Washington DC, 1999. pp. 24–45.
10. Maldonado, S. Overview of the Mechanisms of Failure in Heat Treated Steel Components. Failure Analysis of Heat Treated Steel Component. *ASM International*, Novelty, Ohio, 2008. pp. 43–86.
11. Bressan, C.S. and Calabrisotto, G.A. Effects of environmental and metallurgical conditions on the passive and localised dissolution of Ti-0.15%Pd. *Corrosion*, vol. 9, 2001. pp. 768–774.
12. Petrakov, A.A., Karpov, K.B., and Ostrovsky, M.V. Effect of Ti and Mo additions on the corrosion-mechanical properties of Ti Al alloy, Kolomyisk Production Organization, Kaluga. *Translated from Fiziko-Khimicheskaya Mekhanika Materialov*, vol. 25, no. 3, 1989. pp. 28–32.
13. Schutz, R.W. Ruthenium enhanced titanium alloys. *Platinum Metals Review*, vol. 40, no. 2, 1996. pp. 54–61.
14. Haas, T.P. Increasing the resistance of titanium to non-oxidising acids. influence of addition of platinum metals. *Platinum Metals Review*, vol. 4, no. 2, 1960. pp. 59–64.
15. Pedeferri, J.P. Corrosion of passive alloys. Effect of noble metal additions. *Shreir's Corrosion*, vol. 4, no. 3, 2010. Elsevier, Amsterdam. pp. 2224-2249.
16. Dunerman, J.E. and Bernhus, H.E. Corrosion behaviour of a high-chromium duplex stainless steel with minor additions of ruthenium in sulfuric acid. *Corrosion*, vol. 51, no. 4, 1995. pp. 312–320.
17. Ostrovski, P.A., Pedeferri, J.E., and Consolo, L.A. Corrosion behaviour of superferritic stainless steels cathodically modified with minor additions of Ru in sulphuric and hydrochloric acid solutions. *Materials and Design*, vol. 30, no. 5, 2009. pp. 1451–1457.
18. Mathers, F. The study of the Fe-Cr alloys with particular regard to their solubility toward acids, *Metallurgie*, vol. 8, 1911. pp. 161–176.
19. Strecker, W.A. Alloying stainless steel with the platinum metals increased resistance to corrosion in acids. *Platinum Metals Review*, vol. 21, no. 2, 1977. pp. 51–55.
20. McCoy, I.R. Platinum metals in stainless steels. *Platinum Metals Review*, vol. 34, no. 3, 1990. pp. 144–154.
21. Kim, Y.H. and Pyun, S.I. Effect of noble metal alloying on passivity and passivity breakdown of nickel. *Journal of the Electrochemical Society*, vol. 154, 2007. pp. 26–42.

22. Kobe, L.J. and Olson, D.L. Corrosion. *ASM Handbook*, vol. 13, no. 9, 1987. pp. 375–498.
23. Potgieter, J.H., Heyns, A.M., and Skinner, W. Cathodic modification as a mean of improving the corrosion resistance of alloys. *Journal of Applied Electrochemistry*, vol. 20, 1990. pp. 711–715.
24. Van der Lingen, E. and Sauerbrunn, R.F. The cathodic modification behaviour of ruthenium additions to titanium in hydrochloric acid. *Corrosion Science*, vol. 43, 2001. pp. 577–590.
25. Krasicka-Cydzik, E., Kierzkowska, A., and Glazowska, I. Behaviour of anodic layer in Ringer's solution on Ti-6Al-4V ELI alloy after bending. *Archives of Materials Science and Engineering*, vol. 28, no. 4, 2007. pp. 231–237.
26. Lee, C.P., Chen, Y.Y., Hsu, C.Y., Yeh, J.W., and Shih, H.C. Enhancing pitting corrosion resistance of AlxCrFe1.5MnNi0.5 high-entropy alloys by anodic treatment in sulphuric acid. *Thin Solid Films*, vol. 517, 2008. pp. 1301–1305.
27. Černý, M. and Filípek, J. Anodic-modified anticorrosive coatings. *Acta Universitatis Agriculturae Mendelianae Brunensis*, vol. 59, no. 5, 2011. pp. 23–30.
28. Smyrl, H., Shimazoe, K., and Kamburov, F. The crevice corrosion resistance of some titanium materials: A review of the beneficial effects of palladium. *Platinum Metals Review*, vol. 31, no. 3, 1987. pp. 115–121.
29. Potgieter, J.H. Alloys cathodically modified with noble metals. *Journal of Applied Electrochemistry*, vol. 241, 1991. pp. 471–482.
30. Diesel Marine International. Repair of TC casings. Technical Services Bulletin, http://www.dmiglobal.com/downloads/Turbochargers.pdf [Accessed 7 March 2012].
31. Nordtest. http://nordtest.info/index.php/methods/item/combustion-by-products-corrosion-corrosivity-of-combustion-by-products-used-as-fill-around-carbon-steel-structures-nt-mat-001.html.
32. Lozovan, L.P., Kapkov, E.N., Kurbatskov, B.Y., and Mozhi, M.N. Corrosion resistance of gas turbine tested in a high-temperature gas flow. Kiev Institute of Civil Aviation, 1974. *Translated from Problemy Prochnosti*, vol. 9. pp. 87–90.
33. Eliaz, N., Shemesh, G., and Latanision, R.M. Hot corrosion in gas turbine components. *Engineering Failure Analysis*, vol. 9. 2002. pp. 31–43.
34. Szklarska-Smialowska, Z. Pitting corrosion of metals. NACE International, Houston, Texas. 1986. Ricker, R.E., Hall, D.E., and Fink, J.L., The effects of aqueous environments on the fracture behaviour of ductile nickel aluminide. *Scripta Metallurgica et Materialia*, vol. 24. 1990 pp. 291–296.
35. Vargel, C., Jacques, M., and Schmidt, M.P. Corrosion of Aluminium. Elsevier, Amsterdam, 2004. pp.81–109. ◆



Effect of platinum group metal addition on microstructure and corrosion behaviour of Ti–47·5 at-%Al

I. A. Mwamba*[1,2], L. A. Cornish[2] and E. van der Lingen[3]

Plain and alloyed titanium aluminides of composition Ti–47·5 at-%Al were prepared with the addition of 1·0 at-% platinum group metals (PGMs). The as cast alloys were subjected to potentiodynamic scans in 5, 15 and 25 wt-%HCl solutions at room temperature, and the PGM containing alloys were assessed for their abilities to spontaneously passivate by cathodic modification. Plain titanium aluminide had a duplex microstructure consisting of lamellar (α_2 and γ alternating lamellae) and γ-TiAl phase grains. The introduction of 1·0 at-%PGMs (platinum, palladium and iridium) led to the formation of a new phase, developing more in the γ-TiAl phase grains and a general improvement of corrosion resistance by increasing the corrosion potential to nobler values. Platinum group metal additions to plain TiAl resulted in the corrosion potentials falling in the passive region of plain TiAl, indicating spontaneous passivation of PGM alloyed TiAl in 5 and 15 wt-%HCl solutions. In 25 wt-%HCl solution, the addition of PGMs shifted the cathodic process in the transpassive or active region of plain TiAl, resulting in either case in the dissolution of the alloy due to the absence of an extended passivation region. The cathodic modification of PGM alloyed TiAl occurred as a result of PGM accumulation on the surface of the TiAl alloys, which simultaneously improved the hydrogen evolution efficiency and inhibited anodic dissolution.

Keywords: Titanium aluminide, Cathodic modification, Passivation, Platinum group metals, Transpassive region, Active region, Passive region

Introduction

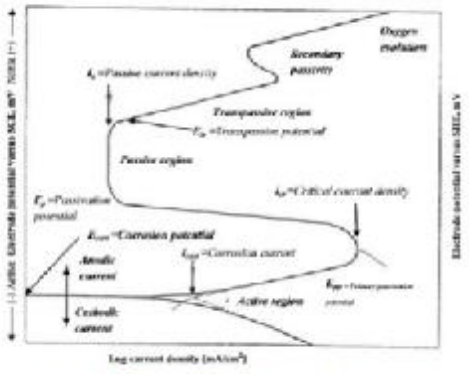
Titanium aluminides are alloys with high potential for elevated temperature applications in turbine components due to their strength at high temperatures, light weight and good oxidation properties.[1–3] Much work has been dedicated to the investigation of the high temperature oxidation properties of titanium aluminides, resulting in various available data. Although significant research was carried out on the corrosion behaviour of pure titanium and titanium based alloys, very limited information is available on the room or near room temperature aqueous corrosion properties of titanium aluminides. The reason is that most investigations conducted on titanium aluminide alloys were aimed at high temperature performance, and therefore, high temperature properties such as oxidation and corrosion resistance were investigated. Gamma titanium aluminide, originally designed for high temperature applications, appears to have excellent potential for bone repair and replacement, with the biological response expected to be similar to other titanium based biomaterials.[6] These observations from early tests have triggered research activities on γ-TiAl for potential use as implants.[7] A growing interest in assessing the corrosion properties of γ-TiAl in aqueous media, simulating human body fluids, is taking place.[8]

In most aqueous environments, titanium and titanium alloys show good corrosion resistance due to the stable oxide films that form spontaneously on the surface. However, in chloride and/or fluoride solutions, titanium alloys are susceptible to attack, showing pitting and crevice corrosion.[9] Alloying elements, including nickel and molybdenum, have been added to titanium and titanium alloys to improve the corrosion resistance.[10] Precious metals were added to titanium to increase the corrosion resistance in non-oxidising acids.[11–14] Platinum group metal (PGM), nickel or molybdenum additions facilitate cathodic depolarisation by providing sites of low hydrogen overvoltage, which shifts the alloy potentials in the positive direction where oxide film passivation is possible. Relatively small concentrations of certain precious metals, in the order of 0·1 wt-%, are sufficient to significantly increase the corrosion resistance of titanium in reducing acid media. The addition of precious metals as

[1]Advanced Materials Division, Mintek, Randburg 2125, South Africa
[2]School of Chemical and Metallurgical Engineering and DST/NRF Centre of Excellence in Strong Materials, University of the Witwatersrand, Johannesburg 2001, South Africa
[3]Department of Engineering and Technology Management, Graduate School of Technology Management, University of Pretoria, Pretoria 0002, South Africa

*Corresponding author, email alainm@mintek.co.za

© 2014 Institute of Materials, Minerals and Mining
Published by Maney on behalf of the Institute
Received 8 February 2013; accepted 2 August 2013
DOI 10.1179/1743278213Y.0000000108



1 Typical polarisation scan of material exhibiting cathodic and anodic regions with active to passive transition[22]

alloying elements to improve the corrosion resistance is not limited to titanium and its alloys. Precious metals are also used to increase the corrosion resistance of stainless steels and nickel.[15–21] Figure 1 is a schematic diagram of a metal showing active to passive transition.

Their use for improving corrosion resistance originated in 1911 when Monnartz reported that the rapid corrosion of iron–chromium alloys in certain acids could be suppressed by winding a platinum wire around the corrosion test specimen or by adding platinum as an alloying element to steel.[18]

In this study, plain titanium aluminide of composition Ti–47·5 at-%Al and titanium aluminide with 1·0 at-%PGM additions were prepared and assessed for the effect of the PGMs on the microstructure and the cathodic modification during corrosion.

Experimental

Sample production

TiAl alloys were prepared by melting titanium grade 2 and aluminium of commercial purity in a button arc furnace under an argon atmosphere. The target composition was Ti–47·5 at-%Al. The melting cycle was repeated four times. Two types of alloys were prepared: plain TiAl and TiAl alloyed with 1·0 at-% PGMs (platinum, palladium, ruthenium and iridium). Different TiAl alloys were obtained containing PGMs substituting for titanium, with the aluminium content remaining at 47·5 at-%.

Microstructure characterisation

The samples were cut, polished and observed with optical and SEM microscopes. Scanning electron microscope imaging and EDX were conducted with a FEI Nova NanoSEM, a high resolution SEM. The chemistry of the samples and the phases were determined using a combination of X-ray diffraction and EDX. For X-ray diffraction, the samples were analysed with a PANalytical X'Pert Pro powder diffractometer with an X'Celerator detector and variable divergence and fixed receiving slits with Fe filtered Co K_α radiation. Phase identification was conducted using a X'Pert Highscore plus software.

Electrochemical tests

Potentiodynamic scans and open circuit potential (OCP) measurements were conducted with an ACM AutoTafel potentiostat/galvanostat system using a conventional three-electrode system with a saturated calomel electrode (SCE). For each alloy system, tests were performed in 5, 15 and 25 wt-%HCl at room temperature to assess the effect of the solution concentration on the corrosion rate. Scans were conducted with plain aluminides ($\alpha_2+\gamma$-TiAl) and aluminides with addition of precious metals.

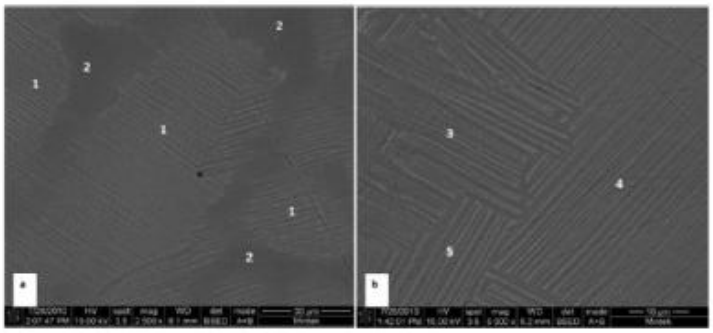
A copper wire was soldered onto the sample, and the sample was cold mounted using a Struers Epofix resin and hardener and left for 12 h to cure. The wire soldered on the sample was placed inside the glass specimen holder, sealed with silicone and left for 3 h to cure. Each sample was ground to 1200 grit SiC paper finish, degreased with methanol, rinsed with distilled water and dried before being immersed in the solution. Polarisation diagrams were determined for the individual metals as well as for the galvanic couples using an ACM AutoTafel potentiostat/galvanostat system and a conventional three-electrode electrochemical cell fitted with a SCE as reference electrode and graphite as counter electrode. The surface was prepared just before starting the polarisation experiment to limit long term oxidation. Before conducting the scan, each sample was immersed in the solution for ~60 min to obtain a stable corrosion potential. Potentiodynamic scans were conducted by scanning from −350 to +1000 mV versus the corrosion potential at a scanning rate of 10 mV min^{-1}. The OPC tests were run for 15 h, during which the samples were exposed to a 5 wt-%HCl solution.

Results and discussion

Microstructural characterisation of alloys and hardness

The duplex microstructure in the plain TiAl alloy is shown in Fig. 2. Figure 2*a* shows that at a target composition of Ti–47·5 at-%Al, the microstructure was duplex, consisting of lamellar grains (area 1) with single phase regions between them (area 2). The grains identified in area 1 comprised alternating light and dark lamellae. In some parts, the lamellar grains were adjacent. Figure 2*b* shows, at higher magnification, such an area that appears to be only lamellar. This figure also shows that different grains could be identified by the orientation of their lamellae (areas 3–5).

Typical EDX results of plain TiAl are reported in Table 1. The overall composition in Table 2 indicates the formation of a duplex TiAl compound, according to the Ti–Al phase diagram shown in Fig. 2.[23] The Ti–Al phase diagram (Fig. 3) shows that Ti_3Al has an aluminium content between 22 and 33·5 at-% at 400°C. Between 33·5 at-% to composition of ~49·5 at-%Al at 400°C is the $Ti_3Al+\gamma$-TiAl two-phase field, which was these samples, with the lamellar region having a composition close to 47·5 at-%Al. The EDX results, together with the Ti–Al phase diagram, also show that area 1 in Fig. 2*a* comprised alternating Ti_3Al (α_2) and γ-TiAl. In the single phase regions (area 2 in Fig. 2*a*), the aluminium content was >50 at-%, showing the sole presence of γ-TiAl. These observations indicated that the microstructure was a mixture of lamellar grains (with alternating α_2 and γ parallel phases) and γ-TiAl grains between the lamellar grains, which is a typical duplex microstructure.[3]



2 Image (SEM-BSE) of plain TiAl showing Ti_2Al (bright) and γ (dark) phases

Typical SEM and EDX results of TiAl alloys containing 1·0 at-%Ru are presented in Fig. 4 and Table 3 respectively. The SEM showed (Fig. 4) that the duplex structure was maintained in spite of the ruthenium addition. In addition, the precipitation of a light phase was observed mainly in the γ-phase regions. The shape of these precipitates was irregular, with no particular trend. This microstructure was also observed in samples doped with other PGMs.

The EDX results in Table 3 showed that the light phases had a higher Ru content than the lamellar and γ phases. The ruthenium content observed in the lamellar grain and γ-TiAl was <1 at-%, which is in the range reported by Khataee *et al.*[24] In a constitutional study of the Ti–Al–Ru system, they concluded that the solubility of ruthenium in γ is higher than in the α_2 (Ti_3Al) phase with reported values of ~0·5 at-%Ru in α_2 and less or equal to 1 at-% in γ-TiAl.

The Al–Ru–Ti isothermal section (Fig. 5) shows that the light phase reported in Table 3 (6·4–10·0 at-%Ru) is located in the phase field containing γ-TiAl and was named G-phase. The EDX results of the G-phase were affected by the surrounding matrix, so that the true value should be extrapolated away from the matrix phase(s). The G-phase is the $Al_{16}Ru_8Ti_6$ ternary compound with the $Mn_{23}Th_6$ structure, a D8a type crystal structure with a complex unit containing 116 atoms based on a body centred cubic structure.[24] The introduction of precious metal led to the precipitation and progression of the new phase in the γ grains, as shown in Fig. 5. In some areas, the growth of the G-phase in the γ grains resulted in a complete separation of lamellar grains.

Table 1 Energy dispersive X-ray spectroscopy analysis of plain TiAl (five analyses)

		Elemental composition/at-%	
Plain TiAl	Area	Ti	Al
	Overall	52·0±1·0	48·0±1·0
	Lamellae 1	52·7±0·7	47·3±0·7
	Plain 2	49·4±1·8	50·6±1·8

Table 2 Elemental composition of alloys

	PGM content/at-%					
Compound	Ti	Al	Ru	Pd	Pt	Ir
Plain TiAl	52·5	47·5	…	…	…	…
TiAl-1Ru	51·5	47·5	1	…	…	…
TiAl-1Pd	51·5	47·5	…	1	…	…
TiAl-1Pt	51·5	47·5	…	…	1	…
TiAl-1Ir	51·5	47·5	…	…	…	1

Effect of PGMs on corrosion behaviour

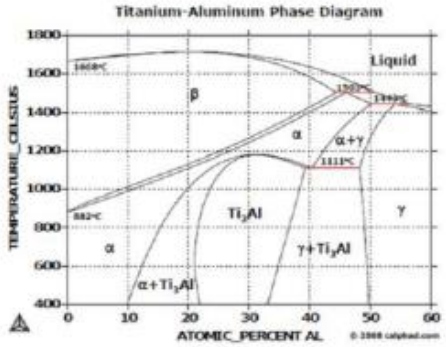
Electrochemical behaviour

A summary of the test results is given in Table 4, showing the current density, corresponding corrosion rate and corrosion potentials at each concentration of the HCl solution. The potentiodynamic scans of plain TiAl and TiAl–1Pd in solutions of different concentrations are shown below (Figs. 6 and 7).

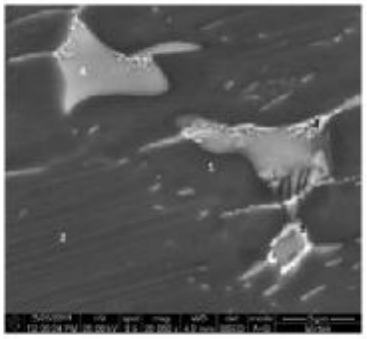
Effect of alloying addition on corrosion potential

Corrosion of plain TiAl

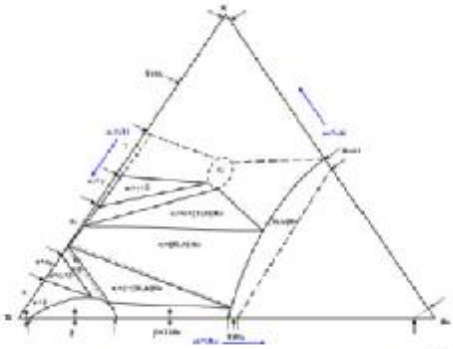
In the 5 wt-%HCl solution, plain duplex titanium aluminide (Table 4 and Fig. 6) had a corrosion potential of about −605 V, which decreased as the concentration of the HCl solution increased. Thus, the primary active to passive zone decreased with increasing concentration of HCl solution. In all solution concentrations, pitting corrosion occurred as can be seen with the increase in current after passivation, e.g. transpassive region. Pitting corrosion occurred at potentials that decreased with increasing acid concentration. This observation is in agreement with the work carried out by Saffarian *et al.*[25]



3 Ti–Al phase diagram[23]



4 Images (SEM-BSE) of TiAl–0·2 at-%Ru alloy showing γ, α_2 and G-phase[3]



5 Isothermal section of ternary Ti–Al–Ru system at 770°C[24]

TiAl alloyed with PGMs

The addition of PGMs to duplex TiAl resulted in an increase in the corrosion potential (Table 4). Typical potentiodynamic scans are shown in Fig. 7 for duplex TiAl alloyed with 1·0 at-%Pd. The addition of palladium shifted the corrosion potential to nobler values. These results suggested that TiAl-1 at-%Pd will passivate spontaneously in 5, 15 and 25 wt-%HCl solutions. Similar results were obtained with TiAl–1·0 at-%Pt, TiAl–1·0 at-%Ru and TiAl–1·0 at-%Ir. Table 5 shows the potential increase observed with increasing solution concentration (5, 15 and 25 wt-%HCl) after 60 min exposure with reference to plain TiAl, as obtained by the following calculations

$$\Delta E_5 = E_5 - E_{\mathrm{TiAl}}$$

$$\Delta E_{15} = E_{15} - E_{\mathrm{TiA}}$$

$$\Delta E_{25} = E_{25} - E_{\mathrm{TiAl}}$$

where ΔE is the potential increase difference, E_5 is the corrosion potential in 5 wt-%HCl solution, E_{15} is the corrosion potential in 15 wt-%HCl solution, E_{25} is the corrosion potential in 25 wt-%HCl solution and E_{TiAl} is the corrosion potential of plain TiAl alloy.

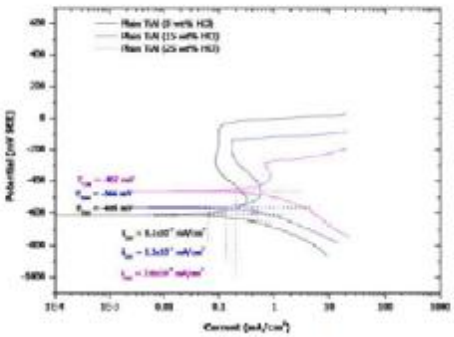
The corrosion potential increases to nobler values are well illustrated (Fig. 8). The evolution of corrosion potentials with HCl concentration in the solution remains between −300 and −200 mV for TiAl containing PGMs, well above the evolution of the corrosion potential for plain TiAl, which remained below −450 mV. These graphs show clearly the shift of corrosion potentials to nobler values with the addition of PGMs to TiAl alloy and suggest an improvement in corrosion resistance.

Cathodic modification

The introduction of precious metals in plain TiAl resulted in a general improvement of corrosion resistance of the TiAl alloys by shifting the corrosion potentials to nobler values. However, the cathodic modification will be achieved only as follows:[24]

(i) when the plain duplex TiAl has a small critical current density i_{cr} that will be easily exceeded by the current of the hydrogen cathodic reaction on TiAl with precious metal addition at the given passivation potential E_p. See schematic diagram in Fig. 1

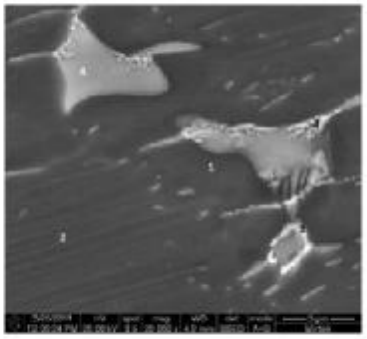
(ii) if the passivation potential E_p of plain duplex TiAl is sufficiently negative to allow the cathodic component that has been introduced to change



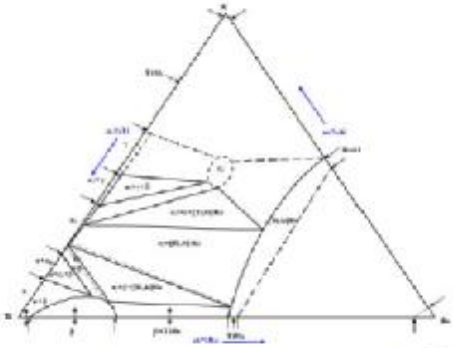
6 Potentiodynamic scans for plain TiAl ($\alpha_2+\gamma$) in HCl solution of different concentrations

Table 3 Typical EDX analysis of Ru containing TiAl (five analyses)

	Alloy TiAl–1Ru			
	Elemental composition/at-%			
Area	Ti	Al	Ru	Possible phase
Overal	49·3±0·3	49·3±0·3	1·0±0·1	γ,α_2, G-phase
Plain -1	46·9±1·5	52·4±1·7	0·7±0·1	γ-TiAl (Ru)
Striped -2	49·5±1·0	50·1±1·2	0·4±0·1	$\gamma+\alpha_2$ (Ru)
Light phase-3	42·0±0·2	48·2±1·9	9·8±2·6	G-phase
Grey-phase-4	53·2±0·8	40·5±0·7	6·3±0·3	G-phase



4 Images (SEM-BSE) of TiAl–0·2 at-%Ru alloy showing γ, α_2 and G-phase[3]



5 Isothermal section of ternary Ti–Al–Ru system at 770°C[24]

TiAl alloyed with PGMs

The addition of PGMs to duplex TiAl resulted in an increase in the corrosion potential (Table 4). Typical potentiodynamic scans are shown in Fig. 7 for duplex TiAl alloyed with 1·0 at-%Pd. The addition of palladium shifted the corrosion potential to nobler values. These results suggested that TiAl-1 at-%Pd will passivate spontaneously in 5, 15 and 25 wt-%HCl solutions. Similar results were obtained with TiAl–1·0 at-%Pt, TiAl–1·0 at-%Ru and TiAl–1·0 at-%Ir. Table 5 shows the potential increase observed with increasing solution concentration (5, 15 and 25 wt-%HCl) after 60 min exposure with reference to plain TiAl, as obtained by the following calculations

$$\Delta E_5 = E_5 - E_{\mathrm{TiAl}}$$

$$\Delta E_{15} = E_{15} - E_{\mathrm{TiA}}$$

$$\Delta E_{25} = E_{25} - E_{\mathrm{TiAl}}$$

where ΔE is the potential increase difference, E_5 is the corrosion potential in 5 wt-%HCl solution, E_{15} is the corrosion potential in 15 wt-%HCl solution, E_{25} is the corrosion potential in 25 wt-%HCl solution and E_{TiAl} is the corrosion potential of plain TiAl alloy.

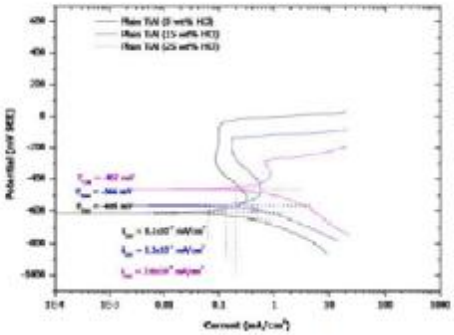
The corrosion potential increases to nobler values are well illustrated (Fig. 8). The evolution of corrosion potentials with HCl concentration in the solution remains between −300 and −200 mV for TiAl containing PGMs, well above the evolution of the corrosion potential for plain TiAl, which remained below −450 mV. These graphs show clearly the shift of corrosion potentials to nobler values with the addition of PGMs to TiAl alloy and suggest an improvement in corrosion resistance.

Cathodic modification

The introduction of precious metals in plain TiAl resulted in a general improvement of corrosion resistance of the TiAl alloys by shifting the corrosion potentials to nobler values. However, the cathodic modification will be achieved only as follows:[24]

(i) when the plain duplex TiAl has a small critical current density i_{cr} that will be easily exceeded by the current of the hydrogen cathodic reaction on TiAl with precious metal addition at the given passivation potential E_p. See schematic diagram in Fig. 1

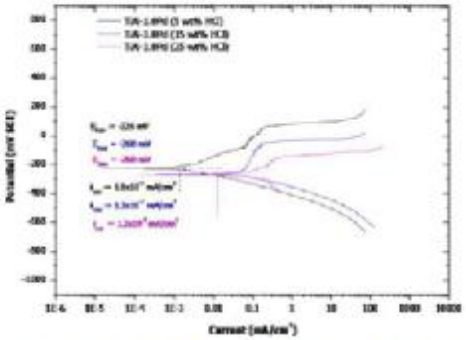
(ii) if the passivation potential E_p of plain duplex TiAl is sufficiently negative to allow the cathodic component that has been introduced to change



6 Potentiodynamic scans for plain TiAl ($\alpha_2+\gamma$) in HCl solution of different concentrations

Table 3 Typical EDX analysis of Ru containing TiAl (five analyses)

	Alloy TiAl–1Ru			
	Elemental composition/at-%			
Area	Ti	Al	Ru	Possible phase
Overal	49·3±0·3	49·3±0·3	1·0±0·1	γ,α_2, G-phase
Plain -1	46·9±1·5	52·4±1·7	0·7±0·1	γ-TiAl (Ru)
Striped -2	49·5±1·0	50·1±1·2	0·4±0·1	$\gamma+\alpha_2$ (Ru)
Light phase-3	42·0±0·2	48·2±1·9	9·8±2·6	G-phase
Grey-phase-4	53·2±0·8	40·5±0·7	6·3±0·3	G-phase

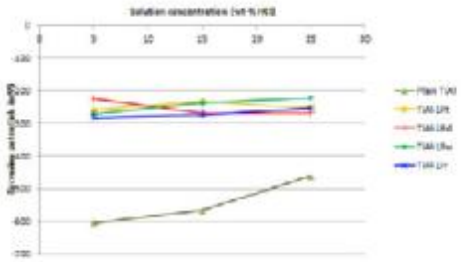


7 Potentiodynamic scans for TiAl+1·0 at·%Pd in HCl solution of different concentrations

the corrosion potential E_{corr} of the TiAl with precious metal to a value in the passive range that is more positive than E_p but less positive than the potential associated with the onset of transpassive processes E_{tr}

(iii) when the transpassive potential E_{tr} of TiAl is sufficiently electropositive to allow a wide passivation region.

Table 6 shows the passivation regions obtained on the plain TiAl scans in the three solutions. This region decreased with increasing solution concentration and completely disappeared in 25 wt·%HCl solution. Whether the cathodic process of the TiAl alloyed with PGMs fell in the active, passive or transpassive region of the plain TiAl was verified by comparing the scans of PGM alloyed TiAl to the plain TiAl scans. Figure 9 shows the potentiodynamic scans of TiAl alloyed with PGMs superposed on the potentiodynamic scan of plain TiAl in 5 wt·%HCl. All



8 Variation of corrosion potential with solution concentration

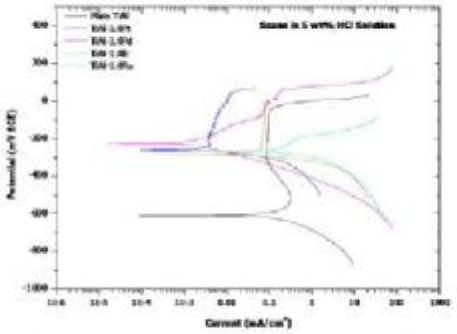
the corrosion potentials of TiAl alloyed with PGMs fell in the passive region, suggesting that TiAl alloyed with PGMs would spontaneously passivate in the 5 wt·%HCl solution due to cathodic modification. A similar trend was observed in the 15 wt·%HCl solution, where all the cathodic processes of TiAl alloyed with PGMs fell within the passivation region (Fig. 10). It is worth saying that the same effect was achieved with 0·1–0·3 at·%Ru or Pd additions to titanium alloys in solutions of 1–5 wt·%HCl,[13] 0·2 at·%Ru or Pd in 25 wt·%HCl.[11] However, in the 25 wt·%HCl solution, the corrosion potentials of TiAl alloyed with PGMs did not intersect the plain TiAl curve in the passive region (Fig. 11). While the cathodic process of TiAl alloyed with platinum and iridium intersected the plain TiAl curve in the transpassive region, the cathodic process of TiAl alloyed with palladium intersected the plain TiAl curve in the active region. In either case, this would result in alloy dissolution. This behaviour of the alloys in the 25 wt·%HCl solution suggested that it would be very difficult to improve the corrosion resistance of TiAl alloys by cathodic modification due to the fact that the passive region did not exist at

Table 4 Test parameters and resulting corrosion potentials, current densities and corrosion rates

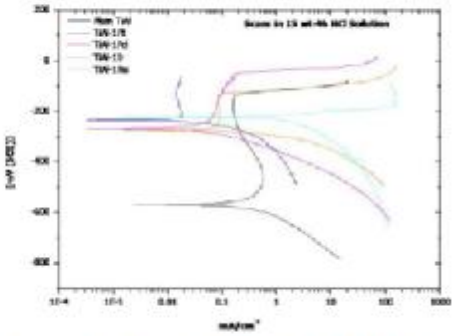
Samples	HCl/wt·%	i_{corr}/mA cm^{-2}	Corr rate/mm/year	E_{corr}/mV(SCE)
Plain TiAl	5	0·061	0·549	−605
Plain TiAl	15	0·130	1·161	−566
Plain TiAl	25	0·200	1·764	−462
TiAl–1Pt	5	0·003	0·030	−260
TiAl–1Pt	15	0·011	0·099	−234
TiAl–1Pt	25	0·240	2·160	−254
TiAl–1Pd	5	0·001	0·009	−226
TiAl–1Pd	15	0·013	0·117	−268
TiAl–1Pd	25	0·013	0·117	−268
TiAl–1Ru	5	0·160	1·440	−270
TiAl–1Ru	15	0·930	8·370	−238
TiAl–1Ru	25	1·500	13·500	−223
TiAl–1Ir	5	0·026	0·234	−282
TiAl–1Ir	15	0·085	0·765	−272
TiAl–1Ir	25	0·096	0·864	−254

Table 5 Corrosion potential increases with precious metal addition

	Corrosion potentials/mV			Potential increase/mV		
Alloy	E_5	E_{15}	E_{25}	ΔE_5	ΔE_{15}	ΔE_{25}
Plain TiAl	−605	−556	−462	0	0	0
TiAl–1Pd	−226	−268	−268	379	288	194
TiAl–1Ru	−270	−238	−223	335	318	239
TiAl–1Pt	−260	−234	−254	345	322	208
TiAl–1Ir	−282	−272	−254	323	284	208



9 Effect of PGM additions on polarisation scans of TiAl in 5 wt-%HCl solution



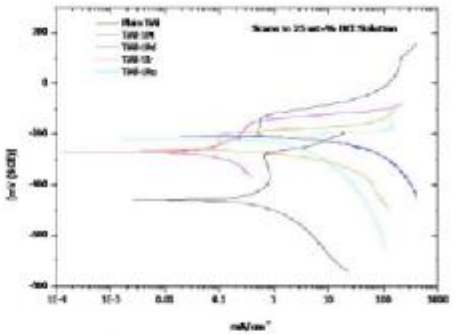
10 Effect of PGM additions on polarisation scans of TiAl in 15 wt-%HCl solution

all on the potentiodynamic scan of the plain TiAl immersed in 25 wt-%HCl solution (Table 6). These results showed that PGM alloyed TiAl would passivate spontaneously in 5 and 15 wt-%HCl solutions, whereas corrosion would take place in 25 wt-%HCl. This was due to the fact that a very large increase in corrosion potential (Table 3) resulted in the cathodic reaction of PGM alloyed TiAl intersecting the anodic reaction in the transpassive region of the plain TiAl, and an increase in current density occurred. This resulted in higher corrosion rates in PGM alloyed TiAl than Plain TiAl, although the corrosion potential values were nobler, as was the case for TiAl-1Ru, TiAl-1Pt and TiAl-1Ir in 25 wt-%HCl solution. However, duplex stainless steel with 0·1 at-%Ru investigated both in low and high concentration solutions showed spontaneous passivation.[27,28]

Analysis of different parameters affecting corrosion behaviour

Solution concentration and corrosion rate

From Table 4, the corrosion rate histograms were drawn as functions of HCl concentration in solution and are presented in Fig. 12. These histograms show that in 5 and 15 wt-%HCl solutions, TiAl alloys with additions of palladium, platinum and iridium had low corrosion rates, indicative of good corrosion resistance. In 25 wt-%HCl solution, the corrosion rate of TiAl alloyed with platinum was higher than the corrosion rate of plain TiAl, even though the addition of platinum to TiAl, like other PGMs, shifted the corrosion potential to nobler values. This observation supported the fact that the high increase in corrosion potential of the Pt alloyed TiAl resulted in the cathodic process falling in the transpassive zone on the potentiodynamic scan of the plain TiAl (Fig. 11). Figure 12 also showed that the best performance in corrosion improvement was achieved



11 Effect of PGM additions on polarisation scans of TiAl in 25 wt-%HCl solution

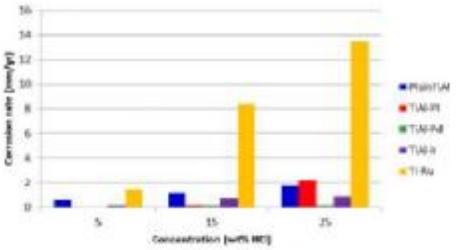
with palladium addition. The addition of iridium resulted in a corrosion rate not significantly affected by the variation of HCl concentration in the solution. The corrosion rate of TiAl alloyed with ruthenium was higher than the corrosion rate of plain TiAl, even though the addition of ruthenium to TiAl, like other PGMs, shifted the corrosion potential to nobler values. This observation is strange as it does not support the fact that ruthenium also promoted cathodic modification. However, previous work has also shown that ruthenium addition tended to shift the potentiodynamic scan towards high current density.[11]

Accumulation of precious metals on corroded TiAl alloys

The accumulation of precious metal on the surface of TiAl can be explained by the corrosion behaviour of PGMs, as presented by Pourbaix *et al.*[29] Platinum,

Table 6 Characteristic values of potentials and current density for plain TiAl

Characteristic values of potential or current density	Solution concentration/wt-%HCl		
	5	15	25
E_{cor}/mV	−296	−251	−282
E_{pp}/mV	−48	−138	−281
Passivation region	From −296 to −48	From −251 to −138	~0



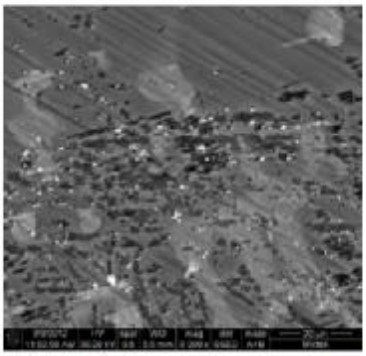
12 Corrosion rates of TiAl alloys with PGM additions in 5, 15 and 25 wt-%HCl solutions

palladium, ruthenium and iridium are very noble metals since, in the potential pH diagrams, their domains of stability cover most of the stability domain of water. According to their respective potential pH diagrams, they are thermodynamically stable in the presence of aqueous solutions of any pH with the exception of strong oxidising agents and complexing substances. At temperatures ~25°C, they remain unaltered in the presence of water or in aqueous solutions of caustic alkalis.

The best known reagent for dissolving platinum, aqua regia, acts by means of a combination of oxidising and complexing actions. Hydrochloric acid, which does not attack platinum on its own, will attack it when it contains chlorine in solution, because it then combines oxidising and complexing actions. Aqua regia (a mixture of hydrochloric and nitric acids) dissolves platinum slowly as chloroplatinic acid $PtCl_6H_2$ with the formation of the complex hexachloroplatinic(IV) acid $H_2[PtCl_6].6H_2O$.

Palladium is unattacked by water, except at high temperatures, and is not tarnished in moist air. Non-oxidising acids, acetic, hydrofluoric, oxalic and sulphuric acids are without action at ordinary temperatures.[29] Dilute nitric acid attacks palladium only slowly, but the metal is corroded quite rapidly by the concentrated acid. At 25°C, iridium is unattacked by water, solutions of caustic alkalis, acids and oxidising agents, including aqua regia. Ruthenium is less noble than the three other platinum metals. Although ruthenium is not attacked by water or non-complexing acids, it is easily corroded by oxidising alkaline solutions, such as peroxides and alkaline hypochlorites.

The solutions used in this work were 5 wt-%HCl (pH −0·11), 15 wt-%HCl (pH −0·52) and 25 wt-%HCl (pH −0·62). In these conditions, titanium and aluminium of the matrix and the precious metal rich phase



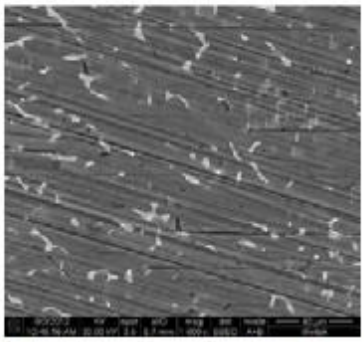
13 Image (SEM-BSE) of surface of TiAl–1·0 at-%Pt after potentiodynamic scan in 25 wt-%HCl solution

were expected to be dissolved, leaving behind particles of high precious metal content on the surface (Fig. 13). The EDX results revealed that the precious metal content in these particles was very high (Table 7), suggesting that these particles were losing titanium and aluminium by dissolution. The poor corrosion resistance performance observed with titanium aluminide alloyed with ruthenium is in agreement with the conclusion made by Pourbaix *et al.*[29] that ruthenium was less noble than the other PGMs and more easily corroded. In terms of the cathodic modification process, even though the corrosion potential of Ti–47·5 at-%Al was shifted to the passive region by the addition of ruthenium, the exchange current density was very high, explaining the high corrosion rate observed in TiAl–1·0 at-%Ru.

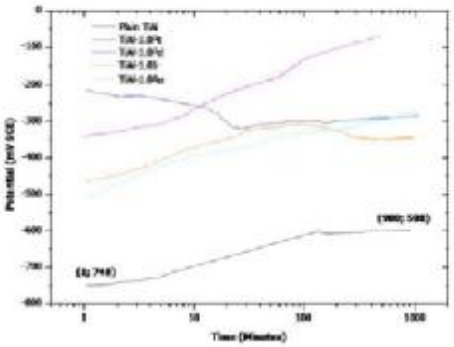
The shift of corrosion potentials to nobler values was attributed to the accumulation of precious metals on the surface of TiAl alloys, which simultaneously improved the hydrogen evolution efficiency and inhibited anodic dissolution.[16] To confirm these explanations, SEM and EDX were conducted on the corroded surfaces to evaluate the precious metal content on the surfaces of alloys subjected to potentiodynamic scans in 25 wt-%HCl solution. The corrosion tests corresponded to an exposure of samples to 25 wt-%HCl solutions for 180 min, 30 min of which were in OCP. The EDX results are shown in Table 8, and the SEM images are shown in Figs. 13 and 14 for Pt alloyed TiAl and Pd alloyed TiAl respectively. Overall, there was an increase in PGM content on the surface of the different TiAl alloys, from 1·0 at-% in the as cast alloys to a maximum of 2·7 at-% for Ru alloyed TiAl. Typical bright phase particles of

Table 7 Energy dispersive X-ray spectroscopy analysis of light particle phases on corroded surface of different alloys

	Precious metal content in light/high intensity particles of different alloys/at-%			
Elements	TiAl–1Pt	TiAl–1Pd	TiAl–1Ir	TiAl–1Ru
Al	44·7	45·3	50·4	43·3
Pt	13·7	…	…	…
Pd	…	8·8	…	…
Ir	…	…	4	…
Ru	…	…	…	13
Ti	41·6	45·9	45·6	43·7
Total	100	100	100	100



14 Image (SEM-BSE) of surface of TiAl–1·0 at-%Ir after potentiodynamic scan in 25 wt-%HCl solution



15 Open circuit potential curves for Ti–47·5 at-%Al alloyed with various PGMs tested in 5 wt-%HCl

high PGM content are shown in Fig. 16 for Pt alloyed TiAl. Similar microstructures were observed when palladium and iridium were added to plain TiAl. The PGM content on the surfaces of the different alloys in Table 8 shows a clear increase, confirming that an accumulation in precious metal took place on the surfaces during the corrosion process. Iridium alloyed TiAl showed the lowest increase, which is in agreement with the moderate effect of the HCl concentration on its corrosion rate and the low amount of pits observed on the corroded samples (Fig. 14).

Open circuit potential measurements

The OPC tests were run for 15 h, during which the samples were exposed to a 5 wt-%HCl solution. The results of the tests are presented in Fig. 15 and Table 9, where the corrosion potential (mV) is reported as a function of time (min) in an open circuit. The general trend was a continuous increase in the corrosion potential with time to a value between −350 and −200 mV, suggesting that the samples became less active. Titanium aluminide alloyed with palladium showed a large decrease in corrosion potential in the first 30 min, indicative of an increase in activity, followed by a continuous increase up to the end of the test. The corrosion potential at the end of the test remained low at −286 mV after 15 h. Even though TiAl with palladium showed a potential decrease from 0 to −30 min, the decrease remained higher than −350 mV, which was well above all the other corrosion potentials observed at 1 min. At that time, the corrosion potential was −500 mV for TiAl alloyed with ruthenium, −341 mV for TiAl alloyed with platinum and −466 mV for TiAl alloyed with iridium. Platinum alloyed TiAl showed a very high increase in corrosion potential and was above −100 mV after 15 h of exposure. This behaviour is in agreement with the high corrosion rate observed with this alloy during potentiodynamic scan in 25 wt-%HCl. An exposure to a relatively less aggressive solution for a long time would lead to the same results as an exposure to a more aggressive solution for a short period of time. Iridium and palladium alloyed TiAl showed small variation of OCP with time, indicating that the addition of iridium and palladium to TiAl resulted in an alloy that showed some stability towards the solution. This observation is consistent with the low variations in corrosion rate observed in these alloys (Fig. 12).

The shift of OCP towards nobler or less active potentials before stabilising is usually attributed to the progressive formation of a passive oxide film on the sample surface during immersion. Stabilisation at active potentials is due to the breakdown of the passive film as dissolution takes place. The tested samples did not exhibit

Table 8 Energy dispersive X-ray spectroscopy analysis of alloy surface after potentiodynamic tests in 25 wt-%HCl solution

	Surface composition after corrosion test/at-%					
Alloy	Al	Ti	Pd	Pt	Ir	Ru
TiAl–1Pd	52·6±1·7	45·0±1·4	2·4±0·3	…	…	…
TiAl–1Pt	49·9±0·1	48·9±0·1	…	1·2±0·1	…	…
TiAl–1Ir	50·1±0·5	48·8±0·4	…	…	1·2±0·1	…
TiAl–1Ru	39·3±3·6	58·0±3·1	…	…	…	2·7±0·6

Table 9 Starting and finishing OCPs

	Open circuit potential/mV(SCE)		
Alloy	Potential start at 1 min	Potential end at 900 min	Potential variation/mV(SCE)
Plain TiAl	−748	−598	150
TiAl–1Pt	−341	−70	271
TiAl–1Pd	−214	−286	−72
TiAl–1Ru	−510	−285	225
TiAl–1Ir	−466	−340	126

potential stabilisation but rather a continuous increase in potential. The continuous increase in OCP was due to the accumulation of precious metal on the surface of the samples. As the amount of precious metal increased, the OCP shifted to nobler values. However, the displacement of OCPs to values in excess of the passivation potential of the plain Ti–Al alloy into its passive range was an indication that there was a secondary process of spontaneous passivation and oxide film formation, or at least partial oxide formation, also at play and contributing to the displacement of the corrosion potentials of the alloys containing PGMs to more noble values.

Conclusions

Titanium aluminide of composition Ti–47·5 at-%Al has a duplex microstructure consisting of lamellar (α_2 and γ alternating lamellae) and γ-TiAl phase grains. The introduction of 1·0 at-% PGMs (platinum, palladium and iridium) resulted in the formation of a new phase, developing more in the γ-TiAl phase grains and an improvement of the corrosion resistance by cathodic modification.

The cathodic modification was achieved in solutions of low acidic concentration. Platinum, palladium and iridium additions to the TiAl alloy gave good result of modification of the cathodic process corresponding to a spontaneous passivation of the TiAl alloy. In solutions of high acidic concentration, the addition of PGMs shifted the cathodic process in the transpassive region, resulting in the dissolution of the alloy. The cathodic modification of PGM alloyed TiAl occurred as a result of PGM accumulation on the surface of the TiAl alloys, which simultaneously improved hydrogen evolution efficiency and inhibited anodic dissolution.

Acknowledgements

The authors would like to thank the Department of Science and Technology, Advanced Metals Initiative-Precious Metals Development Network and Mintek for permission to publish this work and financial support, and Wits for hosting the project. L.A. Cornish would like to thank the National Research Foundation.

References

1. H. A. Lipsitt: 'Titanium aluminides – an overview', *Mater. Res. Soc. Symp. Proc.*, 1984, **39**, 351–365.
2. J. H. Westbrook and R. L. Fleischer(eds): 'Intermetallic compounds, principles and practice', 2, Chap. 2, 91–131; 1995, Chichester, John Wiley & Sons Ltd.
3. J. H. Westbrook and R. L. Fleischer(eds): 'Intermetallic compounds, principles and practice', 2, Chap. 2, 73–90; 1995, Chichester, John Wiley & Sons Ltd.
4. J. H. Westbrook and R. L. Fleischer(eds): 'Intermetallic compounds, principles and practice', 2, Chap. 2, 147–173; 1995, Chichester, John Wiley & Sons Ltd.
5. S. Djanarthany, J.-C. Viala and J. Bouix: 'An overview of monolithic titanium aluminides based on Ti_3Al and TiAl', *Mater. Chem. Phys.*, 2001, **72**, (3), 301–319.
6. O. Rivera-Denizard, N. Diffoot-Carlo, V. Navas and P. A. Sundaram: 'Biocompatibility studies of human foetal osteoblast cells cultured on gamma titanium aluminide', *J. Mater. Sci., Mater. Med.*, 2008, **19**, (1), 153–158.
7. B. B. Zhang, Y. F. Zheng and Y. Liu: 'Effect of Ag on the corrosion behaviour of Ti–Ag alloys in artificial saliva solutions', *Dent. Mater.*, 2009, **25**, 672–677.
8. S. A. Bello, I. Maldonado, E. Rosim-Fachini, P. A. Sundaram and N. Diffoot-Carlo: 'In vitro evaluation of human osteoblast adhesion to a thermally oxidized γ-TiAl intermetallic alloy of composition Ti–48Al–2Cr–2Nb (at.%)', *J. Mater. Sci., Mater. Med.*, 2010, **21**, 1739–1750.
9. C. S. Brossia and G. A. Cragnolino: 'Effects of environmental and metallurgical conditions on the passive and localised dissolution of Ti-0·15%Pd', *Corrosion*, 2001, **9**, 768–779.
10. A. A. Trufanov, K. B. Katsov and M. V. Chervonyi: 'Effect of Ni and Mo additions on the corrosion-mechanical properties of Ti–Al alloy', *Khimiral' Prod. Org. Kal.*, translated from *Fiziko-khimicheskaya Mekhanika Materialov*, 1989, **25**, (3), 28–32.
11. E. Van der Lingen and R. F. Sandenbergh: 'The cathodic modification behaviour of ruthenium additions to titanium in hydrochloric acid', *Corros. Sci.*, 2001, **43**, 577–590.
12. R. F. Sandenbergh and E. van der Lingen: 'The use of Tafel back extrapolation to clarify the influence of ruthenium and palladium alloying on the corrosion behaviour of titanium in concentrated hydrochloric acid', *Corros. Sci.*, 2005, **47**, 3308–3311.
13. R. W. Schutz: 'Ruthenium enhanced titanium alloys', *Platinum Met. Rev.*, 1996, **40**, (2), 54–61.
14. T. P. Hoar: 'Increasing the resistance of titanium to non-oxidising acids, influence of addition of platinum metals', *Platinum Met. Rev.*, 1960, **4**, (2), 59–64.
15. R. Cottis, M. Graham, R. Lindsay, S. Lyon, T. Richardson, D. Scantlebury and H. Stott(eds): 'Shreir's corrosion', 1st edn, 3, 'Corrosion and degradation of engineering materials', Chap. 3, 22, 'Corrosion of passive alloys: the effect of noble metal addition', 2224–2249; 2010, Amsterdam, Elsevier.
16. J. H. Potgieter and H. C. Brookes: 'Corrosion behaviour of a high-chromium duplex stainless steel with minor additions of ruthenium in sulfuric acid', *Corrosion*, 1995, **51**, (4), 312–320.
17. P. A. Olubambi, J. H. Potgieter and L. A. Cornish: 'Corrosion behaviour of superferritic stainless steels cathodically modified with minor additions of Ru in sulphuric and hydrochloric acid solutions', *Mater. Des.*, 2008, **30**, (5), 1451–1457.
18. P. Monnartz: 'The study of the Fe–Cr alloys with particular regard to their solubility toward acids', *Metall.*, 1911, **8**, 161–176 and 193–209.
19. M. A. Streicher: 'Alloying stainless steel with the platinum metals increased resistance to corrosion in acids', *Platinum Met. Rev.*, 1977, **21**, (2), 51–55.
20. I. R. McGill: 'Platinum metals in stainless steels', *Platinum Met. Rev.*, 1990, **34**, (3), 144–154.
21. Y. H. Kim and G. S. Frankel: 'Effect of noble metal alloying on passivity and passivity breakdown of nickel', *J. Electrochem. Soc.*, 2007,**154**, 36–42.
22. 'Standard practice for conventions applicable to electrochemical measurements in corrosion testing', G 3, 'Annual book of ASTM standards', ASTM, Philadelphia, PA, USA, 1985.
23. 'The titanium-aluminium (Ti-Al) phase diagram calculated with Thermo-Calc software, coupled with SSOL2 thermodynamic database'. http://www.calphad.com/pdf/Ti_Al_Phase_Diagram_Atomic_Pct_Celsius.pdf (accessed 22 Jun 2011).
24. A. Khataee, H. M. Flower and D. R. F. West: 'The alloying of titanium aluminides with ruthenium', *Platinum Met. Rev.*, 1989, **33**, (3), 106–113.
25. H. M. Saffarian, Q. Qian, R. Hudkar and G. W. Warren: 'Corrosion behaviour of binary titanium aluminide intermetallics', *Corros. Sci.*, 1996, 626–633.
26. J. H. Potgieter, A. M. Heyns and W. Skinner: 'Cathodic modification as a mean of improving the corrosion resistance of alloys', *J. Appl. Electrochem.*, 1990, **20**, 711–715.
27. E. M. Sherif, JH. Potgieter, J. D. Comins, L. Cornish, P. A. Olubambi and C. N. Machio: 'Effects of minor additions of ruthenium on the passivation of duplex stainless-steel corrosion in concentrated hydrochloric acid solutions', *J. Appl. Electrochem.*, 2009, **39**, 1385–1392.
28. E. M. Sherif: 'Corrosion behaviour of duplex stainless steel alloy cathodically modified with minor ruthenium additions in concentrated sulfuric acid solutions', *Int. J. Electrochem. Sci.*, 2011, **6**, 2284–2298.
29. M. Pourbaix, N. de Zoubovand J. van Muylder(eds): 'Atlas d'équilibres électrochimiques', Chap. 4, 'Établissement et interprétation de diagrammes d'équilibres tension-pH', 343–383 ; 1963, Paris, Publication du Centre Belge d'Etude de la Corrosion.

Milling of titanium hydride powder and aluminium for the production of TiAl with ruthenium additions

I.A. Mwamba* and L.A. Cornish†
*Mintek
†University of the Witwatersrand

Titanium aluminide alloy powder of composition Ti-47.5% at.Al-*x* at.% Ru (*x*=0, 0.2, 0.5, 1.5) was prepared by milling titanium hydride powder or titanium elemental powder together with aluminium elemental powder and ruthenium sponge powder. The mechanically alloyed powder was characterized for apparent density, particle size and size distribution, particle morphology, microstructure, transformations upon heating, and high-temperature oxidation behaviour.

It was established that TiAl alloy can be prepared by milling. The mechanically alloyed powders had an apparent density around 1.0 g/cm^3. The use of titanium hydride resulted in angular and rounded particles with a bimodal distribution due to a high level of agglomeration. Fine particles, smaller than 1 µm across were obtained, and they either agglomerated to form larger particles or became satellites to large particles. The use of elemental titanium powder resulted in flake-like particles showing a monomodal distribution with a large mean diameter. The addition of ruthenium improved the high-temperature oxidation behaviour of the TiAl alloy powders. Heating to 1000°C in air resulted in the formation of TiAl, Ti_2AlC, Al_2O_3, and TiO_2 for the ruthenium-free powder and powder containing 0.2 at % ruthenium. In addition to these phases, powders containing 0.5 at.% Ru or more showed also RuAl and a ternary phase close to $Ti_xRu_yAl_{10}$.

Introduction

Titanium aluminide TiAl is a component of alloys that have been under extensive investigation over the last three decades because they have potential as aerospace materials[1-2]. This is due to their highly refractory nature, low densities, high specific strength, high melting temperature, and environmental resistance at elevated temperatures[3-4]. Breakthroughs in the investigation of the TiAl have been accomplished, leading to very interesting applications. However, many obstacles need to be overcome to achieve widespread production and applications of these interesting alloys. Among the difficulties hindering the use of titanium aluminides are the difficulties in synthesizing these alloys by the traditional method of melting and casting, resulting in the exploration of other production techniques such as mechanical alloying[5]. Casting leads to segregation and poor mechanical properties[1,5].

Data available on the synthesis of titanium aluminides and other aluminides indicates that most mechanically alloyed powders were produced from elemental powders of titanium, iron, and nickel in combination with aluminium[6-7]. A work by Ivasishin *et al.*[8] showed that the use of titanium hydride, instead of elemental titanium in powder mixtures with aluminium, resulted in a significant activation of diffusion, and led to an accelerated production of single-phase titanium aluminides upon isothermal heating. Titanium hydride was also successfully used to prepare a $TiAl_3$ alloy[9]. The transformations during synthesis included phase formation, total or partial amorphization and particle size reduction down to the nanometer scale[6,10,11].

In this work, titanium aluminide alloys powder of composition Ti–47.5% at.Al-*x* at.% Ru (*x*= 0, 0.2, 0.5, 1.5) and Ti-47.5% at.Al 0.2 at.% Pt were prepared by milling titanium hydride powder or titanium elemental powder together with elemental aluminium powder and ruthenium or platinum sponge powder. This composition range was chosen to see the effect of ruthenium or platinum in solid solution and after precipitation in new phases. The mechanically alloyed powder was characterized for apparent density, particle size and size distribution, particle morphology, microstructure, transformations upon heating, and high temperature oxidation behaviour.

Experimental procedure

Powder preparation

Titanium hydride powder (TiH_2) of 98.0% purity and –44 μm, elemental aluminium powder of 99.7% wt.% purity and 57 μm mean size, and precious metal sponge powder were mixed in a planetary mill for 15 minutes with 6.0 wt % stearic acid as the process control agent (PCA). The total weight of the powders and the process control agent was 106 g. The mixing was done to achieve the atomic proportions shown in Table I.

The powder mixture was then transferred into a grinding jar containing 800 g of 20 mm diameter stainless steel ball's and 200 g of 10 mm diameter stainless steel (Hardened & Tempered Stainless Chromium Steel - BS 420S37) balls giving a ball to powder ratio (BPR) of 10. The powder transfer into the grinding mill was carried out in glove box under an argon atmosphere.

The mixtures of titanium hydride powder (TiH_2), elemental aluminium powder and precious metal powder were then milled together in a Retsch Mill Machine PM100, the target material being γ-TiAl and named as follows:

- TiH_2 Al 15: titanium hydride aluminium powder milled for 16 hours
- TiH_2 Al 20 0.2 at.% Ru: titanium hydride aluminium powder milled for 20 hours with 0.2 at.% Ru addition
- Ti-Al-20-0.2 at.% Pt: titanium aluminium powder milled for 20 hours with 0.2 at.% Pt addition
- TiH_2 Al 32 *x* at.% Ru: titanium hydride aluminium powder milled for 32 hours with *x* at.% Ru addition (*x* – 0.5, 1.0 and 2.0).

In this work, mechanically alloyed powder is referred to as MA powder.

Table I. Elemental composition of the alloys

Compound	Content (at.%)			
	Ti	Al	Ru	Pt
Plain TiAl	52.5	47.5	-	-
Ru-containing TiAl (Pt-containing TiAl)	52.3	47.5	0.2	(0.2)
Ru-containing TiAl	52.0	47.5	0.5	-
Ru-containing TiAl	51	47.5	1.5	-
Ru containing TiAl	50.5	47.5	2.0	

The different MA powders were subjected to heat treatment at 900°C for 1 hour. The temperature 900°C was chosen as holding temperature because it is within the temperature range where good diffusion was expected to take place.

Powder characterization

Properties characterized were apparent density, particle size, size distribution, particle morphology, and chemical composition. The apparent densities of the different mixtures were determined using the Arnold apparent density meter. The size and size distribution of powder particles was determined by laser diffraction using a Malvern Mastersizer00 2000 in the size range of 0.02 2000 μm with water as the dispersant. The particle shapes were determined by scanning electron microscopy (SEM) on the FEI Nova NanoSEM®. The XRD analyses were conducted with a PANalytical X'Pert Pro powder diffractometer with X'Celerator detector and variable divergence and fixed receiving slits with Fe filtered Co Kα radiation. The chemical composition of the powders and phases was determined using a combination of X ray diffraction (XRD) and energy dispersive X ray spectroscopy (EDX).

The mechanical alloying process was evaluated by a combination of XRD and differential scanning calorimetry (DSC). The high-temperature transformation and oxidation behaviour of the MA powders was assessed by thermogravimetric analysis (TGA). The DSC and TGA were conducted in a Netzsch STA 429 instrument.

Results and discussion

Powder characterisation

Apparent density

The apparent density of powder was 1.06 +0.04 g/cm^3 for the powder obtained by milling aluminium with titanium hydride, and 0.96 +0.03 g/cm^3 for MA powder obtained by milling aluminium with elemental titanium powder. Since the apparent density is highly dependent of the packing of the powder particles, it was anticipated that packing in the

powder obtained with titanium hydride powder would be better than packing obtained with elemental titanium powder. Low apparent densities are also known to occur in powder with a very narrow size distribution, and high densities in powder with wide size distribution or a bimodal distribution[14-16].

Particle size and size distribution

For the different MA powders, typical statistical parameters of the size distribution are given in Table II and the particle distribution curves are given in Figures 1 to 3.

Table II. Statistical parameters of the particle size distribution in different MA powders

Statistical parameters	Powder			
	Plain TiH_2-Al 16	Ti-Al 20- 0.2 at.%Pt	TiH_2-Al 20- 0.2 at.%Ru	TiH_2-Al 32-1.0 at.% Ru
$D[1,3]$, μm	65	161.7	180	149
$D[3,2]$, μm	18	63.3	21	19
d_{10}μm	8	30.9	7	5
d_{50}μm	31	103.8	113	108
d_{90}μm	140	380.2	471	371
Specific surface area, m^2/g	0.337	0.092	0.264	0.389

where:

- $D^{[4,3]}$: volume moment mean or De Brouckere Mean Diameter reflects the size of those particles which constitute the bulk of the sample volume. It is most sensitive to the presence of large particulates in the size distribution
- $D^{[3,2]}$: Sauter mean diameter, defined as the diameter of a sphere that has the same volume/surface area ratio as a particle of interest
- d_{10}: 10 wt% of the particles are smaller than d_{10} and 90 wt% are larger than d_{10}
- d_{50}: Also known as median diameter or medium value of particle diameter is a particle diameter or size value in case where a cumulative distribution percentage reaches 50%. 50 wt% of the particles are smaller than d_{50} and 50 wt% are larger than d_{50}.
- d_{90}: 90 wt% of the particles are smaller than d_{90} and 10 wt% are larger than d_{90}.

The shapes of curves indicated the trend of the particle size in the powders obtained with titanium hydride. The three powders showed a trend to a bimodal distribution, due to the agglomeration in the powders. In plain TiH_2 Al 16 powder, even though the curve showed a bimodal distribution, there were more fine particles than coarse particles (Figure 1 and Table II).

The TiH_2 Al 20 0.2 at.% Ru powder showed the highest peak towards coarse particles, indicating a large amount of agglomeration. TiH_2 Al 20 0.2 at.% Ru had more agglomerated particles than the plain TiH_2 Al 16 (Table II and Figure 2).

The powder prepared with elemental titanium powder (Ti Al 20 0.2 at.% Pt) showed a monomodal distribution, with large mean diameter, indicative of high agglomeration (Table II and Figure 3). The agglomeration effect was confirmed by the high value of the Sauter mean diameter and the low value of the specific surface area. The agglomeration and flattening of particles is believed to be the result of extensive smearing and cold welding of small particles, typical to ductile metals such as titanium and aluminium.

Powder TiH_2-Al 32-0.5 at.% Ru showed a trend similar to TiH_2-Al 16-0.2 at.% Ru (Table II and Figure 4). The powder obtained after 32 hours of milling gave the highest specific surface area, indicating the presence of more fine particles. After 32 hours milling, similar data were obtained with MA powders from TiH_2 and aluminium with addition of 1.0 and 2.0 at.% Ru.

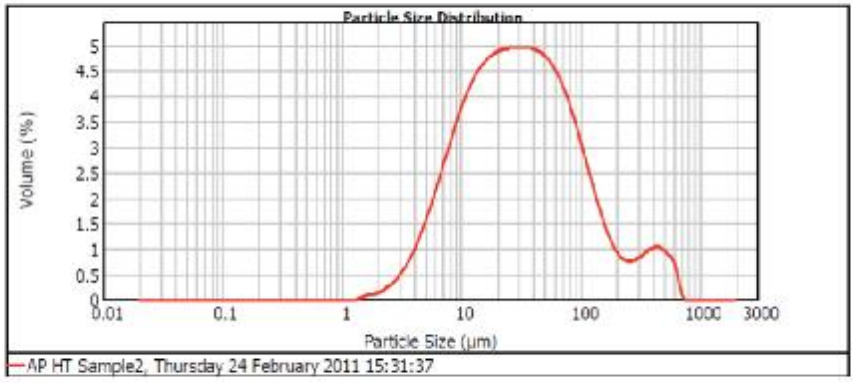


Figure 1. Particle size distribution of plain powder TiH_2-Al 16

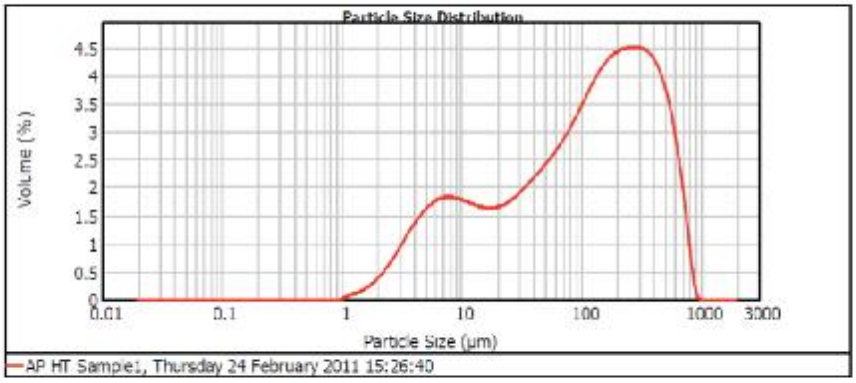


Figure 2. Particle size distribution of powder TiH_2-Al 20- 0.2 at.% Ru

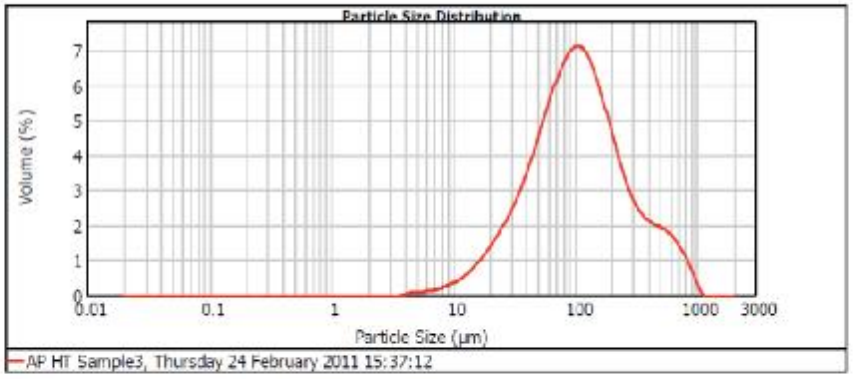


Figure 3. Particle size distribution of powder Ti-Al-20-0.2 at.% Pt

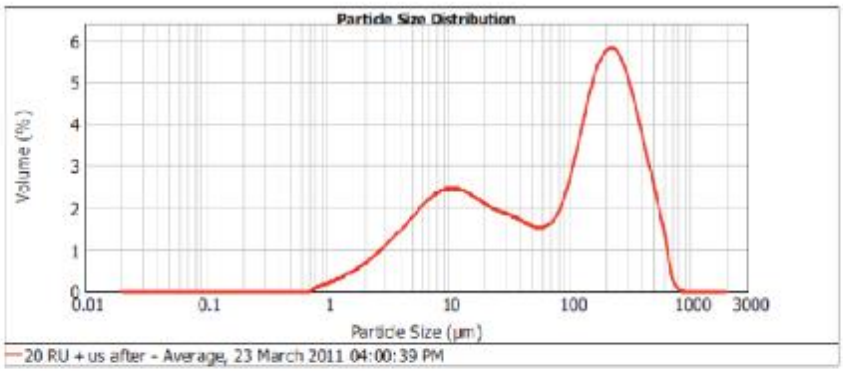
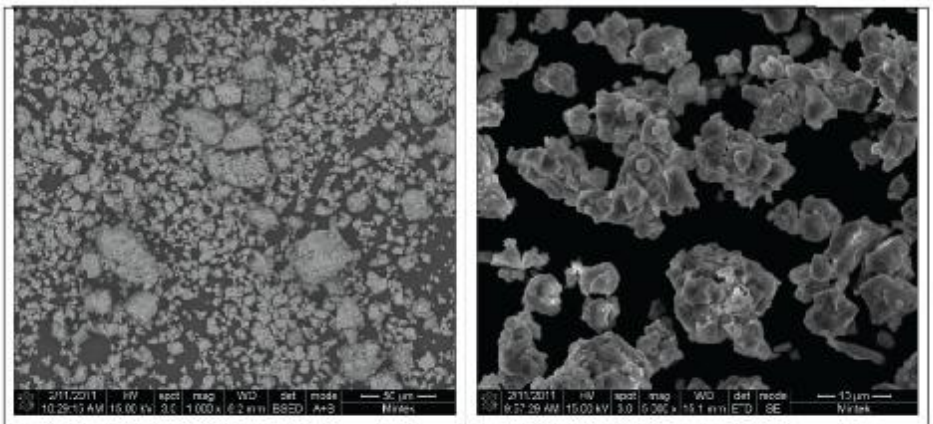


Figure 4. Particle size distribution of powder TiH2-Al 32-9.5 at% Ru

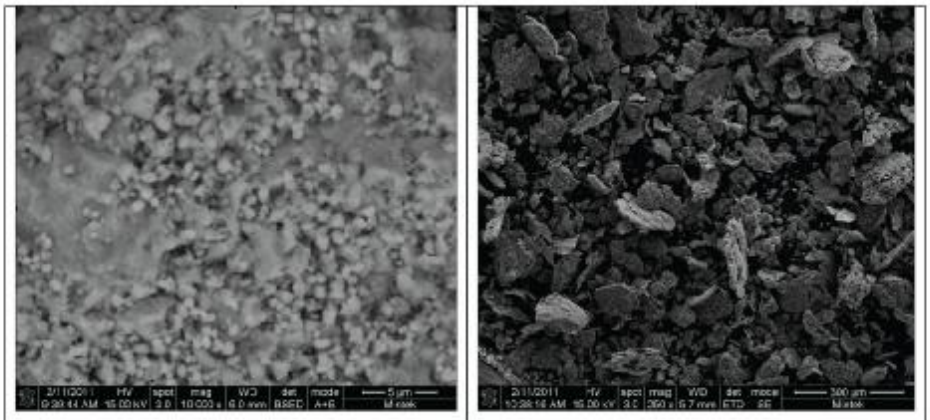
Particle morphology

The morphology of particles in the different powders is shown in Figures 5 to 7. These micrographs indicate that, in the cases of MA powders from TiH_2 and Al, the powders consisted of very fine particles of mostly rounded irregular shape. Angular shapes were also visible. Many individual particles were smaller than 1 μm. In the midst of the fine particles were large particles with size varying from 50 to 500 μm (Figure 1). The large particles were agglomerates of fine particles (Figures 5, 6a, and 7). Particles in the MA powder from elemental Ti and Al powder were flaky with a noticeable appearance of smearing (Figure 6b). The difference in morphology of the particles in the two powders was due to the brittleness of titanium hydride particles and the softness and ductility of pure titanium particles. Titanium hydride particles readily broke into smaller rounded irregular particles while pure titanium smeared and flattened.



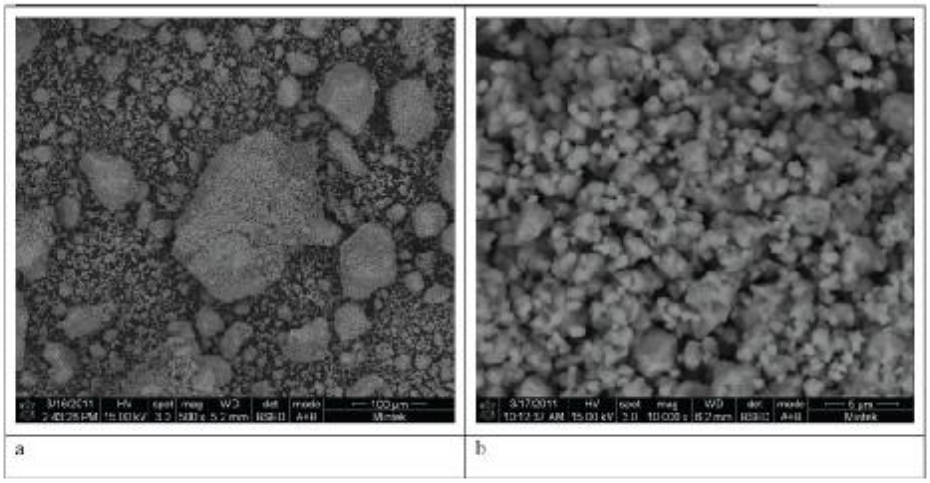
a b

Figure 5. Typical SEM micrographs (a-BSE and b-SE) of plain TiH2-Al 16 powder



a b

Figure 6. Typical SEM micrographs (a-BSE and b-SE) of (a)TiH2-Al 20-0.2 at.% Ru and (b) Ti-Al 20-6.2at.% Pt.



a b

Figure 7. Typical SEM-BSE micrographs of MA TiH2-Al 32 powder.

Phase identification

Phases formed during mechanical alloying and after heat treatment of mechanically alloyed powders were determined by a combination of XRD and EDX analyses. The results of EDX are summarized in Tables III and IV. The results of XRD analyses are presented in Figures 8 to 15.

In all cases, the as-mechanically alloyed powders showed XRD patterns with expected broad peaks, indicative of small crystallites in the powder particles, as a result of the milling. The formation of the target alloy was difficult to observe as it was difficult to identify with accuracy any expected phases and other phases formed concurrently during milling.

The as mechanically alloyed TiH_2 Al 20 0.2 at.% Ru (Figure 8) did not show either Ti_3Al (α_2) or γ TiAl, although the titanium and TiH_2 broad peaks were still visible. No aluminium peak was visible, indicating the dissolution of aluminium in titanium. The XRD pattern also showed the presence of Al_2O_3 as the result of reaction with oxygen in the air. The oxygen is believed to have contaminated the powder during milling and/or handling operations.

After heat treatment at 900°C for 1 hour and furnace cooling, the XRD pattern of the TiH_2 Al 20 0.2 at.% Ru powder (Figure 9) showed very narrow peaks of TiAl, indicative of crystallization. Peaks of aluminium-titanium carbide $AlCTi_2$ were also visible. $AlCTi_2$ was formed by the reaction between:

$$Ti_3Al + C \rightarrow AlCTi_2$$

Carbon was present as a result of contamination by the carbon of the stearic acid which was used as the process control agent (PCA). Stearic acid is a fatty acid with an 18 carbon chain, whose molecular formula is $C_{18}H_{36}O_2$ and the structural formula is $CH_3(CH_2)_{16}COOH$. The contamination by the PCA was inevitable, as milling could not be conducted without PCA.

No ruthenium or ruthenium containing phase peaks were visible in as mechanically alloyed or heat treated TiH_2 Al 20 0.2 at.% Ru powders, suggesting that at 0.2 at.% Ru, all the ruthenium was in solid solution. The appearance of TiAl peaks on the XRD pattern of the heat treated powder was due to the doubled diffusion of aluminium and titanium that led to the transformation of the titanium solid solution of aluminium into TiAl crystals and the subsequent growth of these crystals.

The presence of $AlCTi_2$ was confirmed by EDX analysis, which showed the presence of carbon in all the powders after heat treatment (Table III). EDX also showed the presence of Fe, Cr, and Ni in the powder, even though no peaks of phases containing those elements were visible on the XRD patterns. This was an indication that these elements were in solid solution, both in the as mechanically alloyed and the heat treated powders. Iron, chromium and nickel originated from the grinding media used in the milling process. These grinding balls were made of nickel chromium stainless steel and so contamination with Fe, Cr and Ni could be expected, in mechanical alloying, and the level of contaminants increases with milling time[8]. This was the case in this work, as shown in Table III. The level of Fe increased from 1.2 at.% in powder milled for 20 hours to almost 4 at.% after a milling for 32 hours. The level of chromium and nickel increased from 0.4 at.% after milling for 20 hours to 0.7 and 0.9 at.% after a milling time of 32 hours. Thus, the contaminant content increased with milling time.

As the ruthenium content in the powders increased, ruthenium-containing phases appeared on the XRD patterns. At 0.2 at.% Ru, the XRD patterns did not show any ruthenium-containing phase peak in as-mechanically alloyed condition and after heat treatment (Figures 8 and 9). At 0.5, 1.0 and 2.0 at. % Ru, the XRD patterns of the heat treated powders show RuAl and $Ti_2Ru_xAl_{10}$ peaks (Figures 11, 13, and 15).

The XRD patterns of as MA TiH_2 Al 32 2.0 at.% Ru were similar to the patterns of other powders after milling, and showed Ti, TiH_2, Al_2O_3 and Ru peaks after milling (Figure 14). After heat treatment, the MA TiH_2-Al 32- 2.0 at.% Ru powder showed TiAl, Ti_3Al, RuAl and $Ti_6Ru_xAl_{16}$ peaks (Figure 15). The $Ti_6Ru_xAl_{16}$ peak was not clearly visible. AlN and TiN peaks were also present, showing the formation of these compounds during heat treatment. AlN and TiN are believed to be the result of air contamination during heat treatment.

The MA powder Ti-Al-20-0.2 at.%Pt powder prepared from elemental powders of titanium and aluminium gave an XRD pattern where Ti, Al and Pt peaks were visible in the as-mechanically alloyed condition (Figure 16). After heat treatment, the XRD pattern showed Ti_3Al, $AlCTi_2$ and TiAl peaks (Figure 17). The absence of Pt peaks in the heat treated powder was an indication that Pt was entirely in solid solution. The XRD patterns of as mechanically alloyed TiH_2 Al powders milled for 16, 20 and 32 hours showed broad peaks, typical of small crystallites and the beginning of amorphization.

A typical microstructure of heat treated TiH_2-Al 32-2.0 at.% Ru powder is shown in Figure 18. A Ru-containing phase is visible as white fine particles on agglomerate particles. The fine particles were in a sintered condition at 900°C.

The contaminants listed in Table III were left out to give only titanium, aluminium, and Ru as constitutive elements. The results of the modified composition are reported in Table IV. From Table IV and the phase diagram in Figure 19, the microstructure of all the particles analysed consisted of Ti_3Al and γ-TiAl as the composition fell in the range 40-50 at.% Al., corresponding to the dual phase region[17].

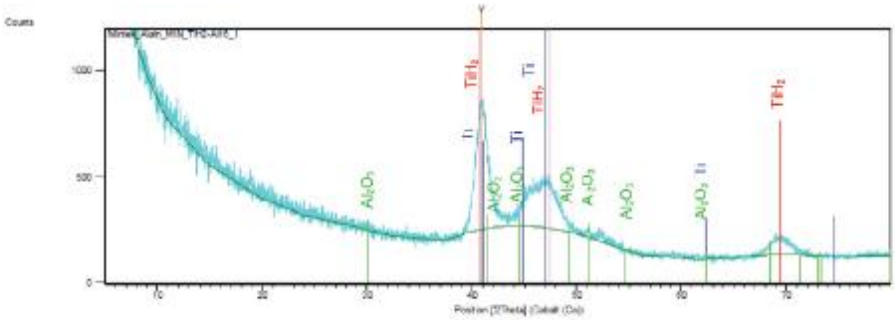


Figure 8. XRD patterns of mechanically alloyed TiH_2-Al 20-0.2 at.% Ru powder showing Al_2O_3, Ti and TiH_2 peaks

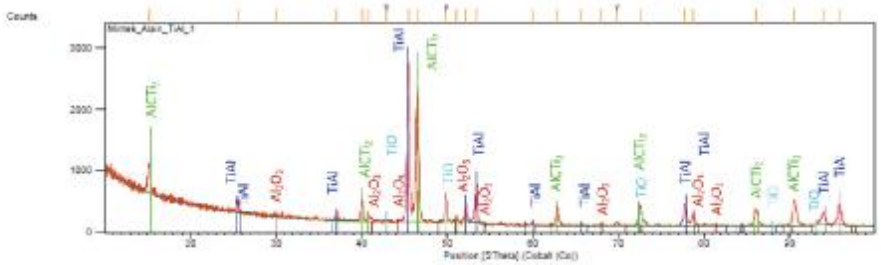


Figure 9. XRD patterns of TiH_2-Al 20-0.2 at.% Ru powder after heat treatment showing Al_2O_3, $AlCTi_2$, TiAl and TiO peaks

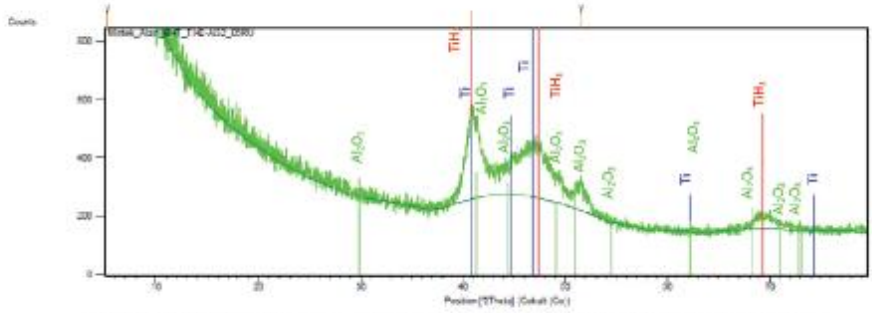


Figure 10. XRD patterns of mechanically alloyed TiH_2-Al 32-0.5 at.% Ru powder showing Al_2O_3, Ti and TiH_2 peaks

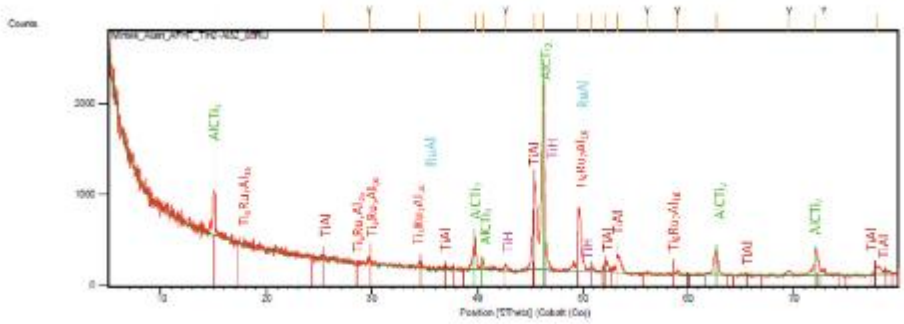


Figure 11. XRD patterns of TiH_2-Al 32 0.5 at.% Ru powder after heat treatment showing TiAl, $AlCTi_2$, and $Ti_5Ru_2Al_{10}$ peaks

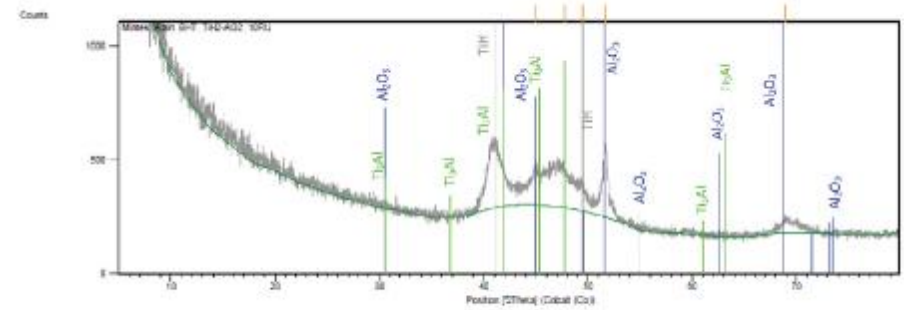


Figure 12. XRD patterns of mechanically alloyed TiH_2-Al 32-1.6 at.% Ru powder showing Al_2O_3, Ti_3Al and TiH peaks

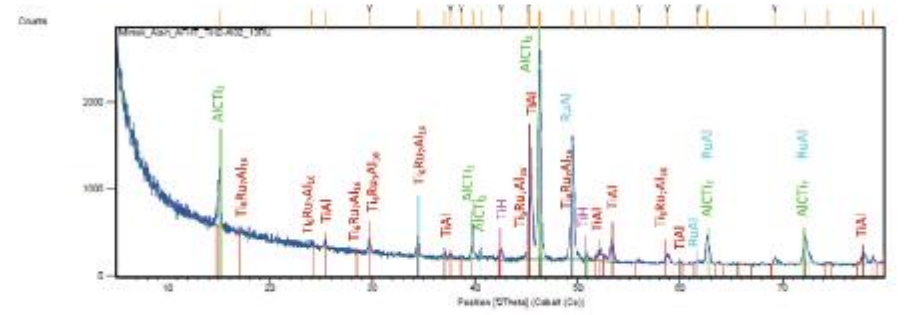


Figure 13. XRD patterns of TiH_2-Al 32-1.6 at.% Ru powder after heat treatment showing TiAl, $AlCTi_2$, TiH, RuAl and $Ti_5Ru_2Al_{10}$ peaks

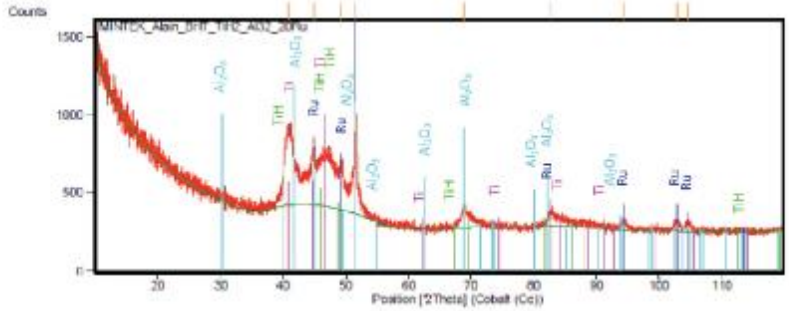


Figure 14. XRD patterns of mechanically alloyed TiH_2-Al 32-2.0 at.% Ru powder showing Al_2O_3, Ru, Ti and TiH peaks

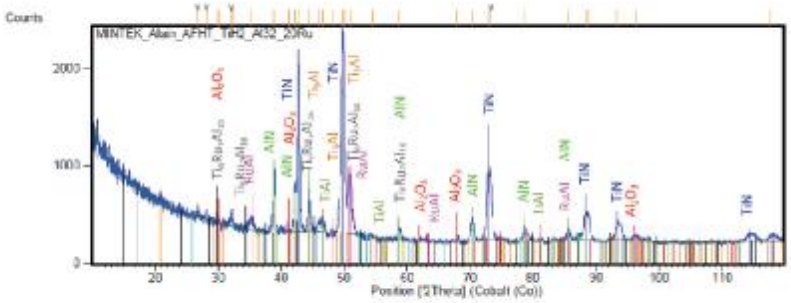


Figure 15. XRD patterns of TiH_2-Al32 2.0 at.% Ru powder after heat treatment showing TiN, Al_2O_3, TiAl and $Ti_6Ru_2Al_{36}$ peaks

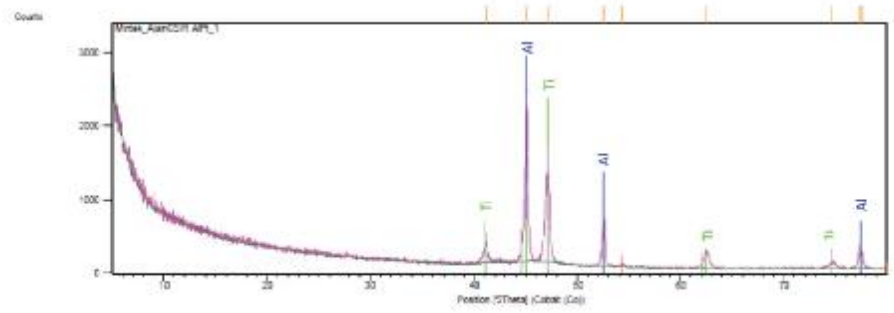


Figure 16. XRD patterns of mechanically alloyed Ti-Al-20-0.2 at.% Pt powder

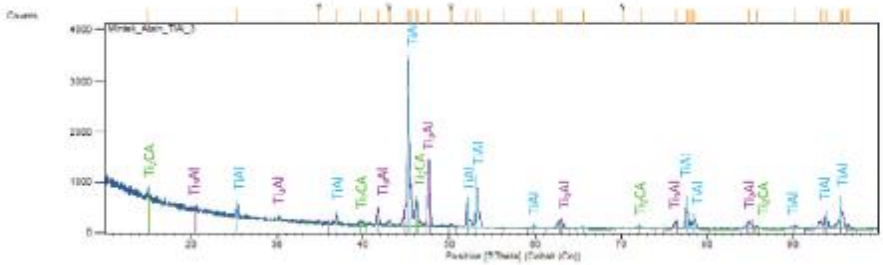


Figure 17. XRD patterns of Ti-Al-20-0.2 at.% Pt powder after heat treatment

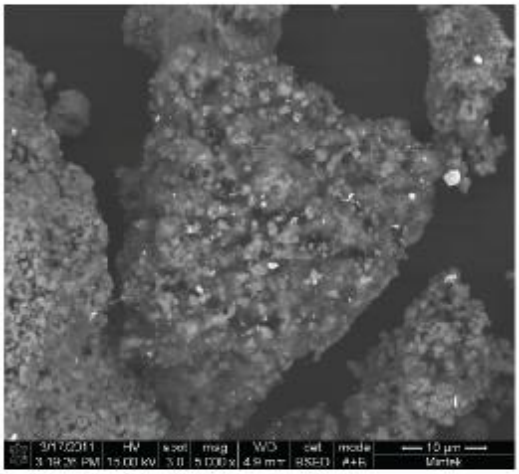


Figure 18. SEM-BSE image of agglomerate particles with white Ru-containing particles in heat treated TiH_2-Al32 2.0 at.% Ru powder

Table III. EDX analyses of the as-cast (BHT) and heat-treated (AHT) powders

Powder type	Composition (at.%)						
	Ti	Al	Ru or Pt	Fe	C	Cr	Ni
TiH_2-Al20 BHT	16.9±2.2	56.2±1.4	-	1.0±0.1	15.8±1.5	-	-
TiH_2-Al20 AHT	43.1±4.1	35.9±1.4		1.2±0.6	16.5±3.1		
TiH_2-Al16 0.2 at.%Ru BHT	47.4±6.5	33.2±4.6	0.11±0.1	2.05±0.3	16.8±2.9	0.4±0.1	0.4±0.1
TiH_2-Al16 0.2 at.%Ru AHT	43.5±3.6	37.0±2.1	0.1±0.03	1.7±0.3	17.2±2.2	0.3±0.1	0.3±0.1
TiH_2-Al32 0.5 at.%Ru BHT	44.1±2.1	31.3±4.0	1.1±0.1	3.9±0.6	17.7±2.1	0.9±0.1	0.7±0.1
TiH_2-Al32 0.5 at.%Ru AHT	43.2±3.9	34.3±1.4	0.4±0.04	3.3±0.2	17.8±2.3	0.8±0.05	0.5±0.07
TiH_2-Al32 1.0 at.%Ru BHT	41.7±3.5	32.6±2.5	1.1±0.1	3.7±0.4	19.4±2.1	0.9±0.08	0.6±0.1
TiH_2-Al32 1.0 at.%Ru AHT	41.0±5.4	35.2±3.0	0.7±0.2	3.7±0.3	19.9±2.7	0.9±0.2	0.6±0.1
TiH_2-Al32 2.0 at.%Ru BHT	44.0±7.1	31.9±3.8	1.5±0.1	4.2±0.6	16.7±5.2	1.0±0.1	0.8±0.1
TiH_2-Al32 2.0 at.%Ru AHT	29.1±2.7	45.4±6.6	1.1±0.3	2.4±0.4	17.5±4.1	0.6±0.2	0.3±0.03
TiAl-Pt20 0.2 at.%Pt BHT	44.7±2.4	33.3±2.7	0.2±0.01	2.5±0.8	16.4±2.5	0.5±0.1	0.4±0.1
TiAl-Pt20 0.2 at.%Pt AHT	45.7±2.3	33.4±5.0	0.20±0.02	2.7±0.7	16.5±1.5	0.8±0.3	0.6±0.2

Table IV. EDX analyses of the powders without contamination elements

Powder type	Composition (at.%)		
	Ti	Al	Ru or Pt
TiH_2-Al20 0 at.% Ru BHT	56.2±2.0	43.8±2.0	-
TiH_2-Al20 0 at.% Ru AHT	53.7±3.3	46.3±3.3	
TiH_2-Al16 0.2 at.% Ru BHT	58.2±8	41.7±8.0	0.1±0.01
TiH_2-Al16 0.2 at.% Ru AHT	59.6±6.0	40.2±6.2	0.2
TiH_2-Al32 0.5 at.% Ru BHT	58.5±4.7	40.1±4.5	1.4±0.3
TiH_2-Al32 0.5 at.% Ru AHT	54.5±1.1	45.0±1.1	0.5±0.1
TiH_2-Al32 1.5 at.% Ru BHT	56.2±3.2	42.3±3.2	1.5±0.1
TiH_2-Al32 1.5 at.% Ru AHT	53.0±4.0	45.9±3.5	1.1±0.3
TiH_2-Al32 2.0 at.% Ru BHT	57.4±6.4	40.6±5.3	2.0±0.1
TiH_2-Al32 2.0 at.% Ru AHT	38.1±5.2	60.4±5.5	1.5±0.4
TiAl-Pt 20 0.2 at.%Pt BHT	57.2±2.3	42.6±3.8	0.26±0.08
TiAl-Pt 20 0.2 at.%Pt AHT	57.6±3.2	42.1±2.7	0.4±0.2

Transformations upon heating and high-temperature oxidation behaviour

Transformations upon heating and high-temperature oxidation of the powders were examined by simultaneous differential scanning calorimetry (DSC) and thermogravimetric analysis (TGA) on the powders.

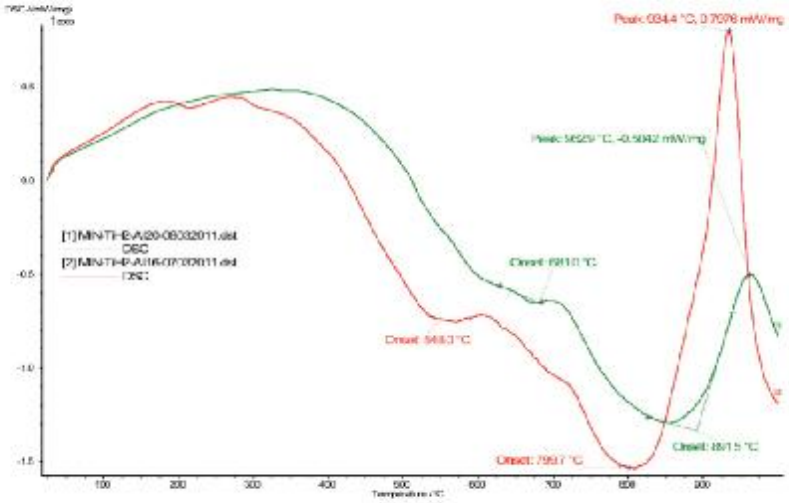
Figure 19 shows the curves of TiH_2 Al 16 and TiH_2 Al 20 0.2 at.% Ru and figure 20 shows the curves for TiH_2 Al 32 with addition of 0.5, 1.0 and 2.0 at.% Ru. The DSC curves in figures 19a and 20a showed a broad and shallow endothermic peak in the temperature range 500-520°C, which is taken to correspond to stress relaxation. As the temperature increased, there were two exothermic peaks in the range of 700-720°C and 910-980°C. The exothermic peaks observed in the 700-720°C range are believed to be from the formation of TiAl, Ti_3Al and Ti_2AlC. When formation of a new compound takes place from mechanically alloyed powder during heating in a DTA or DSC cell, the heat released gives rise to an exothermic peak[163]. This observation is consistent with the results of XRD analysis of heat treated powder, which exhibited TiAl, $TiCAl_2$ and TiAl, three phases that were absent in the mechanically-alloyed powder and were thought to have formed during heating of the powders. The peaks observed in the 910-980°C were from recrystallization taking place in the powder particles.

The absence of endothermic peaks corresponding to the melting point of aluminium indicated that after a nominal milling time of 16 hours, aluminium was in solid solution in titanium, in some cases, some residual TiH_2 or TiH as observed on the XRD patterns of the mechanically alloyed powders.

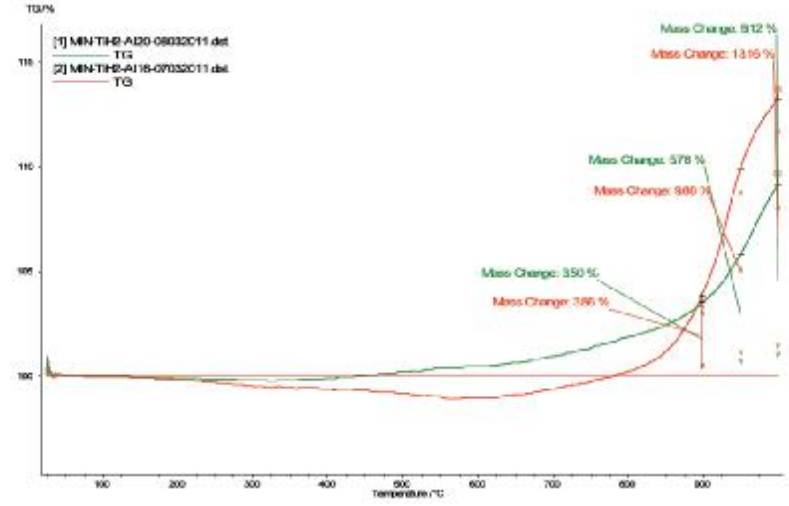
The absence of XRD Ti_3Al peaks is in agreement with Suryanarayana[4], who could not synthesise Ti_3Al, even after a very long period of milling, from TiH_2 and TiAl powders [18]. In the current work, Ti_3Al was also absent in the MA powders obtained with TiH_2 and aluminium powders as raw materials.

Figures 19b and 20b are TGA curves showing the mass changes that occurred with increasing temperature. Particular temperatures (800°C, 950°C, and 1050°C) were selected, and the mass changes at these temperatures assessed. As a general trend for all powders obtained by milling TiH_2 and Al, the TGA graphs showed mass losses from about 180°C to 800°C. The mass loss observed at the early stage of the TGA run was from the decomposition of residual titanium hydride. Beyond 800°C, the samples increased in mass up until 1050°C, when each run was stopped.

Figure 20b showed that TiH_2-Al32 0.5 at.% Ru had the highest mass increase at all selected temperatures, with 3.38% mass increase at 900°C, 8.02% at 950°C and 16.83% at 1050°C, followed by TiH_2 -Al32 1.5 at.% Ru with 1.97% mass increase at 900°C, 8.07% at 950°C and 11.06% at 1050°C. The TiH_2 Al32 2.0 at.% Ru powder exhibited the lowest mass increase with 1.34% mass increase at 900°C, 5.40% at 950°C and 8.52% at 1050°C. Given that the mass increase observed was due to oxygen pick-up by the different powders, it is evident that TiH_2-Al32 2.0 at.% Ru with the highest ruthenium content exhibited the lowest oxygen pick-up. This effect was more visible when the temperature was increased to 1050°C. These observations showed that as the ruthenium content was increased, the oxidation resistance of the powder was increased. The results of DSC and TGA have shown that 900°C was in the temperature ranges (890 – 960°C) where agglomeration of particles took place.

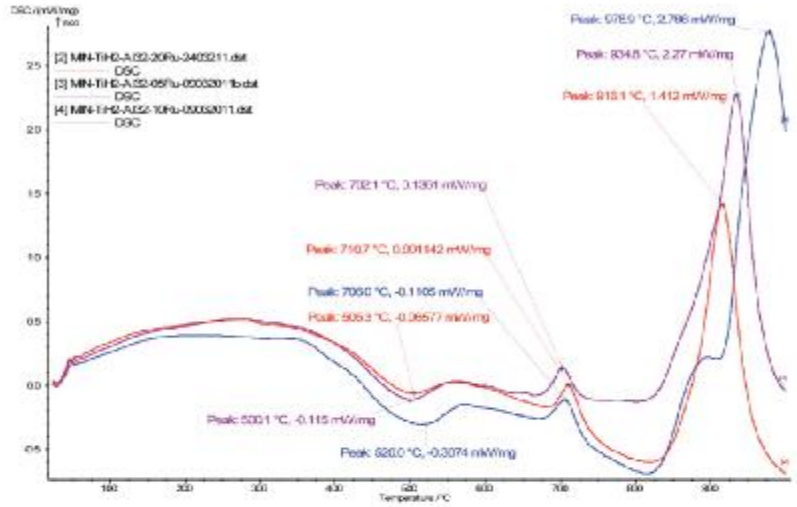


a. DSC

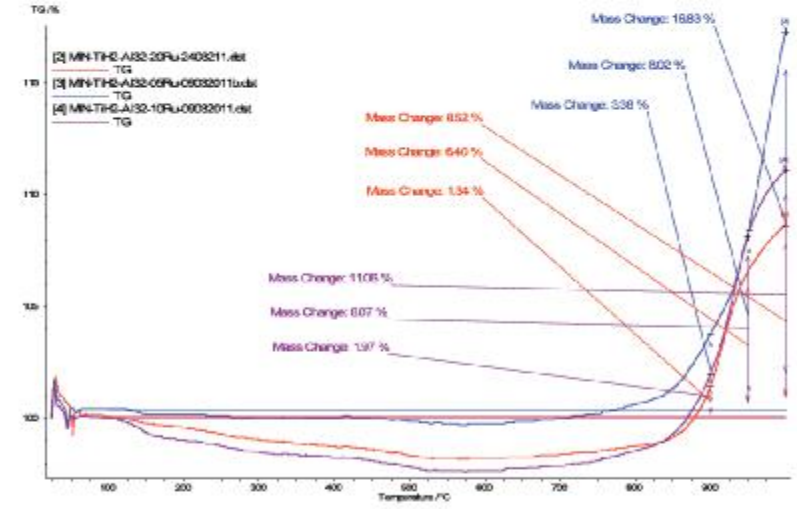


b. TG

Figure 19. (a) DSC and (b) TG curves for TiB_2-Al 16 and TiB_2-Al 20-6.2 at.% Ru powders



a. DSC



b. TG

Figure 20. (a) DSC and (b) TG curves for TiH_2-Al32 with 0.5, 1.5 and 2.0 at.% Ru

Conclusion

Elemental titanium powder or titanium hydride powder (TiH_2) were mixed with elemental aluminium powder, and milled for mechanical alloying in the presence of stearic acid as a process control agent. These powders were characterized for the apparent density, particle size and size distribution, particle morphology, microstructure, transformations upon heating, and high temperature oxidation behaviour. The following conclusions were drawn.

- Mechanically alloyed powders had a very low apparent density around 1.0 g/cm^3
- Mechanically alloyed powders obtained with titanium hydride exhibited a bimodal distribution due to a high level of agglomeration. Particles smaller than 1 µm across were obtained and they agglomerated to form larger particles up to 500 µm
- The morphology of the milled particles was rounded and angular, with more rounded particles among the fines. This occurred for MA powders obtained with TiH_2 powder, while pure titanium gave MA powder consisting of flake like particles
- No particular phase was visible in the mechanically alloyed powder, and heat treatment at 900°C for 1 hour resulted in the formation of TiAl, Ti_2AlC, Al_2O_3 and TiO_2 for the ruthenium-free powder and powder containing 0.2 at % ruthenium. In addition to these phases, powders containing 0.5 at % Ru or more also showed RuAl and the $Ti_6Ru_2Al_{16}$ ternary phase
- After heat treatment, powder obtained from elemental titanium powder comprised TiAl, Ti_2AlC, and Ti_3Al
- The different phases formed during heat treatment, with crystallization occurring between 900 and 1000°C
- The high-temperature oxidation resistance increased with the ruthenium content
- Powder with 0.2 at % Pt showed a behaviour close to powder containing 0.2 at % Ru

Acknowledgements

The authors would like to thank the Department of Science and Technology, Advanced Metals Initiative Precious Metals Development Network and Mintek for permission to publish this work and financial support, and the University of the Witwatersrand for hosting the project. L.A. Cornish thanks the National Research Foundation.

References

[1] C. Leyens and M. Peter. 2003. Titanium and titanium alloys: Fundamentals and applications, Wiley-VCH Verlag GmbH & KGaA, pp.333–496.

[2] F Appel, J.D.H. Paul and M. Oehring, 2011, Gamma titanium aluminide alloys: Science and Technology, Wiley VCH Verlag GmbH & KGaA, pp 249-515.

[3] T. Tetsui and Y. Miura, 2002, Heat resistant cast TiAl alloy for passenger vehicles, *Mitsubishi Heavy Industries, Ltd., Technical Review*. 39(1), pp.1-5.

[4] S.C. Huang and J.C. Chesnutt, 1994, Gamma TiAl and its alloys, *Intermetallic Compounds*, 2, John Wiley & Sons Ltd, pp. 73-89.

[5] B. Mer and Y. Miyamoto, 2001, Preparation of Ti-Al intermetallic compounds by spark plasma sintering, *Metallurgical and Materials Transactions A*, 32A, pp.843-847.

[6] C. Suryanarayana, Mechanical alloying and milling, Marcel Dekker edition, 270 Madison Avenue, New York, USA, 2004

[7] C.C. Koch and J.D. Wittenberg, 1996, Mechanical milling/alloying of intermetallics, *Intermetallics* 4, pp 339-355.

[8] O.M. Ivasishin, A.N. Demidik, and D.G. Savvakin, 1996, Use of titanium hydride for the synthesis of titanium aluminides from powder materials, *Powder Metallurgy and Metal Ceramics*, 35(9-10), pp.482-487.

[9] L.A. Mwamba and L. Chown, 2011, The use of titanium hydride in blending and mechanical alloying of Ti-Al alloys, *Journal of The Southern African Institute of Mining and Metallurgy*, 111, pp.159-165.

[10] V. Jacob, R. Baccino and F. Moret, 1993, Microstructural transformation during the mechanical alloying of Ti-47.5Al-3Cr titanium aluminide powder, *Proceedings of the 2nd Conference on Structural Applications of Mechanical Alloying*, Vancouver, British Columbia, Canada, 20-22 September, pp. 33-39.

[11] M. Sherif El-Eskandarany. 2011, Mechanical Alloying: for Fabrication of Advanced Engineering Materials. Noyes Publications. 13 Eaton Avenue. Norwich, NY 13815.

[12] M. Hüller, G.G. Chanik, E.L. Fokina and N. I. Budin. 2008, Mechanical alloying in planetary mills of high acceleration, *Review of Advanced Materials Science*, 18. pp.366-374.

[13] A. Manaf and M.A. Elita Hafizah. 2012, Particle size of mechanically alloyed La0.5Sr0.5Fe0.5Mn0.25Ti0.25O3 powders prepared with the assistance of ultrasonic irradiation. *Journal of Materials Science Research*, 1(2), pp.98-105.

[14] R.M. German. 2005, Powder Metallurgy and Particulate Materials Processing, Metal Powder Industries Federation. pp.55-92.

[15] M. Rhodes, 1990, Principles of Powder Technology, John Wiley & Sons Ltd, Chichester, England. pp.55-68.

[16] R.L. Saud and C.R. Shakespeare, 1956, Powder metallurgy: Practice and applications, George Newnes Limited, London, England, pg.7-27.

[17] The Titanium-Aluminum (Ti-Al) Phase Diagram calculated with Thermo-Calc software, coupled with SSOL2 thermodynamic database. http://www.calphad.com/pdf/Ti_Al_Phase_Diagram_Atomic_Per_Celsius.pdf [Accessed 22 June 2011].

[18] L. Lu and M.O Lai, 1998, Mechanical Alloying, Kluwer Academic Publishers, Norwell, Massachusetts.

ASSESSMENT OF COATING OBTAINED BY COLD SPRAYING MECHANICALY ALLOYED POWDER ONTO TITANIUM GRADE 2 AND Ti-6Al-4V

I.A. Mwamba[1,2,3], L.A. Cornish[2,3], J.S. Moema[1,3] and J.M. Papo[1,3]

[1]Advanced Materials Division, Mintek, Randburg, South Africa, [2]School of Chemical & Metallurgical Engineering, [3]DST-NRF Centre of Excellence in Strong Materials, University of the Witwatersrand, Johannesburg

Titanium aluminides show promise as materials for high-temperature turbine components, due to their strength at high temperatures, light weight and good oxidation properties[1]. However, the resistance to oxidation above 800°C is low. Below this temperature, the oxidation resistance is better than conventional titanium-based alloys, making γ-TiAl alloys a promising coating material for titanium-based alloys.

Many attempts have been made to improve the high temperature oxidation resistance of γ-TiAl, including the sputtering of an Al film and subsequent interdiffusion treatment at 600 °C for 24 h in a high vacuum[1-2], sputtering of a Ag-containing TiAl coating and insertion of silicon in the coating material of TiAl[3]. The improved oxidation resistance is due to the aluminium-rich silicon-modified $TiAl_3$ phase[4]. Niobium, W, and Cr[5] significantly improve the oxidation resistance of γ-TiAl based alloys.The purpose of this study was to investigate the adhesion and oxidation resistance of PGM-doped γ-TiAl coatings on titanium-based alloys.

Ti-47.5 at.% Al with additions of 0.5 at.% PGMs (Pd, Pt, Ru and Ir) was prepared by mechanical alloying and used as coatings on titanium Grade 2 and Ti-6Al-4V substrates. The coatings and substrates were characterized by SEM and EDX (Table 1), in the as-sprayed condition, and after exposure to air at 950°C in a tube furnace for 24 hours under a flow of mixed argon and air, and furnace cooled.

The coating layers adhered well to the substrates. Alumina particles from the surface cleaning operation by sandblasting were embedded in the substrate at the coating-substrate interface. The interface between the substrate and the coating layer was irregular. Oxidation tests conducted on the coated substrates revealed that the coating layers provided protection, as there was no oxide layer emanating from the substrate under the coating layer. As expected, the uncoated sides of substrates showed oxide formation for both titanium Grade 2 and Ti-6Al-4V. Figure 1 is BSE image showing the Al_2O_3 particles at the interface of the Ti-6Al-4V substrate, and Figure 2 is an image of the cross section surface of the uncoated Ti-6Al-4V substrate.

In conclusion, mechanically alloyed γ-TiAl powder can be successfully coated on titanium substrates with sufficient adhesion to provide enough protection against oxidation.

References:
1. Froes, F.H., *et al.* (1992) J. Mat. Sci., 27, 5113.
2. Chu, M.S. and Wu, S.K., (2003) A. Mat. 51, 3109.
3. Hui-ren, J., *et al.* (2008) Trans. Non-fer. Met. Soc. China 6, 512.
4. Braun, R., *et al.*, (2010) Internet. 10, 479.
5. L. Xin, L., *et al.*, (2008), Internet. 11, 661.
6. Cesal, M., *et al.*, (2006) J. of Ach. Mat. Man. Eng. 18, 459.
7. Huang, S.C. and Chesnutt, J.C., (1994) Westbrook, J.H. and Fleischer, R.L. (Ed.), 73.



Figure 1. SEM-BSE image of the coating layer and interface of Ti-6Al-4V.

Table 1. EDX analyses of the coating layer shown in Figure 1.





Figure 2. SEM-BSE images of cross sectional surfaces of coated Ti-Al-4V substrate.

Corresponding author: alainm@mintek.co.za